Dissertation

submitted to the

Combined Faculties of the Natural Sciences and Mathematics
of the Ruperto-Carola University of Heidelberg, Germany

for the degree of

Doctor of Natural Sciences

Put forward by

Nicolas Wink

born in: Leimen, Germany
Oral examination: May 6th, 2020

Towards the spectral properties and phase structure of QCD

Referees: Prof. Dr. Jan M. Pawlowski
Prof. Dr. Jörg Jäckel

Towards the spectral properties and phase structure of QCD

In this thesis we explore a multitude of aspects concerning strongly coupled quantum field theories, with a special focus on QCD. The first part of the thesis is concerned with formal developments, with the noteworthy highlight of enabling the use of hydrodynamic numerical methods in Functional Renormalization Group equations. This lead to the subsequent discovery of discontinuous solutions for the effective potential in the vicinity of first order phase transitions.

The second part of the thesis concerns the calculation of momentum dependencies of elementary correlation functions. Hereby, the main focus is the determination of said correlation functions in Minkowski space-time. Embracing the implications of having a spectral representation, we calculate the spectral function of a scalar theory, making use of dimensional regularization in a fully numerical set-up. Making appropriate use of the underlying analytic structure we devise a novel method for spectral reconstruction, which we apply to the gluon.

The third part concerns the subsequent extraction of observables based on the moments of the Quantum Effective Action. Most notably: we calculate the shear and bulk viscosity of Yang-Mills; we make use of the retarded correlation functions to look at the out-of-equilibrium evolution of a low energy effective theory of QCD and estimate the equilibration times for different equilibrium backgrounds.

Fortschritte in der Untersuchung spektraler und phasenstruktureller Eigenschaften der QCD

In dieser Arbeit untersuchen wir mehrere Aspekte stark korrelierter Quantenfeldtheorien, hierbei liegt der Hauptfokus auf der Untersuchung von QCD. Der erste Teil der Arbeit beschäftigt sich mit Methodenentwicklung, wobei das ansehnlichste Ergebniss die Anwendung von numerischen Methoden aus der Hydrodynamik auf Gleichungen, die aus der Funktionalen Renormierungsgruppe hervorgehen. Diese Entwicklung führte zur Entdeckung von diskontinuierlichen Lösungen des Effektiven Potenzials in der unmittelbaren Umgebung von Phasenübergängen erster Ordnung.

Der zweite Teil der Arbeit beschäftigt sich mit der Berechnung von Impulsabhängigkeiten der elementaren Korrelationsfunktionen. Dabei ist der Hauptfokus diese Korrelatiosfunktionen in der Minkowski Raumzeit zu bestimmen. Durch Ausnutzen der Implikationen einer Spektraldarstellung gelang es uns dimensionelle Regularisierung in einer rein numerischen Rechnung zu verwenden und konnten so die Spektralfunktion in einer Skalartheorie ausrechnen. Weiterhin konnten wir die implizierte analytische Struktur verwenden um ein neues Rekonstruktionsverfahren für Spektralfunktionen herzuleiten und es auf das Gluon anzuwenden.

Im letzten Teil dieser Arbeit beschäftigen wir uns mit der Extraktion von Observablen, basierend auf Momenten der Quantum Effective Action. Am nennenswertesten ist dabei einerseits die Berechnung der Scheerviskosität und Zähigkeitsviskosität in Yang-Mills. Andererseits konnten wir die retadierten Korrelationsfunktionen verwenden um die Nichtgleichgewichtsevolution einer Niederenergietheorie der QCD anzugucken und dabei die Equilibrierungszeit zu bestimmen.

Contents

1. Introduction

1.1. Motivation

The notion of strongly correlated quantum systems is omnipresent in our modern understanding of physics. Ranging from condensed matter systems, cold atom experiments, the infrared regime of quantum chromodynamics or ultraviolet regime of quantum gravity, their understanding is closely connected to the successful handling of strongly correlated quantum systems. Here we are particularly interested in the understanding of the infrared regime of quantum chromodynamics, the theory describing quarks and gluons. The rich infrared phenomenology of the theory is closely linked to the rich infrared phenomenology of the purely gluonic dynamics. The non-Abelian gauge theory describing the glue sector was introduced by Yang and Mills [15] in 1954, hence the name Yang-Mills theory.

Despite being known for over 65 years, the mechanism behind confinement, i.e. that the theory is mass gapped and that gluons cannot be observed, is not fully understood yet. From a theoretical perspective this problem is extremely challenging, in fact its one of the seven Millennium Prize Problems [16], as its closely related to proving the existence of the associated quantum field theory. Apart from this fundamental problem in Yang-Mills theory one has to deal with the complications of a resonant four-quark interaction in full quantum chromodynamics. This induces a rich bound state structure, which makes up a significant portion of the matter around us. Experimentally, hadron properties are to a large extend very well known. However, theoretically they still pose a major problem when considering higher and/or broad resonances.

Another major challenge presented by QCD is the determination of its phase structure at finite baryon number densities. One aspect of this question that attracted a lot of attention over the last years is whether or not there exists a critical endpoint. Experimentally, the phase structure is approached by heavy-ion collisions, currently this includes RHIC [17] and LHC [18] and additionally CBM [19] and NICA [20] in the near future. Connecting experimental signatures to precise features in the phase diagram, such as a critical endpoint, poses major obstacles. On the theoretical side two major non-perturbative first principle approaches exists: Lattice QCD and Functional Methods. Both approaches come with their own set of advantages and disadvantages. Focusing on the question of the phase structure, Lattice QCD has yielded remarkable results at vanishing and small net baryon densities, see e.g. [21–24]. However, its progress to the entire phase structure have been hindered by the infamous sign-problem, see e.g. [25, 26]. Functional Methods on the other hand, do not face any further technical complications when introducing a finite net baryon density. Their major drawback is establishing the convergence, within their own version of an "continuum limit". For recent works on the phase structure from Functional Methods see e.g. [27–29].

When trying to connect theoretical results for the phase structure of QCD with experimental signatures one is faced with yet another problem. The phase diagram of QCD is inherently a quantity associated with equilibrium. The situations in heavy-ion collisions

is, however, far from equilibrium. This is immediately obvious when considering the initial stages of such a collision, see e.g. [30]. How and on what time scales the system approaches local equilibrium, and hence allows for a connection to equilibrium QCD questions such as the phase structure, is still subject of ongoing research.

The problems outlined above are the driving questions for the projects considered in this thesis. Our main tool for addressing these questions are Functional Methods, i.e. the Functional Renormalization Group and Dyson-Schwinger Equations. Throughout this thesis we balance the technical development of these methods as well as physics applications with the overarching goal of addressing the questions outlined above. The individual projects that contribute to our understanding of QCD in the infrared regime, and strongly correlated systems in general, which are covered in this thesis, are motivated and put into context at the beginning of their chapter/section.

1.2. Publications

The thesis was written solely by the author, however most results were obtained in collaboration with colleagues. At the beginning of each section the corresponding collaboration is stated. Figures and texts taken from the resulting publications are not marked again. These publications are:

[1] **Finite temperature spectral functions in the O(N)-model**
Jan M. Pawlowski, Nils Strodthoff, Nicolas Wink
Published in Phys.Rev. D98 (2018) no.7, 074008
E-Print: arXiv:1711.07444

[2] **Reconstructing the gluon**
Anton K. Cyrol, Jan M. Pawlowski, Alexander Rothkopf, Nicolas Wink
Published in SciPost Phys. 5 (2018) no.6, 065
E-Print: arXiv:1804.00945

[3] **Time-evolution of fluctuations as signal of the phase transition dynamics in a QCD-assisted transport approach**
Marcus Bluhm, Yin Jiang, Marlene Nahrgang, Jan M. Pawlowski, Fabian Rennecke, Nicolas Wink
Published in Nucl.Phys. A982 (2019) 871-874
E-Print: arXiv:1808.01377

[4] **Bound state properties from the functional renormalization group**
Reinhard Alkofer, Axel Maas, Walid Ahmed Mian, Mario Mitter, Jordi París-López, Jan M. Pawlowski, Nicolas Wink
Published in Phys.Rev. D99 (2019) no.5, 054029
E-Print: arXiv:1810.07955

[5] **Resolving phase transitions with Discontinuous Galerkin methods**
Eduardo Grossi, Nicolas Wink
To be published in SciPostPhys
E-Print: arXiv:1903.09503

[6] **Spectral Reconstruction with Deep Neural Networks**
Lukas Kades, Jan M. Pawlowski, Alexander Rothkopf, Manuel Scherzer, Julian M. Urban, Sebastian J. Wetzel, Nicolas Wink, Felix Ziegler
E-Print: arXiv:1905.04305

[7] **Dynamics of critical fluctuations: Theory – phenomenology – heavy-ion collisions**
Marcus Bluhm, Marlene Nahrgang, Alexander Kalweit *et al.*
E-Print: arXiv:2001.08831
Comment: Report summarizing the presentations and discussions during the Rapid Reaction Task Force with the same title as the publication, which was organized by the ExtreMe Matter Institute EMMI and held at GSI, Darmstadt, Germany in April 2019.

Additionally, parts are taken from so far unpublished works, listed here:

[8] **-The Functional Renormalization Group- & applications to gauge theories and gravity**
Jan M. Pawlowski, Jacqueline A. Bonnet, Stefan Rechenberger, Manuel Reichert, Nicolas Wink
Comment: Lecture notes introducing the Functional Renormalization Group, with a particular focus on applications to Yang-Mills and Gravity

[9] **QMeS - Derivation**
Jan M. Pawlowski, Coralie S. Schneider, Nicolas Wink
Comment: A Mathematica package that expands a master equation in its moments based on the superfield formalism

[10] **An upwind Finite Difference scheme for Functional Renormalization Group equations**
Eduardo Grossi, Jan M. Pawlowski, Nicolas Wink
Comment: Extension of [5] – going beyond the large N limit with upwind Finite Difference Methods.

[11] **Spectral representations of elementary correlation functions**
Jan M. Pawlowski, Nicolas Wink
Comment: Spectral representations for elementary correlation functions are derived. We show that a single spectral representation is sufficient to represent any n-point function in the entire complex momentum domain.

[12] **Spectral functions in the ϕ^4-theory from DSE using dimensional regularization**
Jan Horak, Jan M. Pawlowski, Nicolas Wink
Comment: Using spectral representations we are able to dimensional regularization in DSEs, while staying in a completely numerical setting

[13] **Robust determination of the trace anomaly in gauge theories from the Functional Renormalization Group**
Jan M. Pawlowski, Nicolas Wink
Comment: The thermal trace anomaly of Yang-Mills is determined via a metric variation of the Quantum Effective Action.

[14] **Shear and Bulk viscosity of Yang-Mills from first principles**
Jan M. Pawlowski, Nicolas Wink
Comment: The shear and bulk viscosity are extracted from a diagrammatic representation of the Energy-Momentum Tensor.

2. Functional Methods

This chapter is in parts based on [8].

This chapter introduces Functional Methods. For the purpose of this thesis, a particular focus is put on Dyson-Schwinger Equations (DSE) [31–33] and the Functional Renormalization Group (FRG) [34–36] in the context of high energy physics. Only a brief outline of these methods will be given in this introducing, more complete reviews can be found in the literature. For FRG related reviews see e.g. [8, 37–43]. For DSE related reviews see e.g. [27, 44–49].

2.1. Generating functionals

This introduction considers only Quantum Field Theories (QFT) in Euclidean space-time, the equivalence to formulations in Minkowski space-time is discussed in Chapter 6. In order to keep expressions traceable a condense notation is used, i.e. $f \cdot g = \int_x f(x)g(x)$.

For illustrative purposes the following is restricted to a real scalar field $\varphi(x)$ in d dimensions in Euclidean space-time, generalizations will be considered later. The basic object under consideration in the a QFT is its generating functional $\mathcal{Z}[J]$, as a function of some external source $J(x)$. The knowledge about the generating functional can equivalently be expressed by the knowledge of all its moments, the correlation functions or also called Green functions

$$\langle \varphi_1 \dots \varphi_n \rangle_J = \frac{1}{\mathcal{Z}[J]} \frac{\delta^n \mathcal{Z}[J]}{\delta J_1 \dots J_n} , \tag{2.1}$$

where the index denotes the space-time dependence, i.e. $\varphi_i \equiv \varphi(x_i)$. The subscript J at the correlation function marks its dependence on the source $J(x)$ that determines the background. In principle it's sufficient to work with the set of correlation functions (2.1) since they define the generating functional $Z[J]$ and an explicit representation is not necessary. Nevertheless, a path integral makes the heuristic derivation of the required equations simple and serves as an appropriate illustrative tool. In this context, the path integral representation of the generating functional is given by

$$\mathcal{Z}[J] = \frac{1}{\mathcal{N}} \int [\mathrm{d}\varphi]_{\mathrm{ren}} \exp\left\{-S[\varphi] + J \cdot \varphi\right\} , \tag{2.2}$$

where $S[\varphi]$ is the classical action. The expression $[\mathrm{d}\varphi]_{\mathrm{ren}}$ denotes the flat functional measure, where flat denotes the invariance under space-time dependent shifts $d(x)$ of the field and the subscript "$_{\mathrm{ren}}$ denotes the fact that we assume it to be regularized and renormalized. The normalization factor $\mathcal{N}$ is arbitrary, since its irrelevant for correlation functions, cf. (2.1). The resulting set of correlation functions contains a large number of redundant information since a part of the correlation functions at a given order n contain disconnected pieces that can be expressed entirely in terms of lower order correlation functions.

In diagrammatic descriptions the associated diagrams are disconnected, hence the name. The disconnected parts can be removed if one considers the *Schwinger functional*, which is simply given by the logarithm

$$\mathcal{W}[J] = \log \mathcal{Z}[J] \,. \tag{2.3}$$

This can be proven via induction by considering the FRG or DSE for (2.3), see e.g. [8]. In particular, its two-point function is the propagator, a fundamental object in functional approaches, which is given by

$$G_{1,2} \equiv G(x_1, x_2) = \frac{\delta^2 \mathcal{W}[J]}{\delta J_1 \delta J_2} = \langle \varphi_1 \varphi_2 \rangle - \langle \varphi_1 \rangle \langle \varphi_2 \rangle = \langle \varphi_1 \varphi_2 \rangle_{\mathrm{c}} \,. \tag{2.4}$$

In (2.4) the subscript c denotes the connected part. In a Euclidean QFT the propagator is necessarily positive for semi-definite and its spectrum is positive, including zero, for all backgrounds. For a discussion regarding the convexity of the Schwinger functional itself see e.g. [50]. Despite the huge reduction in redundancies when going to the Schwinger functional its moments still contain a large amount of trivial redundancies. This redundancy can be expressed by separating connected correlation functions into a one-particle irreducible (1PI) and one-particle reducible ones. In a diagrammatic language, 1PI diagrams are the ones, which cannot be separated into two disconnected parts by cutting a single line. If the diagram can be separated by cutting a single line, it can be expressed by multiplying the two disconnected parts, times the cut propagator. Generically, the disconnected parts are then of the same or lower loop order, and hence already contained. Consequently, 1PI diagrams are already encode the entire information of the theory. The generating functional for 1PI correlation functions is called the *Quantum Effective Action* (QEA), or just *Effective Action*, and is the Legendre transform of the Schwinger functional. Introducing the expectation value of the field $\phi = \langle \varphi \rangle$, the relation between the QEA and the Schwinger functional is

$$\Gamma[\Phi] = \sup_J \{ J \cdot \phi - \mathcal{W}[J] \} = J_{\mathrm{sup}} \cdot \phi - \mathcal{W}[J_{\mathrm{sup}}] \,, \tag{2.5}$$

where $J_{\mathrm{sup}} = J_{\mathrm{sup}}[\phi]$ is a field dependent current. From now one we will understand the supremum implicitly and drop the subscript. The 1PI property can be proven similar to the corresponding connected property of the Schwinger functional. Another very important property of the QEA is its convexity, which follows directly from being a Legendre transform, see e.g. [50]. The QEA can be seen as the quantum analogue of the classical action. The field ϕ is the mean field at a given background current J. Restricting to differentiable situations, with a maximum at J_{sup}, for illustrative simplicity, the desired property can be seen by taking a derivative of the second term in (2.5), which equals zero, and using (2.3),

$$\phi(x) = \frac{\delta \mathcal{W}[J]}{\delta J(x)}\bigg|_{J_{\mathrm{sup}}} = \frac{1}{\mathcal{Z}[J]} \frac{\delta \mathcal{Z}[J]}{\delta J(x)}\bigg|_{J_{\mathrm{sup}}} = \langle \varphi(x) \rangle_{J_{\mathrm{sup}}} \,, \tag{2.6}$$

where the last equality is simply the definition of the expectation value (2.1). Taking a derivative with respect to the field instead of the source provides us with the one-point function

$$\frac{\delta \Gamma[\phi]}{\delta \phi(x)} = J \,, \tag{2.7}$$

where the field dependence of the source cancels since the source is understood at a maximum. Equation (2.7) are the quantum equations of motion (EoM) at a given background current J. Particularly, for a vanishing source they reduce to the vacuum equation of motion, since the QEA $\Gamma[\phi = \phi_{a\,\text{EoM}}] = -\mathcal{W}[J=0]$ becomes the vacuum free energy.

From the perspective of functional approaches, the QEA is the central object. Hence, its natural to work in moments of the QEA, which we will denote by

$$\Gamma^{(n)}(x_1, \ldots, x_n) = \frac{\delta^n \Gamma[\phi]}{\delta\phi_1 \ldots \delta\phi_n} \,. \tag{2.8}$$

In order to facilitate the fact that these are the fundamental objects appearing in Functional Methods, we refer to them as *elementary correlation functions*. As already pointed out, the propagator is fundamental in functional methods. This is underlined by its connected to the two-point function of the QEA, they are the inverse of each other

$$\begin{aligned} \int_{x_3} G(x_1, x_3)\, \Gamma^{(2)}(x_3, x_2) &= \int_{x_3} \frac{\delta^2 \mathcal{W}[J]}{\delta J_1 \delta J_3} \frac{\delta^2 \Gamma[\phi]}{\delta\phi_3 \delta\phi_2} \\ = \int_{x_3} \left(\frac{\delta}{\delta J_1} \frac{\delta \mathcal{W}[J]}{\delta J_3} \right) \left(\frac{\delta}{\delta\phi_3} \frac{\delta\Gamma[\phi]}{\delta\phi_2} \right) &= \int_{x_3} \frac{\delta\phi_3}{\delta J_1} \frac{\delta J_2}{\delta\phi_3} = \delta(x_1 - x_2) \,. \end{aligned} \tag{2.9}$$

So far all equations were mostly of defining nature and introducing the necessary quantities for Functional Methods. In the following a diagrammatic representation for general correlation functions in terms of the propagator G and n-point functions $\Gamma^{(n>2)}$ is introduced. Such expansions are the hearth of Skeleton expansions, but are also of importance when considering composite operators. We start by pulling a J derivative out of the original definition of the correlation functions (2.1), where we have to compensate for the normalisation

$$\frac{1}{\mathcal{Z}[J]} \frac{\delta^n \mathcal{Z}[J]}{\delta J_1 \ldots J_n} = \left(\frac{\delta}{\delta J_1} + \phi_1 \right) \frac{1}{\mathcal{Z}[J]} \frac{\delta^{n-1} \mathcal{Z}[J]}{\delta J_2 \ldots J_n} \,. \tag{2.10}$$

This can be repeated recursively and hence the correlation function can be expressed in terms of J derivatives and the expectation value of the field. Therefore, its desirable here to express the J derivative in terms of a derivative with respect to the field expectation value ϕ. This can be done in a straight forward manner

$$\frac{\delta}{\delta J_1} = \int_{x_2} \frac{\delta\phi_2}{\delta J_1} \frac{\delta}{\delta\phi_2} = \int_{x_2} G(x_1, x_2) \frac{\delta}{\delta\phi_2} \,, \tag{2.11}$$

which used the fact that ϕ is the first moment of the Schwinger functional. Using (2.11) its possible to rewrite (2.10) in a self-contained manner

$$\langle \varphi_1 \ldots \varphi_n \rangle = \prod_{i=1}^{n} \left(\int_{x_j} G(x_i, x_j) \frac{\delta}{\delta\phi_j} \right) . \tag{2.12}$$

This relation underlines the fundamental role of the propagator once more. While the equation (2.12) is rather impressive and important by itself, as it allows for an easy and systematic access to the full correlation function in terms fo the propagator and the moments of the QEA. However, it allows for a much stronger relation between correlation

functions, as it generalizes immediately to any operator that has a well defined series representation. More explicitly, for an operator $\mathcal{O}[\varphi]$ the expectation value can be expressed as

$$\langle \mathcal{O}[\varphi] \rangle = \mathcal{O}\left[\varphi = G \cdot \frac{\delta}{\delta\phi} + \phi\right] . \tag{2.13}$$

To this end, it might not be obvious that the resulting expressions arising from the application of (2.13) encode the result in terms of the propagator and the elementary correlation functions. This can be easily seen by working out the derivative of the propagator with respect to the field expectation value

$$\frac{\delta}{\delta\phi_3} G(x_1, x_2) = -\int_{z_1,z_2} G(x_1, z_1)\, \Gamma^{(3)}(z_1, x_3, z_2)\, G(z_2, x_2) . \tag{2.14}$$

2.1.0.1. Example: three-point correlation function $\langle \varphi_1 \varphi_2 \varphi_3 \rangle$

To close this part, we give an illustrative example of (2.13). Additionally, this allows us to easily introduce the associated diagrammatic notation.

Within the current setting of a real scalar field, we want to access $1 \to 2$ scattering, i.e. want to access the three-point correlation function $\langle \varphi_1 \varphi_2 \varphi_3 \rangle$. Suppose we got from some method the QEA, we are only left with applying (2.13).

$$\begin{aligned} \langle \varphi_1 \varphi_2 \varphi_3 \rangle = &\left(\int_{x_4} G(x_1, x_4) \frac{\delta}{\delta\phi_4} + \phi_1 \right) \left(\int_{x_5} G(x_2, x_5) \frac{\delta}{\delta\phi_5} + \phi_2 \right) \times \\ &\times \left(\int_{x_6} G(x_3, x_6) \frac{\delta}{\delta\phi_6} + \phi_3 \right) . \end{aligned} \tag{2.15}$$

After a straightforward calculation and the application of (2.14) we obtain

$$\begin{aligned} \langle \varphi_1 \varphi_2 \varphi_3 \rangle = &\phi_1\phi_2\phi_3 + \phi_1 G(x_2, x_3) + \phi_2 G(x_1, x_3) + \phi_3 G(x_1, x_2) \\ &- \int_{x_4,x_5,x_6} G(x_1, x_4) G(x_2, x_5) G(x_6, x_3) \Gamma^{(3)}(x_5, x_4, x_6) . \end{aligned} \tag{2.16}$$

This result is of course easy to interpret, as it's almost trivial. The first four terms in (2.16) are the disconnected pieces, where parts are given by the expectation value of the field and the last term is the fully dressed vertex.

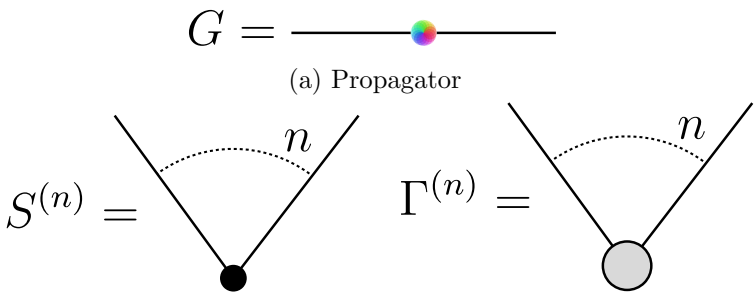

(a) Propagator

(b) Classical vertex

(c) Full vertex

Figure 2.1.: Summary of the diagrammatic notation used for Dyson-Schwinger Equations.

2.2. Dyson-Schwinger equations

This section introduces Dyson-Schwinger equations, one of the main tools in Functional Methods. So far we refrained from making explicit use of the path integral representation. However, in the following its use is convenient and illustrative. In order make practical use, we first express the path integral representation of correlation functions (2.2) entirely in terms of the QEA by making use of (2.3) and (2.5)

$$e^{-\Gamma[\phi]} = \int [\mathrm{d}\chi]_{\mathrm{ren}} \exp\left\{ - S[\phi+\chi] + \chi \cdot \frac{\delta\Gamma[\phi]}{\delta\phi} \right\}, \tag{2.17}$$

where we made use of the aforementioned invariance of the flat path integral measure under shifts. Let us mention again, that this is a rather non trivial property, given that the renormalization is hidden in this measure. Note that by definition the expectation value of the new field χ vanishes by construction, as the shift was precisely the mean field. Taking a ϕ derivative and multiplying (2.17) with a factor of $\exp\Gamma[\phi]$ leads to

$$\frac{\delta\Gamma[\phi]}{\delta\phi(x)} = \left\langle \frac{\delta S[\phi+\chi]}{\delta\phi(x)} \right\rangle. \tag{2.18}$$

In particular, the quantum equation of motion is given by the expectation value of the classical equation of motion. A closed form expression is now easily obtained by utilizing (2.13), given that the action has a well defined series representation. In particular this is the case for the Standard Model of particle physics, a simple ϕ^4 theory and many more. This leads us to the Dyson-Schwinger equation

$$\frac{\Gamma[\phi]}{\delta\phi(x)} = \frac{\delta S}{\delta\varphi(x)}\left[\varphi = G\cdot\frac{\delta}{\delta\phi} + \phi\right], \tag{2.19}$$

one of the quantum master equations we will work with in this thesis. From (2.19) the elementary correlation functions $\Gamma^{(n\geq 1)}$, and their equations, can be obtained by taking functional derivatives of the equation. In turn, the zero-point function cannot be obtained directly from (2.19) and has to be determined differently.

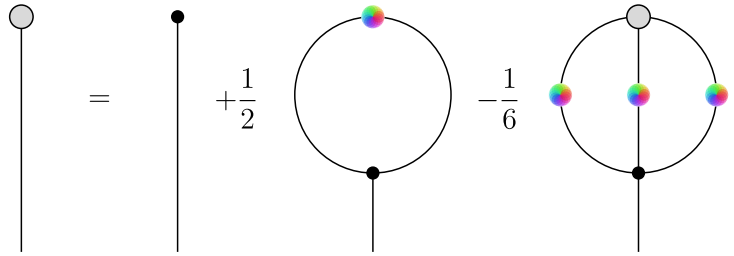

Figure 2.2.: Diagrammatic representation of the master DSE in scalar theory (2.21).

2.2.0.1. Example: ϕ^4-theory

In order to outline the general procedure when working with DSEs (2.19) we show a short example for a real scalar field with a cubic and quartic interaction. The classical action for this theory is given by

$$S[\varphi] = \int_x \left[\frac{1}{2}\partial_\mu\varphi(x)\partial_\mu\varphi(x) + \frac{m^2}{2}\varphi(x)^2 + \frac{\lambda_4}{4!}\varphi(x)^4 \right] . \tag{2.20}$$

From this we obtain in a straightforward manner the master DSE, based on (2.19),

$$\Gamma^{(1)}[\phi] = S^{(1)}[\phi] + \frac{\lambda_4}{2}\, G\cdot\phi - \frac{\lambda_4}{6}\, G\cdot\Big(G\cdot\Gamma^{(3)}\cdot G\Big) , \tag{2.21}$$

where λ_4 denotes the classical four-point function. Our diagrammatic notation for such equations in the context of DSEs is introduced in Figure 2.1, based on this (2.21) can be expressed diagrammatically, shown in Figure 2.2. As discussed previously, the equations for the elementary correlation functions, i.e. the n-point functions, are now simply obtained by taking functional derivatives of the master DSE (2.21). Taking one derivative, we arrive at the equation for the two-point function

$$\begin{aligned}\Gamma^{(2)}[\phi] = S^{(2)}[\phi] &+ \frac{\lambda_4}{2}\, G - \frac{\lambda_4}{2}\,\phi G\cdot\Gamma^{(3)}\cdot G \\ &+ \frac{\lambda_4}{2}\Big(G\cdot\Gamma^{(3)}\cdot G\Big)\cdot\Big(G\cdot\Gamma^{(3)}\cdot G\Big) - \frac{\lambda_4}{6}\, G\cdot\Big(G\cdot\Gamma^{(4)}\cdot G\Big) .\end{aligned} \tag{2.22}$$

The diagrammatic representation of (2.22) is given in Figure 2.3.

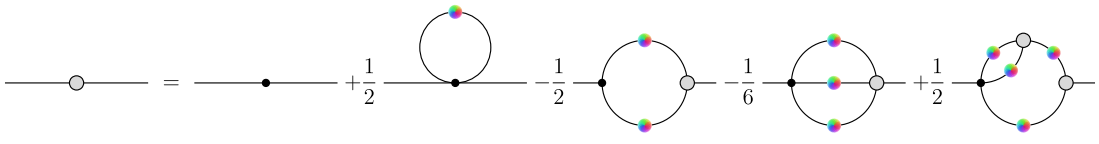

Figure 2.3.: Diagrammatic representation of the DSE for the two-point function a scalar theory (2.22). The diagrams are called *tadpole*, *polarization*, *sunset* and *squint*, respectively.

2.3. Functional Renormalization Group

In this section we introduce another important tool of Functional Methods, the Functional Renormalization Group. As for the DSE, it is easiest to motivate the FRG initially by considering a path integral approach. Heuristically, it provides a functional implementation of the Kadanoff block spinning idea [51], and its continuum formulation by Wilson [52, 53]. Technically, it amounts to solve the theory successively by integrating out momentum shells. To this end, let us consider a path integral measure, where modes of the field $\varphi(p)$ below a certain momentum scale k are excluded in a soft manner

$$\int [\mathrm{d}\varphi]_{\mathrm{ren},p^2\gtrsim k^2} = \int [\mathrm{d}\varphi]_{\mathrm{ren}} \exp\left\{-\Delta S_k[\varphi]\right\} . \tag{2.23}$$

The suppression factor is suggestively written as a modification of the classical action and chosen quadratic in the field

$$\Delta S_k[\varphi] = \frac{1}{2}\int_p \varphi(p) R_k(p) \varphi(-p) . \tag{2.24}$$

We want the regulator $R_k(p)$ to suppress the propagation of modes with momenta $p^2 \lesssim k^2$ and leaves the propagation of modes with momenta $p^2 \gtrsim k^2$ untouched. This is achieved by requiring the following properties:

1. Suppression of IR modes

$$\lim_{p^2\to 0} R_k(p) > 0 \tag{2.25}$$

2. Physical limit

$$\lim_{k\to 0} R_k(p) = 0 \tag{2.26}$$

3. UV asymptotics

$$\lim_{k\to\infty} R_k(p) = \infty . \tag{2.27}$$

In the limit of vanishing cutoff, $k \to 0$, the regulator is removed and the full theory is recovered, independent of the choice of the intermediate infrared regularisation. Further details will be given later after the introduction of the flow equation for the QEA.

The scale dependent generating functional is introduced by substituting the flat measure with its regularized version (2.23)

$$\mathcal{Z}_k[J] = \int [\mathrm{d}\varphi]_{\mathrm{ren}} \exp\left\{ - S[\varphi] - \Delta S_k[\varphi] + J\cdot\varphi \right\} . \tag{2.28}$$

We would like to note that if the original generating functional $\mathcal{Z}[J]$ defined in (2.1) is finite, then also the IR regularized version (2.28) is finite. However, as previously pointed out, we do not require a path integral. Mapping the φ dependence of the regulator term to a derivative of the external source it can be introduced as

$$\mathcal{Z}_k[J] = e^{-\Delta S_k\left[\frac{\delta}{\delta J}\right]} \mathcal{Z}[J] . \tag{2.29}$$

The change with lowering the cutoff scale can be expressed as derivative with respect to the scale k. However, it is convenient to introduce a reference scale Λ, which is typically taken as the UV cutoff scale, and work with the dimensionless RG-time

$$t = -\log \frac{k}{\Lambda} \,. \tag{2.30}$$

Please note that the RG-time is more commonly defined without the minus, With this at hand we get the flow equation for the scale dependent generating functional (2.29)

$$\partial_t \mathcal{Z}_k[J] = -\partial_t \Delta S_k \left[\frac{\delta}{\delta J}\right] \mathcal{Z}_k[J] \,. \tag{2.31}$$

Integrating the theory from some UV scale down to the physical limit $k = 0$ corresponds flowing with the RG-time from $t = 0$ to $t = \infty$ if the reference scale Λ and the UV scale are identified. Using (2.24) we can rewrite (2.31) as

$$\partial_t \mathcal{Z}_k[J] = -\frac{1}{2} \int_p \frac{\delta^2 \mathcal{Z}_k[J]}{\delta J(p) \delta J(-p)} \, \partial_t R_k(p) \,. \tag{2.32}$$

This is the flow equation for the generating functional $\mathcal{Z}[J]$. Based on this, it is trivial to obtain the flow equation for the Schwinger functional, the *Polchinski equation* [54], from its definition (2.3)

$$\partial_t \mathcal{W}_k[J] = -\frac{1}{2} \int_p \left[\mathcal{W}_k^{(2)}[J] + \left(\mathcal{W}_k^{(1)}[J]\right)^2 (p, -p) \, \partial_t R_k(p) \right] , \tag{2.33}$$

with a notation similar to the one introduced for the QEA, c.f. (2.8). The splitting into a two-point function and the one-point function squared in (2.33) is nothing but the splitting in a connected and a disconnected piece. Please note that the structure of the equation (2.33) does not change when using a UV instead of an IR cutoff. Finally, we are interested in the flow equation of the QEA. For this we take a closer look at the term containing the one-point connected correlation functions in (2.33)

$$\frac{1}{2} \int_p \mathcal{W}_k^{(1)}(p) \mathcal{W}_k^{(1)}(-p) \, \partial_t R_k(p) = \frac{1}{2} \int_p \phi(p) \phi(-p) \, \partial_t R_k(p) = \partial_t \Delta S_k[\phi] \,, \tag{2.34}$$

which shows the triviality of this term. Hence its convenient to subtract it from the QEA and define it as a modified Legendre transformation of $\mathcal{W}_k[J]$

$$\Gamma_k[\phi] = J \cdot \phi - \mathcal{W}_k[J] - \Delta S_k[\phi] \,, \tag{2.35}$$

which reduces to (2.5) in the full theory after all fluctuations have been integrated out. As before, J is understood as the ϕ dependent supremum of (2.35). Equation (2.7) gets modified and becomes

$$\frac{\delta(\Gamma_k[\phi] + \Delta S_k[\phi])}{\delta \phi(x)} = J(x) \,. \tag{2.36}$$

With this at hand, we can obtain the flow equation for the QEA by taking an RG-time derivative of (2.35) and inserting the flow equation for the Schwinger functional (2.33)

$$\begin{aligned}\partial_t\Gamma_k[\phi] =& -\partial_t\mathcal{W}_k[J] - \partial_t\Delta S_k[\phi] - \partial_t J\cdot\left(\phi - \mathcal{W}^{(1)}[J]\right)\\ =&\frac{1}{2}\,\mathrm{Tr}\;\mathcal{W}^{(2)}[J]\partial_t R_k + \partial_t\Delta S_k[\phi] - \partial_t\Delta S_k[\phi]\\ =&\frac{1}{2}\,\mathrm{Tr}\;G_k[\phi]\partial_t R_k\,.\end{aligned} \tag{2.37}$$

The second term in the bracket in the last term arises from the k-dependence of the current and the bracket subsequently cancels, as the first moment of the Schwinger functional is precisely the expectation value of the field. Additionally, we have switched to denoting the summation over internal degrees of freedom as a trace, which would be momentum integral in this case. In the last term in (2.37) we have introduced the scale dependent, regularized propagator which is given by the inverse of the two-point function of the Legendre transformation, i.e.

$$\Big[G_k[\phi]\Big]^{-1} = \Gamma_k^{(2)}[\phi] + \Delta S_k^{(2)} = \Gamma_k^{(2)}[\phi] + R_k\,. \tag{2.38}$$

With this at hand, we arrive at the Wetterich equation [34], the flow equation of the QEA

$$\partial_t\Gamma_k[\phi] = \frac{1}{2}\,\mathrm{Tr}\,\left(\Gamma_k^{(2)}[\phi] + R_k\right)^{-1}\partial_t R_k\,. \tag{2.39}$$

This equation will act as master equation for RG settings considered in this work. To be more precise, all equations the flow of all correlation functions can be obtained from (2.39).

2.3.1. Properties of the Wetterich equation

Due to its importance for this work, we would like to discuss it in more detail in the following.

2.3.1.0.1. Connection to the classical action

Being a differential equation, its important to discuss the initial conditions for (2.39). This is only done up to renormalization of the cutoff action Γ_Λ, which we will comment on below. Looking at the path integral representation for the QEA, analogously to (2.17), we get an equation where its suitable to study the limit $k\to\infty$

$$e^{-\Gamma_k[\phi]} = \int[\mathrm{d}\chi]_{\mathrm{ren}}\,\exp\left\{-S[\phi+\chi] - \Delta S_k[\chi] + \chi\cdot\frac{\delta\Gamma_k[\phi]}{\delta\phi}\right\}. \tag{2.40}$$

In the limit of large RG-scales k, the infrared cutoff dominates the path integral and all other dependencies on the fluctuating field χ can be neglected as subleading terms in an expansion in powers of said scale k. As a result, the term proportional to $\delta\Gamma_k[\phi]/\delta\phi$ drops out and $S[\phi+\chi]\to S[\phi]$. Subsequently, the scale dependent QEA reduces to the classical action at large cutoff scale.

However, this discussion is actually incomplete, since it ignores subtleties arising from renormalizing the theory. Since (2.39) is valid at the UV scale $k = \Lambda$, the scale dependent effective action $\Gamma_\Lambda[\phi]$ contains all UV relevant terms in the theory that are allowed by the symmetries (or breaking of symmetries) of the theory in the presence of ΔS_k, denoted as $S_{\mathrm{UV}}[\phi, R_\Lambda]$. When considering the QEA at vanishing cutoff $\Gamma[\phi]$, it knows nothing about the UV scale Λ. More generally, it must not depend on the choice of the regulator $R_k(p)$ and hence we arrive at

$$\frac{\delta\Gamma[\phi]}{\delta R_k(p)} = 0\,, \tag{2.41}$$

which encodes the RG-consistency of the underlying renormalization procedure. In summary, the scale dependent QEA is closely related to the classical action, but may contain further operators which have a relevant RG running in the UV. We will refrain here from going into more details and refer the interested reader to [38, 40, 55].

2.3.1.0.2. Finiteness & momentum locality of flows

We want to briefly comment on the UV and IR finiteness of flows as well as their momentum locality. The accompanying necessary conditions are listed in (2.25), (2.26) and (2.27). Making the d-dimensional momentum factor in (2.39) explicit, in the UV we require the finiteness of

$$\lim_{p^2/k^2\to\infty} p^d \frac{1}{\Gamma_k^{(2)}[\phi] + R_k}(p,-p)\,\partial_t R_k(p) = 0\,. \tag{2.42}$$

Hence, the regulator needs to decay sufficiently fast for large momenta. Typical regulators, introduced later, decay either exponentially fast or are identical zero. Therefore, this is manifestly finite for typical, classical dispersion relations encountered, e.g. p^2 for standard bosonic relativistic theories.

The infrared finiteness of the flow equation for $p^2 \to 0$ follows from the fact that the regulator functions act as a mass for low momenta. Without loss of generality we normalize regulators to $R_k(0) = k^2$. Restricting ourselves to constant fields, for simplicity, we get

$$\lim_{p^2/k^2\to 0} \frac{1}{\Gamma_k^{(2)}[\phi] + R_k}(p,-p)\,\partial_t R_k(p) = \frac{2k}{\Gamma_k^{(2)}[\phi] + R_k}(0,0)\,, \tag{2.43}$$

which makes it obvious that the regulator acts like a mass term in the IR. In particular, even a massless theory becomes massive at finite cutoff scales. However, this doesn't guarantee the finiteness of $\Gamma_k^{(2)}[\phi] + R_k$, because $\Gamma_k^{(2)}[\phi]$ can be negative. In cases with spontaneously broken symmetry this is also a very common occurrence. Nevertheless, it's a operator with positive eigenvalues in the full theory. This can be seen from the fact that $\Gamma_k^{(2)}[\phi] + R_k$ is the Hessian of $\Gamma_k + \Delta S_k$, which is the Legendre transformation of the Schwinger functional $\mathcal{W}_k$. Subsequently it is convex with a positive semi-definite Hessian. Indeed one can show that the flow equation has convexity restoring properties, and a pole in the propagator cannot be reached, more details can be found in [56].

Finally, we want to briefly comment on the momentum locality of flows. Using a Lorentz invariant, decaying regulator, it relates to the operator $[\phi(x)R_k(\mathrm{i}\partial_x)\phi(x)]$, which is not a relevant operator in the QFTs under investigation. Therefore, it can be seen as a perturbation of a fixed QFT, compared to momentum independent regulators which relate

to the operator $[\phi(x)\phi(x)]$ and hence modify the underlying QFT. This consideration leads us to a necessary property for functional renormalization group flows that supposedly integrate out momentum shells in a fixed physical QFT. Such an FRG should lead to subleading changes of the ultraviolet relevant correlation functions, with an example being the mass. This momentum locality can be summarised in a relative decay of the flow of the correlation function $\partial_t \Gamma_k^{(n)}$ in comparison to the correlation function itself, with $\Gamma_k^{(n)}$ at the symmetric point

$$\lim_{p^2/k^2\to\infty} \frac{\partial_t \Gamma_k^{(n)}(p_1,\dots,p_n)}{\Gamma_k^{(n)}(p_1,\dots,p_n)}\bigg|_{p_i^2=p^2} = 0\,, \tag{2.44}$$

see [57] for more details. Note that (2.44) cannot hold for general momentum configurations with $p_i^2 \to \infty$ as one has to guarantee that also all momentum transfers diverge. We also would like to emphasise that (2.44) is a necessary but not a sufficient condition for a local RG procedure, for more details see [57].

2.3.2. Expansion schemes

In this section we introduce the relevant expansion schemes for this work. Thereby, we are refraining from giving an overview and focus on the *derivative expansion* and the *vertex expansion*, being among the most popular once. Let us briefly note that a perturbative expansion is also possible, see e.g. [8].

2.3.2.1. Derivative expansion

The derivative expansion is a standard, and very well-working, expansion scheme for low energy effective theories. Assuming we are dealing with a fundamental theory where a mass gap m_{gap} is present, as for example Λ_{QCD} in Yang-Mills theory. In the presence of such a infrared mass scale we can expand the low energy effective theory with a classical action $S_{\text{low}}[\phi]$, which describes long range phenomena with $r \gtrsim 1/m_{\text{gap}}$, in powers of p^2/m_{gap}. This certainly valid as long as the physical momentum scales of interest p^2 satisfy

$$\frac{p^2}{m_{\text{gap}}^2} \ll 1\,, \tag{2.45}$$

an expansion of the quantum corrections about $p^2/m_{\text{gap}}^2 = 0$ is well-defined and should show good convergence properties. Such a systematic expansion scheme for quantum corrections, $\Gamma[\phi] - S[\phi]$, is called the *derivative expansion*. For our present approach the situation is even bettered at least at a finite cutoff scale k the regulator heuristically increases the mass gap of the theory by

$$m_{\text{gap}}^2 \to m_{\text{gap}}^2 + k^2\,. \tag{2.46}$$

This idea can be made even more precise within an investigation of the flow equation. The regulator derivative cuts by definition the integral off for $p^2 \lesssim k^2$, where p is the loop momentum in (2.39). Therefore, the condition $p^2/k^2 \lesssim 1$ is valid in the loop and consequently (2.45) is approximately fulfilled, with the mass gap given by the renormalization scale k. In particular, it does not require the presence of a physical mass gap and is also valid in massless theories. This analysis suggests using rapidly decaying regulators, which

lead to smaller momentum tails in the flow. However, the Taylor expansion coefficients of rapidly decaying regulators $R_k(p)$ increase more rapidly with the order of the number of the derivatives and hence with the order of the derivative expansion. These two conflicting properties have to be optimised for optimising the derivative expansion. A functional optimisation criterion for any systematic expansion scheme, and in particular for general orders of the derivative expansion, has been put forward in [38]. Functional optimisation in terms of an optimisation criterion for the regulator has first been suggested by Litim in [58, 59], where it led to the Litim regulator as the optimal choice for the zeroth order of the derivative expansion.

2.3.2.1.1. Example: ϕ^4-theory

As a short example we want to discuss the theory use throughout this chapter, a real scalar field. The classical action is given by (2.20). At lowest order, the quantum corrections to $\Gamma[\phi] - S[\phi]$ carry no momentum dependence and we are left with a RG-scale dependent function of the field. Therefore, the QEA is given in the zeroth order derivative expansion by

$$\Gamma_k[\phi] = \int_x \left\{ \frac{1}{2}\partial_\mu\phi\partial_\mu\phi + V(\rho) + \mathcal{O}(\partial^2) \right\}. \tag{2.47}$$

Higher orders are obtained by including systematically all possible combinations of gradients of the field to given order. The present approximation (2.47) is called *Local Potential Approximation* (LPA). Note that in (2.47) $\mathcal{O}(\partial^2)$ only applies to the quantum fluctuations, the classical kinetic term is not dropped. The effective potential $V(\rho)$ contains all powers of the field, including a mass term and a ϕ^4 term. It is a function of $\rho = \phi^2/2$ due to the Z_2-symmetry of the theory under $\phi \to -\phi$.

Plugging the ansatz (2.47) into the Wetterich equation (2.39), we have to project onto the only dynamic coupling $V(\rho)$, and derive an expression for the two-point function $\Gamma_k^{(2)}[\phi]$. Addressing the projection first. As the effective potential is precisely the momentum independent part, it is obtained by evaluating the scale dependent QEA at a constant field and dividing out the remaining volume factor. The two point function is straightforward to derive and reads after going to momentum space

$$\Gamma_k^{(2)}[\phi](p,q) = (2\pi)^d\delta(p+q)\,\Gamma_k^{(2)}(p) \equiv (2\pi)^d\delta(p+q)\,\left[p^2 + V'(\rho) + 2\rho\,V''(\rho)\right], \tag{2.48}$$

where primes denote the derivative with respect to the argument. The derivative terms in (2.48) act like a mass term $m^2(\rho) = V'(\rho) + 2\rho\,V''(\rho)$, the curvature mass. With this at hand its easy to arrive at the partial differential equation for the effective potential

$$\partial_t V(\rho) = \frac{1}{2}\int_q \frac{1}{q^2 + V'(\rho) + 2\rho\,V''(\rho) + R_k(q)}\partial_t R_k(q)\,. \tag{2.49}$$

This equation has been at length in the literature and quite a lot of mechanisms arising in RG flows can already be deduced from (2.49). We will refrain from repeating these points here, but will comment on them when they are relevant. A detailed analysis can for example be found in [8] and references therein. For QCD related applications see e.g. [4, 37, 60–64].

2.3.2.2. Vertex expansion

The one-loop structure of the Wetterich equation (2.39) and the fact that only the propagator and the QEA appear make it very appealing. In fact, the latter fact gives rise to a very intuitive expansion scheme, the *vertex expansion*. Taking derivatives of the left-hand side of the equation produces immediately equations for the moments of the QEA. Furthermore, this structure is preserved on the right-hand side of the equation. This expansion has been widely used, see for example: QCD [1, 4, 63–67], quantum gravity [57, 68–75], condensed matter systems [76–79].

Expanding the scale dependent QEA around a potentially non-vanishing background $\bar{\phi}$, the expansion reads for our real scalar field

$$\Gamma_k[\phi] = \lim_{N\to\infty} \sum_{n=0}^{N} \frac{1}{n!} \int_{\{x_n\}} \Gamma_k^{(n)}[\bar{\phi}](x_1,\dots,x_n) \left[\phi_1 - \bar{\phi}_1\right] \dots \left[\phi_n - \bar{\phi}_n\right] , \tag{2.50}$$

where we have the elementary correlation functions of the theory, the 1PI vertices, as expansion coefficients $\Gamma_k^{(n)}[\bar{\phi}]$. Taking derivatives of the Wetterich equation (2.39) generates a tower of equations the elementary correlation functions. Condensing our notation further and dropping the "$\cdot$" denoting the contraction between functions they read

$$\begin{aligned}
\partial_t \Gamma_k[\bar{\phi}] &= \frac{1}{2} \operatorname{Tr} \left\{ G_k \, \partial_t R_k \right\} \\
\partial_t \Gamma_k^{(1)}[\bar{\phi}] &= -\frac{1}{2} \operatorname{Tr} \left\{ \Gamma_k^{(3)} \, G_k \, \partial_t R_k \, G_k \right\} \\
\partial_t \Gamma_k^{(2)}[\bar{\phi}] &= -\frac{1}{2} \operatorname{Tr} \left\{ \left[\Gamma_k^{(4)} - 2\, \Gamma_k^{(3)} \, G_k \, \Gamma_k^{(3)} \right] \left[G_k \, \partial_t R_k \, G_k \right] \right\} \\
&\vdots
\end{aligned} \tag{2.51}$$

This tower of equations makes their structure already very apparent. In the flow of an elementary correlation function $\Gamma_k^{(n)}$ only moments with at most $(n+2)$ appear. The diagram containing the $n+2$ vertex is always a tadpole diagram. Furthermore the zero and one-point function do not couple back in the equation and already suggests the use of the flow equation for $\Gamma_k^{(2)}$ for general fields as the master equation instead of the flow equation for the QEA.

The tower of equations (2.51) is expected to show good convergence properties, as long as higher order n-point are suppressed. This can in general be expected, since the equations for these elementary correlation functions are naturally phase-space suppressed, as it can be seen from (2.51), as long as they are not present classically. Of course there are loop holes around this argument, in particular the presence of symmetry breaking or bound states might enhance higher order n-point function. A prominent example for this is chiral symmetry breaking in QCD, where the quark four-point function is of utmost importance.

We are left to specify how exactly one truncates (2.50). What is usually referred to as *vertex expansion* is obtained by just dropping the limit and cutting the expansion at some finite N off. For practical reasons this is usually restricted to a not too large number, e.g.

$N = 4 \dots 6$. Alternatively, one cuts the expansion (2.50) off at N and instead of neglecting $\Gamma_k^{(N+1)}$ and $\Gamma_k^{(N+2)}$, one approximates based on the other correlation functions. This is for example done in the BMW scheme [80]. However, so far it is not known how different variants of truncations perform against each other. This is partially due to the fact that considering all dependencies at the level of $N = 4$ is already technically non-trivial, see e.g. [81–83].

We want to close this section with some notes about momentum dependencies. First of all, in all relevant calculations considered, the n-point functions are in equilibrium and we assume a homogeneous space-time. Hence, the momentum dependence is constraint, i.e. any n-point function depends on only $n-1$ independent momentum arguments, which is represented in the notation

$$\Gamma^{(n)}(p_1, \dots, p_n) = \Gamma^{(n)}(p_1, \dots, p_{n-1})\,(2\pi)^d\,\delta(p_1 + \dots + p_n)\,. \tag{2.52}$$

Ignoring all but the momentum dependence within this setting for now, it is usually helpful to make the FRG-analogue of the wave function renormalization explicit

$$\Gamma_k^{(2)}(p) = Z(p)(p^2 + m^2)\,. \tag{2.53}$$

This parametrization is chosen such that the function $Z(p)$ part carries the anomalous scaling of the two-point function with the anomalous dimension

$$\eta(p) = -\frac{\partial_t Z(p)}{Z(p)}\,. \tag{2.54}$$

Additionally, we can use (2.53) to take care fo the renormalization group properties of vertices by dressing them appropriately

$$\Gamma^{(n)}(p_1, \dots, p_{n-1}) = \left[\prod_{i=1}^{n} \sqrt{Z(p_i)}\right] \lambda(p_1, \dots, p_{n-1})\,, \tag{2.55}$$

where we have introduced the form factor λ. The such defined form factor carries the momentum dependence of scattering processes. A similar parametrization and notation will also be used in more general theories.

The momentum structure of n-point functions is best expressed in the appropriate Lorentz invariants, reducing the complexity drastically. Having the momenta $p_1, \dots, p_n$, the last one is of already constraint by momentum conservation. Hence, a set of Lorentz invariants in vacuum is given by

$$\left\{p_i^2, \theta_{ij} = \frac{p_i p_j}{|p_i||p_j|}\right\} \quad \text{with} \quad 1 \le i < j \le n-1\,. \tag{2.56}$$

For example, for a three-point function this amounts to three invariants and for a four-point function one gets six invariants. While they form a complete set, they might not be the best possible choice. A discussion related to the three-point function can be found in [84] and the four-point function is discussed in [85]. Unfortunately, the resulting phase-space of n-point vertices is still quite large. Furthermore, external parameters such a temperature, chemical potential, magnetic fields etc extend the dimension of the phase-space significantly. This makes the need for approximations thereof obvious. A very popular and well motivated choice, see e.g. [66, 84, 85] is the *symmetric point* configuration defined by

$$\bar{p}^2 = p_i^2 \quad \text{and} \quad \bar{\theta} = \theta_{ij} \quad \text{with} \quad 1 \le i < j \le n\,, \tag{2.57}$$

where the magnitude of all external momenta is chosen equal.

2.3.3. Regulator

So far we have only discussed generic properties of the regulator, c.f. Section 2.3.1. In this section we want to introduce some common choices and illustrate them. For this purpose it is convenient to introduce some more notation

$$R_k(p) = p^2\, r(x_p) = k^2\, \tilde{r}(x_p) \quad \text{with} \quad x_z = z^2/k^2\,. \tag{2.58}$$

While the former parametrization in (2.58) is usually better suited for theoretical discussion, because the prefactor p^2 of the shape-function r is directly related to the dispersion relation of the associated two-point function, the latter is usually better suited for numerical investigations due to the finiteness of $\lim_{x\to 0} \tilde{r}(x)$. The two shape functions in (2.58) are obviously trivially related $\tilde{r}(x) = x\, r(x)$.

One of the most commonly used regulators is the Litim regulator, which was introduced by Litim in [58, 59] and follows from certain optimization criteria. For a more complete discussion of the subject see [38] and references therein. The *Litim regulator* is given by

$$\tilde{r}^{\text{Litim}}(x) = (1-x)\,\theta(1-x)\,. \tag{2.59}$$

In purely numerical applications sometimes the non-analyticity in (2.59) is unwanted. Therefore, the *smeared Litim regulator* is also quite often considered

$$\tilde{r}^{\text{Litim}}_\alpha(x) = (1-x)\left(1 + e^{\frac{x-1}{\alpha}}\right)^{-1}, \tag{2.60}$$

which is obviously not unique. The next regulator we want to consider is the *sharp regulator*

$$\tilde{r}^{\text{Sharp}}(x) = x\left(\frac{1}{\theta(x-1)} - 1\right). \tag{2.61}$$

The sharp (2.61) and the Litim regulator (2.59) lead quite often to analytic flow equations, adding to their popularity. The next regulator, which is being used in a lot of numerical applications, is the *exponential regulator*

$$\tilde{r}^{\text{Exp}}_\alpha(x) = \frac{x^\alpha}{\exp(x^\alpha) - 1}\,. \tag{2.62}$$

Common choices for the parameter α in (2.62) are $\alpha = 1$ and $\alpha = 2$. Also the *simple exponential regulator* is used quite often

$$\tilde{r}^{\text{sExp}}(x) = e^{-x}\,. \tag{2.63}$$

Additionally, we would like to introduce a new regulator which was used in some parts of this work, the *Gaussian regulator*

$$\tilde{r}^{\text{Gauss}}_\alpha(x) = \left[\operatorname{erfc}\left(-\frac{1}{\alpha}\right)\right]^{-1} \operatorname{erfc}\left(\frac{x-1}{\alpha}\right), \tag{2.64}$$

where $\operatorname{erfc}(z) = 1 - \operatorname{erf}(z)$ denotes the complementary error function. Typical values for the parameter α in (2.64) are at around one. The shape of (2.64) is chosen such that

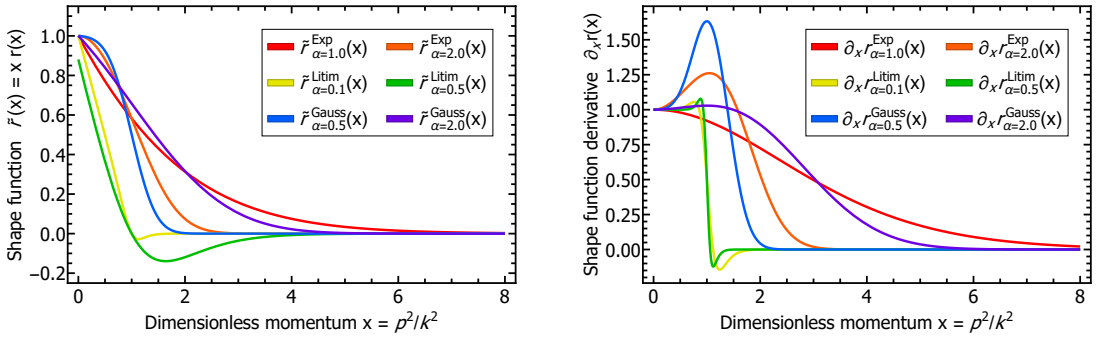

(a) Regulator shape function

(b) Regulator derivative

Figure 2.4.: Shape function and its derivative for typical regulators used in practical FRG applications.

integrands are peaked with a Gaussian at $x_p \approx 1$ with the loop momentum being p. The exponential and Gaussian regulator are quite similar, but the $x \to 0$ behaviour of the Gaussian regulator is better suitable for numerical applications.

The smeared Litim (2.60), exponential (2.62) and Gaussian regulator (2.64) are shown in Figure 2.4a and their related derivatives in Figure 2.4b. Please note that Figure 2.4a shows $\tilde{r}(x)$, while Figure 2.4b shows $\partial_x r(x)$, i.e. not the direct derivative. However, the figures show the relevant information of the regulator and its derivative. The regulator shape function $\tilde{r}(x)$ shows how the effective mass is being introduced in the IR, while the regulator derivative $\partial_x r(x)$ shows how the diagram is being regularized in the UV and integrand is being peaked by regulator additionally.

Apart from the actual shape function, the quality, however defined, of the regulator can usually be improved upon by dressing it properly. To leading order this is done by including the wave function renormalization, i.e. $R_k(p) = Z(p)p^2 r(x_p)$. A more detailed discussion on this subject can be found in [38].

We would like to comment on the situation with fermions, despite not having introduced them yet. A good choice is usually given by the following identity, see e.g. [38, 59]

$$1 + r_{\mathrm{F}}(x) = \left[1 + r_{\mathrm{B}}(x)\right]^{\frac{1}{2}}, \tag{2.65}$$

which reflects the different dispersion relations between bosonic and fermionic degrees of freedom.

Finally, the intricacies arising when considering flows in Minkowski space-time are discussed in the relevant chapter, Chapter 6.

2.4. Superfield formalism & generalizations

This part is additionally based on [9].

So far we have only discussed the case of a real, bosonic scalar field. However, the present setting is easily generalized to generic QFTs. In order to do so, we introduce a superfield Φ_a with an index a that collects all indices of the field, including the field species itself. A contraction of indices therefore also implies integration over space-time. This space is equipped with a metric γ, which implicitly includes a delta function of the space-time indices, if present, i.e. its ultra-local. The bosonic part of the metric is trivially symmetric and for non-mixing fields it is diagonal. While for fermions it is anti-symmetric with no entries on the diagonal, e.g.

$$\left(\gamma\right)^{ab} = \begin{pmatrix} 0 & -1 \\ 1 & 0 \end{pmatrix} , \tag{2.66}$$

for the purely fermionic content $\Phi_a = (\psi, \bar{\psi})$. The metric has the properties

$$\begin{aligned} \gamma_b{}^a &= \gamma^{ac}\gamma_{bc} = \delta_b^a \\ \gamma^a{}_b &= \gamma^{ac}\gamma_{cb} = (-1)^{ab}\,\delta_b^a \,, \end{aligned} \tag{2.67}$$

where the minus sign appears for purely fermionic permutations, i.e.

$$(-1)^{ab} = \begin{cases} -1, & a \text{ and } b \text{ fermionic} \\ 1, & \text{otherwise} \end{cases} . \tag{2.68}$$

This factor appears of course every time fields are commuted. Therefore, it is convenient to define this sign for multiple pairs of indices

$$(-1)^{\{a_1b_1,\ldots,a_nb_n\}} = (-1)^{a_1b_1}(-1)^{\{a_2b_2,\ldots,a_nb_n\}} \quad \text{with} \quad (-1)^{\{\}} = 1 \,. \tag{2.69}$$

The convention concerning the order of derivatives is

$$F_{a_1,\ldots,a_n}[X] = \frac{\delta}{\delta X_{a_1}} \ldots \frac{\delta}{\delta X_{a_n}} F[X] \,, \tag{2.70}$$

for some superfield X and a functional $F[X]$. Indices can be raised and lowered in the usual fashion in the NW-SE convention, i.e. indices are raised from the left and lowered from the right. In particular, we will drop the (n) part in $\Gamma^{(n)}$, if indices are present, as it is immediately clear which n-point function is considered, given by the number of indices. Additionally we will drop the k subscript as it should be clear from the context whether or not the quantity depends on the RG-scale and restore it only when differentiating between the result at $k = 0$ and intermediate correlation functions.

With this at hand it is straightforward to repeat the derivations of this chapter. For the Dyson-Schwinger equations, c.f. (2.19), we obtain

$$\Gamma^a[\Phi] = \left\langle S^a[\hat{\Phi}] \right\rangle , \tag{2.71}$$

where the hat denotes the field operator, similarly to φ and ϕ in Section 2.1. The necessary expectation value of operators in (2.71) we obtain the generalization of (2.13)

$$\langle \mathcal{O}[\Phi] \rangle = \mathcal{O}\left[\hat{\Phi}_a = G_{ab}\frac{\delta}{\delta \Phi_b} + \Phi_a\right] . \tag{2.72}$$

For convenience we also give the explicit relation between the propagator and the two-point function, which reads

$$G_{ab} = \left(\Gamma^{(2)} + R\right)^{-1}_{ab}, \tag{2.73}$$

where R denotes the obvious generalization of the regulator and carries the same indices and structure as the two-point function. This leads us to the Wetterich equation, c.f. (2.39),

$$\partial_t \Gamma[\Phi] = \frac{1}{2} \operatorname{Tr}\, G_{ab}\, \partial_t R^{ab}\,. \tag{2.74}$$

Finally, in order to derive equations, we need the derivative of the propagator with respect ot the expectation value of the field, c.f. (2.14), which is given by

$$\frac{\delta}{\delta \Phi_c} G_{ab} = -(-1)^{ac}\, G_{ai} \Gamma^{icj} G_{jb}\,. \tag{2.75}$$

This collects all necessary identities to work with Functional Methods in arbitrary theories involving bosons and/or fermions.

2.5. Finite density & temperature

The description of phase structures requires the theory in the presence of external parameters such as temperature, chemical potentials or magnetic fields. In this section we provide a few details on their introduction into the theory based on a path integral formalism. The parameters we introduce into the theory is restricted to the ones being relevant for the remainder of this work, i.e. finite density and finite temperature. We assume some standard notation, in particular for fermions, which can be found in every QFT textbook, see e.g. [86, 87]

2.5.1. Finite density

Typically, and in particular in QCD, we investigate theories within the *Grand Canonical Ensemble*, where the effective action $\Omega(T,\mu_\psi) = \Gamma[\Phi_{\mathrm{EoM}};T,\mu_\psi]$ is the *Grand Potential*. The (fermionic) particle number N is the derivative of the grand potential with respect to the chemical potential μ_ψ

$$N_\psi = \frac{\partial\Gamma[\Phi_{\mathrm{EoM}}]}{\partial\mu_\psi}\,, \tag{2.76}$$

and hence $\Gamma \propto -\mu_\psi N_\psi$. Usually we consider a chemical potential related to the particle number

$$N_\psi = \int_x n_\psi(x) \quad \text{with} \quad n_\psi(x) = \bar\psi\gamma_0\psi\,. \tag{2.77}$$

with the fermionic density $n_\psi(x)$. Equation (2.77) adds a chemical potential to fermions. To add a chemical potential for fermions we add the respective term to the Dirac action

$$S_{\mathrm{D}}[\psi,\bar\psi;\mu_\psi] = \int_x \bar\psi(x)\left(\not\partial + m_\psi - \mu_\psi\gamma_0\right)\psi(x)\,. \tag{2.78}$$

In frequency space this amounts to a shift of the frequency into the complex plane

$$p_0 \to \tilde p_0 = p_0 + i\,\mu_\psi\,, \tag{2.79}$$

and the classical fermionic propagator reads in the presence of a chemical potential

$$G_\psi(p;\mu_\psi) = \frac{1}{i\not p - \gamma_0\mu_\psi + m_\psi} = \frac{-i\not{\tilde p} + m_\psi}{\tilde p^2 + m_\psi^2}\,, \tag{2.80}$$

where

$$\begin{aligned}\tilde p &= (p_0 + i\,\mu_\psi, \boldsymbol{p})\\ \not{\tilde p} &= \gamma_0(p_0 + i\,\mu_\psi) + \boldsymbol{\gamma}\boldsymbol{p}\,.\end{aligned} \tag{2.81}$$

This generalizes to the full propagator in a straightforward manner. The typical parametrization chosen is

$$G_\psi(p;\mu_\psi\psi) = \frac{1}{Z_\psi}\frac{-\mathrm{i}\left(s_\psi^{1/2}\gamma_0\tilde p_0 + \not{\boldsymbol{p}} + M_\psi\right)}{s_\psi\tilde p_0 + \boldsymbol{p}^2 + M_\psi^2}\,, \tag{2.82}$$

where the dressings Z_ψ, s_ψ and M_ψ are fully momentum and chemical potential dependent. Additionally, the form (2.82) also holds at finite temperature, with all dressings now also depending on temperature. The factor s_ψ takes into account that the spatial and temporal dressing are different as both density/chemical potential and temperature single out a rest frame.

2.5.2. Finite temperature

Instead of given a full account of thermal QFTs, we will restrict ourselves to the Matsubara formalism, one way introducing finite temperatures. More complete introductions can be found in the literature, see e.g. [88–91]. In statistical physics one notes that the factor of inverse temperature $\beta = 1/T$ is the prefactor in front of the Hamiltonian in the partition function.

2.5.2.1. Bosonic fields at finite temperature

One views temperature as a finite extend along imaginary times with $t = \mathrm{i}\beta$. As a consequence the fields have to be periodic with extend beta, i.e. $\varphi(t+\beta, \mathbf{x}) = \varphi(t, \mathbf{x})$ and the imaginary time direction is compactified to the interval $x_0 \in [0, \beta)$. With this at hand we arrive at the finite temperature path integral

$$Z_T[J] = \int_{\varphi(\beta,\mathbf{x})=\varphi(0,\mathbf{x})} [\mathrm{d}\varphi]_{\mathrm{ren}}\, e^{-S_T[\varphi]+J\cdot\varphi}\,, \tag{2.83}$$

Where all integrals along imaginary time are understood to be only over the interval $[0, \beta)$. Apart from this, the classical action is usually unaltered in applications of interest for this work. This complicates obviously the process of undoing the Wick rotation and going back to real times and Minkowski space-time. At this point we refrain from touching this subject further as it is discussed in detail in Chapter 6 and only state that it is uniquely possible. As a consequence of this procedure, called *Matsubara formalism*, all correlation functions are periodic in imaginary time

$$\langle \varphi(x_1) \dots \varphi(t_i + \beta, \mathbf{x}_i) \dots \varphi(x_n) \rangle = \langle \varphi(x_1) \dots \varphi(t_i, \mathbf{x}_i) \dots \varphi(x_n) \rangle\,. \tag{2.84}$$

Practically, the biggest difference when going to momentum space amounts to the frequency. Due to the finite extend of the imaginary time domain the zero component of the momentum, called frequency $\omega = p_0$, which becomes discrete. This is easily demonstrated at the example of the propagator

$$G_\phi(\omega_n, \mathbf{p}) = \int_\beta d^d x\, e^{i\,(\omega_n t + \mathbf{p}\,\mathbf{x})}\, G_\phi(t, \vec{x}) \quad \text{with} \quad \omega_n = 2n\pi T \quad (n \in \mathbb{Z})\,, \tag{2.85}$$

where the index β on the integral sign denotes the finite extend along the imaginary time direction. With $p_0 \to p_0 = \omega_n = 2\pi n T$ the integration along imaginary time p_0 turns into a summation over all $n \in \mathbb{Z}$.

2.5.2.2. Fermionic fields at finite temperature

The construction is similar to the bosonic one. However, when constructing the necessary coherent state one finds that the field must be anti-periodic instead of being periodic, i.e.

$$\psi(t+\beta, \mathbf{x}) = -\psi(t, \mathbf{x})\,. \tag{2.86}$$

Completely analougsly we obtain for the path integral for a fermionic theory

$$Z_T[\eta, \bar{\eta}] = \int_{\psi(\beta,\mathbf{x})=-\psi(0,\mathbf{x})} \left[\mathrm{d}\psi \mathrm{d}\bar{\psi}\right]_{\mathrm{ren}} e^{-S_T[\psi,\bar{\psi}]+\bar{\eta}\cdot\psi-\bar{\psi}\cdot\eta}\,, \tag{2.87}$$

with the sources η and $\bar{\eta}$. As in the bosonic case, the zero component of the momentum becomes discrete. In the fermionic case the frequencies are given by $p_0 \to p_0 = \omega_n = (2n+1)\pi T$ with $n \in \mathbb{Z}$.

2.5.3. Embedding into Functional Methods

The way we have introduces finite chemical potentials in Section 2.5.1 and finite temperature in Section 2.5.2 makes it very easy to incorporate them into the tools presented in this chapter. Since both operate essentially on the same momentum component we can summarise the modifications as

$$p_0 \to \omega_{n,\Phi_i} = 2\pi T\left(n + \frac{1}{2}\delta_{\Phi_i \mathbf{F}} + \mathrm{i}\frac{\mu_{\Phi_i}}{2\pi T}\right), \tag{2.88}$$

where Φ_i are components of the superfield Φ and $\delta_{\Phi_i \mathbf{F}}$ is one for a fermionic component and zero for a bosonic one. Consequently, the Wetterich equation (2.74), the Dyson-Schwinger equation (2.71) and the Dyson-Schwinger representation of composite operators (2.72) stay unaltered. One only has to keep in mind that the integration along the zero component of momenta in all loops gets transformed into the appropriate sum.

3. Quantum chromodynamics

This chapter is in parts based on [8].

The theory of strong interactions, quantum chromodynamics (QCD), has been developed on the basis of scattering experiments that showed an internal $SU(3)$-symmetry and related charges much the same way quantum electrodynamics (QED) shows the $U(1)$-symmetry related to the electric charge. The corresponding gauge theory, $SU(3)$ Yang-Mills theory, is non-Abelian and hence self-interacting, i.e. the (quantized) pure gauge theory is already non-trivial, in contrast to the $U(1)$-based QED. The introduction is given from an FRG perspective, suitable for the use in Functional Methods. In particular, it does not aim at giving a full introduction to the long history and developments in QCD, but rather focuses on the non-perturbative sector.

3.1. Non-Abelian gauge theories

We start our discussion of QCD by discussing the pure gauge part or Yang-Mills part of QCD, a non-Abelian gauge theory with gauge group $SU(N_c)$ with N_c being the number of colours . This discussion is also used to fix our conventions and to remind the reader of some key features of a non-Abelian gauge theory. The $SU(2)$ gauge theory has the the same qualitative features as physical QCD with the $SU(3)$ gauge group, namely asymptotic freedom and confinement. As it is technically simpler we shall discuss some qualitative feature in the $SU(2)$ case. Note however, that this $SU(2)$ gauge theory should not be confused with the weak $SU(2)$ gauge theory in the Standard Model.

As for QED, the classical action of QCD can be derived from the gauge-invariant (minimal) extension of the action of a free spin-one particle. The requirement of invariance of physics under local $SU(N_c)$ or colour rotations with $\mathcal{U} \in SU(N_c)$ combined with a minimal coupling, leads us from partial to covariant derivatives

$$\partial_\mu \to D_\mu(A) = \partial_\mu - \mathrm{i}gA_\mu \,, \tag{3.1}$$

with $A_\mu \in su(N_c)$, the Lie algebra of $SU(N_c)$, and the gauge coupling g. Accordingly, the gauge field is matrix valued, and hence gauge fields do not commute with each other. The latter fact leads to the pivotal qualitative difference between Abelian and non-Abelian gauge theories, the self-interaction of the gauge field. This property which is responsible for asymptotic freedom and in turn is also responsible for the rise of the coupling at low momenta. However, confinement is not simply the presence of a large coupling, this would still imply a Coulomb force between colour charges. Confinement, in a pure gauge theory, is linked to a linear potential between colour charges. More mathematically speaking confinement can be formulated as the existence of the mass gap in pure Yang-Mills theory, see [16] and references therein. In the present scope this mass gap is reflected by the mass gap in the gluon propagator.

3.1.1. Basics of Yang-Mills theories

In this subsection we discuss the heart of QCD, the pure glue theory.

3.1.1.1. Classical action of Yang-Mills theory

Here we introduce the Yang-Mills action and our notation for the gauge group and gauge fields. The gauge field A_μ^a with

$$A_\mu = A_\mu^a t^a \,, \qquad \text{with} \qquad a = 1, ..., N_c^2 - 1 \,, \tag{3.2}$$

carries the adjoint representation of the gauge group. In (3.2) we have introduced the generators of the Lie-algebra $su(N_c)$. In the physical case $SU(3)$ the eight t^a are the Gell-Mann matrices, in $SU(2)$ the three t^a are proportional to the Pauli matrices, $t^a = \tau^a/2$ where τ^a are the Pauli matrices, cf. (3.110).

The generators t^a satisfy the commutation relation

$$[t^a, t^b] = \mathrm{i} f^{abc} t^c \,, \tag{3.3}$$

with f^{abc} being the structure constants of the Lie algebra $su(N_c)$. The normalisation is chosen as

$$\mathrm{tr}_f (t^a t^b) = \frac{1}{2}\delta^{ab} \,, \tag{3.4}$$

where the trace is in the fundamental representation. In the adjoint representation the generators read $\left(t^c_{adj}\right)^{ab} = -\mathrm{i} f^{abc}$. Inserting this representation into the general covariant derivative (3.1), we obtain the covariant derivative in the adjoint representation

$$D_\mu^{ab}(A) = \partial_\mu \delta^{ab} - g f^{abc} A_\mu^c \,. \tag{3.5}$$

Turning now to gauge transformations $\mathcal{U} = e^{\mathrm{i}\,\omega}$, with $\omega \in \mathrm{su(N)}$, we demand that the covariant derivative (3.1) transforms in a covariant manner

$$D_\mu(A) \to D_\mu(A^{\mathcal{U}}) = \mathcal{U} D_\mu \mathcal{U}^\dagger \,. \tag{3.6}$$

From this we conclude immediately

$$A_\mu \to A_\mu^{\mathcal{U}} = \frac{\mathrm{i}}{g}\mathcal{U}\left(D_\mu \mathcal{U}^\dagger\right) = \mathcal{U} A_\mu \mathcal{U}^\dagger + \frac{\mathrm{i}}{g}\mathcal{U}(\partial_\mu \mathcal{U}^\dagger) \,. \tag{3.7}$$

The field strength tensor is introduced as the curvature tensor corresponding to the covariant derivative

$$F_{\mu\nu} = \frac{\mathrm{i}}{g}[D_\mu, D_\nu] = F_{\mu\nu}^a t^a \quad \text{with} \quad F_{\mu\nu}^a = \partial_\mu A_\nu^a - \partial_\nu A_\mu^a + g f^{abc} A_\mu^b A_\nu^c \,. \tag{3.8}$$

Defined as the commutator of covariant operators, the field strength tensor $F_{\mu\nu}$ also transforms in a covariant manner under gauge transformations

$$F_{\mu\nu}(A^{\mathcal{U}}) = \frac{\mathrm{i}}{g}[D_\mu(A^{\mathcal{U}}), D_\nu(A^{\mathcal{U}})] = \mathcal{U} F_{\mu\nu}(A) \mathcal{U}^\dagger \,. \tag{3.9}$$

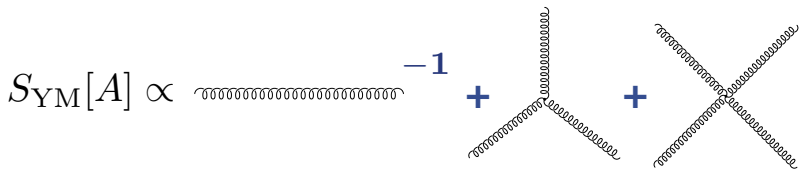

Figure 3.1.: Diagrammatic representation of the classical Yang-Mills action (3.10).

Therefore we can introduce the gauge invariant Yang-Mills action

$$S_{\mathrm{YM}}[A] = \frac{1}{2}\int_x \mathrm{tr}\ F_{\mu\nu}F_{\mu\nu} = \frac{1}{4}\int_x F^a_{\mu\nu}F^a_{\mu\nu}\,, \tag{3.10}$$

which is trivially gauge invariant due to the cyclic nature of the trace in (3.10). Clearly, the action (3.10) with the field strength (3.8) is a self-interacting theory with coupling constant g. It has a quadratic kinetic term and three-gluon and four-gluon vertices. This is illustrated diagrammatically in Figure 3.1. As in QED we can identify colour-electric and colour-magnetic fields as the components in the field strength tensor,

$$\begin{aligned} E^a_i &= F^a_{0i} \\ B^a_i &= \frac{1}{2}\epsilon_{ijk}F^a_{jk}\,. \end{aligned} \tag{3.11}$$

In contrast to QED these colour-electric and magnetic fields are not observables, they change under gauge transformations. Only $\mathrm{Tr}\ \vec{E}^2, \mathrm{Tr}\ \vec{B}^2$, and $\mathrm{Tr}\ \vec{E}\vec{B}$ are observables. The latter is related to anomalous chiral symmetry breaking.

3.2. Quantization and gauge fixing

Having introduced the classical action (3.10) we can now turn to the issue of quantization and, closely related, gauge fixing. For now we will turn back to a path integral picture, but stress again that this is not necessary. Naïvely, the generating functional of pure YM-theory reads

$$Z[J] = \int \mathrm{d}A \exp\left(S_{\mathrm{YM}}[A] + \int_x J^a_\mu A^a_\mu\right) . \tag{3.12}$$

However, the fundamental problem with (3.12) is the integration over infinite degenerate configurations due to the gauge invariance, c.f. (3.9). To be more precise, the equivalent gauge configurations are physically equivalent since they leave the action invariant, and are called gauge orbit $\{A^{\mathcal{U}}\}$. In terms of classical correlation functions this is reflected by the inversion problem of the two point function $S^{(2)}_{\mathrm{YM}}(p)$, that does not exist due to the transversality of the two-point function

$$p_\mu \, S^{AA}_{\mu\nu}(p) = p_\mu \left(p^2 \delta_{\mu\nu} - p_\mu p_\nu\right) = 0 \, . \tag{3.13}$$

Hence, we cannot define even a classical propagator, leave aside a full propagator G_A, the latter been the pivotal ingredient for a FRG approach to gauge theories. In order to remedy this problem we remove this redundancy via a gauge fixing condition

$$\mathcal{F}[A_{\mathrm{gf}}] = 0 \, , \tag{3.14}$$

which corresponds to choosing one, up to potential Gribov copies, representative per gauge orbit. We will leave this issue aside for now and assume the existence of a unique solution of the gauge fixing condition for each orbit. The gauge of chief interest for the present work is the covariant or Lorenz gauge,

$$\partial_\mu A_\mu = 0 \, . \tag{3.15}$$

The covariant gauge has the technical advantage that it does not single out a space-time direction. This property reduces the possible tensor structure of correlation functions and hence simplifies computations significantly.

For a general gauge condition (3.14) the path integral measure $\mathrm{d}A$ in (3.12) can be split into an integration over physically inequivalent configurations A_{gf} and the gauge transformations $\mathcal{U}$

$$\mathrm{d}A = J \, \mathrm{d}A_{\mathrm{gf}} \, \mathrm{d}\mathcal{U} \, , \tag{3.16}$$

where J denotes the Jacobian of the transformation and $\mathrm{d}\mathcal{U}$ is the Haar measure of the gauge group. Then, the integration over the gauge group factorises, since the action is gauge invariant, and it can be dropped. The computation of the coordinates transformation, including the Jacobian J in (3.16), is done using the standard Faddeev-Popov quantisation. In order to achieve this we insert a one into the path integral

$$1 = \Delta_{\mathcal{F}}[A] \int \mathrm{d}\mathcal{U} \, \delta\left(\mathcal{F}[A^{\mathcal{U}}]\right) \quad \Leftrightarrow \quad \Delta_{\mathcal{F}}[A] = \left(\int \mathrm{d}\mathcal{U} \, \delta\left[\mathcal{F}[A^{\mathcal{U}}]\right]\right)^{-1} . \tag{3.17}$$

We notice that $\Delta_{\mathcal{F}}[A]$ is gauge invariant due to the property $\mathrm{d}(\mathcal{U}\mathcal{V}) = \mathrm{d}\mathcal{U}$ with $\mathcal{V} \in SU(N_c)$ of the Haar measure: the Haar measure is invariant under multiplication with a gauge group element. In order to illustrate the effect of inserting (3.17) into path integral let us consider a general observable $\mathcal{O}$, which is necessarily local and gauge invariant,

$$\langle \mathcal{O} \rangle = \frac{\int \mathrm{d}A\, \mathcal{O}[A] e^{-S_{\mathrm{YM}}[A]}}{\int \mathrm{d}A\, e^{-S_{\mathrm{YM}}[A]}} = \frac{\int \mathrm{d}A\, \mathrm{d}\mathcal{U}\, \delta\left(\mathcal{F}[A^{\mathcal{U}}]\right)\, \Delta_{\mathcal{F}}[A]\, \mathcal{O}[A]\, e^{-S_{\mathrm{YM}}[A]}}{\int \mathrm{d}A\, \mathrm{d}\mathcal{U}\, \delta\left(\mathcal{F}[A^{\mathcal{U}}]\right)\, \Delta_{\mathcal{F}}[A]\, e^{-S_{\mathrm{YM}}[A]}}\,, \tag{3.18}$$

where all terms are gauge invariant except for the δ-distribution. Hence we can absorb the $\mathcal{U}$ dependence via $A \to A^{\mathcal{U}^\dagger}$ and as a result the infinite integral over the Haar measure decouples in the numerator and denominator and the resulting expression is

$$\langle \mathcal{O} \rangle = \frac{\int \mathrm{d}A\, \delta\left(\mathcal{F}[A]\right)\, \Delta_{\mathcal{F}}[A]\, \mathcal{O}[A]\, e^{-S_{\mathrm{YM}}[A]}}{\int \mathrm{d}A\, \delta\left(\mathcal{F}[A]\right)\, \Delta_{\mathcal{F}}[A]\, e^{-S_{\mathrm{YM}}[A]}}\,. \tag{3.19}$$

In (3.19) the gauge redundancy is eliminated, and $\mathrm{d}A_{\mathrm{gf}} = \mathrm{d}A\ \delta\left(\mathcal{F}[A]\right)$. This leaves us with the computation of the Jacobian $J = \Delta_{\mathcal{F}}[A]$, which we can obtain from a suitable coordinate transformation

$$\delta\left(\mathcal{F}[A^{\mathcal{U}}]\right) = \frac{\delta\left(\omega - \omega_1\right)}{\left|\det \frac{\delta \mathcal{F}}{\delta \omega}\right|}\,, \tag{3.20}$$

where $\mathcal{U} = e^{\mathrm{i}\,\omega}$. We define the algebra element $\omega_1[A]$ as

$$\mathcal{F}[A_{\mathrm{gf}} = A^{\mathcal{U}(\omega_1)}] = 0\,, \tag{3.21}$$

for which the gauge fixing condition is satisfied. We emphasise again that typically the solution of the gauge fixing condition is not unique and several Gribov copies exist. Using the definition (3.17) the resulting expression reads

$$\Delta_{\mathcal{F}}[A] = \left|\det \mathcal{M}_{\mathcal{F}}[A_{\mathrm{gf}}]\right| \quad \text{with} \quad \mathcal{M}_{\mathcal{F}}[A] = \left.\frac{\delta \mathcal{F}}{\delta \omega}\right|_{\omega=0}\,. \tag{3.22}$$

The inverse Jacobian $\det \mathcal{M}_{\mathcal{F}}$ is called the Faddeev-Popov determinant and it can be computed by considering infinitesimal gauge transformations.

We are left with the specification of the gauge fixing function (3.14). Here we restrict ourselves to linear gauges,

$$\mathcal{F}[A] = l_\mu A_\mu\,, \tag{3.23}$$

where l_μ can be a differential operator, space-time dependent, a constant vector or a combination thereof. Common choice are

$$\text{Covariant gauge}: \quad \mathcal{F}[A] = \partial_\mu A_\mu \tag{3.24a}$$

$$\text{Coulomb gauge}: \quad \mathcal{F}[A] = \partial_i A_i \tag{3.24b}$$

$$\text{Fock-Schwinger gauge}: \quad \mathcal{F}[A] = x_\mu A_\mu \tag{3.24c}$$

$$\text{Axial gauge}: \quad \mathcal{F}[A] = n_\mu A_\mu \tag{3.24d}$$

$$\text{Polyakov gauge}: \quad \mathcal{F}[A]: \ A_0(x) = A_0^c(\vec{x})\,. \tag{3.24e}$$

In the condition for the Polyakov gauge, A_0^c denotes an element of the Cartan subalgebra, which can be formulated as a combination of gauge fixing conditions, see e.g. [92]. The general covariant gauge (3.24a) and the Fock-Schwinger gauge (3.24c) have the technical advantage that they do not single out a space-time direction and therefore reduces the number of possible tensor structures of correlation functions.

In turn, Coulomb gauge (3.24b), axial gauge (3.24d) and the Polyakov gauge (3.24e) single out specific frames. For Hamiltonian formulations this singles out the Coulomb, temporal or Weyl gauge, (3.24d) with $n_\mu = \delta_{\mu 0}$, as technically convenient gauges. Note also, that most of these gauges are incomplete, residual gauge transformations are not fixed. Whether or not a gauge fixing is sufficiently complete for our purposes is decided with whether or not the propagator, $1/S^{(2)}_{\mathrm{YM}}$ and more importantly G_A exists.

Seemingly, the Weyl gauge is also useful at finite temperature, density and external magnetic fields, where a rest frame is already singled out. However, this gauge cannot be fixed with periodic boundary conditions, the gauge fields are only periodic in $t \to t + \beta$ up to gauge transformations, the transition functions. Note that otherwise the Polyakov loop, the Wilson loop in time directions, would be trivial. Trying to make the A_0 as simple as possible, while insisting on periodic fields, we are lead to the Polyakov gauge (3.24e).

We are now in the position to compute the Faddeev-Popov determinant for the case of general covariant gauges (3.24a). For its computation we consider an infinitesimal gauge transformation $\mathcal{U} = 1 + i\,g\,\omega$, where we have rescaled the transformation with the strong coupling g for convenience. Such a rescaling gives global factors of powers of $1/g$ that drop out in normalised expectation values. Then, the infinitesimal variation of the linear gauge (3.23) with $l_\mu A_\mu = 0$, e.g. (3.24), follows as

$$\mathcal{F}[A^{\mathcal{U}}] = l_\mu A^{\mathcal{U}}_\mu = l_\mu A_\mu - l_\mu D_\mu \omega + O(\omega^2) \stackrel{!}{=} 0\,. \tag{3.25}$$

Hence we arrive at the Faddeev-Popov matrix

$$\mathcal{M}_{\mathcal{F}}[A] \frac{\delta l_\mu D_\mu \omega}{\delta \omega} = -l_\mu D_\mu \frac{\delta \omega}{\delta \omega} = -l_\mu D_\mu \mathbb{1}\,. \tag{3.26}$$

Its determinant is $\Delta_{\mathcal{F}}[A]$ in the given gauge, here we show it explicitly for the covariant gauge, (3.24a), with $l_\mu = \partial_\mu$ We assume that $-\partial^\mu D_\mu$ is a positive definite operator and arrive at

$$\Delta_{\mathcal{F}}[A] = \det \mathcal{M}[A] = \det\left(-\partial_\mu D_\mu\right)\,. \tag{3.27}$$

A useful observation is that determinants can be represented by a Gaussian integral. In regular space such a Gaussian integral reads

$$\int_x e^{-\frac{1}{2}x^T M x} = \frac{(2\pi)^n}{\sqrt{\det M}}\,. \tag{3.28}$$

We want to use this relation to replace the Faddeev-Popov determinant (3.27) in the Lagrangian. It turns out that the usual form does not give a useful action or Lagrangian. However, we can instead use two anti-commuting Grassmann fields $c, \bar{c}$ and arrive at

$$\det \mathcal{M}_{\mathcal{F}}[A] = \int \mathrm{d}c\,\mathrm{d}\bar{c}\,\exp\left\{\int_{x,y} \bar{c}^a(x)\mathcal{M}^{ab}_{\mathcal{F}}(x,y)c^b(y)\right\}\,. \tag{3.29}$$

Finally we slightly modify the gauge by introducing a Gaußian average over gauges

$$\delta\left[\mathcal{F}[A^{\mathcal{U}}]\right] \to \int \mathrm{d}\mathcal{C}\,\delta\left[\mathcal{F}[A^{\mathcal{U}}-\mathcal{C}]\right]\exp\left\{-\frac{1}{2\xi}\int_x \mathcal{C}^a\mathcal{C}^a\right\}, \tag{3.30}$$

leading to the usually considered linear covariant gauges.

In summary, we arrive at the gauge fixed generating functional for Yang-Mills

$$Z[J_A,J_c,\bar{J}_c] = \int \mathrm{d}A\,\mathrm{d}c\,\mathrm{d}\bar{c}\,e^{-S_A[A,c,\bar{c}]+J_A\cdot A+\bar{J}_c\cdot c-\bar{c}\cdot J_c}, \tag{3.31}$$

where the gauge fixed action is given by

$$S_A[A,c,\bar{c}] = \frac{1}{4}\int_x F^a_{\mu\nu}F^a_{\mu\nu} + \frac{1}{2\xi}\int_x\left(\partial_\mu A^a_\mu\right)^2 - \int_x \bar{c}^a\partial_\mu D^{ab}_\mu c^b\,. \tag{3.32}$$

Particular values of the gauge fixing parameter ξ are special, because they simply computations under certain circumstances. *Landau gauge* is given by the choice $\xi = 0$, which is understood as a limit after equations have been derived. Landau gauge is particularly useful in Functional Methods, because it decouples the longitudinal and the transversal part of the flow equations. This will be discussed further in Section 3.5. Another useful choice is $\xi = 1$, called *Feynman gauge*, which simplifies perturbative calculations considerably.

Note that the ghost action implies a negative dispersion for the ghost, related to the determinant of the positive operator $\mathcal{M}_{\mathcal{F}} = -\partial_\mu D_\mu$. However, this is a matter of convention, we might as well use a positive dispersion, the minus sign drops out for all correlation functions which do not involve ghosts, and only those are related to scattering amplitudes.

3.3. QCD

In the previous section we have discussed the pure gauge part of QCD. To arrive at the full theory we have to introduce quarks. The classical action of the quark part is given by the free action of fermions in the fundamental representation, where the partial derivative has been promoted to a covariant one, c.f. (3.1). This couples the fermions minimally to the gluons and the resulting action is given by

$$S_{\mathrm{M}}[q,\bar{q},A] = \int_x \bar{q}\left(\mathrm{i}\not{D} + m_q + \gamma_0\,\mu_0\right)\,. \tag{3.33}$$

The quark field carries a Dirac index, defining a four-component spinor, gauge group indices in the fundamental representation and flavour indices. The covariant derivative is diagonal in flavour space, just like the chemical potential. The current quark mass contains in principle six different values, corresponding to up, down, strange, charm, bottom and top quark. However, for most applications it is not necessary to consider all flavours, as the quark masses rise quickly from one flavour to the next, with the exception of up and down quark. Therefore, we will only consider a 2-flavour setting, where up and down quarks are assumed to be degenerate, as well as a 2+1-flavour setting, where also the strange quark is included. Within these approximations all relevant degrees of freedom, for the problems of interest in this thesis are cover, as the next heavier quark, the charm quark, is only becomes relevant at scales far above the phase transition temperature in QCD, which is at 156 MeV at vanishing chemical potential. In turn, the mass of the strange quark has the same order of magnitude and cannot be neglected for a quantitatively accurate description. Nevertheless, for quite some applications the underlying mechanics do not change when the strange quark is dropped. This justifies the 2-flavour approximation, which is technically in some applications considerably simpler.

Again in analogy to the Yang-Mills action we describe the quantised theory using its generating functional. The full generating functional of QCD is the straightforward extension of the Yang-Mills version in (3.31). The quark fields are Grassmann fields because of their fermionic nature, and we are led to the generating functional

$$Z[J] = \int \mathrm{d}\Phi\, e^{-S_{\mathrm{QCD}}[\Phi]+J_\Phi\cdot\Phi}\,, \tag{3.34}$$

with the super-field Φ, and super-current J,

$$\begin{aligned}\Phi &= (A, c, \bar{c}, \psi, \bar{\psi})\\ J_\Phi &= (J_A, J_c, J_{\bar{c}}, J_q, J_{\bar{q}})\,.\end{aligned} \tag{3.35}$$

The gauge-fixed action S_{QCD} in (3.34) in the Landau gauge is given by

$$S_{\mathrm{QCD}}[\Phi] = \frac{1}{4}\int_x \left\{F^a_{\mu\nu}F^a_{\mu\nu} + \frac{1}{2\xi}\left(\partial_\mu A^a_\mu\right)^2 - \bar{c}^a\partial_\mu D^{ab}_\mu c^b + \bar{q}\left(\mathrm{i}\not{D} + m_q - \gamma_0\mu_q\right)q\right\}. \tag{3.36}$$

The action (3.35) is shown diagrammatically in Figure 3.2 . For physical observables the gauge dependence entering through the ghost terms is cancelled by the hidden gauge fixing dependence of the inverse gluon propagator.

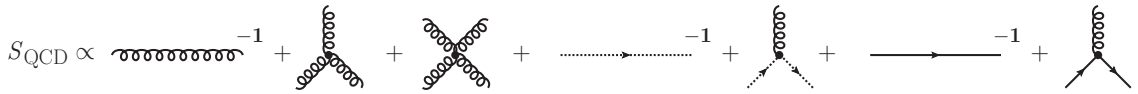

Figure 3.2.: Diagrammatic representation of the classical QCD action (3.36).

3.3.1. Flow equations for QCD

With the previous discussion we are finally in the position to derive the flow equation for the effective action of QCD. The consequences of using a momentum cutoff in a gauge theory are discussed partially at the end of this section and in the following one Section 3.4. In fact, working in the superfield formalism, we have the flow equation in a generic form already available, c.f. (2.74). The only thing left to do is to specify the regulator within this formalism and carry out the index summations over field indices. As in Section 2.4, the IR cutoff term $\Delta S_k[\Phi]$ is defined as

$$\Delta S_k[\Phi] = \frac{1}{2}\Phi_a R^{ab}\Phi_b\,, \tag{3.37}$$

where the regulator matrix is given by

$$\left(R^{ab}\right) = \begin{pmatrix} R_A & 0 & 0 & 0 & 0 \\ 0 & 0 & -R_c & 0 & 0 \\ 0 & R_c & 0 & 0 & 0 \\ 0 & 0 & 0 & 0 & -R_q \\ 0 & 0 & 0 & R_q & 0 \end{pmatrix}. \tag{3.38}$$

With the generic structure in momentum space

$$R_{\Phi_i}(p) = \mathcal{P}_{\Phi_i}(p) r_{\Phi_i}(x_p)\,, \tag{3.39}$$

where x_p is defined in (2.58). The parametrization (3.39) depends on a dimensionless shape function, which was discussed in Section 2.3.3. The prefactor $\mathcal{P}_{\Phi_i}$ carries the same index structure as the two-point function of the respective field. For the case of interest in this thesis, general covariant gauges (3.24a), the generalization is straightforward. After dropping the δ-function of momentum conservation and get in vacuum

$$\begin{aligned} \left[S^{AA}\right]^{ab}_{\mu\nu}(p) &= \left[p^2\delta_{\mu\nu} - \left(1-\frac{1}{\xi}\right)p_\mu p_\nu\right]\delta^{ab} \\ \left[S^{c\bar{c}}\right]^{ab}(p) &= p^2\delta^{ab} \\ \left[S^{q\bar{q}}\right]^{AB}(p) &= \left(\mathrm{i}\not{p} + m_q\right)\delta^{AB}\,. \end{aligned} \tag{3.40}$$

It turns out that (3.40) already comprises the general tensor structure of the two-point functions $\Gamma^{(2)}$ of QCD in a covariant gauge. For the gauge field it turns out to very useful to express the tensor structure in terms of the longitudinal and transversal projector

$$\begin{aligned} \Pi^{\perp}_{\mu\nu}(p) &= \delta_{\mu\nu} - \frac{p_\mu p_\nu}{p^2} \\ \Pi^{\parallel}_{\mu\nu}(p) &= \mathbb{1} - \Pi^{\perp}_{\mu\nu}(p)\,. \end{aligned} \tag{3.41}$$

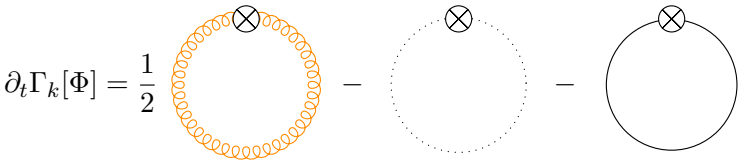

Figure 3.3.: Flow equation of QCD. The orange, curly line represents the full gluon propagator, the dotted line represents the full ghost propagator and the solid line the full quark propagator. The cross insertion denotes the regulator derivative.

At vanishing field the colour structure is trivial, i.e. δ^{ab} in the adjoint and δ^{AB} in the fundamental representation. With that at hand, the full two-point functions can be expressed as

$$\begin{aligned}
\left[\Gamma^{AA}\right]^{ab}_{\mu\nu}(p) &= \left(Z_A^{\perp}(p)\Pi^{\perp}_{\mu\nu}(p) + Z_A^{\parallel}(p)\Pi^{\parallel}_{\mu\nu}(p)\right) p^2\,\delta^{ab} \\
\left[\Gamma^{c\bar{c}}\right]^{ab}(p) &= Z_c(p) p^2\,\delta^{ab} \\
\left[\Gamma^{q\bar{q}}\right]^{AB}(p) &= Z_q(p)\left(\mathrm{i}\not{p} + M_q(p)\right)\delta^{AB}\,.
\end{aligned} \tag{3.42}$$

The classical values of the wave function renormalizations are given by $Z_A^{\perp}(p) = Z_c(p) = Z_q(p) = 1$ and $Z_A^{\parallel}(p) = 1/\xi$. In a gauge invariant regularization scheme the longitudinal wave function renormalization $Z_A^{\parallel}(p)$ does not receives quantum corrections, guaranteed by the Slavnov-Taylor Identities (STI). In the FRG framework the regularization breaks gauge invariance, and the modified STI (mSTI) guarantee $Z_A^{\parallel}(p) \to 1/\xi$ only in the limit $k \to 0$. This will be discussed in detail in Section 3.4.4.

With (3.42) we define the dispersion prefactors (3.39) for the regulator matrix

$$\begin{aligned}
\left[\mathcal{P}_A\right]^{ab}_{\mu\nu}(p) &= \left(\bar{Z}_A^{\perp}(p)\Pi^{\perp}_{\mu\nu}(p) + \bar{Z}_A^{\parallel}(p)\Pi^{\parallel}_{\mu\nu}(p)\right) p^2\,\delta^{ab} \\
\left[\mathcal{P}_c\right]^{ab}(p) &= \bar{Z}_c(p) p^2\,\delta^{ab} \\
\left[\mathcal{P}_q\right]^{AB}(p) &= \bar{Z}_q(p)\not{p}\,\delta^{AB}\,.
\end{aligned} \tag{3.43}$$

The modified wave function renormalization $\bar{Z}_{\Phi_i}$ are prefactors here, which are chosen such that they lead to RG adapted regulators and/or facilitate numerical computations. Carrying out the summations over field space indices in (2.74), we arrive at the flow equation for the scale dependent QEA in QCD

$$\partial_t\Gamma[\Phi] = \frac{1}{2}\,\mathrm{Tr}\; G_{AA}\,\partial_t R_A - \mathrm{Tr}\; G_{\bar{c}c}\,\partial_t R_c - \mathrm{Tr}\; G_{\bar{q}q}\,\partial_t R_q\,. \tag{3.44}$$

Its diagrammatic representation is shown in Figure 3.3.

As in the other examples studied before we now have to initialise the theory at a large momentum scale $\Lambda/\Lambda_{\rm QCD} \gg 1$, deep in the perturbative regime. Thanks to asymptotic freedom we get an excellent grip on the initial QEA

$$\Gamma_\Lambda[\Phi] = S_{\rm UV}[\Phi]\,, \tag{3.45}$$

where $S_{\rm UV}$ comprises all UV-relevant terms. This certainly includes all terms in the classical action (3.36). However, (broken) gauge symmetry leads to a mass term in the UV action Γ_Λ

$$S_{\rm UV} \propto \frac{1}{2} m^2_{A,\Lambda} \int_x A^a_\mu A^a_\mu \quad \text{with} \quad m^2_{A,\Lambda} \propto \Lambda^2\,. \tag{3.46}$$

We would like to emphasise that (3.46) does not imply a massive gauge theory. The physical theory is defined at $k = 0$, where we have

$$m^{\parallel\,2}_{A,k=0} = \Big[\, p^2 Z^\parallel_A(p)\Big]_{p^2=0} = 0\,, \tag{3.47}$$

the longitudinal mass vanishes, as necessary, in QCD. The fate of the transversal mass parameter, $m^{\perp\,2}_{A,k=0}$, is directly related to the *physical* mass gap in QCD In particular,

$$m^{\perp\,2}_{A,k=0} = \Big[\, p^2 Z^\perp_A(p)\Big]_{p^2=0} > 0\,, \tag{3.48}$$

the transversal gluon propagator has a mass gap. The property (3.48) has profound consequences. For example, it is a necessary condition for confinement at low temperatures [93–95]. Its generation in Yang-Mills theory and in QCD is not fully settled yet: while a lot of progress was made in the past two decades in terms of both, conceptual and technical/numerical advances, it is fair to say that a fully satisfactory consistent computation of the mass gap has not been achieved yet.

3.3.1.1. Vertex expansion in QCD

The flow equation for the effective action for QCD can obviously not be solved exactly. In QCD we resort to a systematic vertex expansion, Section 2.3.2, in quantitative approximations this vertex expansion is enhanced by full effective potentials of multi-quark interactions at low energies in the form of mesonic potentials. For this vertex expansion we introduce a general parametrization of the n-point functions $\Gamma^{(n)}$ with an expansion in a complete set of tensor structures $\mathcal{T}^{(i)}_{\{Phi\}_{1\ldots\Phi_n}}$ with $i = 1\ldots i_{\rm max}$,

$$\Gamma^{\Phi_1\ldots\Phi_n} = \sum_i \lambda^{(i)}_{\Phi_1\ldots\Phi_n}\, \mathcal{T}^{(i)}_{\Phi_1\ldots\Phi_n}\,. \tag{3.49}$$

The coefficients, dressing functions or form factors $\lambda^{(i)}_{\Phi_1\ldots\Phi_n}$ encode the dynamics of the theory. More specifically, they carry the dispersion relations and masses of the theory. For example, the tensor structures for the two-point functions in QCD are

$$\begin{aligned}
\mathcal{T}^{(1)}_{AA} &= p^2\, \Pi^\perp_{\mu\nu}(p)\delta^{ab} \\
\mathcal{T}^{(2)}_{AA} &= p^2\, \Pi^\parallel_{\mu\nu}(p)\delta^{ab} \\
\mathcal{T}^{(1)}_{c\bar c} &= p^2\, \delta^{ab} \\
\mathcal{T}^{(1)}_{q\bar q} &= \not{p}\mathbb{1} \\
\mathcal{T}^{(2)}_{q\bar q} &= \mathbb{1}\,,
\end{aligned} \tag{3.50}$$

where the $\mathbb{1}$ in the quark tensor structures collects the delta function from all indices. With (3.50) we can read of the relation between the dressings $\lambda_{\Phi_1\Phi_2}$ and the parametrization given in (3.42)

$$\begin{aligned}
\lambda^{(1)}_{AA}(p) &= Z_A^{\perp}(p) \\
\lambda^{(2)}_{AA}(p) &= Z_A^{\parallel}(p) \\
\lambda^{(1)}_{c\bar{c}}(p) &= Z_c(p) \\
\lambda^{(1)}_{q\bar{q}}(p) &= \mathrm{i}\, Z_q(p) \\
\lambda^{(2)}_{q\bar{q}}(p) &= Z_q(p)\, M_q(p)\,.
\end{aligned} \tag{3.51}$$

The strong coupling α_{S} is by definition related to the coupling g as

$$\alpha_{\mathrm{S}} = \frac{g^2}{4\pi}\,. \tag{3.52}$$

With the classical tensor structures, which are always the first one, of the three- and four-point functions, which make up the primitively divergent vertices in QCD, we are able to define the strong coupling as well. Perturbatively, the coupling agree, independent from which tensor structure they are extracted. The relation to the different structures is given by

$$\begin{aligned}
\alpha_{\bar{c}cA}(\bar{p}) &= \frac{1}{4\pi}\frac{\left[\lambda^{(1)}_{\bar{c}cA}(\bar{p})\right]^2}{Z_A(\bar{p})Z_c^2(\bar{p})} \\
\alpha_{A^3}(\bar{p}) &= \frac{1}{4\pi}\frac{\left[\lambda^{(1)}_{A^3}(\bar{p})\right]^2}{Z_A^3(\bar{p})} \\
\alpha_{A^4}(\bar{p}) &= \frac{1}{4\pi}\frac{\left[\lambda^{(1)}_{A^4}(\bar{p})\right]}{Z_A^2(\bar{p})} \\
\alpha_{\bar{q}qA}(\bar{p}) &= \frac{1}{4\pi}\frac{\left[\lambda^{(1)}_{\bar{q}qA}(\bar{p})\right]^2}{Z_A(\bar{p})Z_q^2(\bar{p})}\,,
\end{aligned} \tag{3.53}$$

where $\bar{p}$ denotes the symmetric point configuration. The strong coupling is marginal in four dimensions and therefore, these running couplings are two-loop universal. Note that this universality neither entails universality of $\partial_t\alpha_i$ beyond one loop with $i = \bar{c}cA, A^3, A^4, \bar{q}qA$, nor does it imply the same momentum-dependence beyond one loop. More details about the tensor structures of the different n-point functions are given in Section 3.5.1. Qualitative and quantitative features of this are discussed in Section 3.5.

3.4. Quantum gauge symmetry

So far we have only discussed the flow of QCD and mentioned the importance of the STIs. Additionally, the STIs in the presence of the regulator are of eminent importance for the existence of the mass gap in the gluon propagator, and hence directly important for confinement. Consequently we now discuss the manifestation of gauge invariance in the present gauge fixed approach. We discuss both, the STI that is related to standard gauge transformations on the fields, as well the BRST (C. Becchi, A. Rouet, R. Stora [96] and I. V. Tyutin [97]) transformations, that allow us to write the symmetry transformations in form of an exact derivative. The latter property leads to a purely algebraic form of the symmetry identity.

3.4.1. Gauge transformations & Slavnov-Taylor identities

Here we restrict ourselves to gauge fixed Yang-Mills theory, as introduced in Section 3.2. The inclusion of charged matter fields is straightforward. Gauge transformations with $\mathcal{U} = e^{i\omega}$ for gluon and ghost fields read

$$\begin{aligned} A_\mu^U &= \frac{\mathrm{i}}{g} U \left(D_\mu U^\dagger \right) &&= A_\mu + [D_\mu, \omega] &&+ \mathcal{O}(\omega^2) \\ c^U &= U c U^\dagger &&= c - \mathrm{i}g\,[c, \omega] &&+ \mathcal{O}(\omega^2) \\ \bar{c}^U &= U \bar{c} U^\dagger &&= \bar{c} - \mathrm{i}g\,[\bar{c}, \omega] &&+ \mathcal{O}(\omega^2)\,, \end{aligned} \tag{3.54}$$

where ghost and anti-ghost have been set to transform as tensors under gauge transformations. The generator of the gauge transformations in (3.54) can be written as

$$\delta^a_{\text{gauge}} = -D^{ab}_\mu \frac{\delta}{\delta A^b_\mu} - \mathrm{i}g\, f^{abc} \left(c_c \frac{\delta}{\delta c_b} + \bar{c}_c \frac{\delta}{\delta \bar{c}_b} \right) . \tag{3.55}$$

One easily sees that $\int_x \omega^a(x) \delta^a_{\text{gauge}}(x) \Phi(y)$ generates the terms linear in ω in (3.54). Note that (3.54) or (3.55) is not an invariance of the gauge fixed action: while the Yang-Mills action is gauge invariant, neither the gauge fixing term nor the ghost action is. Still, the operator δ_{gauge} has the form of the operator in the generalised Dyson-Schwinger equation [8, 38]. The total derivative operator inserted there is $\delta/\delta\varphi(x)\Psi[\varphi] = \delta^a_{\text{gauge}}$. This is seen explicitly within the representation

$$\delta^a_{\text{gauge}} = -\frac{\delta}{\delta A^b_\mu} D^{ab}_\mu + \mathrm{i}g \left(\frac{\delta}{\delta c_b} f^{abc} c_c + \frac{\delta}{\delta \bar{c}_b} \bar{c}_c \right) , \tag{3.56}$$

where the derivatives act on everything to the right and we have used that $f^{abb} = 0$. Let $\Phi = (A, c, \bar{c})$ denote the superfield in Yang-Mills, we arrive at

$$\frac{1}{Z[J]} \int \mathrm{d}\Phi\, \delta^a_{\text{gauge}} \left[e^{-S_A[A,c,\bar{c}] + J_\Phi \cdot \Phi} \right] = \left\langle J_\Phi \cdot \delta^a_{\text{gauge}} \Phi - \delta^a_{\text{gauge}} \left(S_{\text{gf}} + S_{\text{gh}} \right) \right\rangle = 0\,. \tag{3.57}$$

This equation entails that δ^a_{gauge} carries a projection of the shift invariance of the theory represented by the Dyson-Schwinger equations. The generator δ^a_{gauge} carries indeed the gauge invariance of the theory, this is seen within a restriction to gauge invariant observables $\langle \mathcal{O}[A] \rangle$ with $[A] = [A^U]$. With this we arrive at

$$-\frac{\delta}{\delta A^b_\mu} D^{ab}_\mu \left[\mathcal{O}[A] \int \mathrm{d}c\, \mathrm{d}\bar{c}\, e^{-S_A[A,c,\bar{c}]} \right] = 0\,. \tag{3.58}$$

In (3.58) we have used that in the absence of sources for the ghost and anti-ghost we can integrate out $c, \bar{c}$, thus undoing the introduction of the unity inserted by the Faddeev-Popov trick. Carrying out the δ^a_{gauge} variations in (3.57) explicitly leads us to

$$\left(D^{ab}_\mu J^b_\mu - \mathrm{i}g f^{abc}\left(\bar{\eta}^b\langle c^c\rangle - \langle\bar{c}^c\rangle\eta^b\right)\right) = \left\langle \frac{1}{\xi} D^{ab}_\mu(x)\partial_\mu\partial_\nu A^b_\nu(x) - \frac{g}{2} f^{abc}\partial_\mu\left[\bar{c}^b D^{cd}_\mu c^d\right]\right\rangle . \tag{3.59}$$

In summary, δ^a_{gauge} indeed carries the underlying gauge symmetry in terms of a projected (on the gauge fibre) DSE. These projected DSEs, (3.57), are the *Slavnov-Taylor identities* (STIs), see (3.59).

While such a representation of gauge symmetry encodes all information, it is not a symmetry of the gauge fixed theory. It is the latter fact that will lead to loop terms in the STIs, see the right hand side of (3.59). In other words, the symmetry transformation looses its algebraic nature on the quantum level. An invariance of the gauge fixed action requires also the transformation of the gauge fixing itself. This is achieved by the BRST transformations discussed in the following subsection.

3.4.2. BRST symmetry

We want to give a brief account on BRST symmetry for the current setup. Without much ado, the BRST symmetry is a combined transformation of the fields $\Phi = (A, c, \bar{c})$ and the infinitesimal BRST transformation δ_{BRST} reads

$$\delta_{\text{BRST}}\Phi = \delta\lambda\, \mathfrak{s}\Phi\,, \tag{3.60}$$

with the BRST generator $\mathfrak{s}$ acting on Φ and an infinitesimal Grassmann parameter $\delta\lambda$. The BRST operator $\mathfrak{s}$ acts on the fields as

$$\begin{aligned} \mathfrak{s}\, A^a_\mu &= D^{ab}_\mu c^b\,, \\ \mathfrak{s}\, c^a &= -\frac{g}{2} f^{abc} c^b c^c\,, \\ \mathfrak{s}\, \bar{c}^a &= \frac{1}{\xi}\mathcal{F}^a[A]\,, \end{aligned} \tag{3.61}$$

and is a Grassmann number. Accordingly, the Grassmann number $\delta\lambda$ ensures that the BRST variations $\delta_{\text{BRST}}\Phi_i$ are Grassmannian for $\Phi_i = c, \bar{c}$ and commute with $c, \bar{c}$ for $\Phi_i = A_\mu$. In fact, the BRST transformations $\mathfrak{s}\,\Phi_i$ of gauge field and ghost are simply gauge transformations with the Grassmannian algebra element $\omega \sim c$. The BRST transformation of the anti-ghost is the shift of the gauge fixing condition that arranges for the invariance of the gauge fixed action (3.32). While the Yang-Mills action and $D_\mu c$ are invariant under the combined BRST transformations of gauge field and ghost, the gauge transformation of the gauge fixing term, due to $A_\mu \to A_\mu + \delta_{\text{BRST}} A_\mu$, is compensated by the BRST transformation of the anti-ghost.

With this at hand the BRST variation can be written as

$$\mathfrak{s} = \int_x (\mathfrak{s}\Phi_i)\frac{\delta}{\delta\Phi_i} \tag{3.62}$$

and the invariance of the classical action reduces to

$$\mathfrak{s}\, S[\Phi] = 0\,. \tag{3.63}$$

As for the standard gauge transformation, the BRST operator $\mathfrak{s}$ in (3.62) can be written in terms of a total derivative

$$\mathfrak{s} = \int_x \frac{\delta}{\delta\Phi_i}(\mathfrak{s}\Phi_i)\,, \tag{3.64}$$

where we have again used that $f^{abb} = 0$. Moreover, $(\mathfrak{s}\Phi_i)$ commutes with $\delta/\delta\Phi_i$ as the BRST transformations of the ghost and anti-ghosts are not Grassmanian. This leads us directly to the projected DSE

$$\frac{1}{Z[J_\Phi]} \int \mathrm{d}\Phi\, \mathfrak{s} \left[e^{-S_A[\Phi] + J_\Phi \cdot \Phi} \right] = 0\,, \tag{3.65}$$

In contradistinction to the projected DSE (3.57) for gauge transformations, the projected DSE (3.65) carries a symmetry of the underlying gauge-fixed action, see (3.63). This leads straightforwardly to

$$\langle J_A \cdot \mathfrak{s}\, A - J_c \cdot \mathfrak{s}\, c - J_{\bar{c}} \cdot \mathfrak{s}\, \bar{c} \rangle = 0\,, \tag{3.66}$$

the STI in terms of BRST transformations. Equation (3.66) makes apparent that the BRST transformations are symmetry transformations, i.e. the equation only encodes the transformation of the source terms, and hence simply carries the classical, algebraic, BRST symmetry of Yang-Mills theory in the extended field space. Note however, that the BRST variations of the fields are quadratic in the fields. This entails in particular, that $\langle \mathfrak{s}\, A_\mu \rangle$ and $\langle \mathfrak{s}\, c \rangle$ involve non-trivial two-point functions in contradistinction to the expectation values of the gauge variations of the fields.

3.4.2.1. Gauge fixing fermion, Nakanishi-Laudrup field and anti-field formalism

The latter fact seems to imply that we loose the algebraic nature of the symmetry on the quantum level. A way out of the seeming non-algebraic nature of the STI (3.66) is the introduction of source terms for the BRST variations of the fields in the generating functional $Z[J] \to Z[J, Q]$, with the additional source term

$$\mathcal{Q} \cdot \mathfrak{s}\Phi = \mathcal{Q}_A \cdot \mathfrak{s}A + \mathcal{Q}_c \cdot \mathfrak{s}c + \mathcal{Q}_{\bar{c}} \cdot \mathfrak{s}\bar{c}\,. \tag{3.67}$$

Then, the non-trivial expectation values $\langle \mathfrak{s}\Phi \rangle$ in (3.66) can be represented in terms of derivatives with respect to the BRST sources Q_i with $i = A_\mu, c, \bar{c}$, rendering the STI algebraic again. However, the source term for the anti-ghost is not BRST invariant, $\mathfrak{s}^2\bar{c} = \frac{1}{\xi}\,\mathfrak{s}\,\mathcal{F}[A] \neq 0$, and triggers further non-trivial contributions to (3.66), leading to

$$\int_x \left\langle J_A \cdot \mathfrak{s}\, A - J_c \cdot \mathfrak{s}\, c - J_{\bar{c}} \cdot \mathfrak{s}\, \bar{c} - \frac{1}{\xi}\,(\partial_\mu Q_{\bar{c}})\; \mathfrak{s} A_\mu \right\rangle = 0\,. \tag{3.68}$$

In (3.68) we have restricted ourselves to a covariant gauge and have performed a partial integration, leading to the minus sign in the last term. The form of the STI in (3.68) makes even more apparent that the invariance under a BRST transformation of the gauge field and the ghost requires a respective transformation of the gauge fixing condition.

The most elegant resolution for this fact is the introduction of a field for the BRST variation of the anti-ghost $\bar{c}$, or rather the gauge fixing. This is the Nakanishi-Laudrup field B^a with

$$S_{\mathrm{gf}}[A, B] = \int_x \left(B^a \partial_\mu A^a_\mu - \frac{\xi}{2} B^a B^a \right)\,, \tag{3.69}$$

which reduces to the standard gauge fixing term $S_{\rm gf}[A]$ on-shell, that is on the equation of motion for B

$$S_{\rm gf}[A] = S_{\rm gf}[A, B_{\rm EoM}] \quad \text{with} \quad B^a_{\rm EoM} = \frac{1}{\xi}\partial_\mu A^a_\mu \,. \tag{3.70}$$

If we now use this formulation off-shell, the anti-ghost BRST transformation (3.61) is given by $\mathfrak{s}\bar{c} = B^a$. The BRST transformations in this extended field space read,

$$\begin{aligned} \mathfrak{s}\, A^a_\mu &= D^{ab}_\mu c^b \\ \mathfrak{s}\, c^a &= -\frac{g}{2} f^{abc} c^b c^c \\ \mathfrak{s}\, \bar{c}^a &= B^a \\ \mathfrak{s}\, B^a &= 0 \,. \end{aligned} \tag{3.71}$$

With this at hand, the BRST generator $\mathfrak{s}$ in (3.71) is now nilpotent

$$\mathfrak{s}^2 = 0 \,. \tag{3.72}$$

Then, the gauge fixed action in Yang-Mills theory reads

$$S_A[\Phi] = S_{\rm YM}[A] + \int_x \mathfrak{s}\, \psi[\Phi] \,, \tag{3.73}$$

with the *gauge-fixing fermion*, see e.g. [98],

$$\psi[\Phi] = \bar{c}^a \partial_\mu A^a_\mu - \frac{\xi}{2}\bar{c}^a B^a \,, \tag{3.74}$$

with $\int_x \mathfrak{s}\, \psi[\Phi] = S_{\rm gf}[A, B] + S_{\rm gh}[A, c, \bar{c}]$. To show this identity one has to take into account that

$$\mathfrak{s}\bar{c}^a \partial_\mu A^a_\mu = (\mathfrak{s}\bar{c}^a)\, \partial_\mu A^a_\mu - \bar{c}^a \partial_\mu \left(\mathfrak{s} A^a_\mu\right) \,. \tag{3.75}$$

The superfield Φ now also includes the Nakanishi-Laudrup field

$$\Phi = (A_\mu, c, \bar{c}, B) \,. \tag{3.76}$$

Equation (3.73) is manifestly BRST invariant. The Yang-Mills action is manifestly gauge invariant and $\mathfrak{s}^2\psi$ is invariant as $\mathfrak{s}$ is nilpotent, c.f. (3.72). In summary we have

$$\mathfrak{s}\, S_A[\Phi] = 0 \,. \tag{3.77}$$

We emphasise again, that $S_A[A, c, \bar{c}, B]$ reduces to the standard gauge fixed action on the equation of motion for B, see (3.69), $S_A[A, c, \bar{c}] = S_A[A, c, \bar{c}, B_{\rm EoM}]$. Within this formulation the last term in (3.68) is missing, and the anti-ghost term is trivial.

3.4.3. Slavnov-Taylor Identities for the QEA

Compliance with (3.59) or (3.66) guarantees the gauge invariance of observables. However in computation approaches one usually works with the QEA $\Gamma[\Phi]$. Recalling the basic relation between the effective action and the sources

$$J_A = \frac{\delta\Gamma}{\delta A} \,, \quad J_c = -\frac{\delta\Gamma}{\delta c} \,, \quad J_{\bar{c}} = -\frac{\delta\Gamma}{\delta \bar{c}} \,, \tag{3.78}$$

we are able to translate equations in the usual fashion to the QEA.

3.4.3.1. STI for gauge transformations

Now we substitute the relations (3.78) into (3.59). We also use that the field dependence on the right hand side is, linear: $\langle \delta_{\text{gauge}} \hat{\Phi} \rangle = \delta_{\text{gauge}} \Phi$ with $\Phi = \langle \hat{\Phi} \rangle$. This leads us to

$$W[\Phi] = 0 \qquad \text{with} \qquad W[\Phi] = \delta^a_{\text{gauge}} \Gamma[\Phi] - \left\langle \delta^a_{\text{gauge}} \left(S_{\text{gf}} + S_{\text{gh}} \right) \right\rangle , \tag{3.79}$$

encoding the condition for gauge invariant observables in terms of the QEA. The right hand side of (3.79) can be written in terms of loop diagrams. As in the DSE this leads to one and two loop diagrams in classical vertices, full vertices and full propagators.

3.4.3.2. STI for BRST transformations

A more concise representation of the underlying gauge invariance is achieved with the BRST formulation discussed in Section 3.4.2.1. With the Nakanishi-Laudrup field B and sources $\mathcal{Q}_i$, with $i = A, c, \bar{c}$, for the BRST variations $\mathfrak{s}\,\Phi$, the generating functional reads

$$Z[J, \mathcal{Q}] = \int \mathcal{D}\Phi \, e^{-S[A,c,\bar{c},B] + J_A \cdot A + J_c \cdot c - \bar{c}\, J_{\bar{c}} + \mathcal{Q}_A \,\mathfrak{s} A + \mathcal{Q}_c \,\mathfrak{s} c + \mathcal{Q}_{\bar{c}} \,\mathfrak{s} \bar{c}} . \tag{3.80}$$

Note that the BRST source term $\int_x \mathcal{Q}_{\bar{c}} \,\mathfrak{s}\, \bar{c}$ corresponds to a source term for B, since $\mathfrak{s}\, \bar{c} = B$. As the BRST source terms only involve $\mathfrak{s}\,\Phi$, they are invariant under BRST transformations, $\mathfrak{s} \int_x \mathcal{Q} \cdot \mathfrak{s}\Phi = 0$. Accordingly, the STI (3.66) does not change, and reads in terms of the generating functional $Z[J, Q]$

$$\int_x \left(\frac{\delta Z}{\delta \mathcal{Q}_A} \cdot J_A - \frac{\delta Z}{\delta \mathcal{Q}_c} \cdot J_c - \frac{\delta Z}{\delta \mathcal{Q}_{\bar{c}}} \cdot J_{\bar{c}} \right) = 0 . \tag{3.81}$$

In (3.81) we have brought all currents to the right. This is possible as either the current J_i or the BRST-transformation $\mathfrak{s}\,\Phi_i$ is Grassmannian, but never both. The QEA is the Legendre transform of the logarithm of $Z[J_\Phi, \mathcal{Q}_\Phi]$ with respect to the current J_Φ, while $\mathcal{Q}_\Phi$ is a spectator,

$$\begin{aligned} \Gamma[\Phi, \mathcal{Q}_\Phi] &= \int J_\Phi \cdot \Phi - \ln Z[J_\Phi, \mathcal{Q}_\Phi] \\ \text{with} \quad \frac{\delta \Gamma[\Phi, \mathcal{Q}_\Phi]}{\delta \mathcal{Q}_i} &= - \frac{1}{Z[J_\Phi, \mathcal{Q}_\Phi]} \frac{\delta Z[J_\Phi, \mathcal{Q}_\Phi]}{\delta \mathcal{Q}_i} , . \end{aligned} \tag{3.82}$$

Collecting everything, we are led to the *Quantum Master Equation* (QME),

$$\frac{\delta \Gamma}{\delta \mathcal{Q}_\Phi} \cdot \frac{\delta \Gamma}{\delta \Phi} = 0 , \tag{3.83}$$

where the left hand side of (3.83) reads more explicitly

$$\frac{\delta \Gamma}{\delta \mathcal{Q}_\Phi} \cdot \frac{\delta \Gamma}{\delta \Phi} = \int_x \left(\frac{\delta \Gamma}{\delta \mathcal{Q}^a_{A,\mu}(x)} \frac{\delta \Gamma}{\delta A^a_\mu(x)} + \frac{\delta \Gamma}{\delta \mathcal{Q}^a_c(x)} \frac{\delta \Gamma}{\delta c^a(x)} + \frac{\delta \Gamma}{\delta \mathcal{Q}^a_{\bar{c}}(x)} \frac{\delta \Gamma}{\delta \bar{c}^a(x)} \right) . \tag{3.84}$$

As a simple example we consider the classical action, $\Gamma = S$ in (3.83). After a straightforward calculation one arrives at $\mathfrak{s}\, S[\phi] = 0$, i.e. the BRST invariance of the classical action.

We can use (3.83) to define a generator of quantum BRST transformations

$$\mathfrak{s}_\Gamma = \frac{\delta\Gamma}{\delta\mathcal{Q}^a_A}\cdot\frac{\delta}{\delta A} + \frac{\delta\Gamma}{\delta\mathcal{Q}_c}\cdot\frac{\delta}{\delta c} + \frac{\delta\Gamma}{\delta\mathcal{Q}_{\bar{c}}}\cdot\frac{\delta}{\delta\bar{c}}\,, \tag{3.85}$$

which we can use to rewrite (3.83) as

$$\mathfrak{s}_\Gamma\Gamma = 0\,. \tag{3.86}$$

Finally, the anti-ghost field appears only linearly in the generating function Z. Utilising the DSE with an anti-ghost derivative, we arrive at

$$\langle\partial_\mu D_\mu c\rangle - \eta = 0 \quad\Leftrightarrow\quad \partial_\mu\frac{\delta\Gamma}{\delta\mathcal{Q}_{A,\mu}} + \frac{\delta\Gamma}{\delta\bar{c}} = 0\,, \tag{3.87}$$

Integrating out the B-Field and using (3.87), we arrive at

$$\frac{\delta\Gamma}{\delta\mathcal{Q}_A}\cdot\frac{\delta\Gamma}{\delta A} + \frac{\delta\Gamma}{\delta\mathcal{Q}_c}\cdot\frac{\delta\Gamma}{\delta c} - \int_x\left\{\frac{1}{\xi}\left(\partial_\nu A^a_\nu\right)\partial_\mu\frac{\delta\Gamma}{\delta\mathcal{Q}^a_{A,\mu}}\right\} = 0\,. \tag{3.88}$$

In (3.88) it is evident that the variation of the anti-ghost simply amounts to a gauge transformation of the gauge fixing term, as it was introduced in the first place.

3.4.4. Modified Slavnov-Taylor Identities

The STIs discussed in the last chapter get modified by the gauge or BRST variation of the cutoff term, leading to *modified Slavnov-Taylor Identities* (mSTI). These mSTIs reduce to the standard ones for a vanishing regulator $R_k = 0$.

We start with a brief discussion of the mSTI in terms of δ_{gauge}. Adding the additional term to the classical action simply changes the expression on the right hand side of (3.59) and (3.79). Moreover, due to the modification of the Legendre transform in the definition of the scale-dependent QEA $\Gamma_k[\Phi, \mathcal{Q}]$ in (2.5). Here we already allow for the general case with BRST sources. In the present case the relations between the sources and currents are

$$J_A = \frac{\delta(\Gamma_k + \Delta S_k)}{\delta A}\,, \qquad J_c = -\frac{\delta(\Gamma_k + \Delta S_k)}{\delta c}\,, \qquad J_{\bar{c}} = -\frac{\delta(\Gamma_k + \Delta S_k)}{\delta\bar{c}}\,. \tag{3.89}$$

Note also that the BRST charges are spectators in the Legendre transform, and hence we have

$$\mathfrak{s}\,\Phi = \frac{\delta\Gamma_k[J,\mathcal{Q}]}{\delta\mathcal{Q}} = -\frac{\delta Z_k[J,\mathcal{Q}]}{\delta\mathcal{Q}}\,, \tag{3.90}$$

as the cutoff term does not depend on the BRST charges $\mathcal{Q}$.

3.4.4.1. mSTI for gauge transformations

We first restrict ourselves to the case $\mathcal{Q} = 0$ with $\Gamma[\Phi] = \Gamma[\Phi, \mathcal{Q} = 0]$, and consider gauge transformations. Hence, (3.79) translates into

$$W_k[\Phi] = 0\,, \tag{3.91}$$

with $\Phi = (A_\mu, c, \bar{c})$ and

$$W_k[\Phi] = \delta^a_{\text{gauge}}\Gamma_k[\Phi] - \left\langle \delta^a_{\text{gauge}} \left(S_{\text{gf}} + S_{\text{gh}}\right)\right\rangle - \left(\left\langle \delta^a_{\text{gauge}} \Delta S_k\right\rangle - \delta^a_{\text{gauge}} \Delta S_k\right) , \tag{3.92}$$

where the last term in the definition of the Slavnov-Taylor operator W_k comes from the modification of the Legendre transform in the definition of $\Gamma_k[\Phi]$. This modification of the STI can be written in terms of a one loop term similar to the flow equation itself. Evidently, it is proportional to the regulator and vanishes for $R_k = 0$, leaving us with the standard STI (3.79).

3.4.4.2. mSTI for BRST transformations

In the STI on the basis of BRST variations, (3.83), we have to take into account the missing BRST invariance of the cutoff term in the STI for the generating functional. This leads us to

$$\int_x \left(\frac{\delta Z}{\delta \mathcal{Q}_A} \cdot J_A - \frac{\delta Z}{\delta \mathcal{Q}_c} \cdot J_c - \frac{\delta Z}{\delta \mathcal{Q}_{\bar{c}}} \cdot J_{\bar{c}} \right) = \langle \mathfrak{s}\, \Delta S_k[\Phi] \rangle \, , \tag{3.93}$$

with $\Phi = (A_\mu, c, \bar{c}, B)$. Inserting (3.89) for the currents, and (3.90) for the BRST variations, we arrive at

$$\frac{\delta \Gamma_k}{\delta \mathcal{Q}_\Phi} \cdot \frac{\delta(\Gamma_k + \Delta S_k)}{\delta \Phi} = -\langle \mathfrak{s}\, \Delta S_k \rangle \quad \rightarrow \quad \frac{\delta \Gamma_k}{\delta \mathcal{Q}_\Phi} \cdot \frac{\delta \Gamma_k}{\delta \Phi} = -\langle \mathfrak{s}\, \Delta S_k \rangle - \frac{\delta \Gamma_k}{\delta \mathcal{Q}_\Phi} \cdot \frac{\delta \Delta S_k}{\delta \Phi} \, . \tag{3.94}$$

The right hand side of (3.94) is computed in Section B.1, and gives a term similar to the loop in the flow equation, see (B.4). We also drop the subscript k again, it is implicitly understood, and quote

$$-\left[\langle \mathfrak{s}\, \Delta S_k \rangle + \mathfrak{s}\, \Delta S_k\right] = R^{ij} G_{jl} \frac{\delta^2 \Gamma_k[\Phi, \mathcal{Q}]}{\delta \Phi_l \delta Q^i} \, , \tag{3.95}$$

where G is the regularized propagator. The derivation of (3.95) can be found in Section B.1. With this at hand, we arrive at the modified Slavnov-Taylor Identity

$$\frac{\delta \Gamma}{\delta \mathcal{Q}_\Phi} \cdot \frac{\delta \Gamma}{\delta \Phi} = R^{ij} G_{jl} \frac{\delta^2 \Gamma_k[\Phi, \mathcal{Q}]}{\delta \Phi_l \delta Q^i} \, . \tag{3.96}$$

Understanding the mSTIs is of great importance for practical calculations in Yang-Mills. They provide a set of self consistency equations that are not automatically fulfilled in truncations and should therefore be monitored closely. Their importance should already obvious from the statement they encode, the gauge invariance of observables. In particular, they encode relations regarding the gluon mass gap , as it can be seen in the following.

3.4.4.3. mSTI for the longitudinal gluon mass

Here we discuss a crucially important example for the consequences of the mSTIs, the gluon mass term. First we recall, that the standard STI entails that the quantum corrections of the gluon two point function, Γ^{AA} are purely transversal. To that end we take a ghost and a gluon derivative of the master equation at vanishing regulator $R_k = 0$, evaluated at the

equations of motion and at vanishing BRST sources, with $\mathcal{Q}_\Phi = 0$ given by $\Phi_0 = (0, B_{\text{EoM}})$, c.f. (3.69),

$$\begin{aligned}&\frac{\delta^2}{\delta A_\mu(x)\delta c(y)}\left[\frac{\delta\Gamma}{\delta\mathcal{Q}_\Phi}\cdot\frac{\delta\Gamma}{\delta\Phi}\right]_{\Phi=\Phi_0,\mathcal{Q}=0}\\ &=\left[\frac{\delta}{\delta c(y)}\frac{\delta\Gamma}{\delta\mathcal{Q}_{A,\nu}}\right]\cdot\left[\frac{\delta}{\delta A_\mu(x)}\frac{\delta\Gamma}{\delta A_\nu}\right]+\left[\frac{\delta}{\delta A_\mu(x)}\frac{\delta\Gamma}{\delta\mathcal{Q}_{\bar{c}}}\right]\cdot\left[\frac{\delta}{\delta c(y)}\frac{\delta\Gamma}{\delta\bar{c}}\right]\Bigg|_{\Phi=\Phi_0,\mathcal{Q}=0}=0\,.\end{aligned}\tag{3.97}$$

No we use the anti-ghost equation (3.87) and arrive at

$$\left[\frac{\delta}{\delta c(y)}\frac{\delta\Gamma}{\delta\mathcal{Q}_{A,\nu}}\right]\cdot\left[\Gamma^{AA}_{\nu\mu}-\partial_\mu\frac{\delta}{\delta A_\mu(x)}\frac{1}{\xi}\partial_\nu A_\nu\right]\Bigg|_{\Phi=\Phi_0,\mathcal{Q}=0}=0\,,\tag{3.98}$$

where we have also used that $\delta\Gamma/\delta\mathcal{Q}_{\bar{c}} = B_{\text{EoM}} = 1/\xi\partial_\mu A_\mu$.

The c-derivative of the BRST-variation of the gauge field at vanishing fields and BRST sources is proportional to p_ν in momentum space. Since no other Lorentz vector is present, we obtain in momentum space

$$p_\nu\Gamma^{(2)}_{\nu\mu}=\frac{1}{\xi}p^2p_\mu=p_\nu S^{(2)}_{\text{gf},\nu\mu}\,.\tag{3.99}$$

We immediately conclude from (3.99) that the longitudinal wave function renormalization is trivial within a gauge invariant regularisation and reads

$$Z_A^{\parallel}=\frac{1}{\xi}\,.\tag{3.100}$$

This can of course be extended by the use of (3.96), which indicates loop corrections to this result in the FRG. In particular, it indicates a quadratic RG running of the longitudinal mass, which is already present at the one-loop level. The result for the longitudinal gluon mass at the one-loop level has been derived in [99–101] and reads

$$\begin{aligned}(m^{\parallel})^2=\alpha_s\frac{N_c}{4\pi}\,k^{d-2}\int dy\,y^{\frac{d}{2}-2}\frac{r(y)}{(1+r(y))^2}\times\\ \times\left(\frac{11}{2}-d-\frac{5}{d}+\xi\left(1-\frac{1}{d}\right)+\left(\frac{7}{2}-\frac{6}{d}\right)\frac{y\,r'(y)}{1+r(y)}\right)\gtrless 0\,,\end{aligned}\tag{3.101}$$

where the shape function of the regulator is chose to be equal for ghost and gluon and the sign depends on the dimension.

3.4.4.4. QMeS : Derivation

This subsubsection is in parts based on [9].

In order to expand quantum master equations such as the Wetterich equation (2.74), the Dyson-Schwinger equation (2.71) or the modified Slavnov-Taylor identities (3.96) efficiently in terms of the elementary correlation functions of the theory. Working in the superfield formalism introduced in Section 2.4, the procedure to expand these master equations reduces to the task of taking functional derivatives thereof. This is straightforward to implement, and we've done so in a Mathematica [102] module, called "QMeS : Derivation".

Our main motivation is the systematic investigation of (3.96) within Functional Methods in order to improve upon the reliability of truncations. For the FRG and DSE its functionality and usability is quite similar to DoFun [103, 104]. The module is planned on publishing this module soon.

3.5. Yang-Mills in Landau gauge

Having discussed the theoretical set-up at large, we would like to give a brief overview of the existing results for correlation functions in Yang-Mills from the FRG in vacuum. This allows us to discuss some features of these correlation functions that will become important later.

For this we restrict ourselves to Landau gauge $\xi = 0$, due the technical simplifications that come along with this choice. Consequently, Landau gauge is the gauge for which by far the most results for elementary correlation functions are available.

One of the most important properties of Landau gauge is the decoupling of the transversal sector, i.e. in Functional methods the equations for fully transversally projected correlation functions only depend on other fully transversally projected correlation functions. This is easily seen from the fact that the gluon propagator is fully transversal in this gauge. This is not only true in the FRG, but also holds in DSEs and nPI hierarchies, see e.g. [8, 105]. As equations this can be expressed as

$$\begin{aligned} \Gamma^{(n)}_{\perp} &= \mathrm{FunRel}^{(n)}_{\perp}\left[\left\{\Gamma^{(m)}_{\perp}\right\}\right] \\ \Gamma^{(n)}_{\parallel} &= \mathrm{FunRel}^{(n)}_{\parallel}\left[\left\{\Gamma^{(m)}\right\}\right], \end{aligned} \tag{3.102}$$

where the indices $\perp$ and $\parallel$ denote the correspondingly projected elementary correlation functions and FunRel denote the appropriate functional relations arising from some master equation, such as the FRG or DSE. We would like to note, that the longitudinal sector still depends on the transversal sector and cannot be calculated independently.

3.5.1. Vertex expansion with classical tensor structures

Looking at a vertex expansion in Yang-Mills, c.f. Section 3.3.1, we restrict ourselves to classical tensor structures. This is already sufficient to get even quantitatively competitive results and unravel a lot of qualitatively important features. The tensor structures of the two-point functions, and in this case equivalently also the propagator, are given in (3.50). For completeness we also state the classical tensor structures of the three- and four-point functions that are present at the classical level. The classical tensor structure of the ghost-gluon vertex

$$\left[\mathcal{T}^{(1)}_{\bar{c}cA}\right]^{abc}_{\mu}(p_1,p_2,p_3) = \mathrm{i} f^{abc}(p_1)_\mu \,. \tag{3.103}$$

The classical tensor structure of the three gluon vertex

$$\left[\mathcal{T}^{(1)}_{A^3}\right]^{abc}_{\mu\nu\rho}(p_1,p_2,p_3) = \mathrm{i} f^{abc}\Big((p_2-p_3)_\mu\delta_{\nu\rho} + (p_3-p_1)_\nu\delta_{\rho\mu} + (p_1-p_2)_\rho\delta_{\mu\nu}\Big)\,. \tag{3.104}$$

And finally, the classical tensor structure of the four gluon vertex

$$\begin{aligned} \left[\mathcal{T}^{(1)}_{A^4}\right]^{abcd}_{\mu\nu\rho\sigma}(p_1,p_2,p_3,p_4) = {} & f^{ade}f^{bce}\Big[\delta_{\mu\nu}\delta_{\rho\sigma} - \delta_{\mu\rho}\delta_{\nu\sigma}\Big] \\ & + f^{ace}f^{bde}\Big[\delta_{\mu\nu}\delta_{\rho\sigma} - \delta_{\mu\sigma}\delta_{\nu\rho}\Big] \\ & + f^{abe}f^{cde}\Big[\delta_{\mu\rho}\delta_{\nu\sigma} - \delta_{\mu\sigma}\delta_{\nu\rho}\Big]\,. \end{aligned} \tag{3.105}$$

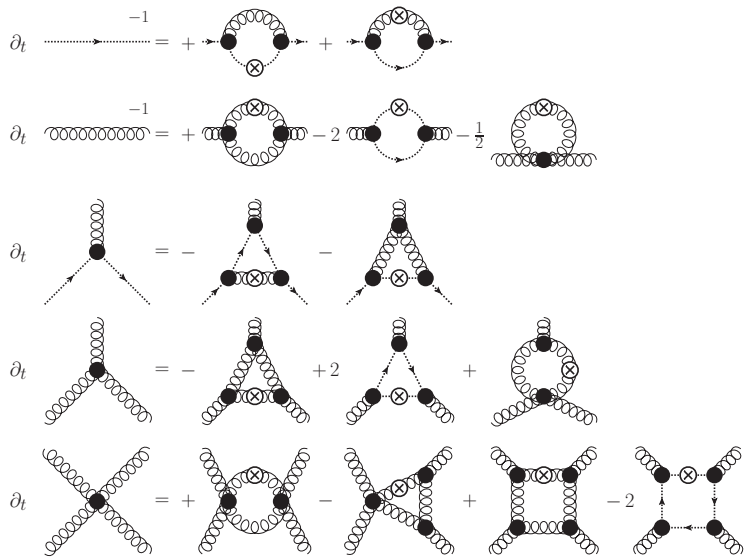

Figure 3.4.: Diagrammatic representation of the flow equations in a truncation where only classical tensor structures are taken into account. Permutations of diagrams, with respect to neither external momenta or regulator insertions, are not shown. Figure taken from [106].

For calculations we have to project onto the coefficients of the these tensor structures, i.e. we are looking for an projection operator $\mathcal{P}$ with the property

$$\mathcal{P}^{(i)}_{\Phi_{j_1}\dots\Phi_{j_n}}\Gamma^{\Phi_{j_1}\dots\Phi_{j_n}} = \lambda^{(i)}_{\Phi_{j_1}\dots\Phi_{j_n}}\,, \tag{3.106}$$

where dressing functions λ are defined in (3.49). Within a truncation that takes only classical tensor structures into account, this turns out to be trivial. Since there is only a single tensor structure around for each vertex we can simply take the projection operator proportional to the tensor structure itself $\mathcal{P}^{(i)}_{\Phi_{j_1}\dots\Phi_{j_n}} \sim \mathcal{T}^{(i)}_{\Phi_{j_1}\dots\Phi_{j_n}}$ and calculate the normalization. Note however, for a tensor basis of an n-point function with more than one element this results in a coefficient matrix that has to be inverted. The diagrammatic set of equations is shown in Figure 3.4.

A crucial point in these calculations concerns the initial values of the scale dependent QEA. The value of the vertices are fixed via the STIs, i.e. the dressings are initialized momentum independent and adjusted such that the aliases of the strong coupling (3.53) agree perturbatively, see e.g. [66]. More delicate is the transversal mass, which is not

present in the classical action S, but as a relevant coupling, is present in Γ_Λ. We refrain from a full discussion on this issue here and refer the interested reader to [8, 106] and references therein. Summarized, we require a mass gap gluon propagator in Landau gauge as a necessary condition for confinement. In particular, the gluon has to be gapped relative to the ghost. As we have seen in Section 3.4, the longitudinal gluon propagator does not receive any quantum correlations, so a mass gapped transversal gluon mass

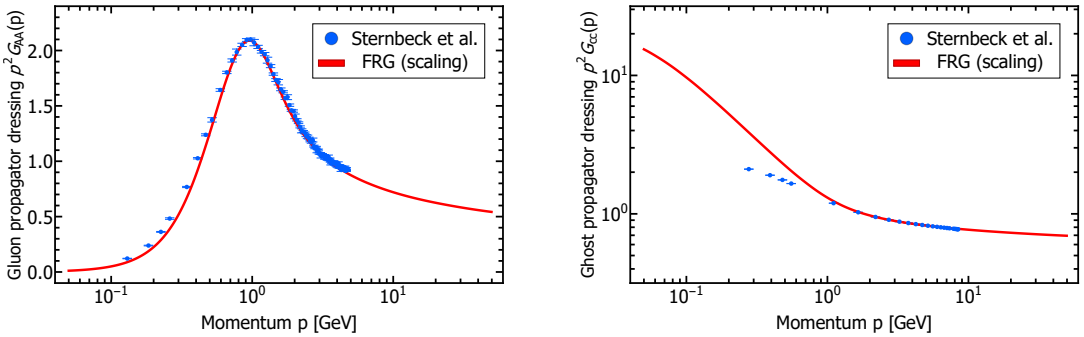

(a) Gluon propagator dressing.

(b) Ghost propagator dressing.

Figure 3.5.: Dressings of the propagators in Yang-Mills theory. Our scaling solution obtained with the FRG in the symmetric point approximation with only classical tensor structures is compared to the Lattice results from [107]. Note that a comparison in the deep IR does not necessarily make sense due to the issue of non-perturbative gauge fixing [108].

requires different contributions to these masses. The so called *scaling solution* [109–117] is characterized by

$$\begin{aligned} \lim_{p^2\to 0} Z_A(p) &\sim \left(p^2\right)^{-2\,\kappa} \\ \lim_{p^2\to 0} Z_c(p) &\sim \left(p^2\right)^{\kappa} , \end{aligned} \tag{3.107}$$

where the scaling coefficient is constraint in four dimensions to $1/2 < \kappa < 1$. It has been shown, that a constant ghost-gluon vertex in combination with a scaling ghost propagator is sufficient to introduce the necessary splitting. On the other hand, the so called *decoupling solution*, see e.g. [118, 119], is characterized by

$$\begin{aligned} \lim_{p^2\to 0} Z_A(p) &\sim \left(p^2\right)^{-1} \\ \lim_{p^2\to 0} Z_c(p) &\sim 1 . \end{aligned} \tag{3.108}$$

However, so far it is not clear where the necessary irregularity is generated in this IR scenario. For potential resolutions of this missing irregularity, see [66] and references therein. We will comment more on both scenarios in Section 6.4.

Practically, one finds a non-trivial behaviour of the physical mass gap $m_\perp^2$ as a function of the initial mass m_Λ^2. A diverging mass parameter is identified with the scaling solutions, while the non-trivial minimum is identified with the decoupling scenario.

The dressings of the propagators are shown in Figure 3.5, where the maximum in the gluon propagator, called *backbending*, is of utmost importance for confinement, for a discussion from a Euclidean perspective see [66] and references therein. We will comment on this later in Section 6.4. A comparison with the Lattice results of [107] is not necessarily useful in the deep IR due to the issue of non-perturbative gauge fixing, see [108] and references therein.

Please note that the figures Figure 3.5 where created by the author of this thesis as part of redoing the work done in [66] as preparation for other projects.

3.6. Low energy effective theory of QCD

Having discussed Yang-Mills at large in the two previous sections, we now turn to the matter part of QCD. In this section we want to give a brief summary of chiral symmetry breaking and the emergence of low energy effective degrees of freedom from an FRG perspective.

The electroweak sector of the Standard Model leads to current quark masses for the up and down quarks of a couple of MeVs. However, when looking at the bound state spectrum of QCD, in particular protons and neutron, one would estimate an effective *constituent quark mass* in the range $300 - 400\,\mathrm{MeV}$. The mechanism behind this mass generation is known as *chiral symmetry breaking* and can be explained already in $N_f = 2$, i.e. neglecting heavier quarks. Additionally, we will only discuss vacuum, the story is significantly more complex at large chemical potentials. More complete accounts of the pivotal role of the four-quark coupling in the low energy sector of QCD can be found in [28, 63, 64, 120–122] and references therein.

As we have seen before, generically all n-point functions are being generated by the flow. In particular also non-classical vertices such as the four-quark, which is also called four-fermi, coupling. This coupling is seeded by the quark-gluon interaction, already on the one-loop level. Its the rich structure of the emerging four-quark interaction that gives rise to a lot of interesting phenomenology in the low energy sector of QCD. In vacuum the by far most relevant channel that is being generated it the scalar-pseudoscalar channel. Luckily, this channel also allows for a relatively simple analysis. The full momentum and tensor structure of the four-quark interaction is extremely complicated has not been resolved so far, despite being relevant at large chemical potentials. Taking the coupling momentum independent, i.e. a point-like interaction, one finds for the relevant coupling that is generated in the QEA

$$\Gamma^{(\bar{q}q)^2}[\Phi] = -\frac{\lambda_q}{4}\int_x \left[(\bar{q}q)^2 - (\bar{q}\gamma^5 \boldsymbol{\tau} q)^2\right] + \dots\,, \tag{3.109}$$

which holds for massless quarks in the two-flavour case, i.e. the chiral limit of the $N_f = 2$ case. The vector $\boldsymbol{\tau}$ denotes the Pauli matrices, given by

$$\tau_1 = \begin{pmatrix} 0 & 1 \\ 1 & 0 \end{pmatrix} \qquad \tau_2 = \begin{pmatrix} 0 & -\mathrm{i} \\ \mathrm{i} & 0 \end{pmatrix} \qquad \tau_3 = \begin{pmatrix} 1 & 0 \\ 0 & -1 \end{pmatrix}. \tag{3.110}$$

From a simple dimensional analysis one finds that in RG flows the coupling λ_q behaves approximately as

$$\lambda_q \sim \alpha_{\mathrm{S}}^2 \frac{1}{k^2}\,, \tag{3.111}$$

where k is the RG scale in the sense of the FRG. Based on their quantum numbers, the terms in (3.109) can be identified with the sigma meson and the pions respectively. In the following we will make this explicit, by introducing an auxiliary field that we can approximately identify with the respective particles.

Additionally, the flow of the coupling λ_q contains a term with $\partial_t \lambda_q \sim \lambda_q^2$, see e.g. [65, 123], and therefore the possibility of a resonance in this channel is given. It turns out that this resonant behaviour indeed happens and is precisely the mechanism behind the dynamical mass generation. Detailed discussion about this mechanism can be found

in [41, 63, 65, 123] and references therein. In practical terms, this resonance can be absorbed into auxiliary fields, this process is called *Dynamical Condensation* or *Dynamical Hadronization*, which we will introduce in the following.

3.6.1. Dynamical Condensation

The concept has originally been introduced in the FRG as *rebosonization* in [124]. There, the Hubbard–Stratonovich transformation [125, 126] of the scalar and pseudoscalar bilinear fermionic operators into the scalar and pseudoscalar mesonic sigma σ and pion $\boldsymbol{\pi}$ fields has been discussed. The transformation is done in a scale dependent way, such that the four-quark coupling λ_q says identical to zero and does not get regenerated during the RG flow. A first application to the current context of chiral symmetry breaking in QCD can be found in [127] and an extensive discussion on the subject can be found in [128]. The set-up in these references, as well as in [129, 130] can be understood as a scale dependent version of the Hubbard–Stratonovich transformation. However, conceptually, it removes the respective channel from the full QEA and not the classical action.

This concept has been generalized in [38] that allows for the introduction of generic composite operators, beyond the quadratic or bilinear limitation in the aforementioned approaches. It has been applied to chiral symmetry breaking in [28, 63, 65, 106]. In this approach one introduces sources for the composite operators, that are then defined only implicitly via their flow. The universal applicability to general bound state, resonance or condensation phenomena is responsible for its modern naming convention of *Dynamical Condensation* or, in the context of QCD, *Dynamical Hadronization*.

The starting point is the generating functional $\mathcal{Z}[J_\varphi]$, with the superfield $\varphi = \left\langle \hat{\Phi} \right\rangle$ and the associated currents J_φ. We now introduce the cutoff-dependent composite field $\hat{\phi}[\varphi]$ and add a source term for it to the path integral

$$\mathcal{Z}[J] = \int [\mathrm{d}\hat{\varphi}]_{\mathrm{ren}} \, e^{S[\hat{\varphi}] - \Delta S_k[\hat{\varphi},\hat{\phi}] + J_\varphi \cdot \hat{\varphi} + J_\phi \cdot \hat{\phi}} \,, \tag{3.112}$$

where we have also introduced the combined super-current $J = (J_\varphi, J_\phi)$. The cutoff term in (3.112) also contains a cutoff term for the composite field and reads in terms of the combined superfield $\Phi = (\varphi, \phi)$ simply

$$\Delta S_k[\hat{\Phi}] = \frac{1}{2} \Phi_i R^{ij} \Phi_j \,. \tag{3.113}$$

The Legendre transform then simply reads the same as in (2.35). The resulting QEA is the first principle one in the following sense

$$\Gamma[\varphi] = \Gamma[\varphi, \phi_{\mathrm{EoM}}[\varphi]] \quad \text{with} \quad \left. \frac{\delta \Gamma[\Phi]}{\delta \phi} \right|_{\phi = \phi_{\mathrm{EoM}}} = 0 \,. \tag{3.114}$$

On the equations of motion we have $J_\phi = 0$ and the generating functional $\mathcal{Z}[J]$ reduces to $\mathcal{Z}[J_\varphi]$. We also emphasise that the elementary correlation functions of the fields contained in φ are obtained by taking the respective field derivatives of the condensed effective action after the equation of motion of ϕ is used, i.e. $\phi_{\mathrm{EoM}}[\varphi]$ depends on the fundamental fields φ and is therefore hit by φ derivatives. After some manipulation one finds, see e.g. [8, 28, 38]

the flow equation in the presence of a composite operator

$$\left[\partial_t + \left(\partial_t \phi_k[\Phi] \frac{\delta}{\delta \phi}\right)\right] \Gamma[\Phi] = \frac{1}{2} \operatorname{Tr}\, G[\Phi]\, \partial_t R_k + \operatorname{Tr}\, \Big[G[\Phi]\Big]_{\phi\Phi_i} \frac{\delta \partial_t \phi_k[\Phi]}{\delta \Phi_i}\, \partial_t R_k\,, \tag{3.115}$$

where we have introduced in a slight abuse of notation $\partial_t \phi_k[\Phi] = \left\langle \partial_t \hat{\phi} \right\rangle [\Phi]$. This quantity is also precisely the one at our disposal and can be used to absorb unwanted resonant couplings. Please note that we then fix the expectation value of the flow of the composite operator, not the composite operator itself, nor its derivative. This procedure requires that the choice for $\partial_t \Phi_k[\Phi]$ is consistent with being an expectation value. Additionally, we would like to note that intricacies can arise if one-point functions are present in the transformed QEA, for a detailed discussion see [28]. If we would like for example to capture the resonance arising in (3.109) we would choose the function $\partial_t \Phi_k[\Phi]$ such that it has an overlap with $\bar{q}(x)q(x)$ and $\bar{q}(x)\gamma_5 \boldsymbol{\tau} q(x)$. This will be used in practice in Section 5.2.

In summary, the outlined procedure can be used to introduce low energy effective theories on a rather rigorous level, if all other possibly resonant interactions are monitored and the correct low energy degrees of freedom are identified. In the context of QCD this has been applied in [4, 28, 65] do make direct contact between the fundamental degrees of freedom in QCD and the Quark-Meson model as its unique low energy effective description in vacuum.

4. Field dependence

This chapter is in parts based on [5] and [10].

In Chapter 2 we introduced Functional Methods and in particular the Functional Renormalization Group. Here we focus on systems that are usually described well within a derivative expansion. Truncations of the underlying functional partial differential equation within this framework usually result in system of convection-diffusion equations for the description of phase transitions, c.f. Section 2.3.2. Despite their successful investigation in a tremendous amount of theories, their numerical treatment with non-analytic solutions has so far not been studied in detail. In turns out that this situation is relevant in the vicinity of a first order phase transition, which demands the usage of suitable numerical tools. The leading order equations within such truncations governing the Renormalization Group (RG) evolution can be cast into a conservative form, which is very similar, in some aspects, to the equations studied in hydrodynamics and in general, mathematical physics. This already suggests the use of suitable numerical techniques, incorporating e.g. the directed flow of information.

Equations of this type generally lead to the formation of a discontinuity in the solution. Therefore, the applied numerical scheme has to be able to handle non-analyticities in an appropriate manner. A standard and robust choice is the Finite Volume (FV) scheme, where the equations are solved in a collection of small volumes. Schemes of this type are capable of treating discontinuities in a stable manner. However, they are lacking in accuracy, since it is challenging to adopt higher order formulations while preserving numerical stability. On the other hand, Pseudo-Spectral methods are designed to have an arbitrarily high order accuracy, since the solution is obtained in a functional space spanned by a suitable basis. However, non-analyticities in the solution usually lead to spurious oscillations, which may ruin the stability of the scheme. Discontinuous Galerkin (DG), introduced in [131–135], schemes utilize the strengths of both methods. The domain is decomposed in small volumes; therefore, discontinuities are well treated, and the solution is approximated locally within an appropriate basis to achieve high accuracy. The demand for high accuracy in FRG calculations, combined with the convection dominated nature of the equations, makes DG schemes a natural choice.

Having discussed the FRG at large in Chapter 2 and Chapter 3, we would like to remark that in practice, the partial different equation part of the resulting equations for a given ansatz are usually non-linear convection-diffusion equations. During the most part of the flow, these equations are also convection dominated, since (2.39) is already designed to be dominated by a single scale, set by the RG-time t, in all quantities. We will come back to this point in Paragraph 4.2.2.2.2. Additionally, in our application to the $O(N)$-model in the large N limit, c.f. Section 4.2, this becomes exact, i.e. it the resulting flow equation is a convection equation, c.f. (4.4). Moreover, it can be cast into a conservative form, therefore we will restrict the introduction to DG methods in some parts to conservation laws to keep it simple. Having the equation in a conservative form is particularly convenient, since it allows us to understand how a jump discontinuity in the solution forms and propagates.

Therefore, we start this section with a brief introduction to DG schemes.

4.1. Discontinuous Galerkin methods

We review some basic facts about DG schemes following [136], for simplicity we restrict ourselves to one spatial dimension. For an introduction to foundations of numerical methods for PDEs, that DG schemes build upon, e.g. Finite Element and Finite Volume Methods, the reader is referred to [137–139].

The problem is considered over a domain Ω, with boundary $\partial\Omega$, approximated by a computational domain Ω_h, composed by K non-overlapping elements D^k

$$\Omega \simeq \Omega_h = \bigcup_{k=1}^{K} D^k \,. \tag{4.1}$$

The approximate solution is then represented by

$$u(t,x) \simeq u_h(t,x) = \bigoplus_{k=1}^{K} u_h^k(t,x) \,. \tag{4.2}$$

The local solution is approximated in each element by a polynomial of degree N

$$u_h^k(t,x) = \sum_{n=1}^{N+1} \hat{u}_n^k(t)\psi_n(x) = \sum_{i=1}^{N+1} u_h^k(t,x_i^k) l_i^k(x) \,, \tag{4.3}$$

where the first version is the modal expansion, expressing the solution in terms of a local polynomial basis $\psi_n(x)$. The second approximation in (4.3) is referred to as nodal expansion, which introduces $N+1$ grid points x_i^k and $l_i^k(x)$ is the associated Lagrange polynomial. For calculations we use the usual Legendre basis in the modal expansions and the Legendre-Gauss-Lobatto quadrature points as grid points in the nodal expansion. A few more details are given in Section A.1.

The main task at hand is to solve the conservation law, which turns out to be the relevant form of the equation in our application, posed as an initial value problem

$$\partial_t u + \partial_x f(u) = 0 \,, \tag{4.4}$$

where we assume the flux f to be convex and it may also depend on the time t. We now require that the residual is orthogonal to the basis function *locally* in each element

$$\int_{D^k} \left(\partial_t u_h^k + \partial_x f_h^k(u_h^k)\right)\psi_n \, \mathrm{d}x = 0 \,, \tag{4.5}$$

i.e. the space of test functions for which we require the orthogonality of the residual of the equation is chosen to be the same as the function space of the solution approximation. Choosing test function space and the function space of the solution equal is called Galerkin method, hence the name Discontinuous Galerkin methods. Additionally, due to the disconnected nature of the approach, (4.5) has still more degrees of freedom than

equations. To resolve this, we integrate (4.5) by parts and obtain the locally defined weak formulation

$$\begin{aligned} &\int_{D^k} \left(\left(\partial_t u_h^k\right) \psi_n - f_h^k(u_h^k) \partial_x \psi_n \right) \mathrm{d}x \\ &= - \int_{\partial D^k} f^* \cdot \hat{\mathbf{n}} \; \psi_n \, \mathrm{d}x \,, \end{aligned} \tag{4.6}$$

where we have already replaced the flux on the right-hand side with an approximation thereof, the numerical flux f^*, discussed below. In the one dimensional case the element boundary ∂D^k consists of two points and the outward pointing normal vector is $\hat{\mathbf{n}} = \pm 1$. Integrating (4.6) once more by parts we obtain the strong formulation

$$\begin{aligned} &\int_{D^k} \left(\partial_t u_h^k + \partial_x f_h^k(u_h^k) \right) \psi_n \; \mathrm{d}x \\ &= \int_{\partial D^k} \hat{\mathbf{n}} \cdot \left(f_h^k(u_h^k) - f^* \right) \psi_n \, \mathrm{d}x \,, \end{aligned} \tag{4.7}$$

which we also use throughout this work for all numerical calculations. It is important to stress that the solution is only defined element wise. The value of the flux at the boundary is not necessarily equal to the value of the flux on a boundary node, but depends on the solution of all elements sharing that particular intersection, i.e. two in one dimension. Therefore, the numerical fluxes are define on each intersection and depend non-trivially on the value of the approximate solution on all adjacent elements. Specifying the numerical flux closes the set of equations. For the case of a scalar conservation law one can rely on the results for the choice of numerical fluxes obtained in Finite Volume Methods, where the subject has been studied extensively, see e.g. [136, 138]. The main requirements are consistency, i.e. $f^*(u, u) = f(u)$, and monotonicity. We will refrain here from a more detailed discussion on numerical fluxes and rather state that we work with the Local Lax-Friedrichs flux [140] given by

$$f^*(u_h^-, u_h^+) = \{\{ f_h(u_h) \}\} + \frac{C}{2} [\![u_h]\!] \,, \tag{4.8}$$

where an index $-$ denotes the interior information of the element while an index $+$ denotes the exterior information of the element. The brackets denote the average and jump, respectively

$$\begin{aligned} \{\{u\}\} &= \frac{1}{2} \left(u^- + u^+ \right) \\ [\![u]\!] &= \hat{\mathbf{n}}^- u^- + \hat{\mathbf{n}}^+ u^+ \,. \end{aligned} \tag{4.9}$$

The constant C in (4.8) is chosen as the maximal wave speed in a local manner as

$$C \geq \max_{u^\pm} |\partial_u f(u)| \,, \tag{4.10}$$

which is related to the fastest propagating mode. To be more precise, the numerical flux also ensures the convergence to the correct result in situations where discontinuities are present, i.e. it ensures the convergence to the correct solution. This solution can be interpreted as being fixed by an entropy condition or as the inviscid limit of the equation with an infinitesimal viscosity term.

Additionally, boundary conditions have to be specified for all inflow boundaries, given by $\hat{\mathbf{n}} \cdot (\partial_u f) < 0$.

Finally, we would like to note that (4.7) can be written as

$$\mathcal{M}^k \partial_t u_h^k + \mathcal{S}^k f_h^k = \left[l^k(x)(f_h^k - f^*) \right]_{x_l^k}^{x_r^k}, \tag{4.11}$$

resulting in a fully discretized scheme, where we have introduced the two matrices

$$\begin{aligned} \mathcal{M}_{ij}^k &= \int_{D^k} l_i^k(x) l_j^k(x) \, \mathrm{d}x \\ \mathcal{S}_{ij}^k &= \int_{D^k} l_i^k(x) \partial_x l_j^k(x) \, \mathrm{d}x \,. \end{aligned} \tag{4.12}$$

In the usual manner, the discretized operators (4.12) are calculated for a reference element and the appropriate mappings to the actual elements invoked.

4.2. Scalar $O(N \to \infty)$-theory

The first theory we would like to investigate within this formalism is a $O(N)$-theory in the large N limit, due to the technical simplifications arising in this limit.

4.2.1. $O(N)$-theory preliminaries

We consider the $O(N)$ model in d-dimensional Euclidean space-time. The field can be described by a collection of N scalar fields $\phi_a(x)$ with $a = 1, \cdots, N$. The action for N scalar field is

$$S = \int_x \left\{ \frac{1}{2}(\partial_\mu \phi_a)^2 + V(\rho) \right\}, \tag{4.13}$$

where $V(\rho)$ is the interacting potential. The $O(N)$ symmetry acts on the fields as an orthogonal transformation $\phi_a \to O_{ab}\phi_b$. Consequently, the $O(N)$-invariant terms are those constructed by the modulus of the fields $\phi_a\phi_a$. Given this symmetry, the potential is restricted to depend only on $O(N)$-invariant terms, namely the combination $\rho = \frac{1}{2}\phi_a\phi^a$. This quite simple model can nevertheless describe an immense variety of physical system at different energy scale, from the Higgs sector of the standard model to the phase transition in ferromagnets. The $O(N)$ model is the prototype used to investigate phase transition in different type of systems. For $N = 4$ and $d = 4$ the model describes the scalar sector of the standard model (at zero Yukawa couplings). It also captures the essential features of the chiral phase transition in QCD in the limit of two flavours. Moving to lower energy scales, $N = 3$ corresponds to the Heisenberg model that describes the phase transition of a ferromagnet. In condensed matter, i.e. $d \leq 3$, there are many other application of the $O(N)$ model, as for example $N = 2$ can describe the helium superfluid phase transition or $N = 1$ is the liquid-vapour transition. The motivation for the wide range of applicability of such a simple model comes from the universal behaviour of physical systems close to a phase transition; under these circumstances the microscopic details of a system are not important, only a few characteristics like the underlying symmetry govern the physics close to the phase transition.

For this reason, the O(N) model is the perfect prototype to understand relevant mechanisms that govern a phase transition.

4.2.1.1. Flow equations

To derive flow equations, we need to truncate the effective action, i.e. we need to choose an ansatz. Here we work in a *derivative expansion*, i.e. we expand the action in terms of gradients of the field, c.f. Section 2.3.2. The zeroth order of the expansion is usually referred to as *Local potential approximation* (LPA). For our intended purpose, i.e. $N \gg 1$, this approximation becomes exact [141]. Within LPA the ansatz for the effective action is given by

$$\Gamma_k[\phi] = \int_x \left\{ \frac{1}{2}(\partial_\mu \phi_a)^2 + V(t, \rho) \right\}, \tag{4.14}$$

where $V(t, \rho)$ is the effective potential, which depends only on the RG-time as well as the $O(N)$ invariant $\rho = \frac{1}{2}\phi_a\phi^a$. Having specified the ansatz for the effective action we can derive a PDE for the effective potential by evaluating the right-hand side of (2.39).

This requires the knowledge of the regularized propagator, or equivalently the two-point function

$$\Gamma^{(2)}_{ab}(t,\rho,p) = \left[p^2 + V'(t,\rho)\right]\delta_{ab} + 2\rho V''(t,\rho)\delta_{aN}\delta_{bN}\,, \tag{4.15}$$

where we introduced the shorthand notation $V'(t,\rho) = \partial_\rho V(t,\rho)$ and specified the field direction where it can acquire a non-vanishing expectation value. Plugging (4.15) into (2.39), using a regulator that's diagonal in field space, and carrying out the trace up to the momentum integral one obtains

$$\begin{aligned}\partial_t V(t,\rho) =& \frac{1}{2}\int_q \Bigg[\Bigg(\frac{N-1}{q^2 + V'(t,\rho) + R_k(q)} \\ &+ \frac{1}{q^2 + V'(t,\rho) + 2\rho V''(t,\rho) + R_k(q)}\Bigg)\partial_t R_k(q)\Bigg]\,.\end{aligned} \tag{4.16}$$

As regulator we chose the usual Litim regulator (2.59), which provides the optimal [59] choice in LPA. Additionally, we rescale ρ and $V(t,\rho)$ with factors of $1/N-1$,

$$\begin{aligned}\rho &\to (N-1)\rho \\ V(t,\rho) &\to (N-1)\,V(t,\rho)\,,\end{aligned} \tag{4.17}$$

which allows for easy access to the large N limit. Putting (4.16), (2.59) and (4.17) together, the integration becomes trivial and we arrive at the flow equation for the effective potential

$$\begin{aligned}\partial_t V(t,\rho) =& -A_d(\Lambda e^{-t})^{d+2}\Bigg(\frac{1}{(\Lambda e^{-t})^2 + V'(t,\rho)} \\ &+ \frac{1}{N-1}\frac{1}{(\Lambda e^{-t})^2 + V'(t,\rho) + 2\rho V''(t,\rho)}\Bigg)\,,\end{aligned} \tag{4.18}$$

with $A_d = \Omega_d(2\pi)^{-d}/d$ and $\Omega_d = 2\pi^{d/2}\Gamma(\frac{d}{2})^{-1}$ is the volume of a $d-1$ dimensional sphere. Please note that Γ denotes only in this context the usual Gamma function. Due to the rescaling (4.17) it is very easy to go the limit $N \gg 1$, i.e. we drop the last term in (4.18)

$$\partial_t V(t,\rho) = -A_d\frac{(\Lambda e^{-t})^{d+2}}{(\Lambda e^{-t})^2 + V'(t,\rho)}\,. \tag{4.19}$$

Before doing calculations we still have to fix the dimension d as well as the initial UV-scale Λ in (4.19). For the dimension we chose $d = 3$, enabling us to investigate phase transitions of first and second order. The choice of the UV-cutoff is completely arbitrary and therefore we chose $\Lambda = 1$ a.u.. Where a.u. denotes arbitrary unit, and consequently all dimensionful quantities are rescaled by appropriate powers of Λ to make them dimensionless in a practical manner, but not from an RG perspective. To keep the notation concise, the rescaled quantities are not denoted in a different manner but are understood dimensionless for the remainder of this work. This theory has been studied extensively within the FRG, see e.g. [142–144].

4.2.1.2. Numerical treatment

The flow equation (4.19) is non-linear, since the derivative of the potential with respect to the field expectation value appears on the right-hand side in a non-linear manner. However, for numerical purposes, and to apply DG schemes, its preferable to formulate the problem in conservative form. As $V(t, \rho)$ is related to the zero-point energy of the underlying QFT, its equation should not depend on itself, as it is already the case in (2.39), and consequently also in (4.19). As a direct consequence, the first derivative of the potential is a conserved quantity, in the sense of (4.4). Therefore, we introduce the derivative of the potential as new variable

$$u(t, \rho) = \partial_\rho V(t, \rho)\,, \tag{4.20}$$

as well as the flux

$$f(t, u) = A_d \frac{(\Lambda e^{-t})^{d+2}}{(\Lambda e^{-t})^2 + u}\,. \tag{4.21}$$

Because all derivatives of a solution of a PDE must also satisfy the PDE, we can take a derivative of (4.19) to obtain an equation for the derivative of the potential u, which is easily expressed in terms of the flux (4.21)

$$\partial_t u + \partial_\rho f(t, u) = 0\,. \tag{4.22}$$

Therefore, we are left with the task of solving a scalar conservation law with a flux that depends explicitly on the RG-time, allowing us to make immediate use of the spatial discretization presented in Section 4.1. As boundary condition we need to specify the flux at large field values, the inflow boundary. However, in this case it is naturally suppressed for physical initial conditions, c.f. (4.21). Therefore, we have fixed the flux at the boundary to a flux with the initial derivative of the potential. Additionally, we have verified explicitly that we obtain numerically equivalent results by setting the flux to zero at the boundary. Both cases are therefore sufficiently close to the true boundary conditions, i.e. fixing the flux to the initial conditions at infinite field values. It is noteworthy that the flux (4.21) is convex for all RG-times. Additionally, we would like to note that the weak formulation has already been used in the context of the FRG in [145].

The time dependence is treated with the method of lines, i.e. we use the usual machinery of ordinary differential equations (ODE). Preferably one uses a suitable explicit scheme in this context as numerical stability can be ensured, when the size of the time steps respects the associated Courant–Friedrichs–Lewy (CFL) condition, see e.g. [136]. The condition states that stability is ensured as long as the physical light cone of the system is contained in the numerical one, see e.g. [139]. Therefore, it is related to the propagation of information and is bounded by the physics of the system, e.g. in relativity it should always be less than the speed of light. However, the equation encountered here is quite peculiar from this point of view since the characteristic speed of information $\partial_u f$ is not bounded and time dependent. As we will show in section Paragraph 4.2.2.2.2 in the limit $t \to \infty$ the wave speed generally diverges exponentially fast for a subdomain. Therefore, the time step required by the CFL condition also decreases exponentially fast and becomes infeasible in this region. This can be circumvented using implicit methods, and we resorted to the family of Backward Differentiation Formula (BDF) methods, where we used SUNDIALS [146] through its Mathematica interface [102]. Additionally, we have compared our results

for all qualitatively different solutions to a strong stability persevering scheme Runge-Kutta scheme [147], with a time step chosen through the CFL condition.

The numerical schemes outlined here are generally applicable, in particular also to future applications in relativistic hydrodynamics [139, 148–152]. Additionally, the high-performance aspects of DG methods, see e.g. [153–155], are a promising perspective for complex FRG settings, where the computational complexity grows fast.

4.2.2. Results

4.2.2.1. Riemann problem

The Riemann problem is a well-known problem, usually studied in fluid dynamics, and is designed to understand how discontinuities arises and evolve. It consists of finding the solution to the PDE at hand with piecewise constant initial condition

$$u(0,\rho) = \begin{cases} u_{\mathrm{L}} & \rho \leq \xi_0 \\ u_{\mathrm{R}} & \rho > \xi_0 \end{cases} . \tag{4.23}$$

Where we restrict ourselves to the case $u_{\mathrm{L/R}} \geq 0$, due to the possibly divergent flux (4.21) otherwise. For these initial conditions, the solution will either develop a shock or a rarefaction wave, depending on whether the characteristic curves intersect or not, respectively. For our problem at hand, i.e. equation (4.22) together with the flux (4.21), information is propagating from large ρ to small ρ, therefore we will have a propagating shock when $u_{\mathrm{L}} > u_{\mathrm{R}}$, and consequently a rarefaction wave when $u_{\mathrm{L}} < u_{\mathrm{R}}$.

4.2.2.1.1. Analytic investigation

For the case of a propagating shock the position ξ of it must satisfy the Rankine-Hugoniot condition, see Section B.3 for a derivation or e.g. [136],

$$\frac{\mathrm{d}\xi(t)}{\mathrm{d}t} = \frac{[\![f]\!]}{[\![u]\!]} , \tag{4.24}$$

where the difference bracket is defined in (4.9). Since the flux (4.21) doesn't depend on field space the solution will trivially stay piecewise constant. From (4.24) it can immediately be seen that the speed of shock is time dependent and exponentially suppressed for large times, since it is the case for the flux (4.21), independent of the values of $u_{L/R}$. The differential equation (4.24) can be solved analytically, where we employ as initial condition $\xi(t=0) = \xi_0$. The solution of (4.24) together with (4.21) in d dimensions is

$$\begin{aligned} \xi(t) = \xi_0 + A_d \frac{\Lambda^d}{d\,(u_{\mathrm{R}} - u_{\mathrm{L}})} \Bigg[& {}_2\tilde{F}_1\left(\frac{u_{\mathrm{R}}}{\Lambda^2}\right) - {}_2\tilde{F}_1\left(\frac{u_{\mathrm{L}}}{\Lambda^2}\right) \\ & - e^{-dt}\, {}_2\tilde{F}_1\left(\frac{u_{\mathrm{R}}}{\Lambda^2} e^{2t}\right) + e^{-dt}\, {}_2\tilde{F}_1\left(\frac{u_{\mathrm{L}}}{\Lambda^2} e^{2t}\right) \Bigg] , \end{aligned} \tag{4.25}$$

where ${}_2\tilde{F}_1(z) = {}_2F_1(1, -\frac{d}{2}, 1 - \frac{d}{2}, -z)$ and ${}_2F_1$ is the Gaussian or ordinary hypergeometric function. Specifying to $d = 3$, $\Lambda = 1$ and $u_{\mathrm{R}} = 0$ it is possible to simplify (4.25)

considerably

$$\xi(t) = \xi_0 + \frac{1}{6\pi^2}\left[e^{-t} - 1 + \sqrt{u_{\mathrm{L}}} \times \right. \\ \left. \times \left(\cot^{-1}(\sqrt{u_{\mathrm{L}}}) - \cot^{-1}\left(e^t \sqrt{u_{\mathrm{L}}}\right)\right)\right]. \tag{4.26}$$

We have chosen the specific value of $u_{\mathrm{R}} = 0$, because it will be the situation encountered later in the case of a first order phase transition, c.f. Section 4.2.3. The form (4.26) gives us access to the infinite RG-time limit

$$\xi_\infty \equiv \xi(t \to \infty) = \xi_0 + \frac{\sqrt{u_{\mathrm{L}}}\cot^{-1}\left(\sqrt{u_{\mathrm{L}}}\right) - 1}{6\pi^2}. \tag{4.27}$$

Therefore, the shock freezes in at large RG-time, and it does so exponentially fast at late times. Where the latter statement can be seen from the expansion of the $\cot^{-1}$ term in (4.26).

Having discussed the analytic case of a shock wave, we turn now to the case of a rarefaction wave, i.e. $u_{\mathrm{R}} > u_{\mathrm{L}}$. From the perspective of the characteristic curves, the one at the left boundary is moving faster than the one on the right boundary. Compared to the previous case, here the characteristics aren't overlapping, but rather there is a lack of characteristics. Nevertheless, the problem admits a unique solution, but unfortunately due to the explicit time dependence of the flux (4.21), the explicit solution cannot be constructed in the usual manner. The speed of the boundary points ξ^{B} however is directly related to the associated characteristics and therefore their explicit solution is easily constructed

$$\begin{aligned}\xi^{\mathrm{B}}_{\mathrm{L/R}}(t) =& \xi^{\mathrm{B}}_0 - \frac{A_d \Lambda^d}{2}\left[\frac{e^{-dt}}{u_{\mathrm{L/R}} + (\Lambda e^{-t})^2} - \frac{1}{u_{\mathrm{L/R}} + \Lambda^2}\right. \\ &- \frac{d(\Lambda e^{-t})^{d-2}}{\Lambda^d (d-2)}\, {}_2F_1\left(1, 1 - \frac{d}{2}, 2 - \frac{d}{2}, -\frac{u_{\mathrm{L/R}}}{(\Lambda e^{-t})^2}\right) \\ &\left. + \frac{d\Lambda^{-2}}{d-2}\, {}_2F_1\left(1, 1 - \frac{d}{2}, 2 - \frac{d}{2}, -\frac{u_{\mathrm{L/R}}}{\Lambda^2}\right)\right]. \end{aligned} \tag{4.28}$$

Similarly, as for the case of a propagating discontinuity (4.25), the propagation of the boundaries of the rarefaction wave is also exponentially suppressed and only propagates a finite amount in field space. This can easily be inferred from (4.28) for $d = 3$. Since we did not encounter any rarefaction waves during our investigation of first and second order phase transition, c.f. Section 4.2.3 and Section 4.2.2.2, we will refrain from an in-depth discussion at this point.

4.2.2.1.2. Numerical investigation

Having discussed the solution of the Riemann problem at length from an analytic point of view in Paragraph 4.2.2.1.1, we now turn to its numerical investigation. Here it is

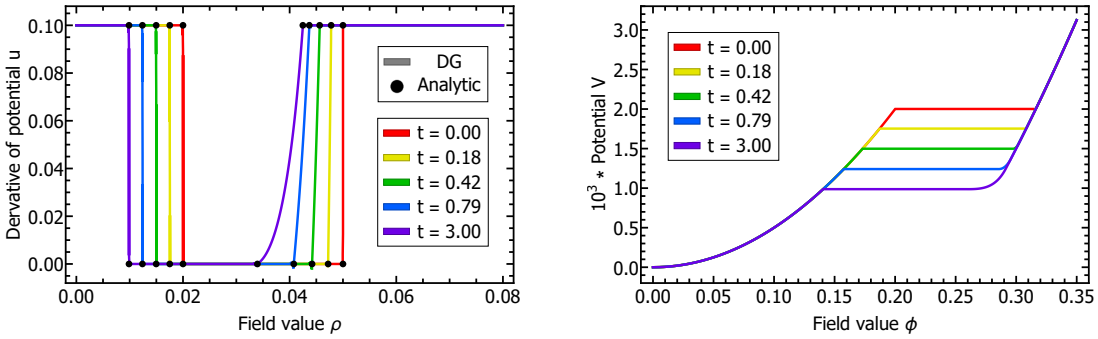

(a) Derivative of the effective potential $u(t, \rho)$

(b) Effective potential $V(t, \phi)$

Figure 4.1.: RG-time evolution of $u(t, \rho)$ for the Riemann problem (4.29). The dots represent the analytic result of the position of the shock (4.25) and the boundaries of the rarefaction wave (4.28). The numerical results were obtained with $K = 1500$ elements and a local accuracy of order $N = 3$. The results for the derivative of the potential were post-processed with a minmod limiter.

convenient to investigate both cases at the same time. To be more precise we chose as initial conditions

$$u(0, \rho) = \begin{cases} 0.1 & 0 < \rho < 0.02 \\ 0 & 0.02 < \rho < 0.05 \\ 0.1 & \rho > 0.05 \end{cases} . \tag{4.29}$$

The solution to the initial conditions (4.29) will evolve a shock in the solution from the jump at $\rho = 0.02$ and a rarefaction wave for the jump at $\rho = 0.05$. Our results are shown in Figure 4.1. The derivative of the potential $u(t, \rho)$, which is resolved numerically, is shown in Figure 4.1a and the corresponding effective potential, obtained by integrating, in Figure 4.1b. We find the expected agreement with the analytic results of Paragraph 4.2.2.1.1. For the calculation we used $K = 1500$ equally sized elements in the domain $0 \leq \rho \leq 0.08$ with a local interpolation order of $N = 3$ and evolved up to the RG-time $t = 3$. This upper RG-time is already relatively close to the infinite RG-time limit, i.e. the position of the shock as well as the rarefaction wave are effectively frozen in. During the RG-time evolution inevitably spurious Gibbs oscillations will form. Here we simply chose to keep them at a minimal level by using a considerable amount of degrees of freedom and post-process the results with a simple minmod limiter, see e.g. [136], but remnants of the oscillations can still be seen in Figure 4.1a. Nevertheless, it should be noted that the result still maintains it spectral accuracy, see e.g. [156], i.e. point wise convergence can be recovered from the numerical result. This is done partially by integrating the result within our polynomial basis, which removes all oscillations, c.f. Figure 4.1b, which is obtained from the result without a limiter. However, for future application we will consider the use of a limiter or utilize a shock capturing scheme, since the numerical approximation of the derivative of the potential $u(t, \rho)$ must become positive semidefinite in the large RG-time limit to avoid potential problems due to an artificially divergent flux.

4.2.2.2. Second order phase transition

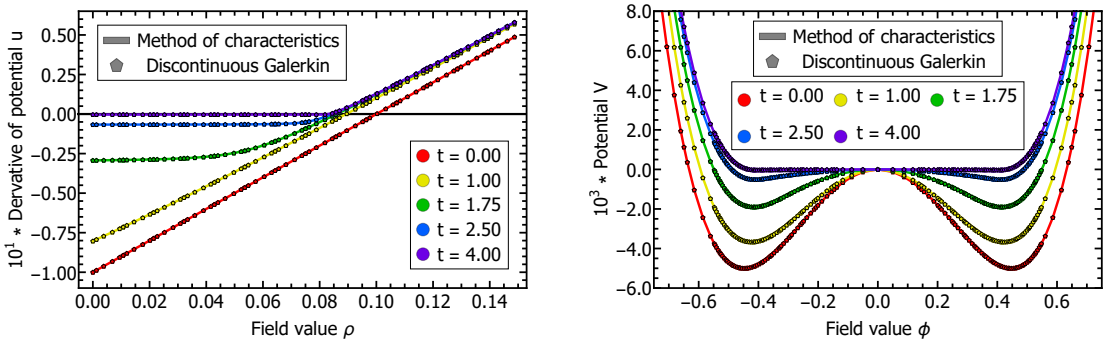

(a) Derivative of the effective potential $u(t, \rho)$

(b) Effective potential $V(t, \phi)$

Figure 4.2.: RG-time evolution for the second order problem (4.30) for $\lambda_2 = -0.1$. The full lines are a semi-analytic result obtained by the method of characteristics, while the hexagon dots are the respective results obtained by a numerical simulation with $K = 30$ elements and a local accuracy of order $N = 5$.

We now turn to the initial conditions usually considered in the context of the $O(N)$-model, i.e. a quadratic potential in the classical action

$$V_\Lambda(\rho) = \lambda_2 \rho + \frac{\lambda_4}{2}\rho^2 \,. \tag{4.30}$$

This is the case usually studied in the literature and it is well known that the classical action (4.30) leads to a second order phase transition as a function of λ_2 for a given positive λ_4. As our main interest is the investigation of a second order phase transition we restrict ourselves here to $\lambda_4 = 1$ for the remainder of the section. Additionally, we could always rescale the fields to have $\lambda_4 = 1$ in this case, since (4.30) has only two free parameters. Utilizing the method of characteristics, for details see Section B.2, it is easy see that local minima are shifted during the flow

$$\rho_{\min}(t) = \rho_{\min}(0) - \Lambda^{(d-2)} \frac{A_d}{d-2} \left(1 - e^{(d-2)t}\right) \,, \tag{4.31}$$

which is independent of the initial conditions. Combining (4.31) with the initial potential (4.30), the flow of the effective potential inherits a second order phase transition.

The RG-time evolution of the effective potential for the case of a finite expectation value, with initial value $\lambda_2 = -0.1$, is shown in Figure 4.2b. To illustrate the behaviour of the individual nodes during the RG-time evolution we have used only a moderate number of elements, i.e. $K = 30$, and a local approximation order of $N = 5$. However, the elements are not equally sized, but here we already utilize one of the strengths of the DG approach and half of the elements are equally distributed in $0 \leq \rho \leq 0.15$ and the other elements are equally distributed in $0.15 \leq \rho \leq 1$. This distribution of elements ensures that the outer boundary is at sufficiently large field values and our boundary conditions are satisfied, as discussed in Section 4.2.1.2, at very little cost. Please note that in Figure 4.2b the potential is shown as a function of the expectation value of the field $\phi = \sqrt{2\rho}$. Correspondingly, the derivative of the potential for the same calculation is shown in Figure 4.2a. The maximal RG-time was chosen to be $t = 4$, where all qualitative features have emerged, and only

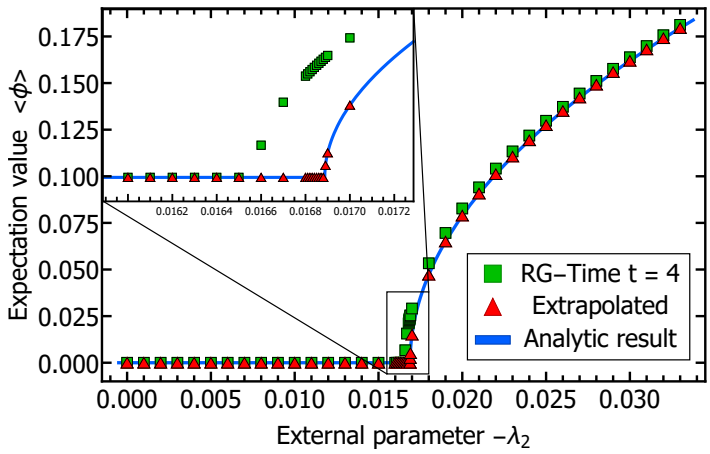

Figure 4.3.: Second order phase transition for the initial conditions (4.30). The result of the numerical simulation is shown with green squares, the extrapolated result with red triangles and the analytic result by a blue line. A detailed description can be found in the main text.

minor quantitative changes occur towards the asymptotic limit $t \to \infty$. The full effective potential has to be convex, which translate to a positive definite derivative of the potential $u \geq 0$ in the infinite time limit. This translate to a flat potential in between the minima, see Figure 4.2b. How this is realised in the current equation under investigation has been discussed at length in the literature, see e.g. [56, 157, 158]. Nevertheless, the numerical stability in the flat region of the potential is a noteworthy advantage of the DG approach.

4.2.2.2.1. Phase structure

We are now in the position to investigate the phase structure of the theory with classical action (4.30), where we set $\lambda_4 = 1$, as previously discussed. For all calculations we used $K = 120$ elements and a local interpolation of order $N = 5$. As in the previous case, the elements are not equally distributed. We used 5 equally spaced elements in the interval $0 \leq \rho \leq 0.001$, 15 equally spaced elements in the interval $0.001 \leq \rho \leq 0.01$, 50 equally spaced elements in the interval $0.01 \leq \rho \leq 0.15$ and 50 equally spaced elements in the interval $0.15 \leq \rho \leq 1$. This ensures a good resolution for small field values, and therefore the relevant region in field space at the second order phase transition. The solution is computed up to the RG-time $t = 4$, however, there is no restriction to continue the numerical simulation to larger RG-times. The result of the simulations is shown in Figure 4.3 with green squares. The final RG-time was also restricted to demonstrate the easy extrapolability of the result to its asymptotic solution at infinite RG-time. For a dimensionful coupling one expects asymptotically an exponential decay

$$\rho_{\min}(t) = \rho_{\min}^{\text{final}} + b\, e^{-ct} \quad \text{for} \quad t \gg 0\,. \tag{4.32}$$

We found compatibility of our numerical results for the position of the minima with (4.32), which is not very surprising as the analytic solution is given in this form (4.31). Nevertheless, the form of (4.32) is a generic feature and valid for couplings with a non-trivial RG-time evolution in this theory, this feature will become relevant in Section 4.2.3. We have extrapolated the global minimum for each coupling with eleven equally spaced

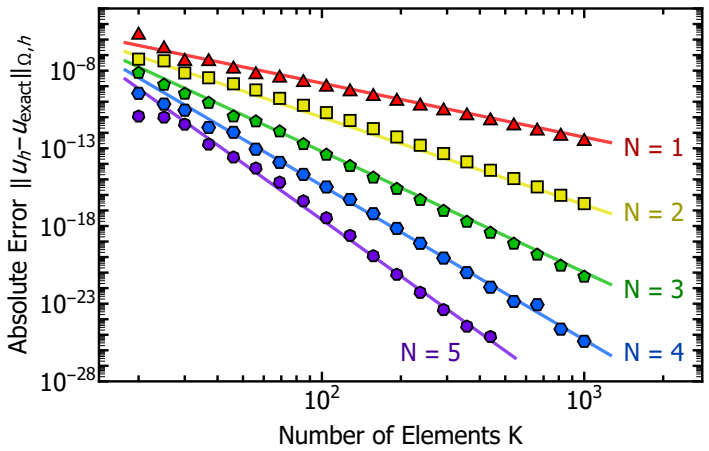

Figure 4.4.: Error of the solution with initial condition (4.30) ($\lambda_2 = -0.1$) at RG-time $t = 1.75$ computed in the interval $0 \leq \rho \leq 1$ for different number K of equally sized elements and local approximation order N. The symbols show the result of the numerical simulations, while the lines show a χ^2-fit with respect to (4.36) with the parameters given in Table 4.2.

points in the RG-time interval $3 \leq t \leq 4$ according to (4.32), the result is shown in Figure 4.3 with blue triangles.

It is very well known that all observables show a power law behaviour in the vicinity of a second order phase transition due to the divergent correlation length at the phase transition. This can be parametrized as

$$\langle \phi \rangle = \begin{cases} \alpha \left| \lambda_2 - \lambda_2^{\text{crit}} \right|^{\nu} & \lambda_2 \leq \lambda_2^{\text{crit}} \\ 0 & \lambda_2 > \lambda_2^{\text{crit}} \end{cases}, \tag{4.33}$$

where α is some prefactor, ν is the critical exponent and λ_2^{crit} is the critical coupling. The exact coefficients can be easily obtained analytically and are given in Table 4.1, as well as being depicted by a blue line in Figure 4.3.

Additionally, we have extracted the parameters from our results, extrapolated to infinite RG-time, using a χ^2 minimization. The resulting parameters, including their 1σ confidence interval, given in terms of the last two digits, are also shown in Table 4.1. Despite not aiming for a quantitative resolution of the critical area around the phase transition, we obtain an accurate estimate for all parameters. In particular, the error of the critical value of the coupling is only $1.5 \cdot 10^{-7}$, but it should be noted that the critical properties, i.e. the critical exponent in this case, can also be obtained from the fixed point equations, where higher accuracy is easier achievable, see e.g. [159].

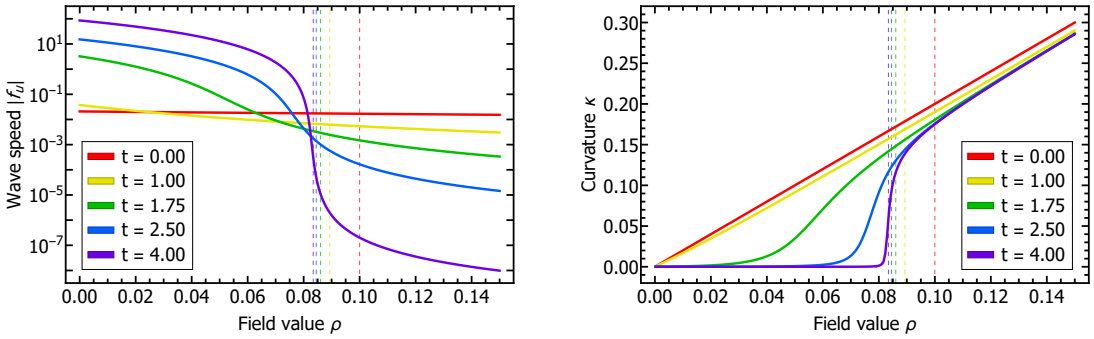

(a) Local wave speed $|f_u(t,\rho)|$.

(b) Local curvature $\kappa(t,\rho) = 2\rho\, V''(t,\rho)$.

Figure 4.5.: Properties relating to the approach towards convexity for the initial values (4.30) with $\lambda_2 = -0.1$. The vertical dashed lines represent the position of the global minimum of the potential at the corresponding RG-time. The numerical simulation was performed with $K = 85$ elements and a local accuracy of order $N = 5$.

4.2.2.2.2. Propagation of information and approach to convexity

It is instructive to have a closer look at the spreading of waves, or to put it differently, the propagation of information during the RG-time evolution. Propagating modes correspond to eigenvalues of the Jacobian of the system of conservation laws, which reduces in our case to $|\partial_u f(u)|$. The direction is always given to smaller field values, which naturally corresponds to the evolution direction from an RG perspective. Therefore, this quantity tells us at least qualitatively something about the locality of the RG-evolution in field space. From a technical perspective, the wave speed is an important quantity in our choice of the numerical flux, as it is directly related to the propagation of discontinuities. Additionally, it is relevant for the maximally allowed time step in explicit schemes to guarantee stability, see e.g. [136].

Turning back to our example case at the beginning of the section, i.e. (4.30) with $\lambda_2 = -0.1$ and $\lambda_4 = 1$, where we have used a local approximation of order $N = 5$ with 60 elements in the interval $0 \leq \rho \leq 0.15$ and 25 elements in the interval $0.15 \leq \rho \leq 1$. The locally resolved wave speed for different RG-times is shown in Figure 4.5a on a logarithmic scale. To guide the eye, the current minimum at each RG-time is indicated by a vertical

	Parameter		
	Prefactor α	Critical exponent ν	Critical coupling $-\lambda_2^{\text{crit}}$
Exact result	$\sqrt{2}$	$\frac{1}{2}$	$(6\pi^2)^{-1}$
	1.4142	0.50000	0.01688686
χ^2-fit	1.4161(16)	0.50023(25)	0.01688684(15)

Table 4.1.: Exact and reconstructed parameters of the power law behaviour (4.33) in the vicinity of the second order phase transition shown in Figure 4.3. The brackets indicate the 1σ uncertainty of the χ^2-fit and the exact result is also given with numerical values for better comparability.

dashed line. It is apparent that with progressing RG-time the wave speed splits into two domains, depending on the field value. For field values larger than the minimum the wave speed is decreasing rapidly, i.e. it is decreasing exponentially fast. On the other hand, for field values smaller than the minimum, i.e. in the flat region of the potential, the wave speed is growing exponentially. A direct consequence is that explicit time steppers work extremely well in the non-flat region, because the time steps can be chosen increasingly larger as RG-time progresses, while in the flat region the time steps would be exponentially smaller and implicit methods are preferred. This comes with implications for Taylor series methods, which are a popular choice in the FRG community, see e.g. [1, 4, 160], i.e. it provides an a posteriori justification for its use away from the flat region, due to the exponentially increasing locality of the solution. However, this should not be used as an a priori justification of its use. Similarly, Finite Difference based methods, see e.g. [37, 161–167], will benefit from taking these considerations, especially the direction of the wave propagation, into account. Additionally, we would like to note that this analysis does not replace a proper stability analysis for these approaches, but simply provides an intuitive understanding with non-binding consequences.

As outlined previously, the separation of the solution at infinite RG-time into two regimes is closely linked to the flatness of the potential, i.e. its convexity. This also implies the vanishing of higher order couplings in the flat region. Therefore, the curvature

$$\kappa(\rho) = 2\rho\, V''(\rho) = 2\rho\, u'(\rho) \tag{4.34}$$

provides a good measure for the flatness of the potential. The full curvature mass of the radial mode in $O(N)$-models is given by

$$m^2_{\text{curv}} = u(\rho) + \kappa(\rho)\,, \tag{4.35}$$

more details can be found in Section 4.2.1. Therefore, a vanishing curvature (4.34) implies a vanishing curvature mass (4.35) of the radial mode in the flat region. The result for the curvature, in the same setting as the wave speed, is shown in Figure 4.5b. As for the wave speed, the minima at the shown RG-times are indicated by vertical dashed lines to guide the eye. The approach towards zero of the curvature in the flat region is clearly visible, similarly to the jump discontinuity that necessarily forms at the minimum. However, this discontinuity forms, just like the non-analytic point in the derivative of the potential itself, only in the asymptotic limit. Additionally, these findings are promising for future calculations in the $O(N)$-model at finite N, since the calculation of the curvature does not introduce new problems and is the only new ingredient entering at finite N. Within this setting we also do not expect a loss of accuracy despite the increasingly non-analytic behaviour of the derivative. This is a clear advantage over pseudo-spectral methods, which are also designed to achieve high accuracy, put forward in [159, 168, 169]. They perform extremely well, if the solution is sufficiently smooth, however this is inherently not the case near phase transitions in the FRG. Additionally, it is worthwhile noting that these properties make pseudo-spectral approximation a good choice for the approximation of the momentum dependence of correlation function in Euclidean space-time, see e.g. [170, 171]

4.2.2.2.3. Convergence

Due to the semi-analytic nature of the solution using the method of characteristics, c.f. Section B.2, we can benchmark the accuracy of our results obtained with the DG method.

As with previous studies we use the initial conditions (4.30) together with $\lambda_2 = -0.1$ and resolve the derivative of the effective potential over the interval $0 \leq \rho \leq 1$. The results are then compared at the RG-time $t = 1.75$, i.e. at the onset of the flattening of the potential. Hereby we assume the result obtained via the method of characteristics to be the exact solution. Please note that this makes such a comparison for the situation with shocks considerably more complicated, which is why we refrain from considering it here. As explained in Section 4.2.1.2, we use an implicit solver for the time evolution. To avoid artificial enhancement of errors due to uncertainties thereof, we set the adaptive accuracy requirements close to machine precision. The results for the broken L2-norm between the two solutions for different orders of the local approximation order as a function of the number of elements, which are all equal in size, are shown in Figure 4.4. For our highest order of approximation $N = 5$ the results are only included for $K \leq 500$ elements, because the difference between the two results is at the level of the machine precision for more elements and a comparison is no longer insightful. The results are compatible with the expected power law like behaviour for the convergence when increasing the number of elements K and an exponential convergence when increasing the local approximation order N. To be more precise, we observe a behaviour that can be parametrized as

$$\begin{aligned} \log_{10} ||u_h - u_{\text{exact}}||_{\Omega,h} = &(a_1 + a_2\, N) \\ &- (b_1 + b_2\, N)\, \log_{10}(K)\,. \end{aligned} \tag{4.36}$$

In (4.36) we have temporarily restored the index h again to denote the approximate solution. A χ^2-fit to (4.36) is also shown in Figure 4.4 as solid lines, the parameters obtained are given in Table 4.2. In (4.36) the norm on the left-hand side denotes the broken L2-norm, i.e. the exact solution is projected to the same polynomial space as the numerical solution and the norm is then calculated elementwise therein and summed up. This result demonstrates the impressive convergence properties of the scheme.

4.2.3. First order phase transition

We now turn to the investigation of first order phase transitions, which have been investigated within the FRG in e.g. [37, 145, 172–177]. Including a $(\phi_a \phi^a)^3$ coupling into the classical action enables us to access a first order phase transition, see e.g. [143], which translates to the initial conditions

$$V_\Lambda(\rho) = \lambda_2 \rho + \frac{\lambda_4}{2}\rho^2 + \frac{\lambda_6}{3}\rho^3\,. \tag{4.37}$$

	Parameter			
	a_1	a_2	b_1	b_2
χ^2-fit	-3.96(28)	2.103(89)	1.32(12)	2.150(40)

Table 4.2.: Parameters obtained from a χ^2-fit to (4.36) of the convergence behaviour shown in Figure 4.4.

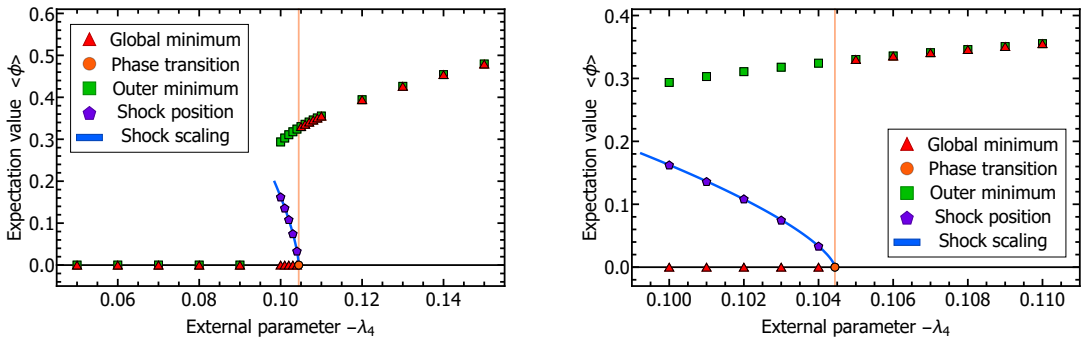

(a) Wider parameter range.

(b) Vicinity around the phase transition.

Figure 4.6.: First order phase transition for the initial conditions (4.37). An extensive description can be found in the main text. The numerical simulation was performed with $K = 200$ elements and a local accuracy of order $N = 5$.

Similarly, to the second order case, c.f. Section 4.2.2.2, we fix all but one parameter and investigate the phase structure with respect to that parameter. To achieve a first order phase transition λ_2 and λ_6 need to be positive, while λ_4 needs to be negative. The initial values are chosen to produce similar scales in the result compared to the results obtained in Section 4.2.2.2. Therefore, we keep λ_4 variable and set $\lambda_2 = 0.0024$, $\lambda_6 = 1$ to fixed values. Throughout this section we use $K = 200$ elements with a local approximation order of $N = 5$, with 150 elements distributed equally in $0 \leq \rho \leq 0.15$ and 50 elements distributed equally in $0.15 \leq \rho \leq 1$. The solution is obtained up to the RG-time $t = 6$, which was sufficiently large for all numerical simulations, i.e. the asymptotic result at infinite RG-time was obtainable via extrapolation if necessary.

A crucial difference between the initial conditions (4.30) and (4.37) concerns the monotonicity of the derivative of the effective potential at the initial scale, i.e. $u(0, \rho)$. While for the second order phase transition $u(0, \rho)$ was monotonically increasing as a function of ρ, in the case considered now, i.e. (4.37), it is not. To be more precise, it possesses a minimum for certain values of $\lambda_4 < 0$ and therefore a jump discontinuity will form as RG-time progresses. The underlying mechanism can easily be understood from the perspective of the characteristic velocity $\partial_u f(t, u)$, more details can be found in Section 4.2.2.1 and Section B.3. However, it is not clear whether the discontinuity forms in the physical relevant regime $\rho \in [0, \infty)$. Additionally, the results from Section 4.2.2.1 let us suspect that the shock will freeze in towards asymptotic RG-times. It turns out that this indeed happens and is the relevant mechanism behind the phase transition.

4.2.3.1. Phase structure I

We investigate the phase structure for the initial conditions (4.37), with the specific setup discussed around the equation. The resulting phase structure is shown in Figure 4.6, where a wider range for the external parameter λ_4 is shown in Figure 4.6a and the vicinity around the phase transition is shown in Figure 4.6b. All quantities in the visualization of the phase structure are extrapolated to $t \to \infty$, the minima according to (4.32) and the final position of a possible jump discontinuity, i.e. shocks, is described later in detail. The outer minimum is depicted with green squares and the disappearance/jump to zero

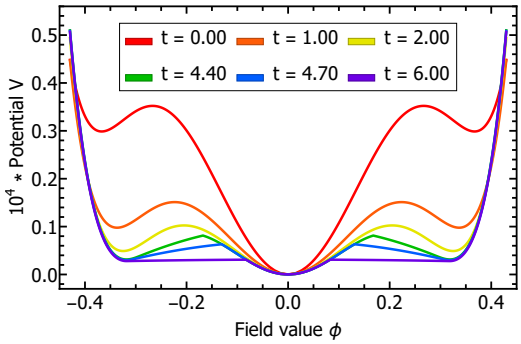

(a) Potential in the symmetric phase.

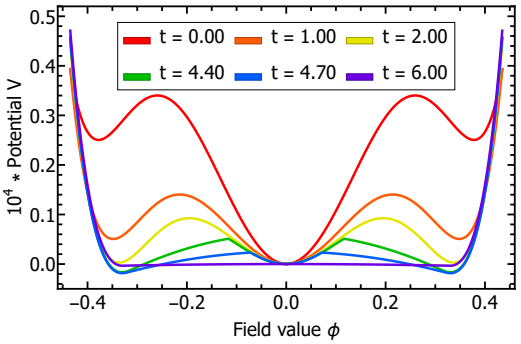

(b) Potential in the broken phase.

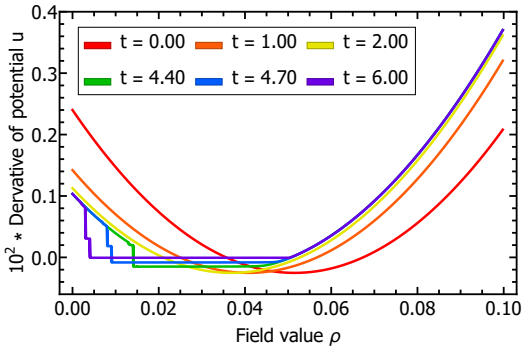

(c) Derivative of the potential in the symmetric phase.

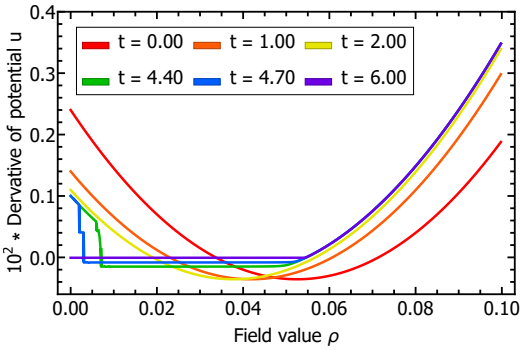

(d) Derivative of the potential in the broken phase.

Figure 4.7.: The effective potential $V(t, \rho)$ and its derivative $u(t, \rho)$ for two different values of the coupling λ_4 close to the first order phase transition shown in Figure 4.6. The numerical simulation was performed with $K = 200$ elements and a local accuracy of order $N = 5$. The results for the derivative of the potential were post-processed with a WENO limiter.

of it reflects the disappearance of the minimum in the initial conditions. However, the global minimum, depicted with red triangles, of the effective potential is either at $\rho = 0$ or agrees with the non-trivial, outer minimum at $\rho \geq 0$. A clear jump is visible where the potential switches between the symmetric and broken phase and the position is shown with a vertical orange line.

Before continuing the discussion of the phase structure and, in particular, the discussion of Figure 4.6b, it is instructive to look at the potential and its derivative at the two values of the coupling λ_4 which are closest to the phase transition, i.e. once in the broken phase and once in the symmetric phase, shown in Figure 4.7. Hereby we note that the results shown for the RG-time $t = 6$ are already sufficiently close to the infinite RG-time limit and for all discussions that follow we can threat them effectively as such. Focusing on the derivative of the effective potential $u(t, \rho)$, in both cases the appearance of a jump discontinuity is clearly visible. For a better depiction we have processed the result using a WENO limiter, following [178], removing the Gibbs oscillations around the shock. This is the source of the flat looking pieces in the solution at the positions of shocks. However, the potential is obtained, as in Section 4.2.2.1, from the original data of the result. The two evolutions of the derivative of the potential, depicted in Figure 4.7c and Figure 4.7d, show a qualitative

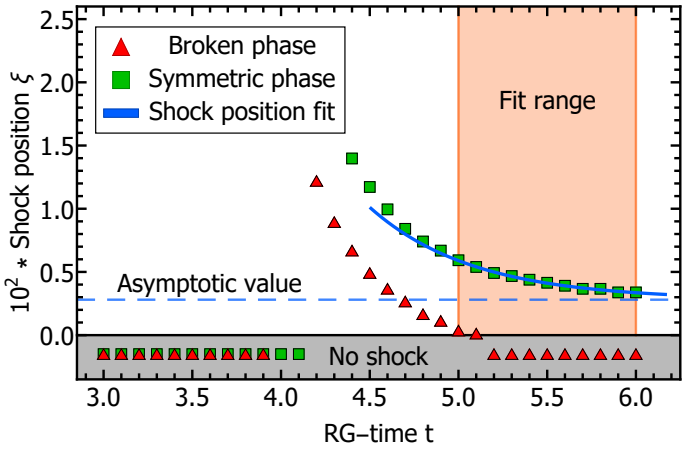

Figure 4.8.: Positions of the shocks for the examples shown in Figure 4.7 together with the fit of the asymptotic behaviour for the case shown Figure 4.7c.

difference. In Figure 4.7c the position of the shock freezes and consequently the global minimum of the effective potential stays at $\rho = 0$ for all RG-times, see Figure 4.7a. This is contradiction to the case depicted in Figure 4.7d, here the position of the shock moves to unphysical values and effectively flattens out the potential for all field values smaller than the outer minimum, making it the global minimum, depicted in Figure 4.7b.

4.2.3.2. Mechanism for a first order phase transition

The analysis above uncovers a potential mechanism for first order phase transitions: In the vicinity of the phase transition a cusp forms in the effective potential, or equivalently a shock in the derivative of the potential, during the RG-time evolution between two minima. The shock now propagates towards smaller field values and if the inner minimum was the preferred one before, the phase transition happens if the shock hits the inner minimum. The final position of the shock $\xi(t \to \infty)$ as a function of some external parameter, e.g. a coupling in the classical potential, temperature or chemical potential, can now be used to describe the phase transition equivalently. The propagation speed of the shock is dominantly driven by the values of the derivative of the potential at larger field values, c.f. (4.24). However, at the roughly the same RG-time, when the shock forms, the potential also starts to flatten, starting from the outer minimum, i.e. the potential approaches convexity. This process is triggered locally from the existence of a zero crossing in the derivative of the potential and therefore independent from the global structure of the potential. Consequently, the propagation of the shock is dominantly driven by auxiliary, massless modes of the flat region and becomes at least partially insensitive to the details of the theory. This mechanism suggests a power law like behaviour of the final position of the shock in the vicinity of the phase transition, which we will confirm for our current setting.

In our present case of the theory in the large N limit, the formation of shock is guaranteed due to conservative form equation (4.22), combined with the non-monotonicity of the initial state. Therefore, the inner minimum is at $\rho = 0$ and the condition for the phase transition turn into $\xi(t \to \infty) = 0$.

Obviously, one should be cautious whether this mechanism generalizes to first order phase transitions in generic theories. We will comment on this at the end of this section, after finishing the discussion of the phase structure in our current setting. However, before continuing we would like to note that the propagation of a discontinuity in the vicinity of a first order phase transition has also been seen in [145], where the method of characteristics was used to resolve the phase structure of an NJL type model.

4.2.3.3. Phase structure II

Having identified the relevant mechanism for the phase transition shown in Figure 4.6, we can turn back to its description, including the final position of the shock, which are displayed with purple pentagons. It is now obvious that we get a good description of the phase structure in terms of the final position of the shock. To obtain the position of the discontinuity at infinite RG-time we follow the logic presented in Section 4.2.2.2, i.e. at large RG-times we expect an exponential decay

$$\xi(t) = \xi_{\text{final}} + a_\xi e^{-b_\xi t} \quad \text{for} \quad t \gg 0\,. \tag{4.38}$$

This expectation is also supported by the asymptotic behaviour extracted analytically from the Riemann problem, c.f. Paragraph 4.2.2.1.1. To apply (4.38) we have extracted the position of the shock at 11 equally spaced points between the RG-times $t = 5$ and $t = 6$ using an appropriate concentration kernel, c.f. Section B.3, and then extracted the relevant information using a χ^2-fit. The trajectories of the shocks from the evolutions shown in Figure 4.7 are depicted in Figure 4.8, which justifies the use of (4.38). Additionally, it should be noted that the trajectory with a finite final position of the shock shown in Figure 4.8 is the most extreme cases present, i.e. the exponential decay started at earlier RG-times for other values of the coupling with $\xi_{\text{final}} > 0$.

Following the discussion presented in Section 4.2.3.2, we expect a power law like behaviour for the final position of the shock as a function of the coupling

$$\xi_{\text{final}} = \begin{cases} \beta \left|\lambda_4 - \lambda_4^{\text{crit}}\right|^\zeta & \lambda_4 \geq \lambda_4^{\text{crit}} \\ 0 & \lambda_4 < \lambda_4^{\text{crit}} \end{cases}\,. \tag{4.39}$$

Indeed, we find a very good agreement between the final positions of the shock and (4.39), the coefficients obtained from a χ^2-fit are collected in Table 4.3. As for the second order phase transition we obtain a very accurate estimate for the critical coupling, also shown with an orange circle in Figure 4.6. The critical exponent comes out at $\zeta = 0.683 \pm 0.013$ and it will be very interesting to investigate whether this value can be obtained from

	Parameter		
	Prefactor β	Critical exponent ζ	Critical coupling $-\lambda_4^{\text{crit}}$
χ^2-fit	6.57(45)	0.683(13)	0.104438(28)

Table 4.3.: Parameters obtained from a χ^2-fit to (4.39) of the positions of the shocks depicted in Figure 4.6.

an associated fixed point potential, which necessarily is either a partial fixed point or discontinuous, for a full study of the fixed points within this theory looking for continuous solutions see [179, 180]. Non-analytic fixed point potentials have been found very recently [181] and it will be very interesting to explore the relation of our results to the ones presented therein, since the results share some qualitative features.

4.2.3.4. Generalization of the mechanism to other theories

It seems rather plausible that the mechanism outlined in Section 4.2.3.2 persists in general, at least to some extent. The first obvious generalization is to go beyond large N and look at the flow equation (4.18) for finite N. Staying close to the conservative formulation employed so far, c.f. (4.22), we can express the flux for finite N by inclusion of a diffusion term

$$f(t, u, \kappa) = f_{\text{Conv}}(t, u) + f_{\text{Diff}}(t, u, \kappa)\,, \tag{4.40}$$

where the diffusion term depends additionally on the curvature defined in (4.34). DG schemes for diffusion terms are a well studied subject, see e.g. [182–184]. The first term on the right-hand side in (4.40) is the flux used in the large N limit (4.21) and the additional term contains the contribution of the radial mode

$$f_{\text{Diff}}(t, u, \kappa) = -\frac{A_d}{N-1}\frac{(\Lambda e^{-t})^{d+2}}{(\Lambda e^{-t})^2 + u + \kappa}\,. \tag{4.41}$$

From a practical perspective (4.41) is a diffusion term, hence it has the possibility to smear out potential shocks. Away from any potential shocks this equation is still convection dominated, since the curvature appearing in the denominator is comparatively small. However, at field values around the shock it might give a sizeable contribution. However, in close proximity of the phase transition, i.e. when the shock, or a slightly smeared shock, approaches zero, it becomes important that (4.41) only depends on the curvature, which vanishes exactly at vanishing field value. Due to this reason we expect a shock to be present in the direct vicinity of the phase transition. This marks a special regime at a first order phase transition, like the scaling regime at a second order phase transition. How this plays out in detail, especially in combination with the approach to convexity, will be extremely interesting to pursue in the near future. Particularly, the Péclet number, i.e. the convection over diffusion rate, might be a good start to quantify the competition between the different terms in (4.41).

Similarly, the presence of Fermions amounts to an additional source term in (4.40) in LPA. This potentially spoils the outlined mechanism in a trivial manner within this truncation. In this situation the phase transition is not fluctuation induced, but simply present due to the mean-field fermionic determinant, and an investigation should involve at least a field dependent Yukawa coupling to have the field dependent masses of fermions and bosons on the same footing. The field dependence of the Yukawa coupling in such theories was investigated in [65, 185–188].

Additionally, the question whether this mechanism can be used to extract properties of a first order phase transitions such as the nucleation rate in a convenient manner will be interesting to pursue.

4.2.4. Conclusion

In this section we have presented the applicability and advantages of applying Discontinuous Galerkin methods to the flow equations arising within the Functional Renormalization Group. As application we considered the $O(N)$-model in the large N limit in the Local Potential Approximation, where the flow equation of the effective potential can be cast into a conservative form, Section 4.2.1.2, which allows for a straightforward application of DG schemes. We considered the associated Riemann problem, as well as initial conditions that lead to a first or second order phase transition. The Riemann problem is considered in Section 4.2.2.1. It mainly led to the conclusion that shocks propagate only a finite range in field space. Therefore, they are still present in the solution at asymptotically large RG-times.

The case of a second order phase transition is presented in Section 4.2.2.2. We reproduced well known results from the literature and demonstrated in addition the expected convergence behaviour of the scheme. The underlying stability and convergence properties also hold in the flat region of the potential, which contrasts with methods that rely on the smoothness of the solution, c.f. Paragraph 4.2.2.2.2.

Initial conditions that lead to a first order phase transition are studied in Section 4.2.3. We discovered the formation of a shock in the derivative of the potential, leading to the mechanism behind first order phase transitions, explained in Section 4.2.3.2. This leads to an additional description of the phase structure in terms of the shock. In the vicinity of the phase transition the position of the shock shows a power law behaviour, like the order parameter in a second order phase transition.

These very promising results are the starting point for exciting follow up projects. One part consists of investigating the mechanism for first order phase transitions further and establishing it in general. This also includes making a connection to the usual observables considered at such a phase transition. On the other hand, applying DG schemes to the PDE part of FRG equations is a promising route for reliable, precision calculations. Our results represent a very important step towards understanding the phase structure of strongly correlated systems such as QCD or the Hubbard model.

4.3. Phase structure of the Quark-Meson model

Having discussed the $O(N)$ model in the large N limit in Section 4.2, we now turn our attention to two extensions. Firstly, the lifting of the large N limit. Secondly, the introduction of static, in an RG sense, quarks. Static refers to the fact that all quantities related to quarks are RG-scale independent. In the language of partial differential equations they act as pure source terms. From a QCD perspective, the Quark-Meson model can be motivated as low energy effective theory, c.f. Section 3.6. Here we will refrain from a in-depth discussion of the model and its phenomenology, which we will discuss later in Section 5.2. The classical action, which coincides with the scale dependent QEA at the UV cutoff Λ, is given by

$$S[q,\bar{q},\phi] = \int_x \left\{ \frac{1}{2}\left(\partial_\mu \phi_a\right)^2 + V(\rho) + h\left[\bar{q}\left(\mathrm{i}\gamma_5 \boldsymbol{T}\boldsymbol{\pi} + \sigma\right) q\right] \right\} , \tag{4.42}$$

where the spinor, flavour and colour indices of the quark are understood implicitly. In order to make contact with QCD, the scalar field is now $O(N=4)$ symmetric, with components $\phi = (\sigma, \boldsymbol{\pi})$ and invariant $\rho = \frac{1}{2}\phi_a\phi^a$, as before. As approximation, we take the simplest possible extension of the case considered in Section 4.2, i.e. we keep the effective potential V as only dynamic quantity and consider the Yukawa coupling h as a constant. In the literature this truncation is usually referred to as LPA.

Additionally, we restrict ourselves to chiral symmetric case. While this does not reflect our physical reality, from a technical perspective it doesn't matter because the term that breaks the symmetry does not couple back into the flow equations. Going to finite temperature and chemical potential, c.f. Section 2.5, it is straightforward to derive the flow equation for the effective potential. Hereby, we are using a spatial version of the Litim regulator (2.59)

$$R_k(p_0, \boldsymbol{p}) = \left(k^2 - \boldsymbol{p}^2\right)\, \Theta\left(k^2 - \boldsymbol{p}^2\right) , \tag{4.43}$$

which result in an analytic flow equation for the effective potential, see e.g. [62]. Apart from this, the regulator has to considered with care, as it spoils Lorentz invariant of the underlying vacuum theory, see e.g. [1, 120, 189]. In order to write the flow equation in a compact manner, we introduce some shorthand notation for the masses

$$\begin{aligned} m_\pi^2 &= \partial_\rho V(\rho) \\ m_\sigma^2 &= \partial_\rho V(\rho) + 2\rho\, \partial_\rho^2 V(\rho) \\ m_q^2 &= 2h^2\rho\,. \end{aligned} \tag{4.44}$$

At a given RG-time t these masses are effectively modified its convenient to introduce the quasi-particle energy

$$\epsilon_x = \sqrt{\Lambda^2 e^{-2t} + m_x^2} \quad \text{with} \quad x \in \{\sigma, \pi, q\}\,. \tag{4.45}$$

The final ingredient we require are the bosonic and fermionic occupation numbers that appear while calculating the Matsubara sums, c.f. Section B.4 for details,

$$n_{\mathrm{B}}(T; z) = \left[e^{\frac{z}{T}} - 1\right]^{-1} \tag{4.46}$$

$$n_{\mathrm{F}}(T, \mu; z) = \left[e^{\frac{z+\mu}{T}} + 1\right]^{-1} . \tag{4.47}$$

With this at hand, the flow equation for the effective potential reads

$$\begin{aligned}\partial_t V(\rho) = -\frac{\Lambda^5 e^{-5t}}{12\pi^2}\Bigg\{ &\frac{1+2\,n_{\mathrm{B}}(T;\epsilon_\sigma)}{\epsilon_\sigma} + (N_f^2-1)\frac{1+2\,n_{\mathrm{B}}(T;\epsilon_\pi)}{\epsilon_\pi} \\ &- 4N_f N_c \frac{1-n_{\mathrm{F}}(T,\mu;\epsilon_q)-n_{\mathrm{F}}(T,-\mu;\epsilon_q)}{\epsilon_q}\Bigg\}\,.\end{aligned} \tag{4.48}$$

Similarly to Section 4.2, we introduce the derivative of the potential as dynamic variable, because the flow of the effective potential (4.48) does not on the potential itself. Additionally, we the second derivative of the potential appears, which leads us to the definitions

$$\begin{aligned} u(t,\rho) &= \partial_\rho V(\rho) \\ \kappa(t,\rho) &= 2\rho\,\partial_\rho u(t,\rho)\,, \end{aligned} \tag{4.49}$$

c.f. (4.20) and (4.34), where we have made the RG-time dependence explicit. With this at hand, we can rewrite (4.48) as a first order system by taking one derivative with respect to ρ and introducing the equation for κ as constraint

$$\begin{aligned} \partial_t u(t,\rho) + \partial_\rho f(t,\rho,u,\kappa) &= 0 \\ \kappa(t,\rho) - 2\rho\,\partial_\rho u(t,\rho) &= 0\,, \end{aligned} \tag{4.50}$$

where the flux $f(t,\rho,u,\kappa)$ is implicitly defined by (4.48). The boundary condition for the derivative of the potential is set as in Section 4.2, i.e. we set the flux f at some large field value $\rho_{\max} \gg \Lambda$ to zero. This only assumes a classical potential that rises fast enough for large field values, which is the case for a ϕ^4 potential. The boundary condition for κ is more subtle, for the correct boundary condition we have to match $\partial_\rho u(t,\rho\to\infty)$ to the classical potential. However, this is non-trivial to enforce in upwind based methods, as one would like to alternate left and right derivatives in a one dimensional system, such that diffusive terms are without orientation. Therefore, we enforce $\kappa(t,0) = 0$, which fits such a scheme very well and is valid as long as $u(t,0)$ is finite. Instead of working with the full machinery of DG schemes, we take here a simpler approach. The same underlying principle of upwinding can also be implemented in a Finite Difference approach, which is considerably simpler to implement and serves as a good test ground for further developments.

4.3.1. Upwind Finite Difference

Here we give a brief motivation of Upwind Finite Difference methods, for a more complete introduction see e.g. [139]. We will restrict ourselves to one spatial dimension, as it is the only case of interest for us and it can be nicely embedded into the more general framework of Section 4.1. As mentioned before, the main motivation for employing the current scheme is the fast test cycle one can achieve. This is particularly convenient when looking at the issue of time stepping or adding higher order terms in an expansion in the FRG. In particular, given a set of collocation points $\{\rho_i\}$ a stable schemes is obtained by using first order derivatives in (4.50). Of course this can be extended to higher order methods, but besides the point for our purposes. The basic idea is equivalent to the one in Section 4.2, i.e. the underlying direction of the propagation of information within the

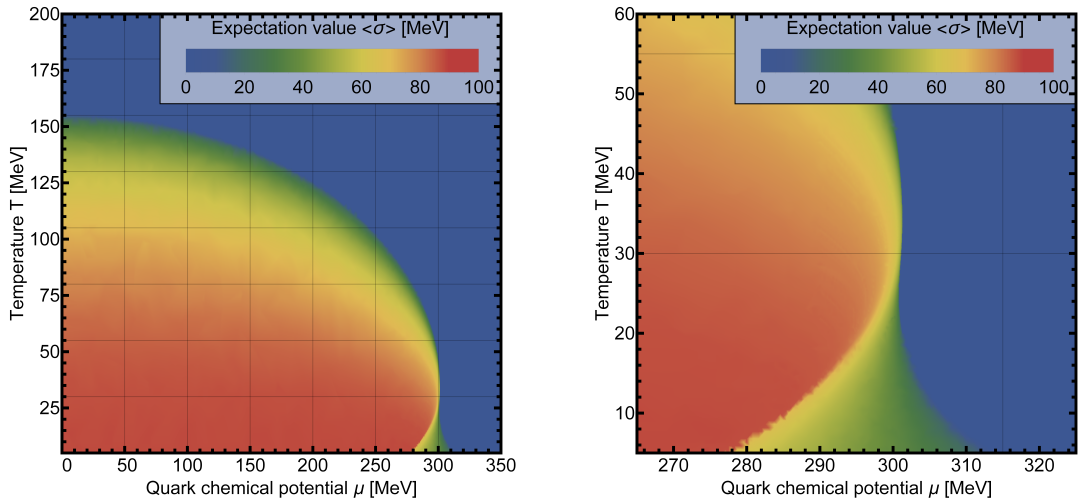

(a) Full phase structure.

(b) Vicinity around the critical end point.

Figure 4.9.: Phase structure of the Quark-Meson model in the chiral limit. The second order transition line starts at vanishing chemical potential and ends at $(T_{\text{crit}}, \mu_{\text{crit}}) \approx (0.03, 0.3)\,\text{GeV}$ in a critical end point with the first order region following.

equation is used to stabilize the scheme, i.e. the spatial discretization (4.50) is given by

$$\begin{aligned} \partial_t u_i^t + \frac{f_{i+1}^t - f_i^t}{\rho_{i+1} - \rho_i} &= 0 \\ \kappa_i^t - 2\rho_i \frac{u_i^t - u_{i-1}^t}{\rho_i - \rho_{i-1}} &= 0\,, \end{aligned} \tag{4.51}$$

where the upper index denotes the current time and the lower index to the spatial stencil used. The alternating use of a right derivative for the first equation and a left derivative for the second equation turns the second derivative appearing in (4.50), after taking the outer ρ derivative in the first equation, into a central difference in the discrete version (4.51). This has the nice property that the underlying convection part still respect the directed flow within the equation, while the diffusive part is term is, up to prefactors, blind to a preferred direction. This scheme introduces implicitly a numerical diffusion, such that the correct solution in the weak sense of the equation is obtained, c.f. Section 4.1.

4.3.2. Results

The Quark-Meson model has been discussed at length in the literature, see e.g. [37, 190–192] for early references and e.g. [185, 193] for more recent references going beyond LPA. Since our main motivation for the current investigation of this model is the advancement in our understanding of the numerical treatment of flow equations, we will refrain from a discussion of the underlying physics and refer to the aforementioned references.

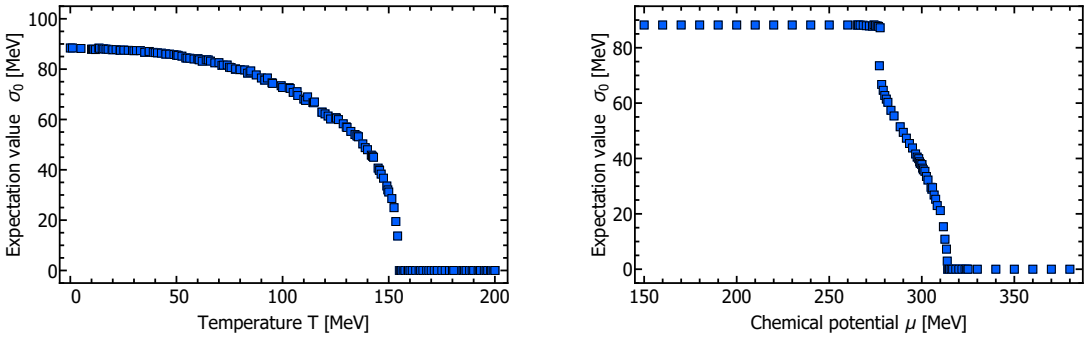

(a) Phase transition along the line of vanishing chemical potential.

(b) Phase transition along the line of a constant temperature $T = 5\,\mathrm{MeV}$.

Figure 4.10.: Different lines through the phase diagram shown in Figure 4.9.

The initial potential is given by

$$V_\Lambda(\rho) = \bar{m}_\Lambda^2 \Lambda^2 \rho + \frac{\lambda_\Lambda}{2}\rho^2 \,. \tag{4.52}$$

We initialize the theory at $\Lambda = 700\,\mathrm{MeV}$, which is a typical value for model applications. The Yukawa coupling is set to $h = 3.41$, which fixes the quark mass to a realistic value of the constituent quark mass of $m_q = 300\,\mathrm{MeV}$, corresponding to chiral condensate of $\sigma_0 = 88\,\mathrm{MeV}$. Being not primarily interested in the interpretation of the result from a physics perspective, we chose the potential with a vanishing initial mass, i.e. $\bar{m}_\Lambda^2 = 0$, but require that the chiral condensate has the correct value, i.e. $\sigma_0 = f_\chi = 88\,\mathrm{MeV}$, resulting in enhanced bosonic fluctuations, while keeping a symmetric initial potential. This condition fixes the quartic coupling to $\lambda_\Lambda = 44.165$. The final RG-time is fixed to $t = 4$, corresponding to 12.8 MeV, which is already considerably below some IR cutoffs used in the literature, demonstrating a first advantage of the demonstrated scheme. The time stepping is done exactly as described in Section 4.2.1.2. The accompanying exponential barrier in the CFL condition, or equivalently, the accuracy barrier for implicit methods is still the limiting factor when attempting to lower the IR cutoff. Nevertheless, it can be used to obtain the phase structure of the model in a robust and efficient manner, the expectation value as a function of temperature and chemical potential is shown in Figure 4.9. The result is very well known in the literature, the second order line that starts at vanishing chemical potential and ends at larger chemical potentials into a critical endpoint.

Additionally, we show the phase transition for zero chemical potential as well as small temperatures in Figure 4.10. We would like to remark that with the currently available accuracy and maximally achievable RG-time it is not absolutely certain that the first order region actually has a first order phase transition, see Figure 4.10b. This calculation reveals the true power behind the mapping of a hydrodynamic language to RG equations from a numerics perspective. Without much effort, we achieved a *unconditionally* stable result. Please note that this level of stability in the numerical set-up is absolutely needed when pushing towards a first principle studies of the high density region in QCD. Nevertheless, we looking closely at the region around the critical end point (CEP), located at $(T_{\mathrm{crit}}, \mu_{\mathrm{crit}}) \approx (0.025, 0.3)\,\mathrm{GeV}$, one can see the finite resolution of the scheme.

5. Momentum dependencies in Euclidean space-time

Having discussed the expectation value dependence extensively in Chapter 4, we will now turn to the momentum dependence. In particular, the momentum dependence in Euclidean space-time. Compared to the momentum dependence in Minkowski space-time, which we will discuss in the next chapter, cf. Chapter 6, accessing Euclidean momentum dependencies is computationally a lot easier. This is because the elementary correlation functions are smooth and singularities are, if present at all, located on boundaries. This is in stark contrast to Minkowski space-time correlation functions, where non analytic structures are very common, e.g. a mass-pole is represented by either a pole or a δ-function. However, both descriptions are equivalent on a fundamental level, given a reasonable set of axioms, see e.g. [194]. Additionally, the interpretation of RG flows is much simpler in Euclidean settings due to the presence of a positive definite momentum scale. These reasons are the reason why most computationally sophisticated computations are performed so far in Euclidean space-time. In cf. chapter we give an outline of the Euclidean side of the calculations performed.

5.1. $O(N)$-theory at finite temperature

This section is in parts based on [1].

We will comment more on the motivation for this work in the section, Section 6.2 concerning the Minkowski momentum dependence of the current setting. Our setting is the $O(N)$-theory with $N = 4$, like in Section 4.3 we only keep a lose connection to QCD since our main interest is the development of computational methods.

One of the main motivations for cf. work was the use of a regulator that perseveres Lorentz symmetry. This is a prior no problem in Euclidean calculations, since we only need to know the elementary correlation functions on the Matsubara modes and at spatial momenta in order to calculate loops. However, things get significantly more possible if one asks for the momentum dependence in-between the Matsubara modes, i.e. the full p_0 dependence. However, it can be shown that the propagator, even at finite temperature, has a unique analytic continuation [195]. While cf. will play an extremely important role when considering momentum dependencies in Minkowski space-time, it's also of relevance here. In particular, when working within the Matsubara formalism it turns out that the simple evaluation of the Matsubara sum in the analytically continued expression does again not lead to the desired contribution to the self-energy of the propagator. However, the mismatch is entirely contained in the occupation numbers, appearing implicitly when evaluating Matsubara sums. This is immediately obvious when considering how Matsubara can be calculated when going into the complex plane, cf. Section B.4. This is closely related to the connection and will be explored in great detail in Chapter 6. Here we simply state

the result at the example of a purely bosonic theory: given a set of external momenta p_i in a diagram, contributions like $n_{\mathrm{B}}(\mathrm{i}([p_i]_0 + [q_i]_0))$, where $[q_i]_0$ are the zero components of the loop momenta. Due to the periodicity of the occupation numbers the external frequencies do not contribute in the occupation numbers if they are set to Matsubara modes. The Euclidean elementary correlation functions are however initially only defined on precisely these point, i.e. we can add and subtract and arbitrary number of external frequencies in the occupation number without changing the result. It turns out that the correct result is obtained when all external frequencies are dropped from all occupation numbers implicitly appearing when performing the Matsubara sum, cf. Section 6.1.

This can be incorporated in a purely numerical fashion when calculating the Matsubara sum as a contour integral in the complex plane, cf. Section B.4, by weighting the contour integration with a weight. In the case of a simple polarization diagram with classical vertices, we have one external momentum p and the loop momentum q, cf. factor is then e.g. given by $n(\mathrm{i}(p_0 + q_0)) - n(\mathrm{i}q_0)$ and amounts to a formal solution of the analytic continuation problem. However, the numerical implementation of cf. procedure turns out to be very challenging as it requires to evaluate contour integrals in the close vicinity of first- and second-order poles (as soon as the regulator term $G\dot{R}G(q)$ is introduced).

The above discussion does not only for the analytic continuation between Matsubara modes, but to the entire complex plane, and therefore also to Minkowski space-time, cf. Chapter 6, and generic theories. In cf. section we will only consider the Euclidean momentum dependence of the present setting of the $O(N)$-model utilizing the FRG.

5.1.1. Truncations

In order to simply the numerical setting, we work in a derivative expansion and only extract the full momentum dependence in addition. This has the advantage of only producing poles in the integrands on the RHS of the flow equation for the two-point function. We have checked in vacuum explicitly that cf. give very good results for the two-point function, compared to taking the full momentum dependence of it into account. With cf. at hand, we use the following ansatz for the scale dependent QEA

$$\Gamma_k = \int \mathrm{d}^4x \, \left(\frac{Z}{2} (\partial_\mu \phi_a)^2 + \frac{Y}{8} (\partial_\mu \rho)^2 + V(\sigma) \right) , \tag{5.1}$$

with the mesonic field $\phi = (\sigma, \boldsymbol{\pi})$. In (5.1) and in the following we assume that all couplings, i.e. $V(\phi)$, Z and Y depend on the RG-scale k. The effective potential, $V(\sigma)$, is split into a part only depending on the $O(4)$-invariant $\rho = \frac{1}{2}(\pi_a^2 + \sigma^2)$, and a part explicitly breaking the symmetry, thus allowing for the Goldstone bosons to acquire a finite mass

$$V(\sigma) = U(\rho) - c\sigma \, . \tag{5.2}$$

Note that the linear breaking term drops out of all dynamical equations, and in particular the flow equations. In order to resolve the effective potential we Taylor expand it in ρ up to a given order, cf. can be justified by the discussion in Paragraph 4.2.2.2.2. The fact that the linear breaking term drops is hidden in an expansion about the flowing minimum, but is very apparent within an expansion around a fixed expansion point in the bare field σ, see [185]. In the present work we choose the latter expansion for both stability and for a self-consistent frequency dependence, see [196]. We choose the expansion point close but above

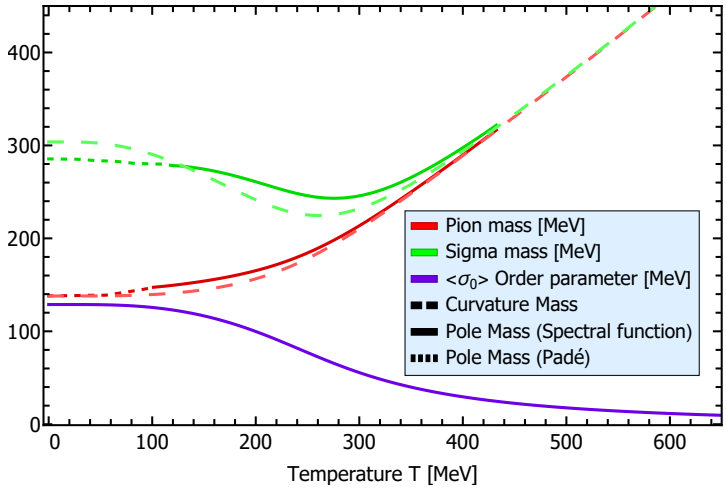

Figure 5.1.: Crossover phase transition in the $O(N)$-model at finite temperature. The order parameter as well as the masses across the phase transition are depicted. For the masses we differentiate between curvature and pole masses. More details about the pole masses are explained in Section 6.2.

the IR minimum $\langle\sigma\rangle$, as argued in [185]. We take into account terms up to ϕ^{14}, and the convergence of the results has been checked. The truncation (5.1) is referred to as LPA'+Y and we additionally consider a second truncation with $Z = 1$, $Y = 0$ corresponding to the usual LPA scheme, cf. Section 2.3.2. In the following we also drop the contribution to the four-point vertex from the Y-term. Then, the two dressing functions Z and Y can effectively be reabsorbed into a dressing for the pion, Z_π, and one for the sigma meson, Z_σ. As argued in [197], we are mostly concerned with regulators depending on the Lorentz invariant momentum configurations q^2 and is discussed at large in said reference. Further details about the regulator in the current work are given in Section B.5 and a comparison with a regulator that breaks Lorentz invariance explicitly is discussed in Section B.6.

5.1.2. Results

The setting is in general very similar to the one discussed in Section 4.3. As a main ingredient we use the curvature masses, which are simply given by (dressed) derivatives of the effective potential (4.44). Alternatively, they are related to the two-point function by

$$m_{\text{cur}}^2 = \lim_{\vec{p}\to 0} \frac{\Gamma_E^{(2)}(0,\vec{p})}{Z(0,\vec{p})}\,. \tag{5.3}$$

The wave function renormalization in (5.3) ensures the RG invariance of the left-hand side. The initial conditions used are described in Section B.5. If we do not mention explicitly that results were obtained in LPA, the full truncation given in (5.1) was used. The flow equations for the effective potential are straightforward to derive. The equations for the two-point function can be found in Section 2.3.2. Details about the numerical implementation can be found in Section B.7.

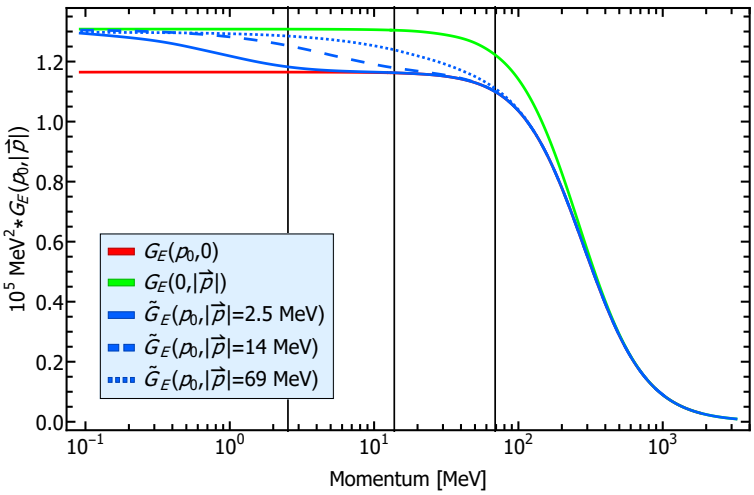

Figure 5.2.: Non-commuting zero momentum limit (5.4) of the sigma propagator at finite temperature in the Matsubara formalism. The temperature is 138 MeV, which corresponds to the vacuum mass of the pion. The combination $\tilde{G} = \left(\Gamma^2(p_0, \boldsymbol{p}) - \boldsymbol{p}^2\right)^{-1}$ subtracts the trivial mismatch at finite momenta with respect to the cases where one component vanishes identically.

We start by looking at the underlying phase structure in order to be able to easily interpret the results of the two-point function. The result for the curvature masses, the order parameter and the pole masses, for later reference, are shown in Figure 5.1.

Within our given parameters, which were an unfortunate by-product of the regulator choice, we find a very smooth crossover, i.e. the two different phases are clearly distinguishable, but there are hardly any remnants of the second order phase transition without the explicit symmetry breaking term left. In the high temperature phase we find the expected increase of the masses with the temperature $m \sim T$, while the expectation value approaches zero.

With cf. at hand we can now investigate the two-point function in more detail. One interesting aspect is the non-commuting zero momentum limit. At finite temperature there is no reason that the limit of vanishing zero component of the momentum and vanishing spatial component commute, and in fact cf. is the case

$$\lim_{\boldsymbol{p}\to 0}\lim_{p_0\to 0}\Gamma^{(2)}(p_0,\boldsymbol{p}) \neq \lim_{p_0\to 0}\lim_{\boldsymbol{p}\to 0}\Gamma^{(2)}(p_0,\boldsymbol{p})\,. \tag{5.4}$$

The order of limits on the left-hand side is referred to as *static* limit and the limit on the right-hand side as *plasmon* limit, for details see e.g. [198], if not stated otherwise $Z(0,0)$ is understood in the *static* limit. Physically, the non-commuting limits imply the existence of a transport peak in the corresponding spectral function, which we will discuss in more detail in Section 6.2. In order to look at cf. quantity, the analytic continuation of the flow equations in-between Matsubara modes is of course of utmost importance, as otherwise the limit does not exist. Evaluated on the zero Matsubara mode, one implicitly obtains the static limit. The resulting propagator for different momentum configurations is shown in Figure 5.2, at the exemplary temperature of $T = 138\,\mathrm{MeV}$.

The differentiation between the two limits is particularly important when defining quantities such as (5.3), as they are directly affected by the choice. In Figure 5.2, we have

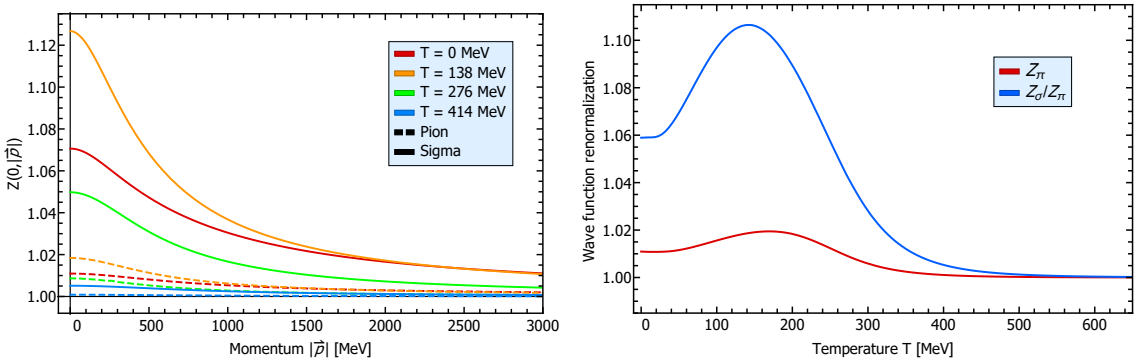

(a) Spatial momentum dependence of the dressing of the two-point function evaluated on the zeroth Matsubara mode for different temperatures.

(b) Temperature dependence of the wave function renormalizations.

Figure 5.3.: Different spatial momentum and temperature dependencies in the Euclidean domain.

defined $\tilde{G} = \left(\Gamma^2(p_0, \boldsymbol{p}) - \boldsymbol{p}^2\right)^{-1}$, which subtracts a trivial mismatch at large momenta. If one considers the propagator as a function of the zero component of the momentum, for various small values of the spatial momentum, its immediately visible that the switching scale to the static behaviour, i.e. $p_0 \equiv 0$, is given by the spatial momentum scale. In particular, for Euclidean correlation functions the static case is also the relevant one, as it is the one entering directly into loops, while the remaining zero momentum component dependence is only taking into via the Matsubara sum. As a result higher modes, i.e. $p_0 = 2\pi n T$ with $n > 0$, are naturally suppressed by the temperature scale. The difference from a free propagator can be encoded in a parametrization of the type

$$\Gamma^{ii}(p_0, \boldsymbol{p}) = Z_i(p_0, \boldsymbol{p}) \left[p^2 + m_i^2\right] , \tag{5.5}$$

where $i \in \{\pi, \sigma\}$ and m_i is implicitly defined such that $Z_i(p^2 \to \infty) = 1$. Note that in the infinite momentum limit there is no problem with commuting limits in cf. case. The flowing QEA does not couple the full momentum dependence back, but only Z and Y. From the discussion above it should be clear that both are defined in the static limit at finite temperature. We show the dressings $Z(0, \boldsymbol{p})$ as well as the dressing Z from (5.1) in Figure 5.3. The spatial momentum dependence shown in Figure 5.3a is rather uneventful, which is good, as it is a necessary condition for expansion schemes to work, cf. Section 2.3.2. As expected the sigma shows way enhanced dynamics compared to the pion, which stays very close to being classical, in particular in the vicinity of the crossover transition. This is necessarily also the case in the wave function renormalization shown in Figure 5.3b. In a rough comparison, the two-point dressing $Z(0, 0^+)$ at zero momentum and the wave function renormalization Z agree, showing the adequacy of the scheme used in the Euclidean domain.

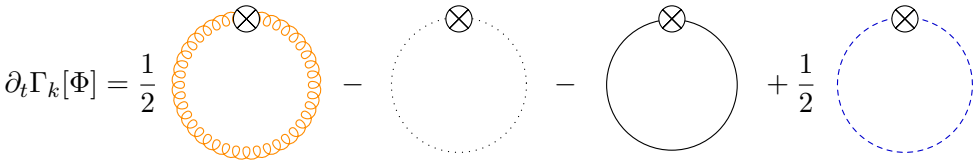

Figure 5.4.: Functional renormalization group equation for QCD in which the $\sigma - \vec{\pi}$-channel is dynamically hadronized. The lines denote gluons, ghosts, quarks and mesons, respectively, and represent fully momentum and field dependent propagators. The cross denotes the regulator insertion $\partial_t R_k(p)$, leading to an effective UV cutoff for modes with $p^2 \gtrsim k^2$.

5.2. Quark-Meson model

This section is in parts based on [4].

Having discussed the $O(N)$-model with a loose connection in Section 5.1, we will now turn to the Quark-Meson model look at a much more detailed comparison to QCD. Particularly, we will restrict ourselves to the case of vacuum again, but work in a much more sophisticated truncation.

The motivation for cf. work is twofold: Firstly, establishing a FRG based framework for the calculation of bound states, based on dynamical hadronization, cf. Section 3.6.1; Secondly, the direction comparison of Euclidean momentum dependencies between the Quark-Meson model and a first principle calculation in QCD. In order to facilitate the first aspect, we start with a rather detailed description of the challenge to calculate bound states from first principles in QFTs.

5.2.1. Bound states in Functional Methods

The efforts of determining bound state properties in a quantum field theoretical approach date back to the seminal work of Bethe and Salpeter [199, 200]. Despite considerable progress in our understanding of bound states and their properties in quantum field theories, the precise computation of their properties and subsequently also the computation of spectra in general remains one of the biggest challenges today. Motivated by the immense significance of reliable predictions of these quantities in essentially all areas of physics there are quite a number of ongoing investigations in cf. field. This applies in particular to QCD because confinement makes only the composite states of quarks and gluons, the hadrons, experimentally accessible.

The study of highly relativistic bound states has also been hampered by the fact that almost all quantitative non-perturbative methods rely on the Euclidean formulation of QTFs. This implies that for determining bound state properties the results for correlation functions have either to be continued to Minkowski space-time or have to be extracted from potentially subleading exponential tails of correlation functions. To cf. end we note that the existence of stable bound states implies poles and of scattering states cuts in the correlation functions for time-like momenta. Unstable particles and virtual states create in

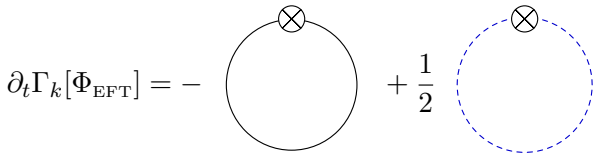

Figure 5.5.: Functional renormalization group equation for the two-flavour Quark-Meson model, for the notation cf. Figure 5.4.

addition further poles in the complex plane. While the lowest excitations typically can be accessed via reconstruction methods such techniques fail to provide trustworthy results for the higher resonances. These higher-lying bound states plainly require an exponentially enhanced precision of the imaginary time data. Moreover, by definition, they lie beyond the radius of convergence for Padé-like analytic continuations of the imaginary time results: Their masses are larger than the ground state mass, and the latter provides the lowest-lying pole in exactly cf. channel.

In the present section we suggest a functional continuum approach to bound state computations, which is also put in perspective to other functional bound state approaches, for the impressive progress on bound state and general low energy properties on the lattice we refer the reader to, e.g. [201]. Due to the bound states poles in the correlation functions, these states, and even higher-lying resonances, can be accessed in continuum approaches via the resonant frequency or momentum structures of higher-order correlation functions of the fundamental degrees of freedom as, e.g. quarks and gluons in QCD. In case of gauge theories physical states will only appear in gauge-invariant channels. However, an understanding of the non-perturbative properties of the elementary correlation functions might necessitate the consideration of bound states in unphysical channels, see, e.g. [202–204].

The correlation functions that feature a pole at the bound state masses satisfy Dyson-Schwinger equations as all correlation functions of a theory, for respective reviews see, e.g. [45, 205, 206]. It has been exactly the achievement of Bethe and Salpeter to realise that employing a Laurent expansion of the respective correlation function around the bound state pole its non-linear and in general inhomogeneous DSE can be reduced to a linear and homogeneous equation, the Bethe-Salpeter equation (BSE), for a simpler quantity, the Bethe-Salpeter amplitude [199, 200]. Hereby, the most challenging of the remaining complications is to find an approximation to the kernel of cf. equation which is on the one hand treatable and on the other hand keeps the most important symmetries of the underlying physics intact. The formulation and discussion of a systematic improvement of employed truncations for the kernel can be found in [206] and references therein. It has to be noted that the by far most used truncation in QCD and hadron physics, a generalised rainbow-ladder truncation, is for quite a number of meson and baryon channels quite successful, see, e.g. the recent references [49, 207–212], but fails nevertheless for a large amount of hadron resonances as it can be inferred for example for a combined DSE-BSE approach for light mesons at the three-particle irreducible three-loop level [213] or by recent investigations within the Functional Renormalisation Group (FRG) [63, 64].

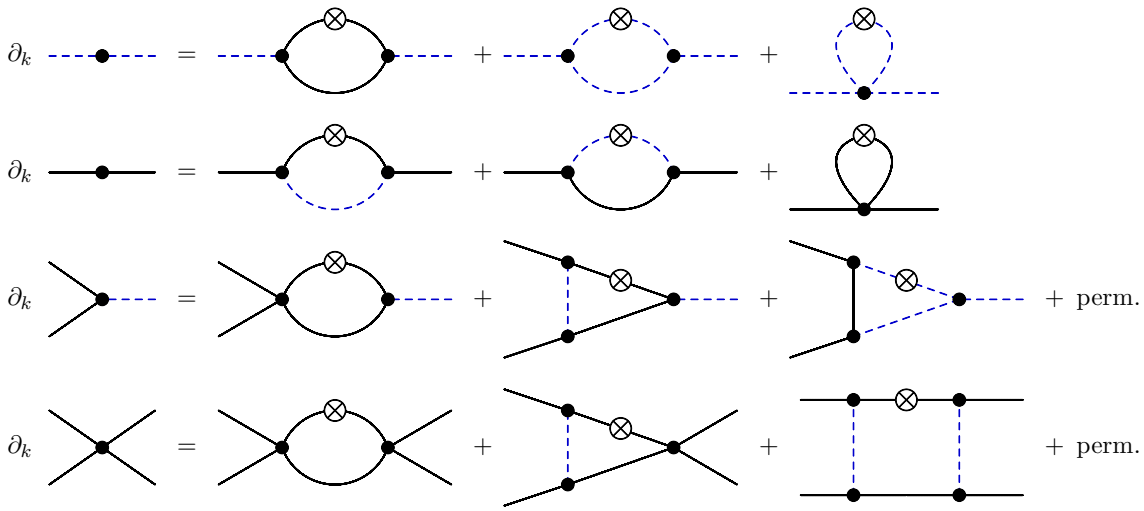

Figure 5.6.: Flow equations for the propagators, Yukawa coupling and four-quark interactions.

It has to be emphasised, however, that keeping the most important symmetries at cf. level intact requires self-consistency of the treatment of a quite large amount of DSEs for the elementary correlation functions of QCD together with the bound state BSEs. This leads to an overwhelming degree of complexity in such calculations. Effectively, it also prevents the use of other available input data for QCD correlation functions, as the most sophisticated calculations imply a high degree of sensitivity of the bound state properties on details of the elementary QCD three-point functions. Note also, that an FRG approach very close to the BSE-DSE framework has been put forward in [35, 214], for recent works in cf. direction see [215, 216].

In the current work we discuss a unified functional renormalization group approach to bound state properties, based on dynamical hadronization, cf. [38, 124, 129, 130], Section 3.6.1, and Section 5.2.2. Within dynamical hadronisation, correlation functions are not treated as in the DSE-BSE approach by partly including the off-shell behaviour and partly restricting to on-shell properties. Instead, both, the quark-gluon correlation functions as well as the Bethe-Salpeter wave functions (on and off-shell), originate from a common effective action. Naturally, such a unified approach resolves the challenge of self-consistent truncations, which is of crucial relevance in the DSE-BSE framework, by construction. Another important ingredient is the fact, that by now the FRG has matured enough to sustain a systematic access to bound state properties.

Here, we initiate cf. bound state program with a detailed study of the Quark-Meson model in the light of the structures explained above. We explain the natural embedding of cf. low-energy model as an Effective Field Theory (EFT) of QCD as formulated in [63–65]. This includes the determination of the EFT couplings directly in QCD from the QCD flows in [63, 64] leading to the QCD-assisted Quark-Meson model. Then we present results for the (Euclidean) momentum dependence of correlation functions relevant for the access to bound states. As so far only the lightest states will be included, an exploratory investigation into the Minkowski realm can still be done by means of a reconstruction of

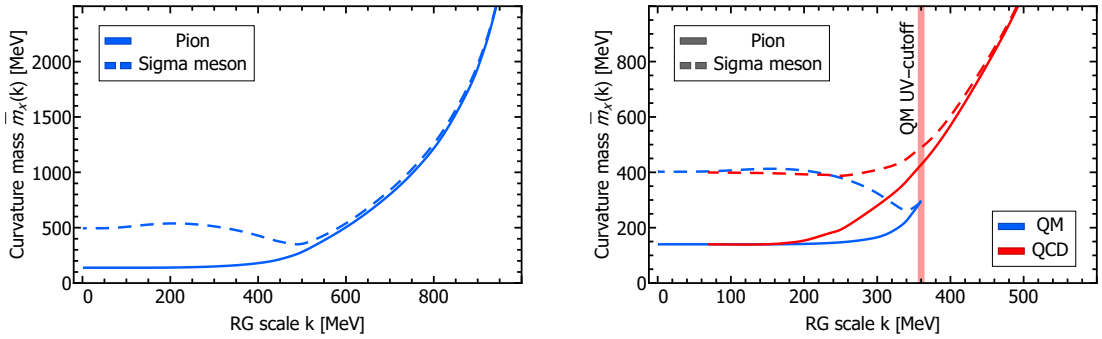

Figure 5.7.: The flow of the curvature masses for the mesons in the Quark-Meson model (left panel). The flow is started in the chirally symmetric regime. During the flow chiral symmetry is broken dynamically and thus the masses of pion and sigma run apart in the Quark-Meson Model. In the right panel the results are compared when the flow of the Quark-Meson-model is QCD-assisted, and compared to those in full QCD from [64].

the real-time meson propagators. This is notwithstanding the problems listed above for reconstructions, and going beyond is our next step.

This section is organized as follows: In Section 5.2.2 dynamical hadronization within the FRG is briefly revisited with a particular focus on the current problem. The adaptation of cf. approach to QCD as well as the motivation for employing the Quark-Meson model as a low-energy effective theory are discussed in Section 5.2.3.1. The truncation of the flow equation for the Quark-Meson model is detailed in Section 5.2.4. Our results are then discussed in Section 5.2.5. In Section 5.2.7 the next steps which are required to treat QCD are outlined. Our conclusions are presented in Section 5.2.8. Technical details as well as a comparison of results in different truncation levels are deferred to the three appendices Section A.2, Section B.8 and Section C.1.

5.2.2. The FRG and bound states

The FRG approach to bound states as outlined in the present work is based on two key ingredients, the calculation of real-time correlation functions and the concept of Dynamical Hadronization, both of which are briefly revisited in cf. section.

5.2.3. Real-time FRG

By now real-time versions of the FRG have been developed that allow to access real-time correlation functions, and, at the same time, making use of the rather well-developed Euclidean correlation functions of the theories at hand, and in particular QCD, for recent works see [1, 3, 165, 166, 197, 217–223].

Here, our task is to extend cf. to dynamically generated bound state properties. To cf. end, regulators that preserve $SO(1,3)$ Lorentz symmetry are of paramount importance, and we will focus our discussion of the space-time symmetric regulators suggested in [1, 197, 217, 218], cf. Section 5.1. Moreover, it is well-studied by now, that the rapid decay of the regularised loops in frequency and momentum space is particularly important in approximations for the full system that do not carry the full frequency and momentum

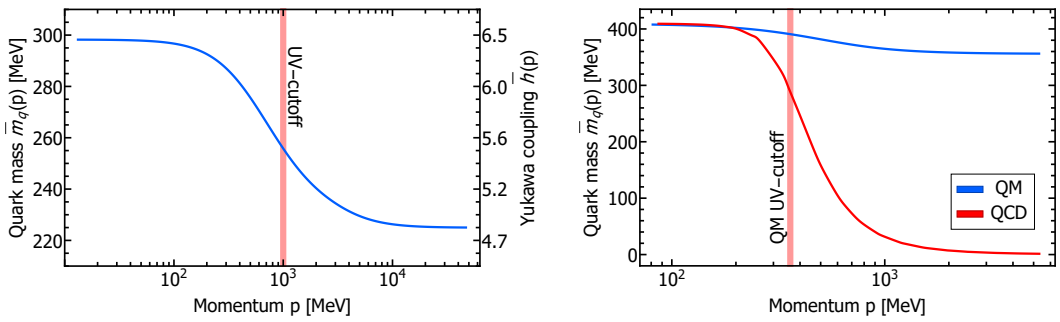

Figure 5.8.: The momentum-dependent quark mass function in the Quark-Meson model (left panel). The right panel shows a comparison of the same quantity between the QCD-assisted Quark-Meson model and QCD.

of the theory. Alternatively, one can study some questions about real time observables by applying reconstruction methods. Combined with Euclidean FRG input cf. option has been used in [2, 196, 224–227]. A detailed analysis of the general complex structure of correlation functions as well as the low and high frequency limits leads to optimised reconstruction schemes, see [2]. An application of cf. novel reconstruction method to QCD spectral functions can be also found in [2]. We will come back to cf. issue in Section 6.4.

5.2.3.1. Dynamical Hadronization

Here we want to give a QCD bound state perspective of Dynamical Hadronization, for a technical introduction see Section 3.6.1.

Bound states and resonances in QCD and other theories manifest themselves in resonant momentum channels in scattering amplitudes and correlation functions. Typically, in an effective field theory approach such a channel can be described as the exchange of an effective field degree of freedom that carries the quantum numbers of the resonant channel. This is the well-known Hubbard-Stratonovitch (HS) transformation, originally introduced as an identity transformation for a local four-point interaction of fermions done on the level of a classical action.

The FRG allows to perform cf. identity transformation on the level of the full QEA, cf. Section 3.6.1, which avoids the well-known double-counting problems of the HS transformation, if quantum fluctuations are taken into account. This transformation, called dynamical hadronization or more generally dynamical condensation/ bosonization has been introduced in [124] and further developed in [38, 129, 130]. While originally introduced for the HS-type transformation for a four-point function it is by now applicable to general and also non-polynomial field operators [38]. Its applicability to the full effective action is intertwined with the Wilsonian idea of integrating out fluctuations iteratively momentum shell after momentum shell. As it is done as an exact identity transformation at each RG step, it avoids any double counting issue. This is the property that elevates it to an identity transformation of the full QEA.

One of the prominent advantages within such a formulation is the following. Typically applications of functional methods to strongly correlated systems such as QCD rely on systematic vertex expansions in the absence of small parameters. The 'small' parameter behind cf. systematics is the phase space suppression of the contributions of diagrams

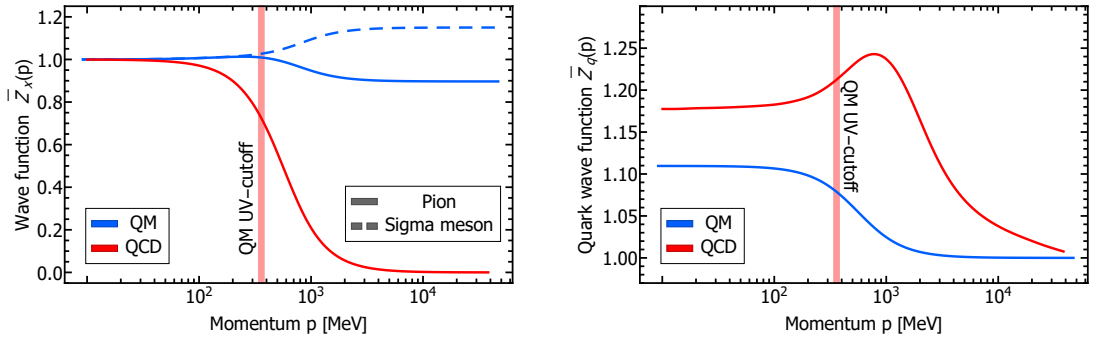

Figure 5.9.: Comparison between the QCD-assisted QM model and QCD for the momentum dependent wave function renormalizations for the mesons (left panel) and quarks (right panel).

with higher order vertices: These vertices have no classical part and are generated by diagrams in the first place, and hence possess for an asymptotically free theory a rapid decay behaviour in momentum space which leads to, after the angular integration, a very efficient suppression of the respective diagrams. This corresponds to a intuitive picture: these n-order vertices describe effectively the local interaction of n particles which is phase space suppressed. However, resonances in interaction channels do not have cf. suppression if their regularised mass is of the same order as the cutoff or below.

Explicitly, for the case of QCD and hadron physics cf. implies that the occurrence of bound states or resonances characterized by two or three valence quarks, e.g. the mesons and baryons, reduces scattering vertices of $(2n)$ or $(3n)$ quarks and anti-quarks to that of n mesons or baryons. This counter-acts significantly the phase space suppression of the relevant channels. Accordingly one either goes to a higher order of the vertex expansion in the fundamental fields in QCD or formulates QCD also in terms of these additional effective degrees of freedom.

We close cf. discussion with two remarks on dynamical hadronization: First, we emphasise again that dynamical hadronization does not entail the reduction of QCD to a low energy EFT. It is only a convenient and efficient reparametrisation of QCD in the dynamical low energy degrees of freedom. Second, even though the phase space suppression is partially lifted in the presence of resonant interactions, it is also the mass scale of these channels that decides about their relevance for quantum fluctuations. In QCD these resonances get strong at low, sub-GeV RG scales k. Note that the loop momenta in the FRG framework are restricted by the cutoff scale, $p^2 \lesssim k^2$. Hence, all but the lowest lying resonances are already decoupled when they are generated. Accordingly it is also quantitatively sufficient to consider the dynamical hadronization of the σ mode and the pions $\vec{\pi}$.

Applications to QCD can be found in [4, 28, 63–65, 127]. In particular, the references [63, 64] contain an application of dynamical hadronization on the quantitative level with full momentum dependencies to QCD with the to date by far largest set of coupled set of correlation functions in functional methods.

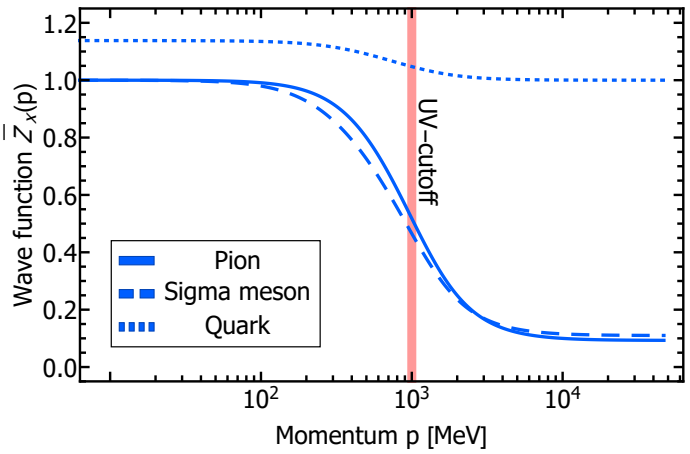

Figure 5.10.: The momentum-dependent wave-function renormalization of the mesons and quarks in the Quark-Meson model.

5.2.3.1.1. Technical aspects

As already described in Section 5.2.3.1 and Section 3.6.1, dynamical hadronization facilitates apparent convergence by means of restoring the canonical phase space suppression ordering of n-point functions.

In the present case we use it for introducing an auxiliary scale dependent mesonic field $\phi_k = (\sigma_k, \vec{\pi}_k)$ with

$$\partial_t \sigma_k = (\partial_t A_k)\, \bar{q} q\,, \qquad \partial_t \vec{\pi}_k = (\partial_t A_k)\, \bar{q}\, i\gamma_5 \vec{\tau} q\,, \tag{5.6}$$

where the scale dependence $\dot{A}_k$ of cf. transformation can be chosen arbitrarily. This freedom is used to successively absorb the scalar–pseudo-scalar u-channel of the four-quark scattering vertex, for more details see Section A.2.4. Then, cf. channel vanishes identically in the four-quark vertex. Inserting (5.6) in (2.39), cf. Section 3.6.1, we are led to a modified flow equation[1]

$$\left(\partial_t + \partial_t \phi_k[\Phi] \frac{\delta}{\delta \phi_k}\right) \Gamma_k[\Phi] = \frac{1}{2} \mathrm{Tr}\, \frac{1}{\Gamma_k^{(2)}[\Phi] + R_k}\, \partial_t R_k\,. \tag{5.7}$$

The auxiliary field can then be interpreted as the resonance of that channel as it carries the physics and the same quantum numbers. Thereby dynamical hadronization allows for a convenient access to resonances and all associated bound state properties.

5.2.3.2. QCD-assisted low energy effective theories

The flow equation for two-flavour QCD in Landau gauge with dynamical hadronization of the σ and $\vec{\pi}$ four-quark channels is depicted in Figure 5.4. When lowering the cutoff scale k successively, the single loops in Figure 5.4 are suppressed if the cutoff scale drops below the mass gap of the respective propagators. This has very important consequences. First of all, the meson loops do not contribute at large cutoff scales: The effective mesonic

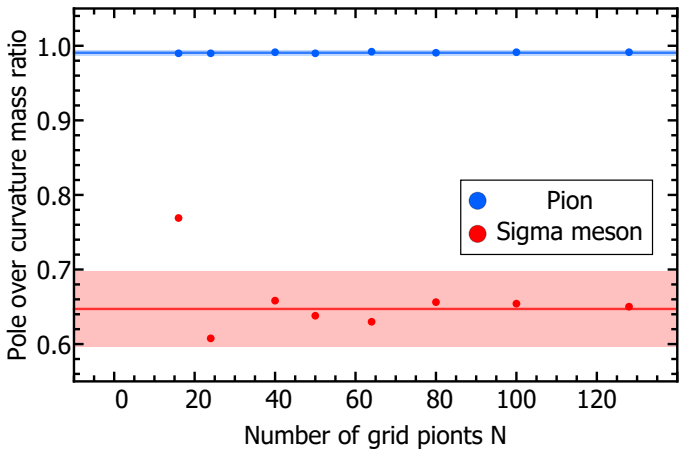

Figure 5.11.: The ratios of the meson pole masses m_{pole} and curvature masses m_{cur} are shown. The ratio is stable for the pion and converges slowly, but eventually, for the sigma as a function of grid points N.

mass scale drops rapidly for large cutoff (and momenta) because the respective momentum channels in the four-quark interaction decay rapidly. This in turn leads to an increased importance of the mesonic loops at low cutoff scales. This is in agreement with the pion mass being the smallest mass scale. Second, the gluon effectively decouples below cutoff

scales of $k \lesssim 1\,\text{GeV}$ as the gluon is gapped in Landau gauge with a mass gap of almost one GeV. Hence, for these scales the gluon loop can be dropped in Figure 5.4 for $k \lesssim 1\,\text{GeV}$. Moreover, to leading order the ghost fields only couple to the matter part of QCD via the gluon. Accordingly, they effectively decouple from the matter sector of QCD as well at the same decoupling scale as the gluon. This leaves us with a Quark-Meson flow equation at low cutoff scales which is depicted in Figure 5.5.

In summary, cf. leaves us with a QCD-assisted low energy effective theory for QCD. Its natural ultraviolet cutoff Λ is at almost 1 GeV, and the 'classical' action $S_{\text{EFT},\Lambda}$ of cf.

[1]Please note that cf. does not take the explicit symmetry breaking properly into account, since the flow equation (5.7) is not manifestly independent with respect to the symmetry breaking parameter and should be revised in future work. For a short discussion see Section 3.6.1 and a longer one [8] or [28].

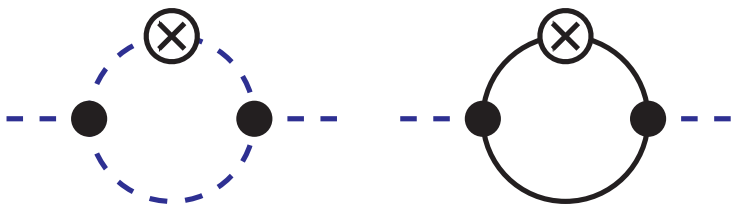

(a) Mesonic contribution (b) Quark contribution

Figure 5.12.: The two dominant diagrams contributing to the wave functions of the mesons in QCD (up to permutations of the regulator).

EFT is the full effective action of QCD at cf. scale, evaluated on the equations of motion for the gauge field and the ghosts: $A_\mu = 0\,,\ c = 0 = \bar{c}$ and thus

$$S_{\mathrm{EFT},\Lambda}[q,\bar{q},\phi] = \Gamma_{\mathrm{QCD},\Lambda}[\Phi_{\mathrm{EFT}}]\,, \tag{5.8}$$

with the superfield

$$\Phi_{\mathrm{EFT}} = (0,0,0,q,\bar{q},\phi)\,, \qquad \phi = (\sigma,\vec{\pi})\,. \tag{5.9}$$

This concludes the discussion of the QCD-embedding of the low energy EFT under investigation here, additional discussions of cf. issue can for example be found in [28, 65, 120, 120, 162, 228–230].

5.2.4. Quark-Meson model

Utilizing the previous discussion we can write down the leading terms of the QCD effective action at a scale where the ghost and gluons are to a large degree already decoupled. Then, the QCD QEA with dynamical hadronisation as described in the previous section reduces to a low energy effective theory with quarks and mesons, the Quark-Meson (QM) model, cf. Section 4.3. Bound state considerations in the QM model were amongst the first application of the FRG, see e.g. [190], for early reviews see [37, 191, 192].

$$\begin{aligned}\Gamma_k = \int_x \Bigg\{ & Z_q \bar{q}\partial\!\!\!/ q + \lambda\left[\frac{1}{2N_f}\left(\bar{q}q\right)^2 - \left(\bar{q}\gamma_5\vec{\tau}q\right)^2\right] \\ & + \frac{1}{2}Z_\sigma(\partial_\mu\sigma)^2 + \frac{1}{2}Z_\pi(\partial_\mu\vec{\pi})^2 + V_k - c\sigma \\ & + h\,\bar{q}\left(\mathrm{i}\gamma_5\vec{\tau}\cdot\vec{\pi} + \frac{1}{\sqrt{2N_f}}\sigma\right)q\Bigg\}\,.\end{aligned} \tag{5.10}$$

The effective action (5.10) consists of three parts: the fermionic and the bosonic ones as well as a Yukawa interaction in between both of them. The latter two, i.e. the second and third line in the effective action (5.10), result from dynamical hadronization. As for the first line, the quarks' kinetic term appears already in the classical action of QCD. On the

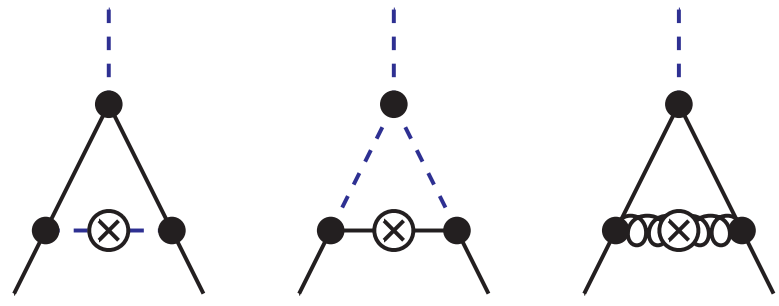

(a) Quark-Meson vertex (b) Quark-Meson vertex (c) Quark-Gluon vertex

Figure 5.13.: The three dominant diagrams contributing to the Yukawa coupling in QCD (up to permutations of the regulator).

other hand, the four-quark interaction is induced by the quark-gluon interaction and is thus created dynamically during the evolution of the scale dependent effective action. Herein, we only consider the scalar–pseudo-scalar u-channel of the four-quark vertex, which is by far the most dominant one (see the discussion above). Consequently, the bosonic part contains the propagators for the sigma meson and the pions. These terms as well as the Yukawa interaction are already obtained by a single Hubbard–Stratonovich transformation (see, e.g. Chapter 3 of [231]). Higher-order terms induce self-interactions between the mesons which are described by the effective potential V_k. Since isospin symmetry remains unbroken it is a functional of the $O(4)$-symmetric combination $\rho = \frac{1}{2}\left(\sigma^2 + \vec{\pi}^2\right)$, cf. Chapter 4. A non-vanishing expectation value of ρ, $\langle\rho\rangle \neq 0$, signals condensation of the sigma meson and thus spontaneous symmetry breaking. Current quark masses lead via an appropriate shift of the σ field to the last term in the second line of the effective action (5.10). It explicitly breaks $O(4)$-symmetry and effectively alters the expectation value of the sigma meson by tilting the effective potential, which in turn results in a finite mass for the Goldstone modes, i.e. the pions. To summarize, the ansatz (5.10) for the scale-dependent effective action captures within a reasonable approximation the leading behaviour of two-flavour QCD at low momenta, a statement tested explicitly in Section 5.2.5.1.

In the effective action (5.10) the wave-function renormalization functions, $Z_\sigma(p)$, $Z_{\vec{\pi}}(p)$ and $Z_q(p)$, the Yukawa coupling $h(p_1, p_2)$ and the four-quark coupling $\lambda(p_1, p_2, p_3)$ are momentum-dependent quantities. Please note that we employ a notation in which momentum conservation is exploited and the three-point vertex h is a function of two independent momenta, the four-point vertex λ of three momenta. To this end, in the Yukawa coupling the quark momenta are singled out As already mentioned, the successive Hubbard–Stratonovich transformations in the Dynamical Hadronization are then used to cancel the flow of the four-quark coupling, i.e. one implements

$$\partial_t \lambda(p, p, -p) = 0\,. \tag{5.11}$$

which yields an additional contribution to the flow of the Yukawa coupling.

In the following we differentiate between bare quantities and renormalised quantities which are then denoted by a bar. The renormalization conditions are imposed at vanishing momentum (which is the simplest choice) by requiring

$$\bar{Z}_{\vec{\pi}}(p = 0) = 1 \qquad \text{and} \qquad \bar{Z}_q(p = 0) = 1\,. \tag{5.12}$$

As a result all dressed quantities are RG invariant, while the bare ones are not.

Further details about the effective action (5.10), the solution of the respective flow equation (cf. (2.39)), and related technical details can be found in Section A.2.

Exploiting the freedom that the four-quark coupling $\lambda(p_1, p_2, p_3)$ can be set to zero at the ultraviolet (UV) cutoff, i.e. for $k = \Lambda_{\mathrm{UV}}$, the four-quark coupling is absent in all flow equations to be solved in the following. Previous studies in QCD, [64], have shown that the full momentum dependence of the resulting Yukawa vertex can be well approximated by a function of only one momentum upon the substitution rule

$$h(p_1, p_2) \to h\left(\sqrt{\frac{1}{4}(p_1 - p_2)^2 + (p_1 + p_2)^2}\right)\,. \tag{5.13}$$

This will be employed in most of the results presented in the next section.

It is also important to note that the quark mass function and the Yukawa coupling are related via the σ condensate,

$$m_q(p) = \frac{h(p,-p)}{\sqrt{2N_f}}\langle\sigma\rangle\,. \tag{5.14}$$

The pion decay constant f_π will in the following be calculated from the σ condensate based on an approximation provided by the Gell-Mann–Oakes–Renner relation. The accuracy of this strongly simplified way to determine the pion decay constant is sufficient for the purpose of the exploratory investigation presented here.

The initial values for the flow are chosen at the UV cutoff such that physical values for observables are achieved in the infrared $k \to 0$. This includes setting the pion decay constant to $f_\pi = 93\,\text{MeV}$, and the curvature masses to $\overline{m}_\pi = 138.7\,\text{MeV}$, $\overline{m}_\sigma = 500\,\text{MeV}$, and $\overline{m}_q = 297\,\text{MeV}$. The specific details on the precise definitions, respectively, the approximations employed for determining the masses are given in the next section. The remaining flow equations can be derived from Figure 5.5. This results in the set of equations depicted in Figure 5.6. The explicit expressions for the flow equations are deferred to Section B.8.

5.2.5. Results and discussion

We start in Section 5.2.5.1 with a discussion of the results for Euclidean momenta. The extension of the results to the real time domain for the extraction of bound state properties is discussed in Section 5.2.6.

5.2.5.1. Solution of the flow equation to Euclidean momenta

The main results of this section are the momentum dependencies of the propagators as well as the Yukawa coupling. In addition to the physical parameters outlined in Section 5.2.4 we are considering an additional parameter set where the IR has been fixed to the values of a first principle calculation of QCD correlation functions with the FRG presented in [64]. This comparison has the advantage of testing the validity of low energy effective descriptions of bound states in QCD.

The first quantity of interest from an RG point of view is the flow of the curvature masses evaluated at the flowing minimum of the effective potential, depicted in Figure 5.7. The flow of the curvature masses is a key ingredient in all diagrams because it sets the dominant scale in integrands. In the left panel the result for the Quark-Meson model with physical IR values is shown. The result is qualitatively similar to previous calculations in the Quark-Meson model, see e.g. [185, 193].

Since we are mostly interested in the description of bound states, e.g. low-energy effective degrees of freedom, the comparison to the full QCD calculation is also of particular interest, since the curvature mass determines mainly the scale in the resulting correlation functions. The comparison is depicted in the right panel of Figure 5.7 and shows that they agree quite well for small and moderate scales. This demonstrate that the QM model indeed describes the dynamics of low energy QCD correctly. However, in order to achieve the same IR values in the QM setting as in the QCD calculation the UV-cutoff of the theory has to be lowered to $\sim 360\,\text{MeV}$, see also [232]. With a higher UV- cutoff it is not possible to decrease the sigma mass further while keeping f_π, m_π and m_q fixed. This is most likely linked to the triviality of the O(N) model, which shrinks the values of achievable IR

values for a given cutoff when increasing the truncation, which has already been observed in [1, 233].

The most significant differences between the QM model and the full QCD calculation is the decoupling of the mesonic masses from the system, which can be seen from comparing both subfigures in Figure 5.7: First, the mesonic degrees of freedom decouple substantially faster in full QCD. This is also immediately visible when looking at the quark mass in Figure 5.8 or at the wave function renormalizations in figures Figure 5.9 and Figure 5.10. Second, the mass function of the scalar σ-channel in QCD does not show the dip towards smaller masses in the region where chiral symmetry is restored, which is also related to the steeper rise of the mass function in QCD. This feature has potentially important consequences for the details of chiral symmetry restoration at finite temperature that deserve further investigation. There, the low UV cutoff scale additionally results in a relatively low highest temperature that can be considered due to the the thermal range of these models, see [196]. More generally, the necessary modification of the initial effective action for large external scales such as temperature, chemical potential, external background (chromo)magnetic and (chromo)electric fields has to be considered, for a detailed discussion see [55]. Again the systematic inclusion of these modifications is facilitated within a QCD assisted low energy theory.

In all plots the red vertical line denote the UV cutoff used in our calculation. The slow decay for large momenta is not very surprising in the Quark-Meson model as there is no other scale involved which could potentially suppress the mesonic degrees of freedom. Nevertheless, it is one of the most prominent differences to the full QCD calculation, resulting in a rather small range of momenta, where the Quark-Meson model properly describes all dynamics of full QCD. However, this does not imply that the description at larger momenta is bad, merely that the question depends strongly on the observable at hand.

5.2.6. Continuation to time-like momenta

The calculation of observables requires in general the knowledge of correlation functions in Minkowski space-time, which will be discussed in more generality in Chapter 6. In functional methods this reduces to essentially two distinct options, the direct calculation via analytically continued equations or the numerical analytic continuation. While the former way is preferable, its application to the quark-meson model is postponed to future work. Here we resort to the latter option, which is for our purposes, i.e. the extraction of the pole masses of the lowest-lying bound states, quite accurate. In addition, numerical analytic continuation is easily possible for this case because the analytic structures of interest are the poles closest to the origin in their respective analytically continued retarded Greens functions, see [2] as well as references therein for a respective detailed discussion. Moreover, it has been already shown in [196] that the momentum-dependence of the mesonic propagator is rather mild which also facilitates the reconstruction of the lowest-lying pole. In summary, this allows us to use a *Padé* based approach, i.e. a rational interpolation. More specifically, we use the Schlessinger's point method [234] to compute the interpolation from a subset of data points.

The pion is the lightest degree of freedom in the Quark-Meson model and thus stable. For the sigma meson it is found in the present calculation that its pole mass slightly exceeds the two pion decay threshold. Therefore, we expect the mass to be dominated by a pole

close to the time-like axis on the second Riemann sheet of the retarded propagator and therefore accessible within this framework to good accuracy. The additional numerical error of the reconstruction is checked by computations with different numbers of grid points. The resulting masses and widths are collected in Table 5.1 and displayed relative to the curvature masses in Figure 5.11. As expected from analytic arguments the pole mass of the pion agrees well with its renormalized curvature mass [1, 196], and its decay width is zero within numerical uncertainties. As outlined above the sigma meson features in our calculation within the quark-meson model only a small decay width, $\Gamma/M \ll 1$, validating our reconstruction approach. Furthermore, the relative difference between the pole and curvature mass is significant with $\sim 35\%$. Such an order of magnitude agrees qualitatively with previous studies [1] in which the momentum dependence of the propagators was not fed back into the equations. This has obvious consequences for low energy effective theories of QCD where the mass of the sigma meson is often used to fix the free parameters.

5.2.7. Systematic improvements towards QCD

The discussion in Section 5.2.5 enables us to systematically improve the current setting towards QCD on a quantitative level. Considering the structure of Figure 5.5, or directly in the corresponding equations in Section B.8, it is immediately clear that only three quantities that are not directly derived from the effective potential enter the equations: $\bar{Z}_\phi(p)$, $\bar{Z}_q(p)$ and $\bar{h}(p,r)$. Please note that we do not need to differentiate between $\bar{Z}_\pi(p)$ and $\bar{Z}_\sigma(p)$ as their difference is negligible for all points discussed here, c.f. Figure 5.10.

While the difference in the quark wave function $\bar{Z}_q(p)$ between the quark-meson model and QCD might appear large in Figure 5.9, the values stay practically at unity for all scales and the bump in QCD at the scale of the gluon mass gap corresponds only to a subleading quantitative correction. Therefore, we can concentrate our discussion on $\bar{Z}_\phi(p)$ and $\bar{h}(p,r)$.

Turning to the pion and sigma meson wave functions, significant differences between the quark-meson and the QCD result are observed, see Figure 5.10. However, the leading diagrams that generate the momentum dependence are the same in both cases and shown in Figure 5.12. As a result, the main difference between the quark-meson and QCD results must be generated by $\bar{h}(p,r)$. In order to confirm this, we can apply the same reasoning to the leading diagrams of the Yukawa coupling in QCD shown in Figure 5.13. The first two diagrams, Figure 5.13a and Figure 5.13b, are again self-consistently contained in the quark-meson model. However, the diagram containing a gluon, Figure 5.13c, is not. It is not possible to include this diagram without the knowledge of the gluon propagator and the quark-gluon vertex building up the one gluon exchange coupling, but QCD-assisted

Particle	Curvature mass	Pole mass	Decay-width
Pion	138.7	137.4 ± 0.5	0.5 ± 0.5
Sigma	494.5	320 ± 25	36 ± 5

Table 5.1.: Curvature mass, pole mass and decay width, as extracted from the full momentum dependence of the respective propagators. A significant deviation between the pole and curvature mass of the sigma meson is observed. All values are given in MeV.

models can be constructed with this input. We conclude from this analysis that the quark-meson model can be systematically improved towards QCD by either including the QCD Yukawa coupling as external input or the gluon exchange coupling in Figure 5.13c. This underlines the strength of the current setting of systematically improvable QCD-assisted low-energy effective theories.

5.2.8. Conclusion

In this section we have outlined an approach to the calculation of bound states within the Functional Renormalisation Group. It is based on the procedure of dynamical hadronization, which comes with the great advantage that the information of bound states can be mapped to lower order n-point correlation functions in a systematic manner. Furthermore, this simplifies the procedure of building self-consistent truncations, as all correlation functions are generated from a single master equation, and external input can be incorporated without further problems. These advantages circumvent many of the problems faced when expressing the bound states exclusively in terms of their constituents.

This framework was applied to the pion and sigma mesons within a quark-meson model motivated via dynamical hadronization from QCD and solving the corresponding flow equation for Euclidean momenta. In order to test the validity of our truncation we have compared the common subset of results with a recent study of the Euclidean system in first principle QCD [64]. While we found at low energies good quantitative agreement, above scales of $\gtrsim 250\,\mathrm{MeV}$ qualitative deviations start to appear. These deviations could be traced back to missing contributions in the Yukawa coupling.

The bound state properties of the pion and the sigma meson were accessed from the Euclidean correlators via a suitable Padé approximation extracting hereby the pole masses. While the pole mass of the pion, the lowest lying excitation, agrees very well with the expectation from the Euclidean curvature mass, we found not unexpectedly a significant deviation of $\sim 35\%$ for the sigma meson.

Most importantly, the here presented approach can and will be systematically extended towards the full bound state spectrum of QCD.

6. Momentum dependencies in Minkowski space-time

So far we have discussed field dependencies in Chapter 4 and momentum dependencies in Euclidean space-time in Chapter 5. In principle the knowledge of the Euclidean elementary correlation functions is sufficient and amounts to having solved the theory at hand, see e.g. [194]. In practice, however, one usually has access to a finite number of those elementary correlation functions and in most applications to strongly correlated systems they are only known numerically. Typically this still allows for convenient and straightforward access to Euclidean observables, i.e. static, thermodynamic quantities. Additionally, the mass and properties of the lowest lying bound states can usually be extracted in a robust fashion, see e.g. Section 5.2 or e.g. [201] for a Lattice QCD perspective. The extraction of observables that are inherent to Minkowski space-time, such as transport properties or decay rates, are exponentially hard to extract from numerical elementary correlation functions in Euclidean space-time, see e.g. [195, 235]. There is essentially only one possibility to get reliable and robust access to elementary correlation functions in Minkowski space-time: extending the conceptual and computational frameworks presented so far to be able to deal with the additional challenges presented by going to real time.

Nevertheless, there are several other possibilities to get at least partial access to dynamical information of the theory

- Improve on existing reconstruction techniques. This includes, in particular, the construction of specialized reconstruction methods for specific observables. This will be explored in detail in Section 6.4 and Section 6.5.
- The use of effective field theory embeddings. Mapping the extraction of 'hard' correlation functions to much easier ones. This was already used in Section 5.2.

In this chapter we will explore the possibility of directly calculating in Minkowski space-time, as well as the construction of specialized reconstruction techniques. The latter one heavily relies on the intuition gained while performing calculations in Minkowski space-time. Both variant heavily rely on the existence of spectral representations of the underlying elementary correlations functions, which we will elaborate on in the following.

6.1. Spectral representations

This section is in parts based on [11].

In this section we want to recap some basic facts of the Källén-Lehmann spectral representation of the propagator and continue and generalize the notion thereof to general n-point functions.

In practice, spectral representations have several interpretations, depending on the current viewpoint. From a purely practical point of view, they correspond to a restriction of

the analytic structure of the corresponding elementary correlation function. To be more precise, they encode the statement that all non-analyticities are contained to certain lower dimensional hypersurfaces in the analytically continued phase-space of the Euclidean elementary correlation functions in momentum space. This originates from the demand that the time-ordered correlation function is well-defined and analytic up to its boundary. This is closely linked to locality. In particular, the axiomatic formulation of local Quantum Field Theories in terms of the Wightman axioms [236] directly demand this property via the spectral condition, for more details see e.g. [194, 237]. From a physics perspective, at least the spectral function associated to the propagator, has a very clear interpretation: encoding the spectrum of the theory. This can be see directly from an alternative derivation of the Källén-Lehmann spectral representation as the sum over energy eigenstates. The following discussion is restricted to equilibrium situations, where finite temperature is, if specified, introduced via the Matsubara formalism, cf. Section 2.5.2. The results obtained here build heavily on the work of Evans, in particular [238], as well as the preparative and complementary works [239, 240]. Other authors at the time have also looked at the issue of relating real time correlation functions with their imaginary time counterparts, see [241–254] and references therein. A similar analysis to ours has recently been performed in [255] for the three-point function .

6.1.1. Källén-Lehmann spectral representation

The spectral representation of the Euclidean propagator is given by the very well known Källén-Lehmann spectral representation [256, 257]

$$G(p) = \int_0^\infty \frac{\mathrm{d}\lambda}{2\pi} \frac{2\lambda\,\rho(\lambda)}{p^2+\lambda^2}\,. \tag{6.1}$$

In the previous sections, in particular in Chapter 2, we have already identified the full propagator as the central object in calculations with Functional Methods. This persists in Minkowski space-time. The spectral representation (6.1) can be seen as a free propagator with mass λ that is integrated with the weight $2\lambda\,\rho(\lambda)$. This gives a nice interpretation of non-perturbative loops, they correspond to perturbative loops, where all masses are free parameters and the entire expression is weighted with the spectral functions as described above.

6.1.2. Spectral representations at finite temperature

However, (6.1) is in practice in this form only applicable in vacuum. In order to generalize on this, we investigate the situation at finite temperature $T = 1/\beta$. Our starting point are the Wightman functions, where we assume the arguments to be ordered with respect to the imaginary part of the analytically continued time. In the usual fashion, we define the corresponding set

$$A_{i_1,\ldots,i_n} = \left\{ (t_{i_1},\ldots t_{i_n}) \middle| \Im(t_{i_n}) \geq \ldots \geq \Im(t_{i_1}) \geq \Im(t_{i_n} - \mathrm{i}\beta) \right\}. \tag{6.2}$$

Turning to the thermal Wightman functions, it can be shown that if they are bounded for $\{t_{i_j}\} \in A_{i_1,\ldots,i_n}$ this implies that they are also analytic within this region [258]. A more detailed discussion of this issue and the underlying assumptions can be found in [238] and references therein. From hereon we will assume that these correlation functions are indeed

analytic in this region and therefore posses a well defined Fourier transform. With this at hand, let us consider the correlation function

$$\gamma_{i_1,\dots,i_n}(t_1,\dots t_n) = \left\langle \phi_1(t_1)\dots\phi_n(t_n)\right\rangle , \tag{6.3}$$

where $(t_1,\dots,t_n) \in A_{1\dots n}$ and the fields ϕ are of arbitrary nature, i.e. bosonic or fermionic. We use the symbol γ to denote the relevant objects of interest, which are typically here either the propagator or n-point functions for $n > 2$, but the derivation holds for a much larger class of correlation functions. According to our prerequisite, the Fourier transform exists and is given by

$$\gamma_{i_1\dots i_n}(t_1,\dots t_n) = \left(\prod_{j=1}^{n}\int_{-\infty}^{\infty}\frac{\mathrm{d}\omega_j}{2\pi}e^{-\mathrm{i}\,\omega_j t_j}\right)\gamma_{i_1\dots i_n}(\omega_1,\dots,\omega_n)\,, \tag{6.4}$$

where we have state the relation directly with n fields for alter convenience. Please not that in the inverse Fourier transform the contour, i.e. the real line, of the time integration has to be infinitesimally tilted such that the structure implied by $A_{i_1,\dots,i_n}$ is respected during the integration. All spatial arguments are suppressed throughout this section as they are not of relevance and can be trivially reconstructed in the end. Being in equilibrium, we can use translational invariance to reduce the number of arguments by one

$$\gamma_{i_1\dots i_n}(\omega_1,\dots,\omega_n) = 2\pi\,\delta\Big(\sum_i^n \omega_i\Big)\,\gamma_{i_1\dots i_n}(\omega_1,\dots,\omega_{n-1})\,, \tag{6.5}$$

in a slight abuse of notation. The such defined correlation functions at finite temperature have to fulfil the Kubo-Martin-Schwinger (KMS) condition, cf. Section 2.5.2, which can be stated as

$$f_{\omega_{i_1}}\gamma_{i_1,\dots,i_n}(\omega_1,\dots,\omega_n) = \gamma_{i_2,\dots,i_n,i_1}(\omega_2,\dots,\omega_n,\omega_1)\,, \tag{6.6}$$

where we have defined $f_\omega = e^{-\beta\omega}$. Please note that the notation in (6.6) differs slightly from the notation in [238], the relative minus sign in notation for fermions is here absorbed into the γ's themselves. We are interested in the imaginary time correlation function, cf. (6.4)

$$\begin{aligned}&\gamma_{i_1,\dots,i_n}\big(\mathrm{i}(p_1)_0,\dots,\mathrm{i}(p_{n-1})_0\big)\\ =&\left(\prod_{j=1}^{n-1}\int_0^\beta \mathrm{d}\tau_j\; e^{-(p_j)_0\tau_j}\right)\left\langle \mathcal{T}\phi_{i_1}(-\mathrm{i}\tau_1)\dots\phi_{i_{n-1}}(-\mathrm{i}\tau_{n-1})\;\phi_{i_n}(0)\right\rangle\,,\end{aligned} \tag{6.7}$$

where the $(p_j)_0$ denote the zero components of the Euclidean momenta and $\mathcal{T}$ denotes time ordering in the sense of (6.2). From here one can derive spectral representations simply by demanding self-consistency, i.e. by inserting (6.4), with the use of (6.5), into (6.7) and carrying out the τ_i integrations. This yields integral relations of the form (6.1), with only the frequency appearing, where the kernel contains real time Wightman functions and factors of f_i. So far this is the main result of [238]. Here we go one step further and utilize the KMS condition (6.6) in order to remove all factors of f_i, which in turn gives the corresponding spectral functions in terms of nested commutators. These can in turn be expressed in the retarded/advanced basis again, which is in practice rather important,

since they can easily be related to the analytic continuations of the Euclidean correlation functions again, hence closing the circle of self-consistent relations.

Consequently, this procedure allows to use the entirety of the Euclidean formalism presented in the previous chapters, Chapters 2 to 5, to be used in Minkowski space-time by analytically continuing the elementary correlation functions and expressing them in terms of spectral functions.

However, it turns out that this is hard to achieve for general n-point functions, mostly because the number of possible distinct analytic continuations grows faster than the number of basis functions in the retarded/advanced basis. In fact starting from $n \geq 4$, the basis elements of the retarded/advanced basis are given as superposition of different analytic continuations. It turns out that the classification of the sub-manifolds/hyperplanes, that carry the non-analyticities in n-point functions, is an open problem. It turns out that this is an open problem that is also of interest in pure mathematics, however so far only upper and lower bounds are known. For a discussion from the current perspective see [259] and references therein. For a mathematics perspective of the problem see e.g. [260, 261] and references therein. While this hinders the construction of such representations for all n-point functions, it is not a practical problem in practice. In practice only n-point functions with small n appear, as discussed at length in the previous chapters, where the explicit construction of all analytic continuations is no problem. Therefore, we will restrict ourselves to the propagator and the three-point function for explicit constructions, where this problem does not appear at all.

6.1.2.1. Propagator

Following the prescription from above, our starting expression, where we have inserted (6.4) into (6.7) is

$$G(p_0) = \int_{-\infty}^{\infty} \frac{\mathrm{d}\lambda}{2\pi} \int_0^{\beta} \mathrm{d}\tau \, e^{\mathrm{i}\, p_0 \tau} e^{-\lambda\tau} \, \gamma_{12}(\lambda) \,, \tag{6.8}$$

where we now go back to a Euclidean argument on the LHS, as in (6.1). In (6.8) it's straightforward to carry out the τ integration

$$G(p_0) = \int_{-\infty}^{\infty} \frac{\mathrm{d}\lambda}{2\pi} \frac{1}{\lambda - \mathrm{i}p_0} \Big(1 - f_\lambda e^{\mathrm{i}p_0\beta}\Big) \gamma_{12}(\lambda) \tag{6.9}$$

.

Using that the external zero component of the momentum p_0 is not continuous, but rather discrete and restricted to the Matsubara modes, the phase factor $e^{\mathrm{i}p_0\beta} = \sigma_\pm$, which is 1 (-1) for bosons (fermions). Using the KMS condition (6.6) in order to cancel the factor f_λ, we arrive finally at

$$G(p_0) = \int_0^{\infty} \frac{\mathrm{d}\lambda}{2\pi} \frac{2\lambda\, \rho(\lambda)}{p_0^2 + \lambda^2} \,, \tag{6.10}$$

where we have symmetrized the λ integration and defined the spectral function

$$\rho(\omega) = \Big[\phi_1(\omega), \phi_2(-\omega)\Big]_\pm \,. \tag{6.11}$$

In (6.11) the index $\pm$ denotes the graded commutator, i.e. the commutator for bosons and the anti-commutator for fermions. Please note that we have suppressed the spatial momentum dependence and both, the propagator and the spectral function, depend on it. We can now use (6.10) by construction to analytically continue the Euclidean propagator to the entire complex p_0-plane. In particular, we can identify the retarded and advanced propagator as

$$\begin{aligned} G_{\mathrm{R}}(\omega) &= \lim_{\varepsilon\to 0^+} G\big(-\mathrm{i}(\omega+\mathrm{i}\varepsilon)\big) \\ G_{\mathrm{A}}(\omega) &= \lim_{\varepsilon\to 0^+} G\big(-\mathrm{i}(\omega-\mathrm{i}\varepsilon)\big)\,. \end{aligned} \tag{6.12}$$

With this at hand, we can also recover the usual relation for its easy to verify the usual relation in equilibrium $G_{\mathrm{R}}(\omega) = \Big[G_{\mathrm{A}}(\omega)\Big]^*$, where $*$ denotes complex conjugation. Additionally, we can use (6.12) combined with the spectral representation (6.10) to derive the relation between the spectral function and the analytic continuation of the Euclidean propagator

$$\rho(\omega) = G_{\mathrm{R}}(\omega) - G_{\mathrm{A}}(\omega) = 2\Im\, G_{\mathrm{R}}(\omega) = 2\,\Im\left\{\lim_{\varepsilon\to 0^+} G\big(-\mathrm{i}(\omega+\mathrm{i}\varepsilon)\big)\right\}. \tag{6.13}$$

With an obvious shorthand notation this becomes

$$\rho(\omega) = 2\,\Im\, G\big(-\mathrm{i}\,\omega + 0^+\big)\,. \tag{6.14}$$

While it might not have been entirely obvious from the discussion in this section so far, the underlying structure arising from this discussion has strong implications for the analytic structure of the analytically continued Euclidean propagator. In particular, it implies that all non-analyticities are on the line $\Re\,(p_0) = 0$. While have been rather loose language wise, some comments are appropriate at this point: The propagator in the complex domain and the spectral function are, of course, not ordinary functions, but tempered distributions. This allows, in principle, for contributions that are not usually discussed in textbooks. While they are interesting, we do not encounter any of those terms in practice in the following and will therefore not comment further on this issue here. Discussions of this issue can be found in in [262–264]. In practice the only relevant distributions appearing are H $1/x^n$, δ-functions and the Heaviside step function $\theta(x)$. For the first term the integration is defined as the Hadamard finite part, which reduces to the principle value for $n = 1$. We will comment further on this when appropriate.

6.1.2.1.1. Example: Free propagator

To close the discussion of the propagator, we want to give a minimal example, the free propagator. For a free scalar field with mass m the Euclidean propagator is given by

$$G(p) = \frac{1}{p^2 + m^2}\,. \tag{6.15}$$

Applying (6.14) we obtain the spectral function of a free boson

$$\rho(\lambda) = \frac{\pi}{\epsilon_{\boldsymbol{p}}}\Big[\delta\left(\lambda - \epsilon_{\boldsymbol{p}}\right) - \delta\left(\lambda + \epsilon_{\boldsymbol{p}}\right)\Big] \quad \text{with} \quad \epsilon_{\boldsymbol{p}} = \sqrt{\boldsymbol{p}^2 + m^2}\,, \tag{6.16}$$

where we recover the wanted anti-symmetry $\rho(\lambda) = -\rho(-\lambda)$ explicitly. This concludes our analysis of the propagator.

6.1.2.2. Three-point function

Turning to the three-point function, we can build directly upon the results presented in the beginning of Section 6.1.2 and Section 6.1.2.1. With this at hand we will not repeat the entire derivation, as it is completely analogous to the one of the propagator in Section 6.1.2.1. With this we obtain the spectral representation of the three-point function

$$\begin{aligned}\Gamma^{ijk}(p_0,q_0) = -\int_{-\infty}^{\infty}\frac{\mathrm{d}\lambda_1}{2\pi}\int_{-\infty}^{\infty}\frac{\mathrm{d}\lambda_2}{2\pi}\,\frac{1}{(\lambda_1+\lambda_2)-\mathrm{i}(p_0+q_0)}\times \\ \times\left[\frac{\rho_1^{ijk}(\lambda_1,\lambda_2)}{\lambda_1-\mathrm{i}\,p_0}+(-1)^{ij}\frac{\rho_2^{ijk}(\lambda_1,\lambda_2)}{\lambda_2-\mathrm{i}\,q_0}\right],\end{aligned} \tag{6.17}$$

which contains now two independent spectral functions. As before, we have suppressed all dependencies on spatial momenta. Before stating the relation between the spectral functions and the analytic continuations of the Euclidean three-point function, we introduce some notation for convenience. We will give the n-point functions an additional index, indicating the sign of ε when continuing the associated momentum into the complex plane according to $(p_j)_0 \to \mathrm{i}(\omega_j + \mathrm{i}\,\varepsilon_j)$. As before, the last argument is still fixed via momentum conservation, i.e. $\sum_j \omega_j = 0$ and $\sum_j \varepsilon_j = 0$. As we have discussed in the beginning of Section 6.1.2, the propagator/two-point function and the three-point function are unique in the sense that relative signs of the different ε_j already fix the limit $\varepsilon_j \to 0$. This property follow from simple combinatorics and momentum conservation and does not carry over to n-point functions with $n \geq 4$. As example, the retarded two-point function in this notation reads

$$\begin{aligned}\Gamma^{ij}_{RA}(\omega_1,\omega_2) &= \lim_{\varepsilon\to 0^+}\Gamma^{ij}\big(-\mathrm{i}(\omega_1+\mathrm{i}\,\varepsilon),-\mathrm{i}(\omega_2-\mathrm{i}\,\varepsilon)\big) \\ &= \lim_{\varepsilon\to 0^+}\Gamma^{ij}\big(-\mathrm{i}(\omega_1+\mathrm{i}\,\varepsilon)\big)\,,\end{aligned} \tag{6.18}$$

where we have made the last argument explicit again for demonstration. In the same notation, we have e.g.

$$\Gamma^{ijk}_{RRA}(\omega_1,\omega_2,\omega_2) = \lim_{\varepsilon\to 0^+}\Gamma^{ijk}\big(-\mathrm{i}(\omega_1+\mathrm{i}\,\varepsilon),-\mathrm{i}(\omega_2+\mathrm{i}\,\varepsilon),-\mathrm{i}(\omega_3-\mathrm{i}\,2\varepsilon)\big) \tag{6.19}$$

$$= \lim_{\varepsilon\to 0^+}\Gamma^{ijk}\big(-\mathrm{i}(\omega_1+\mathrm{i}\,\varepsilon),-\mathrm{i}(\omega_2+\mathrm{i}\,\varepsilon)\big)\,. \tag{6.20}$$

Please note that for $n \geq 4$ the right-hand side of these expressions is a superposition of different analytic continuations. The n-point functions in the retarded/advanced basis have some properties that we would like to state for completeness. Denoting $\bar{R} = A$ and $\bar{A} = R$ we have

$$\Gamma^{i_1\ldots i_n}_{\alpha_1\ldots\alpha_n}(\omega_1,\ldots,\omega_n) = \Big[\Gamma^{i_1\ldots i_n}_{\bar{\alpha}_1\ldots\bar{\alpha}_n}(\omega_1,\ldots,\omega_n)\Big]^*\,, \tag{6.21}$$

i.e. swapping all the retardedness/advancedness of all legs amounts to complex conjugation. This amounts to swapping the signs of all epsilons. Another property that follows trivially from momentum conservation is

$$\Gamma^{i_1\ldots i_n}_{\alpha\ldots\alpha}(\omega_1,\ldots,\omega_n) = 0\,, \tag{6.22}$$

the retardedness/advancedness cannot be the same on every leg without trivializing the n-point function. The associated properties of the propagator follow trivially from those

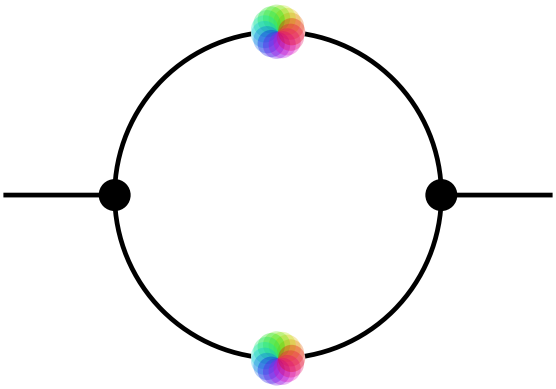

Figure 6.1.: Polarization diagram with full propagators and classical vertices. For convenience we adopted the diagrammatic notion used in Dyson-Schwinger equations throughout this work, cf. Figure 2.1.

of the two-point function. With this at hand, we can state the relation between the retarded-advanced three-point functions and the spectral functions implicitly defined in (6.17)

$$\begin{aligned}\rho_1^{ijk}(\lambda_1,\lambda_2) &= 2\,\Re\left(\Gamma^{ijk}_{ARA}(\lambda_1,\lambda_2)+\Gamma^{ijk}_{AAR}(\lambda_1,\lambda_2)\right)\\ \rho_2^{ijk}(\lambda_1,\lambda_2) &= 2\,\Re\left(\Gamma^{ijk}_{RAA}(\lambda_1,\lambda_2)+\Gamma^{ijk}_{AAR}(\lambda_1,\lambda_2)\right).\end{aligned} \tag{6.23}$$

From (6.23) we can also see, that the spectral function degenerate for identical fields, but the order of the first two arguments is swapped. With this we conclude our discussion of spectral representations, results similar to the one presented in this section for higher n-point functions will be reported elsewhere.

6.1.3. Using spectral representations in Functional Methods

We want to give a short, standard example, how spectral representations are used in practice in order to calculate non-perturbative diagrams. In particular, how we can use the purely Euclidean framework of Chapter 2 to gain access to real time elementary correlation functions via analytic continuation. To this end, we consider a polarization diagram with classical vertices, as it may appear in a skeleton expansion or a DSE with a specific truncation for example. The diagram in question is shown in Figure 6.1. Taking a regularization scheme that only acts on the spatial part and setting the classical vertex to one, the diagram reads

$$\begin{aligned}\mathcal{D}^{\text{pol}}(T;p_0,\boldsymbol{p}) &= \sum\!\!\!\!\!\!\int_{\{T,q\}} G(q)G(p+q)\\ &= \sum\!\!\!\!\!\!\int_{\{T,q\}} \frac{1}{(2\pi)^2}\int_{\lambda_1,\lambda_2\geq 0}\frac{2\lambda_1\,\rho\,(\lambda_1,\boldsymbol{q})}{q_0^2+\lambda_1^2}+\frac{2\lambda_2\,\rho\,(\lambda_2,\boldsymbol{p}+\boldsymbol{q})}{(p_0+q_0)^2+\lambda_2^2}\,.\end{aligned} \tag{6.24}$$

Assuming we have a well defined regularization and renormalization scheme implied, we can swap the order of integration in (6.24). If we would in addition assume that the spectral function at hand is only a function of $p^2 = p_0^2 + \boldsymbol{p}^2$ we could express the diagram as a purely weighted perturbative diagram. However, we won't make this assumption here, as we do not aim at calculating the spatial momentum integral anyway

$$\begin{aligned}\mathcal{D}^{\text{pol}}(T; p_0, \boldsymbol{p}) = \int_{\lambda_1,\lambda_2\geq 0} \frac{4\lambda_1\lambda_2}{(2\pi)^2} \int \frac{\mathrm{d}^{d-1}\boldsymbol{p}}{(2\pi)^{d-1}} \rho(\lambda_1, \boldsymbol{q})\, \rho(\lambda_2, \boldsymbol{p}+\boldsymbol{q}) \times \\ \times\, T \sum_{\{q_0\}} \frac{1}{q_0^2 + \lambda_1^2} \frac{1}{(p_0+q_0)^2 + \lambda_2^2}\,.\end{aligned} \tag{6.25}$$

Using standard techniques, cf. Section B.4 the sum is easily calculated and expressed in terms of bosonic occupation numbers with a simple interpretation

$$\begin{aligned}\mathcal{D}^{\text{pol}}(T; p_0, \boldsymbol{p}) = \int_{\lambda_1,\lambda_2\geq 0} \frac{4\lambda_1\lambda_2}{(2\pi)^2} \int \frac{\mathrm{d}^{d-1}\boldsymbol{p}}{(2\pi)^{d-1}} \rho(\lambda_1, \boldsymbol{q})\, \rho(\lambda_2, \boldsymbol{p}+\boldsymbol{q}) \times \\ \times \Bigg\{ -\frac{1+2\,n_{\text{B}}(T;-\lambda_1)}{4\lambda_1\left((p_0+\mathrm{i}\lambda_1)^2+\lambda_2^2\right)} + \frac{1+2\,n_{\text{B}}(T;\lambda_1)}{4\lambda_1\left((p_0-\mathrm{i}\lambda_1)^2+\lambda_2^2\right)} \\ -\frac{1+2\,n_{\text{B}}(T;-\lambda_2-\mathrm{i}p_0)}{4\lambda_2\left((p_0-\mathrm{i}\lambda_2)^2+\lambda_1^2\right)} + \frac{1+2\,n_{\text{B}}(T;\lambda_2-\mathrm{i}p_0)}{4\lambda_2\left((p_0+\mathrm{i}\lambda_2)^2+\lambda_1^2\right)} \Bigg\}.\end{aligned} \tag{6.26}$$

In the above expression, we are still left with the problem of analytically continuing the diagram to $p_0 \in \mathbb{C}$. Carrying out the Matsubara sum analytically, lets us choice the correct analytic continuation quite easily, because we have the result analytic in p_0. As briefly touched in Section 5.1, the correct analytic continuation is obtained here by dropping the factors of $\mathrm{i}p_0$ from the bosonic occupation numbers. It can be shown, by demanding exactly the properties of the previous section, Section 6.1.2, that this analytic continuation is unique [265]. The resulting expression is than valid in the entire complex p_0 plane. Using the identity $1+2\,n_{\text{B}}(T;-z) = -\left(1+2\,n_{\text{B}}(T;z)\right)$ we can simplify the expression above and arrive at

$$\begin{aligned}\mathcal{D}^{\text{pol}}(T; p_0, \boldsymbol{p}) = \int_{\lambda_1,\lambda_2\geq 0} \frac{4\lambda_1\lambda_2}{(2\pi)^2} \int \frac{\mathrm{d}^{d-1}\boldsymbol{p}}{(2\pi)^{d-1}} \rho(\lambda_1, \boldsymbol{q})\, \rho(\lambda_2, \boldsymbol{p}+\boldsymbol{q}) \times \\ \times \Bigg\{ \frac{\left[p_0^2 - \left(\lambda_1^2-\lambda_2^2\right)\right]\left[1+2\,n_{\text{B}}(T;\lambda_1)\right]}{2\lambda_1\left(-\mathrm{i}p_0+\lambda_1-\lambda_2\right)\left(\mathrm{i}p_0+\lambda_1-\lambda_2\right)\left(-\mathrm{i}p_0+\lambda_1+\lambda_2\right)\left(\mathrm{i}p_0+\lambda_1+\lambda_2\right)} \\ + \frac{\left[p_0^2 + \left(\lambda_1^2-\lambda_2^2\right)\right]\left[1+2\,n_{\text{B}}(T;\lambda_2)\right]}{2\lambda_2\left(-\mathrm{i}p_0+\lambda_1-\lambda_2\right)\left(\mathrm{i}p_0+\lambda_1-\lambda_2\right)\left(-\mathrm{i}p_0+\lambda_1+\lambda_2\right)\left(\mathrm{i}p_0+\lambda_1+\lambda_2\right)} \Bigg\}.\end{aligned} \tag{6.27}$$

Please note that the expressions appears longer, as we have performed a partial fraction decomposition in all terms, this is usually very useful when working with diagrammatic expression. From (6.27) quite a bit of physics, that can be extracted from the polarization diagram, is already visible. In order to extract the self-energy, we have to continue the result (6.27) to Minkowski space-time. In particular, at the one-loop level, (6.27), gives the sole contribution to the imaginary part of the retarded self-energy. Thresholds, i.e.

scattering processes, require a non vanishing imaginary part. The onset of such thresholds is related to the poles of (6.27) as we will see later. Looking at the contribution from mass poles, i.e. δ-function contributions from the spectral functions, we can immediately integrate the frequencies λ_1 and λ_2 and find that $\omega \geq 2m$ gives the only naive threshold at vanishing spatial momentum, where $p_0 \to -\mathrm{i}\,\omega + 0^+$. In vacuum this turns out to be true. However, at finite temperature, additional regions in phase space, i.e. with $|\omega| \leq |\boldsymbol{p}|$. This turns out to be the transport peak, which will dominate long range physics, i.e. transport coefficients. If we assume the two masses to be different, one finds additional regions with support, at $\boldsymbol{p} = 0$, i.e. $0 \leq |\omega| \leq |m_2 - m_1|$. This decay channel in turn induces damping and will be discussed in more detail later.

6.2. $O(N)$-theory at finite temperature

This section is in parts based on [1].

Having discussed the theoretical prerequisites of calculating elementary correlation functions in Minkowski space-time, we can now have a second look at the setting presented in Section 5.1. However, we won't quite follow the full procedure detailed in Section 6.1, but rather use a purely numerical approach. This is because one of the main motivations for the work here was, as described in Section 5.1, the use of a Lorentz invariance preserving regulator. However, this would require a spectral representation for the regulated propagator and to this date no sufficiently fast decaying regulator is know that perseveres the analytic structure induced by (6.10). As briefly described in Section 5.1, we calculate the Matsubara sum numerically and correct the error one makes in the occupation numbers by weighting the contour integrals appropriate, cf. Section B.4 and Section 6.1.3.

Staying within the notation of Section 5.1, we choose to drop the usual normalization of the spectral function and opt for an RG invariant combination instead, i.e.

$$\hat{\rho} = Z(0)\rho\,. \tag{6.28}$$

This choice is of course purely for technical convenience and can be undone at any step. Additional details on technical prerequisites and numerical details are contained in Section B.7. In the remainder of this section we will discuss the result of the spectral functions obtained in such a setting.

6.2.1. Results

6.2.1.1. Spectral functions at vanishing external momentum

Here we show the temperature dependence of the pion and sigma spectral function in the LPA'+Y approximation. The spectral functions feature several district structures with a clear physical interpretation, see e.g. [220] for a detailed discussion of the different processes in the Quark–Meson model. In general there are two different cut structures at finite temperature and vanishing external momentum in the propagator continued to the complex plane. The unitarity cut spans from the multi-particle decay threshold to infinity, i.e. $\omega \in [\mu_{\text{thresh}}, \infty)$, which is present in any interacting theory. Furthermore, the Landau cut is present at smaller frequencies, which is purely medium dependent and gives rise to inverse scattering processes [266] with the heat bath. These scattering processes give rise to Landau damping, hence the name. Finally, delta functions represent stable particles. Our result for the spectral functions at vanishing external momentum in the

LPA and LPA'+Y truncation are depicted in Figure 6.2. For the sigma meson there are two different processes available, i.e. $\sigma^* \to \pi + \pi$ and $\sigma^* \to \sigma + \sigma$ and no Landau cut structure. While for the pion we have $\pi^* \to \pi + \sigma$ for the Unitarity cut and $\pi^* + \pi \to \sigma$ for the Landau cut. While it might seem that the Landau cut vanishes for very small frequencies, we would like to remark that a finite value is possible. However, it will be exponentially suppressed since the contributions are proportional to occupation numbers. Additionally, Figure 6.2 suggest that the Landau cut only has support up to a finite

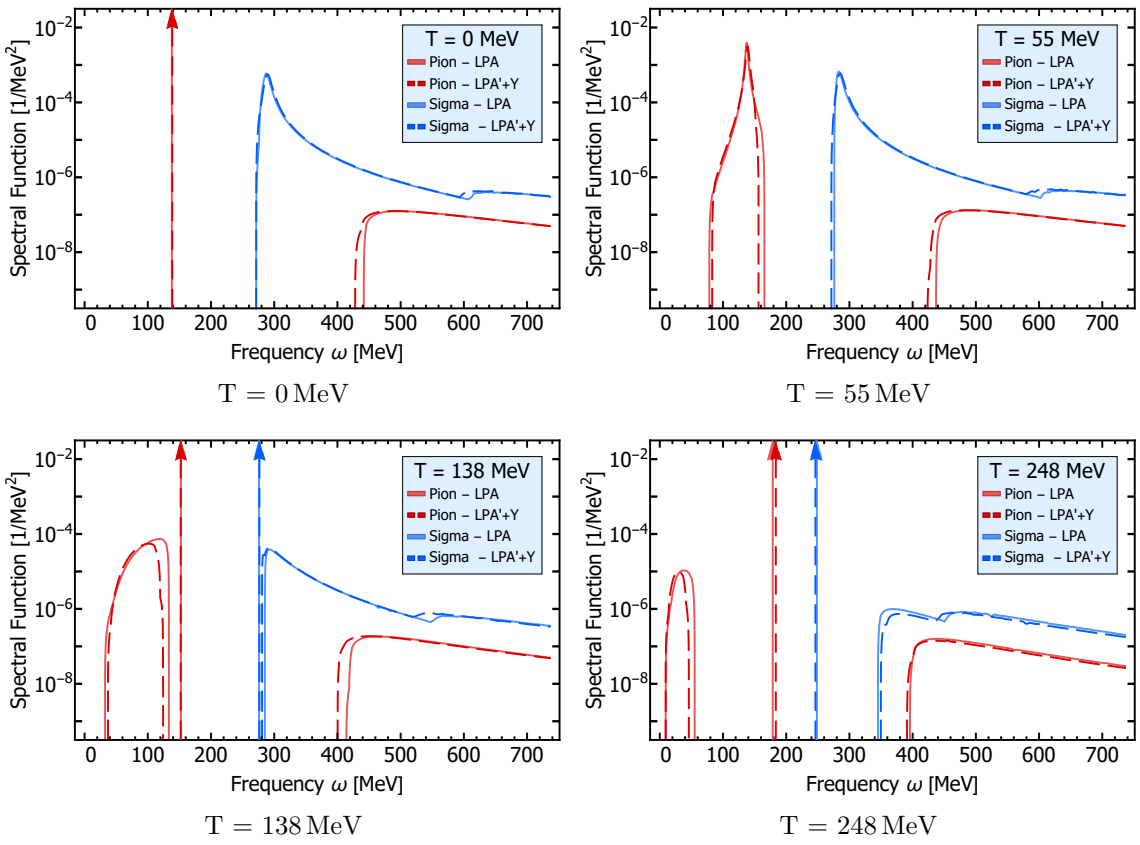

Figure 6.2.: Spectral functions at vanishing three momentum for different temperatures comparing LPA to LPA'+Y.

frequency and vanishes below. At vanishing temperature we have the expected stable pion and no stable sigma particle. At finite temperature the sigma meson emerges as stable particle as O(4)-symmetry gets restored. The presence of stable particles at finite temperatures is an artefact of the current truncation.

The difference between the two truncation is most prominently seen at multiple particle decay thresholds, which involve a sigma meson demonstrating the effect of the wave-function renormalization, shown in Figure 5.3b, on the curvature mass, as in both truncations the proper pole mass is not coupled back into the system. A problem that is numerically not traceable in the current formalism, c.f. discussion in Section B.7. The cut structure of propagators is best seen in the imaginary part of the two-point function, $\Im\Gamma^{(2)}(\omega)$, since a finite value translates directly into a cut of the propagator, the result is shown in Figure 6.3. The finite part at small frequencies, that vanishes for larger temperatures, in the pion shows again the Landau cut. For larger frequencies the unitarity cut shows clear decay thresholds, i.e. in the sigma meson the different thresholds and their degeneracy for high temperatures can be seen nicely.

Our results compare qualitatively well to the results obtained using a spatially flat regulator, c.f. the discussion in Section B.6, in the Quark-Meson model [165, 166, 222, 223].

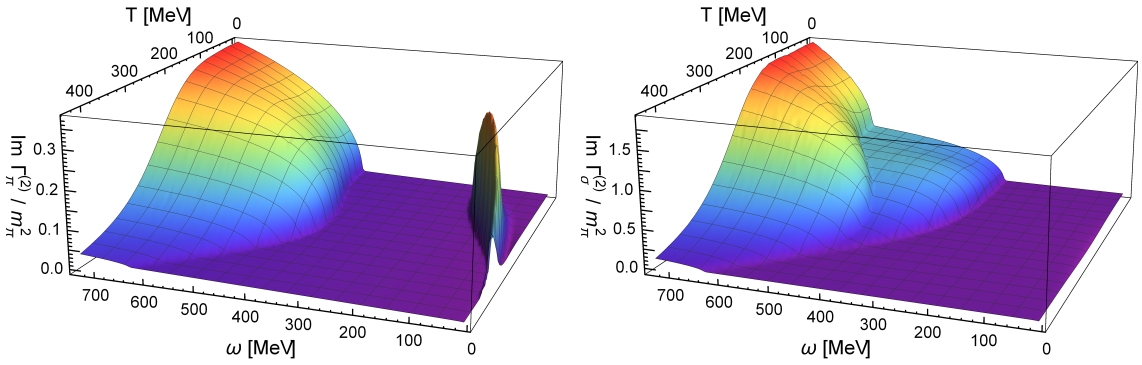

Figure 6.3.: Cut structure of the propagators in the frequency-temperature plane.

6.2.1.2. Pole, screening & curvature masses

It is interesting to compare the real time pole and screening masses with the Euclidean curvature mass, for a detailed discussion of the respective definitions in the present FRG context see e.g. [196]. The curvature mass is typically used in Euclidean computations within low energy effective field theories for QCD. There, the physical pion and sigma masses are input parameters and are identified with the respective curvature masses. However, they have to be identified with the pole mass, and hence we have to check how well such an identification works.

In the case of a stable particle, the position of the pole can be directly extracted from the spectral function. For particles with a finite decay width this is not possible, since the pole leaves the physical sheet of the complex p_0-plane and is found on the second Riemann sheet, i.e. the analytically continued retarded propagator.

On the other hand the pole mass $m_{\text{pole}} = 1/\xi_{\text{t}}$ is the inverse temporal screening length, which can be extracted from the Euclidean propagator

$$\lim_{t\to\infty} G(t,0) \propto e^{-t/\xi_t} \,. \tag{6.29}$$

Furthermore the screening mass is $m_{\text{screen}} = 1/\xi_{\text{spat}}$, that is the inverse spatial screening length,

$$\lim_{|\vec{x}|\to\infty} G(0,\vec{x}) \propto e^{-|\vec{x}|/\xi_{\text{spat}}} \,, \tag{6.30}$$

and the curvature mass is

$$m^2_{\text{cur}} = \lim_{\vec{p}\to 0} \frac{\Gamma_E^{(2)}(0,\vec{p})}{Z(0,\vec{p})} \,. \tag{6.31}$$

Note that the wave function renormalization Z in (6.31) ensures the RG-invariance of the latter. As discussed in Section 5.1.2, the limit in (6.31) is understood in the static sense.

We can now use (6.31) together with the spectral representation of the Euclidean propagator

$$Z(0,0)G_E(p_0,\vec{p}) = \int_{\mathbb{R}} \mathrm{d}\eta \; \frac{\rho(\eta,\vec{p})}{\eta + \mathrm{i}p_0} \tag{6.32}$$

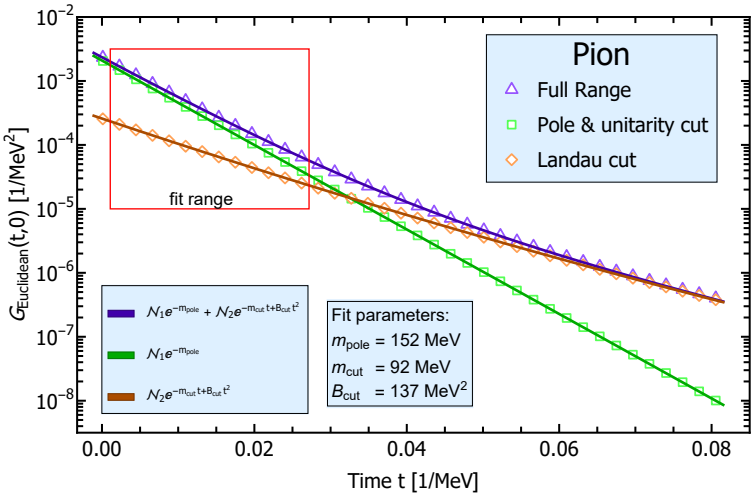

Figure 6.4.: Fourier transform of the pion propagator.

to derive a relation between the curvature mass and the spectral representation

$$m_{\rm cur}^2 = \frac{\int \frac{\mathrm{d}\eta}{\eta}\hat{\rho}(\eta,0)}{\int \frac{\mathrm{d}\eta}{\eta}\frac{1}{\eta^2}\hat{\rho}(\eta,0)}\,, \tag{6.33}$$

with the normalised spectral function (6.28). In case a stable particle is present, the spectral function can be split in two positive parts as follows,

$$\begin{aligned}\hat{\rho} &= \hat{\rho}_{\rm pole} + \hat{\rho}_{\rm cut}\\ \hat{\rho}_{\rm pole} &= \mathrm{sgn}(\omega) Z_{\rm pole}\delta(p^2 - m_{\rm pole}^2)\,.\end{aligned} \tag{6.34}$$

The normalisation of the pole is smaller than one: $Z_{\rm pole} = 1 - \int d\omega^2 \hat{\rho}_{\rm cut} < 1$ which follows from the normalisation of the spectral function and the positivity of $\rho_{\rm cut}$. Using this split in (6.32) we arrive at

$$m_{\rm cur}^2 = m_{\rm pole}^2 \frac{Z_{\rm pole} + m_{\rm pole}^2 \int \frac{\mathrm{d}\eta}{\eta}\rho_{\rm cut}(\eta,0)}{Z_{\rm pole} + m_{\rm pole}^4 \int \frac{\mathrm{d}\eta}{\eta}\frac{1}{\eta^2}\rho_{\rm cut}(\eta,0)}\,, \tag{6.35}$$

Equation (6.35) entails the information when the difference between pole and curvature masses grows large: Firstly, decreasing $Z_{\rm pole}$ increases the importance of the cut-part and hence the difference between curvature and pole mass grows. Secondly, if the spectral weight of $\rho_{\rm cut}$ is taken at smaller spectral values, the integrals in (6.35) grow and hence the difference between curvature and pole mass grows.

Translated back to Euclidean space-time, both processes lead to strong frequency and momentum dependences in the Euclidean propagator. In turn, if the pole term dominates the full spectral function, the full Euclidean propagator is well described by a propagator with a constant wave function renormalization, depicted in Figure 5.3b. A similar conclusion was also drawn in [196, 267], where the relation between pole and curvature mass has also been investigated.

A very good estimate for the pole mass can be obtained from a Padé approximant of the propagator around the zero crossing of the real part of $\Gamma^{(2)}$, if the pole is sufficiently close

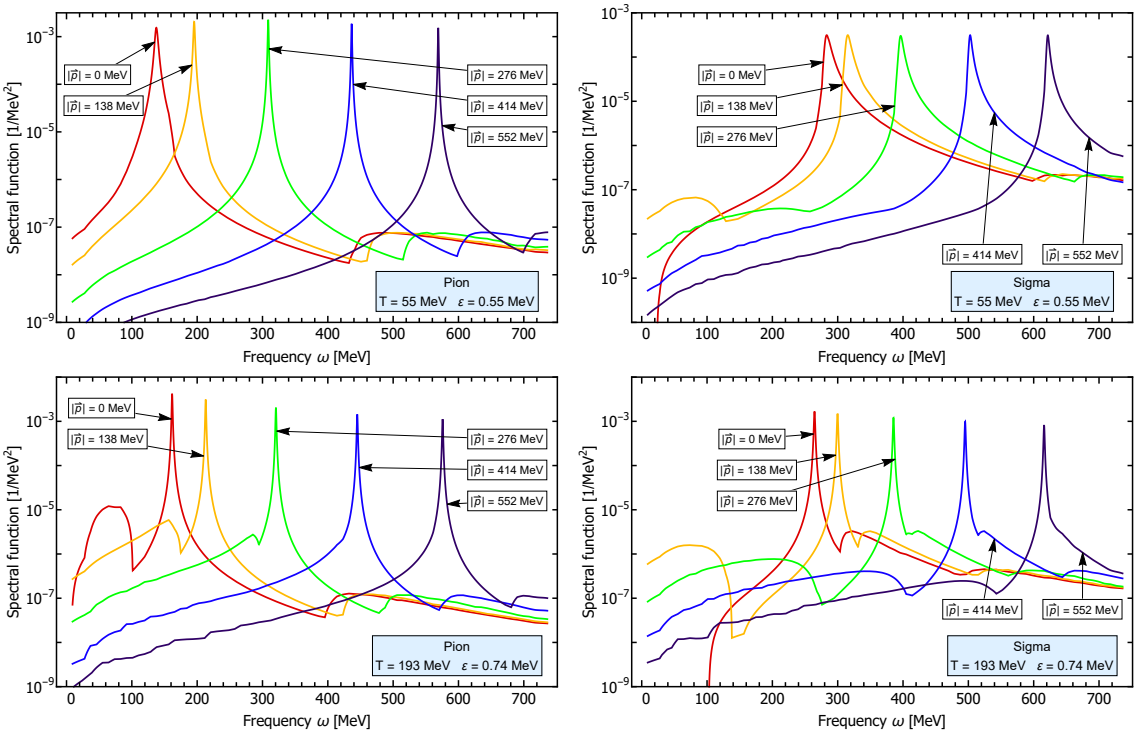

Figure 6.5.: Spectral functions at finite external momenta for different temperatures across the phase transition.

to the Minkowski axis. This is certainly the case for the spectral functions depicted in Figure 6.2. Our result for the different masses is shown together with the order parameter $\langle\sigma\rangle$ in Figure 5.1. The order parameter shows a gentle decrease across the phase transition, signalling an extremely broad crossover, cf. the discussion in Section 5.1.2.

For low temperatures the masses stay roughly constant until the temperature scale get of the order of the lowest mass scale $2\pi T \approx m_\pi$. In the intermediate regime the temperature fluctuations become large enough to trigger the phase transition. The mass of the sigma meson can then also be used as an order parameter, see e.g. [185], and exhibits a clear minimum at the crossover. With an increasing temperature all masses degenerate as they acquire a dominant thermal mass component $\sim T^2$ and the theory becomes effectively trivial.

The more interesting case is the sigma, as its spectral function has no clear mass pole for low temperatures. The pole mass of the sigma mesons behaves more gentle across the phase transition in comparison to the curvature mass, but still exhibits a clear minimum at the cross over. The larger mismatch between the two masses can again be explained by the significantly stronger momentum dependence of the sigma meson at small and medium temperatures compared to the pion, c.f. Figure 5.3a. In general the qualitative strength of the mass difference can already be obtained from the temperature dependence of the constant wave function renormalizations since $Z_k(0, |\vec{p}|) \approx Z_k(0, k)$. Furthermore, we can

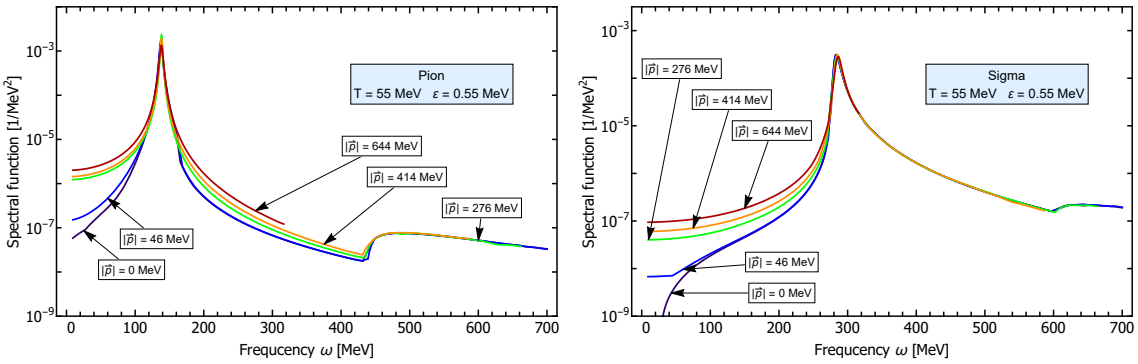

Figure 6.6.: Lorentz invariance of the spectral functions, $\rho(\sqrt{\omega^2+\vec{p}^2},\vec{p})$, at a small temperature.

use (6.29) in order to extract the pole mass from the two-point function. Combining the spectral representation (6.32) with (6.29) we obtain

$$G_E(t,\vec{p}) = \frac{1}{Z(0,0)}\int_0^\infty \mathrm{d}\eta\; e^{-\eta t}\rho(\eta,\vec{p})\,, \tag{6.36}$$

i.e. the Fourier transformed propagator, which reduces to a calculation of a Laplace transform. In the case of a mass pole we are able to extract the correct pole mass from (6.36) again, an example for the pion at a temperature 138 MeV is shown in Figure 6.4. Equation (6.36) allows us to calculate the contributions from different structures in the spectral function individually, i.e. we find the expected exponential decay (6.29) from the mass pole and empirically the contribution from the Landau cut is very well described by additionally introducing a quadratic time dependence in the exponent. Furthermore, their sum is already sufficient to describe the full time dependence at reasonable times, for extremely large times the behaviour is trivially dominated by the necessary numerical cut $\eta_{\min}$. Unfortunately we were unable to extend this definition of the pole mass to the regime without a pole mass in the spectral function, due to a combination of a lack of the functional form of the Landau cut and numerical uncertainties.

6.2.1.3. Spectral functions at finite external momentum

Since there is only a very small difference between LPA and LPA'+Y in our current settings, the results with finite external momentum are calculated in LPA due to reduced numerical cost, due to which we also refrained from extrapolating our results to $\varepsilon \to 0$. The results are depicted in Figure 6.5 for various temperatures and external momenta. The main differences between spectral functions at vanishing and finite external momentum is the uniform Lorentz boost of the mass pole and the unitarity cut, as well as the transport peak, at frequencies $\omega < |\vec{p}|$, arising from space-like scattering processes at finite temperature and momenta with the heat bath, a detailed discussions about the involved kinematics can be found in [220]. Furthermore the transport peak is, like the Landau cut, not Lorentz invariant as it couples directly to the heat bath.

6.2.1.3.1. Lorentz invariance

A non-trivial consistency check of our results at finite external momenta is obtained by

looking at the Lorentz invariance at a vanishing (or small) temperature. A Lorentz invariant function must only depend on $p^2 = \omega^2 - \vec{p}^2$, i.e. for the spectral function this translates to the property that $\rho(\sqrt{\omega^2 + \vec{p}^2}, \vec{p})$ must be independent of $\vec{p}$. Our results for the spectral functions at finite external momenta are depicted for this momentum configuration in Figure 6.6 at a small temperature. The most notably breaking of Lorentz invariance is introduced by the finite value of the small parameter ε, but we also do not expect invariance for these parts of the spectral function. Additional breaking, relative to the fixed heat bath, is visible for small frequencies in the sigma spectral function and for frequencies around the mass pole in the pion spectral function due to the small temperature present, c.f. the discussion in Section 6.2.1.1 and Section 6.2.1.3. The remaining parts of the spectral functions, i.e. the position of the pole, the thresholds and the continuum part, show perfect Lorentz invariance.

This is in contrast to most previous studies of spectral functions within the FRG where a regulator of the form (B.40) was used, and therefore Lorentz invariance explicitly broken [219, 220], and demonstrates one of the strengths of our approach.

6.2.2. Conclusion

In this section we put forward a direct calculation of finite temperature spectral functions within the FRG in the $O(N)$-model. This direct computation is based on a $O(4)$/Lorentz-invariant regularisation scheme, and can be performed on a fully numerical level. i.e. including the full momentum- and frequency dependence of correlation functions. It demonstrates the applicability of the formalism put forward in [197] at finite temperatures.

The spectral functions for the pion and sigma meson are shown across the phase transition as a function of frequency and momentum. The four expected structures in the spectral functions, i.e. the mass pole, unitarity cut, Landau cut and transport peak, are present and discussed in detail.

The spectra obtained allowed us to investigate the important relation between the curvature and the pole mass. We found that the definition of the pole mass as inverse temporal length is accessible within our framework, but unsuitable if particles are unstable and a pole is unidentifiable in the spectrum. An analytic relation between the pole and curvature mass was derived in the case of a stable particle and qualitatively verified that the difference is driven by non trivial momentum dependencies.

Furthermore, we have explicitly verified the Lorentz invariance of the spectral function. Another major advantage of the employed framework is its numerical accessibility, which makes it easily usable in more complex theories. However, we also found that the purely numerical approach put forward here is numerically not manageable for large systems. This can be overcome by embracing the underlying analytic structure fully, and work on the level of the spectral functions themselves. This will be presented in the following sections.

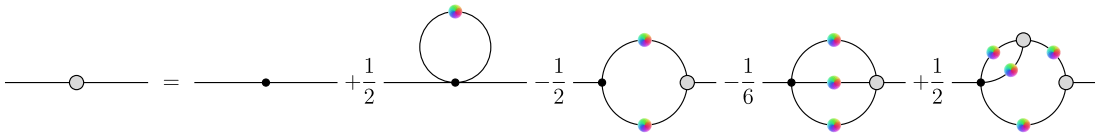

Figure 6.7.: Diagrammatic representation of the DSE for the two-point function, cf. Figure 2.3.

6.3. Dimensional regularization in Functional Methods via spectral representations

This section is in parts based on [12].

In this section we fully utilize the structure connecting Euclidean and Minkowski space-time discussed in Section 6.1. We investigate a ϕ^4-theory in $d = 3$ space-time dimensions with the DSE in a vertex expansion. We truncate the vertex expansion at $N = 2$, i.e. we keep the full two-point function only, cf. Section 2.3.2. The truncation is closed by setting the three-point and four-point function to their classical values

$$\Gamma^{(n\geq 3)} = S^{(n)} \,. \tag{6.37}$$

These are simple to extract from the classical action, which takes in the current context the form

$$S[\phi] = \int_x \frac{1}{2} \left(\partial_\mu \phi\right)^2 + \frac{m_0^2}{2}\phi^2 + \frac{\lambda_0}{4!}\phi^4 \,. \tag{6.38}$$

Having only the two-point function as a dynamic quantity, we obtain the relevant equation to solve by simply taking two derivatives of the master DSE (2.71). The resulting equations is explicitly given in Section 2.2 and shown in Figure 6.7. The basic outline of the calculation is already given in Section 6.1.3, with the only difference that we will work in vacuum here. To be more precise, this means we do not gain anything from splitting the momentum dependence in p_0 and $\boldsymbol{p}$, but rather stay with the Lorentz invariant p^2. Therefore, we will not only move the p_0 integration into the spectral integrals, but also the spatial integration, cf. Section 6.1.3. Subsequently, the inner momentum integration is equivalent to a perturbative loop. Hence, it becomes practically possible to use dimensional regularization, a highly desirable regularization scheme. The motivation for the use of dimensional regularization is of course the trivialization of the right-hand side of the mSTIs discussed in Section 3.4.4. We will give a fully worked out diagram explicitly later in this section. As a consequence we will work with the appropriate spectral representation of the propagator, the Källén-Lehmann spectral representation (6.1). Before getting

into the actual calculation, lets us reiterate a few more things about spectral functions, that are of importance here. The first concerns a splitting of the spectral function into different terms that can arise, i.e. splitting into mass poles (δ-functions) and continuous contributions

$$\rho(\omega) = \sum_i \frac{R_i}{2\omega} \delta\left(\omega - m_i\right) + \tilde{\rho}(\omega) \,, \tag{6.39}$$

where m_i denotes the position of possible mass poles and $\tilde{\rho}$ the continuous contribution, i.e. the cuts of the propagator. The second concerns the sum rule at hand for the spectral function, i.e. its normalization

$$\int_{\mathbb{R}} \frac{\mathrm{d}\lambda}{2\pi} 2\lambda\, \rho(\lambda) = 1\,. \tag{6.40}$$

Another advantage of the renormalization scheme employed here is that (6.40) preserved during the calculation. This has the advantage that certain prefactors are fixed by the normalization and do not have to be calculated explicitly.

6.3.1. Renormalization

The use of dimensional regularization allows, in principle, also naively for the straightforward application of the usually enforced perturbative renormalization conditions. However, while doing so we have to deal with a subtlety one might miss initially. In order to swap the order of integration, we require that the entire integration, over frequencies of the spectral functions and loop momenta, is fundamentally finite. This requires, of course, that the full divergence of the diagram is subtracted, and not only the one appearing directly in the momentum integration over the perturbative kernel. Working in $d - 2\varepsilon$ space-time dimensions, if one neglects this, the momentum integration might be finite, but the spectral integration afterwards might not have a finite $\varepsilon \to 0$ limit. Practically, this is achieved by introducing counter terms such that the leading and subleading term in an expansion in p^2 around the renormalization scale μ^2 in the remaining integrand of the spectral integration is subtracted, after discarding the usual $1/\varepsilon$ term. In order to show the procedure explicitly, let us consider the polarization diagram, the second loop from the left in Figure 6.7. Please note that a similar route to regularizing diagrams in the DSE has been taken in [268], where a system was chose that allows for fully analytic calculations.

6.3.1.1. Example: Polarization diagram

Here we make the aforedescribed procedure explicit at the example of the polarization diagram, which is e.g. divergent in $d = 4$. Note however, that the procedure works in arbitrary space-time dimension and only effects the renormalization and the perturbative kernel. The polarization diagram reads

$$\mathcal{D}^{\mathrm{pol}}(\mu; p) = -\frac{1}{2} \int_{\dim(\mu)} \frac{\mathrm{d}^d q}{(2\pi)^d}\, \Gamma^{(3)}(-p, -q) G(q) G(p+q) \Gamma^{(3)}(-q, -p)\,, \tag{6.41}$$

where the subscript $\dim(\mu)$, denotes that the integral is understood in the sense of dimensional regularization, as described above, with renormalization scale μ. Denoting the classical three-point function as g, the diagram reads after inserting spectral representations

in our truncation

$$\begin{aligned}\mathcal{D}^{\text{pol}}(\mu;p) &= -\frac{g^2}{2}\int_{\dim(\mu)}\frac{\mathrm{d}^d q}{(2\pi)^d}\int_{\{\lambda_i\}}\frac{2\lambda_1\,\rho(\lambda_1)}{q^2+\lambda_1^2}\frac{2\lambda_2\,\rho(\lambda_2)}{(p+q)^2+\lambda_2^2}\\ &\equiv \int_{\{\lambda_i\}} 4\lambda_1\lambda_2\,\rho(\lambda_1)\rho(\lambda_2)F(p^2;\lambda_1,\lambda_2;\mu)\end{aligned} \tag{6.42}$$

$$F(p^2;\lambda_1,\lambda_2;\mu) = -\frac{g^2}{2}\int_{\dim(\mu)}\frac{\mathrm{d}^d q}{(2\pi)^d}\frac{1}{q^2+\lambda_1^2}\frac{1}{(p+q)^2+\lambda_2^2}\,.$$

In (6.42) we have introduced the additional shorthand notation

$$\int_{\{\lambda_i\}} = \prod_{j\in\{i\}}\int_0^\infty \frac{\mathrm{d}\lambda_j}{2\pi}\,, \tag{6.43}$$

which is understood as the integral over all appearing frequency parameters, i.e. $\{i\} = \{1,2\}$ in the current context. The function $F(p^2;\lambda_1,\lambda_2;\mu)$ is the perturbative polarization diagram, where the two appearing scalar propagators now have different masses λ_1 and λ_2. In order to impose renormalization conditions we introduce parameterizations for the full and classical two-point function

$$\begin{aligned}S(2)(p) = \Gamma^{(2)}_\Lambda(p) &= Z_0(\mu)\left(p^2+m_0^2(\mu)\right)\\ \Gamma^{(2)}(p) &= Z(p)\left(p^2+m^2(p)\right)\,,\end{aligned} \tag{6.44}$$

where we have the usual bare/renormalized wave function renormalization and mass. As renormalization condition we choose

$$\begin{aligned}\Gamma^{(2)}(p=\mu) &= \mu^2+m^2\\ \partial_{p^2}\Gamma^{(2)}(p=\mu) &= 1\,,\end{aligned} \tag{6.45}$$

where we have made the particular choice that the renormalized wave function renormalization is set to one. For illustrative purposes we will drop all diagrams from Figure 6.7, expect for the polarization diagram. With this the explicit DSE for the two-point function is given by

$$Z(p)(p^2+m^2) = Z_0(\mu)\left(p^2+m_0^2(\mu)\right)+\mathcal{D}^{\text{pol}}(\mu;p)\,. \tag{6.46}$$

Equation (6.46) is rendered manifestly finite, in combination with the renormalization conditions (6.45), by choosing the counter terms

$$\begin{aligned}Z_0(\mu) &= \lim_{p\to\mu}\left\{1-\partial_{p^2}\left(\int_{\{\lambda_i\}} 4\lambda_1\lambda_2\,\rho(\lambda_1)\rho(\lambda_2)F(p^2;\lambda_1,\lambda_2;\mu)\right)\right\}\\ Z_0(\mu)m_0^2(\mu) &= \lim_{p\to\mu}\left\{m^2-\left(\int_{\{\lambda_i\}} 4\lambda_1\lambda_2\,\rho(\lambda_1)\rho(\lambda_2)\times\right.\right.\\ &\qquad\left.\left.\times\left[F(p^2;\lambda_1,\lambda_2;\mu)-p^2\partial_{p^2}F(p^2;\lambda_1,\lambda_2;\mu)\right]\right)\right\}.\end{aligned} \tag{6.47}$$

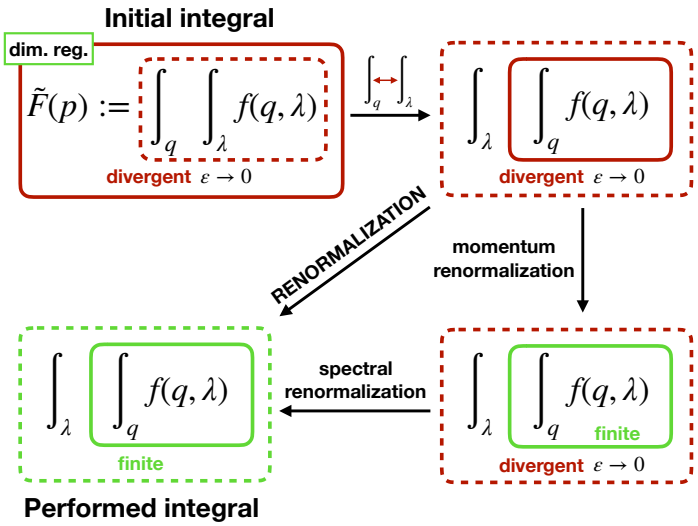

Figure 6.8.: Schematic representation of the the practical realisation of dimensional regularization in Functional Methods.

We can the counter terms explicitly to arrive at the properly renormalized DSE of the two-point function

$$Z(p)(p^2+m^2) = p^2 + m^2 + \lim_{\bar{p}\to\mu} \int_{\{\lambda_i\}} 4\lambda_1\lambda_2\,\rho(\lambda_1)\rho(\lambda_2) \Big[F(p^2;\lambda_1,\lambda_2;\mu) - \\ - F(\bar{p}^2;\lambda_1,\lambda_2;\mu) - (\bar{p}^2-\mu^2)\partial_{\bar{p}^2} F(\bar{p}^2;\lambda_1,\lambda_2;\mu) \Big] . \tag{6.48}$$

The procedure detailed in the previous section and made explicit here removes all quadratic and logarithmic divergences. If higher order divergences are present, this can trivially be accommodated for by subtracting higher order terms as well. In the case of $d = 3$, where we will perform our calculations, we only have to deal with logarithmic divergences and already the first order term, i.e. the derivative term in (6.48) is not necessary to subtract. Please not that while this might seem like two different renormalization steps, its fundamentally not. In fact, it amounts to a full subtraction of the divergent part of the Laurent series of the the result around the desired dimension. This removes all singularities by construction from the full integration, more details can be found in e.g. [269]. In the scheme presented here we only subtracted the minimally divergent part, this can of course be extended by also subtracting finite terms in order to meet different renormalization conditions. A schematic outline of the procedure is shown in Figure 6.8. This carries over to higher loops, where also sub-divergences are cancelled consistently, by design.

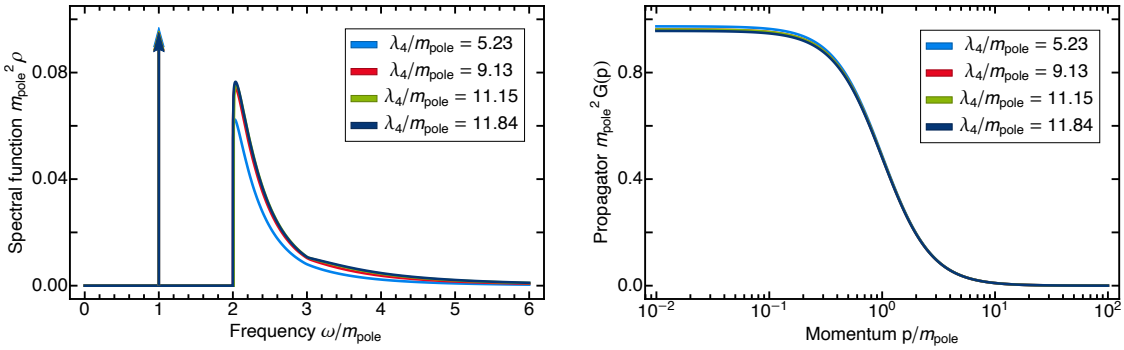

(a) Spectral function

(b) Euclidean propagator

Figure 6.9.: Different representations of the propagator, as spectral function inherent to Minkowski space-time and as Euclidean propagator.

6.3.1.2. Technical realisation

Within our truncation we are left with only one dynamical equation, the DSE of the two-point function, shown in Figure 6.7. In general once can solve DSEs, with elementary correlation functions $\gamma^{j_1\dots j_n}$, iteratively

$$\gamma_{i+1}^{j_1\dots j_n} = \gamma_\Lambda^{j_1\dots j_n} + \underset{j_1\dots j_n}{\text{Diags}}\left[\left\{\gamma_i^{j_1\dots j_n}\right\}\right]. \tag{6.49}$$

Here the set of correlation functions $\left\{\gamma_i^{j_1\dots j_n}\right\} = \left\{\Gamma^{(2)}, \Gamma^{(3)}, \Gamma^{(4)}\right\}$ with a trivial Diags $= 0$ for the three-point and four-point function. The subscript Λ denotes the classical part, i.e. $S^{(n)}$ in the present context. Such a scheme, or slightly more elaborate ones, show empirically very good convergence properties, if the initial guess is close enough to the solution of the equation. In the current application it turns out that the starting guess $\gamma_0^{j_1\dots j_n} = \gamma_\Lambda^{j_1\dots j_n}$ works very well, i.e. the classical two-point function. While on the left-hand side of the DSE the two-point function $\Gamma^{(2)}(p)$ appears, the right-hand side is expressed in terms of the spectral function $\rho(\omega) = \Im\left(\Gamma^{(2)}(-\mathrm{i}\omega + 0^+)\right)^{-1}$. This is, however, not a problem, since we can simply analytically continue the entire equation, because the momentum dependence of the right-hand side is known analytically by design. The iteration then proceeds in two steps, we evaluate the right-hand side and obtain the update for the retarded two-point function $\Gamma^{(2)}(-\mathrm{i}\omega + 0^+)$. Based on this we can then extract the new spectral function by taking the inverse of the imaginary part (6.14).

The kernels of the diagrams on the right-hands side can be calculated straightforwardly with standard perturbative methods, the analytic expressions of all relevant diagrams can be found in [270]. We will not state the expressions here due to their length.

The system is then discretized on a set of collocation points. The retarded two-point function is then interpolated using cubic Hermite splines, the spectral function is accessed from this interpolation. The discretized system is solved in Mathematica [102], where me make use of the implemented numerical integration routines for the spectral integrations. The parameters of accuracy and precision control are tuned such that results are converged by eyesight. Are more detailed investigation will be put forward elsewhere.

6.3.2. Results

In this subsection we want to present results from numerically solving the DSE for the two-point function with the aforedescribed spectral renormalization procedure, utilizing dimensional regularization. We work in $d = 3$ space-time dimension, with the motivation of extending the current truncation in future work in order to resolve the bound state present in this theory. Working with the approximation of classical vertices (6.37) actually leaves us with some freedom, i.e. the expectation value of the field ϕ_0, cf. e.g. Section 5.1. While the classical four-point function is given by the coupling λ_0, the classical three-point coupling is given by $\phi_0\lambda_0$. We resolve this by working in analogy to a derivative expansion, cf. Section 2.3.2, and use the relation

$$\Gamma^{(3)} = m\sqrt{3\Gamma^{(4)}}\,, \tag{6.50}$$

where m is the pole mass. The residual in (6.39) is extracted by evaluating the derivative of the two-point function at its zero crossing, which translates into a δ-distribution in the spectral function. The final thing to discuss before presenting the numerical results are the renormalization condition (6.45). We utilize the freedom of choosing the mass, as well as the unit themselves, to fix the renormalized mass to $m = 1\,\mathrm{GeV}$, where the choice of using GeV is completely arbitrary. The renormalization scale is fixed to $\mu = 0\,\mathrm{GeV}$. We now investigate the spectral function as well as the Euclidean propagator as a function of the four-point coupling. The result is shown in Figure 6.9. Please note while the four-point coupling does not receive any dynamical corrections, it does differ from it is effected by the rescaling of the unit, because the coupling carries the dimension of the mass in three space-time dimensions. The more interesting of the two correlation functions is of course the spectral function in Figure 6.9a. The mass pole and the two particle threshold $\phi^* \to \phi\phi$, located at m and $2m$, respectively, are clearly visible. The three particle threshold $\phi^* \to \phi\phi\phi$ at $3m$ is barley visible, because it's suppressed by powers of the decay energy threshold over mass ratio. Correspondingly, the higher order decay thresholds are not visible easily anymore, but they are present. The main effect of a stronger coupling can be understood intuitively very well, the residue of the mass pole becomes smaller, while the scattering cut gets larger contributions, i.e. scatterings get enhanced. On the Euclidean side, shown in Figure 6.9b, the larger coupling manifests itself in a larger deviation from the free propagator.

6.3.3. Conclusion

In this section we have demonstrated successfully demonstrated two things, the non-perturbative calculation of elementary correlation functions in Minkowski space-time and the use of dimensional regularization in a full blown *numerical* calculation in Functional Methods. In turned out that using the underlying structure of the elementary correlation functions implied by the existence is not only what makes the numerical calculation feasible, but also enables the use of dimensional regularization. We have applied this to a scalar theory in three space-time dimensions, showing results for the spectral function.

6.4. Reconstructing the gluon

This section is in parts based on [2].

In the previous sections we have discussed the possibility of calculating within Functional Methods in Minkowski space-time. However, such calculations come at a severely increased technical and computational costs. An alternative is given by performing the analytic continuation numerically based on previously obtained data in Euclidean space-time. When analytically continuing these to the real-time regime or equivalently reconstructing their spectral function by means of solving an inverse integral transformation, cf. (6.10), one encounters large systematic uncertainties as in the case of single particle spectral functions [2, 224, 271–278] or the energy momentum tensor (EMT) [279–284], to name another pertinent correlator. Typically, the uncertainty even grows larger at small frequency. This is particularly harmful for the computation of transport coefficients which are related to the vanishing frequency limit of correlation functions of the EMT.

This problem of a large systematic uncertainty at low frequencies can be partially circumvented by a diagrammatic representation of the correlation functions of the EMT in terms of loops of real-time correlation functions of quarks and gluons, as discussed in [224, 273]. There the spectral function of the EMT has been computed from the single-particle spectral function of the gluon. The gluon spectral function itself, in the above mentioned paper has been reconstructed via a Bayesian spectral reconstruction method [285], which is a variant of the Maximum Entropy Method (MEM) [286, 287]. This approach also extends to general real-time computations of correlation functions on the basis of real-time single particle spectral functions of quarks and gluons.

A further reduction of the systematic error comes from prior information about the properties of the single particle spectral functions used as input. Often, such prior information is available for the high frequency asymptotics of the spectral function. This is the off-shell limit with the Minkowski four momentum $p^2 \to \infty$.

In the present section we argue that the low frequency asymptotics is determined by the infrared (IR) limit in the Euclidean domain using only rather general assumptions. This leaves us with a well-constrained spectral function, which allows for a qualitatively enhanced spectral reconstruction. We apply this argument to the spectral reconstruction of the single particle gluon spectral function. The results presented here provide the starting point for the computation of transport coefficients in the spirit of the work presented in [224, 273], as well as direct real-time computation of thermodynamical properties and the QCD hadron spectrum.

This paper is organized as follows: In Section 6.4.1 we derive a general relation between the low frequency behaviour of bosonic spectral functions and the infrared (IR) behaviour of the corresponding Euclidean correlator. In Section 6.4.2 we summarize known properties of the gluon spectral function, its normalization and its asymptotics in the ultraviolet regime (UV). Then we turn to the low frequency behaviour of the gluon spectral function in Section 6.4.3. Both the analytic structure of the scaling scenario and several realizations of the decoupling scenario are discussed. In Section 6.4.4, we reconstruct the gluon spectral function with a novel reconstruction method from numerical data from [66]. We conclude in Section 6.4.5 and provide a comparison of different reconstruction approaches in Section C.2.

6.4.1. Low frequency asymptotics of spectral functions

In general, as discussed at length in Section 6.1, a spectral function can be obtained from analytic continuation of its Euclidean propagator or from the inverse integral transformation via the Källén–Lehmann spectral representation. For the convenience of the reader we will state some of facts and corresponding equations about spectral functions here again. In this section we first introduce some basic definitions and then derive a novel general relation, (6.56), between the low frequency behaviour of the spectral function and the infrared behaviour of the Euclidean propagator. The relation is illustrated at a Breit-Wigner example before it is applied to the gluon spectral function in Section 6.4.3.

Throughout this section we assume that the propagator admits the Källén–Lehmann spectral representation, cf. (6.1)

$$G(p_0) = \int_0^\infty \frac{\mathrm{d}\lambda}{2\pi} \frac{2\lambda\,\rho(\lambda)}{\lambda^2 + p_0^2}\,. \tag{6.51}$$

The existence of a spectral representation has strong consequences for the analytic structure of the corresponding propagator, i.e. all non-analyticities are constrained to the $\mathrm{Re}\,p_0 = 0$ line. More details can be found in Section C.2. In (6.51) and in the following we have suppressed the momentum-dependence $\mathbf{p}$ of the spectral function and the propagator. Note that all arguments about $p_0 = 0$ apply equally to $p^2 = 0$ at vanishing temperature. In (6.51) the restriction to positive frequencies in the integral follows from the antisymmetry of the spectral function

$$\rho(\omega) = -\rho(-\omega)\,. \tag{6.52}$$

Equivalently, the spectral function can be obtained from the Euclidean propagator by means of analytic continuation

$$\rho(\omega) = 2\,\Im\, G(-\mathrm{i}(\omega + \mathrm{i}0^+))\,, \tag{6.53}$$

i.e. from the discontinuity of the propagator. The low frequency behaviour can directly be derived from (6.51), which is done in the following. We take a derivative of the spectral representation (6.51) with respect to the Euclidean frequency

$$\partial_{p_0} G(p_0) = -\int_{-\infty}^\infty \frac{\mathrm{d}\lambda}{\pi} \lambda\, p_0\, \frac{\rho(\lambda)}{(\lambda^2 + p_0^2)^2}\,. \tag{6.54}$$

We now take the limit $p_0 \to 0$ in (6.54) in order to access the low frequency behaviour. With the derivative of the Poisson kernel representation of the delta function

$$\delta(x) = \lim_{\varepsilon\to 0} \frac{1}{\pi} \frac{\varepsilon}{\varepsilon^2 + x^2} \tag{6.55}$$

one obtains the simple relation

$$\lim_{p_0\to 0^+} \partial_{p_0} G(p_0) = -\frac{1}{2} \lim_{\omega\to 0^+} \partial_\omega \rho(\omega)\,. \tag{6.56}$$

Equation (6.56) encodes the asymptotic behaviour of the spectral function for small frequencies.

The low frequency behaviour of spectral functions may also have an additional peculiarity at finite temperature, the transport peak. In case it is present, or in general at finite temperature, the limits of vanishing frequency $\omega \to 0$ and momenta $|\mathbf{p}| \to 0$ do not commute anymore, for a more careful discussion on this issue see e.g. [1]. Nevertheless, the analysis performed in this section holds, as all equations are viewed at fixed a $\mathbf{p}$.

As an example for the low frequency asymptotics we take a single pair of complex conjugated poles on the second Riemann sheet, i.e. a Breit-Wigner. The propagator is parametrized by

$$G^{(\mathrm{BW})}(p_0) = \frac{A}{(p_0+\Gamma)^2 + M^2}\,, \tag{6.57}$$

where A is a suitably chosen normalization, Γ is proportional to the width and M is the mass. Expanding the derivative of (6.57) yields

$$\partial_{p_0} G^{(\mathrm{BW})}(p_0) = -\frac{2A\Gamma}{(M^2+\Gamma^2)^2} + \mathcal{O}(p_0)\,. \tag{6.58}$$

Using (6.56), we obtain the small frequency behaviour of the spectral function

$$\rho^{(\mathrm{BW})}(\omega) = \frac{4A\Gamma\omega}{(M^2+\Gamma^2)^2} + \mathcal{O}(\omega^2)\,, \tag{6.59}$$

which is exactly the low frequency behaviour of the full spectral function

$$\rho^{(\mathrm{BW})}(\omega) = \frac{4A\Gamma\omega}{4\Gamma^2\omega^2 + (M^2+\Gamma^2-\omega^2)^2}\,. \tag{6.60}$$

We emphasize that this derivation is based on the assumption of sufficient smoothness of the spectral function at low frequencies. A more careful derivation of (6.56), discussing the assumptions and other subtleties, such as modified spectral representations, is provided in Section C.2.

6.4.2. Known analytic properties of the gluon spectral function

Throughout this section we assume the existence of a spectral representation for the gluon propagator. This entails that the Euclidean gluon propagator $G_A(p)$ with Euclidean momenta $p = (p_0, \vec{p})$ can be written in terms of a gluon spectral function $\rho_A(\lambda, \vec{p})$ as

$$G_A(p_0) = \int_0^\infty \frac{d\lambda}{\pi} \frac{\rho_A(\lambda)}{\lambda^2 + p_0^2} + \sum_{j\in\text{poles}} \frac{R_j}{p_0^2 + M_j^2}\,. \tag{6.61}$$

analogously to (6.51), where $M_j \in \mathbb{C}$ are the position of poles with $\operatorname{Im} M_j \neq 0$ and the R_j the corresponding residues. As there we have suppressed the spatial momentum dependence in (6.61). In (6.61) we also allowed for additional poles for the sake of maximal generality. In most cases these poles will be discarded.

The existence of a spectral representation of the gluon is implicitly underlying various relations and properties used in covariant approaches to QCD. In the present context this is most apparent -but by now means restricted to- for the pinch technique, see e.g. [288]. Further works implicitly using gluon spectral representation can e.g. be found in [289, 290].

While the low frequency properties discussed in the preceding section apply to any bosonic spectral function, we now turn to the gluon spectral function as a specific example. Their normalization and high frequency asymptotics are well-known properties of QCD, which we briefly discuss next. They are exploited in the reconstruction of gluon spectral functions from Euclidean data in Section 6.4.4.

The normalization of the gluon spectral function in Landau gauge follows from the Oehme-Zimmermann superconvergence relation [291, 292]

$$\int_0^\infty \mathrm{d}\lambda\, \lambda\, \rho_\mathrm{A}(\lambda) = 0\,. \tag{6.62}$$

Equation (6.62) entails that $\rho_\mathrm{A}(\lambda)$ has positive *and* negative values in contrast to spectral functions of physical (asymptotic) states, e.g. hadronic spectral functions. Then, the total spectral weight is finite and is typically normalized to one. Its conversation is related to unitarity. When reconstructing the gluon spectral function, (6.62) serves as a highly non-trivial consistency check. Alternatively one may simply enforce it within the reconstruction method as part of the prior information.

Let us further consider the high frequency behaviour of the spectral function. The asymptotic off-shell propagator can be determined in perturbation theory for arbitrary $p_0 \in \mathbb{C}$ [293]. In pure glue theory the only scale is the dynamical QCD scale Λ_QCD. Accordingly, its asymptotic regimes are define with the limits of the dimensional momenta and frequencies,

$$\hat{p}^2 = \frac{p^2}{\Lambda_\mathrm{QCD}^2}\,, \qquad\qquad \hat{\omega} = \frac{\omega}{\Lambda_\mathrm{QCD}}\,. \tag{6.63}$$

With the dimensionless momentum $\hat{p}$ the dimensionless propagator $\hat{G}_\mathrm{A} = \Lambda_\mathrm{QCD}^2 G_\mathrm{A}$ reads

$$\lim_{\hat{p}^2\to\infty} \hat{G}_\mathrm{A}^{(\mathrm{UV})}(p) = \frac{Z_\mathrm{UV}}{\hat{p}^2 \log(\hat{p}^2)^\gamma} + \text{sub-leading}\,, \tag{6.64}$$

where Z_UV is an overall dimensionless normalization and

$$\gamma = \frac{13}{22}\,, \tag{6.65}$$

is the one-loop anomalous dimension of the gluon. Using (6.53) one can easily obtain the asymptotic behaviour of the dimensionless spectral function $\hat{\rho}_\mathrm{A} = \Lambda_\mathrm{A}^2 \rho_\mathrm{A}$ with

$$\lim_{\omega\to\infty} \Lambda_\mathrm{QCD}^2 \rho_\mathrm{A}^{(\mathrm{UV})}(\omega) = -\frac{Z_\mathrm{UV}}{\hat{\omega}^2 \log(\hat{\omega}^2)^{1+\gamma}} + \text{sub-leading}\,. \tag{6.66}$$

One key aspect is the leading order negativity of the spectral function at high frequencies. As a direct consequence, the gluon admits positivity violation in Landau gauge and cannot be an asymptotic state of the theory. As a consequence, the spectral function cannot be interpreted in the usual probabilistic sense anymore. Further details can be found in e.g. [45, 293, 294].

6.4.3. Low frequency properties of the gluon spectral function

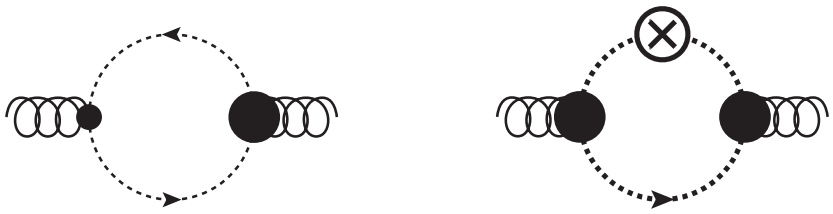

Figure 6.10.: Ghost loops in the gluon propagator DSE (left), see e.g. [105] and FRG (right), see e.g. [66]. Internal dashed (wiggly) lines represent fully dressed ghost (gluon) propagators. Thin (thick) blobs depict undressed (dressed) vertices. The crossed circle in the FRG diagram denotes the regulator insertion. The massless ghost propagator causes these diagrams to yield logarithms as given in (6.76). The dressing of ghost-gluon vertex cannot change this qualitative behaviour since it is constant in the infrared, see Figure 6.11.

In the present section we evaluate the novel frequency relation of (6.56) for the gluon spectral function. We show that for the scaling solution in the Landau gauge, derived from the Kugo-Ojima criterion [295], the low frequency asymptotics is negative. For the decoupling solution found on the lattice and in various analytic approaches the situation is less clear. However, for the expansion schemes used in the literature we also find negative spectral functions.

The derivation of (6.56) has been quite general and holds for a large class of operators. The application of (6.56) only requires the knowledge of the asymptotic infrared (IR) behaviour of the theory at hand. Despite the tremendous progress in understanding the IR sector of Yang Mills theory and QCD, we still lack a comprehensive picture. Various approaches have been put forward to predict the analytic IR behaviour of the Euclidean gluon propagator, which we use to determine the small frequency behaviour of the gluon spectral function in the following. In general the Landau gauge gluon propagator $\hat{G}_{\mathrm{A}} = \Lambda_{\mathrm{QCD}}^2 G_{\mathrm{A}}$ in the deep IR can be parametrized by

$$\hat{G}_{\mathrm{A}}(p_0) = Z_{\mathrm{IR}}\, x^{-1+2\kappa}\,, \tag{6.67}$$

with the scaling coefficient κ and an overall dimensionless IR normalization Z_{IR} and

$$x = \hat{p}^2 + \gamma_G \left(m_{\mathrm{gap}}^2 + z_G\, \hat{p}^2 \ln \hat{p}^2\right)\,, \tag{6.68}$$

with $z_G > 0$. The remainder of this section concerns the structure of (6.67), additionally all equations are understood in the deep IR limit, i.e. $\hat{p}^2, |\hat{\omega}| \ll 1$.

The parameter $\gamma_G \in [0,1]$ is related to the Gribov ambiguity, together with an appropriate definition of m_{gap}^2. The lower limit $\gamma_G \to 0$ recovers the *scaling* solution, while the upper limit $\gamma_G \to 1$ can be considered as implementing the maximal breaking of global BRST symmetry. In the following we call the set of solutions with $\gamma_G > 0$ *decoupling*. Despite their differences in terms of scaling both solutions have in common that their p^2-derivative diverges in the infrared

$$\lim_{p^2 \to 0} |\partial_{p^2} G_A(p^2)| \to \infty\,. \tag{6.69}$$

For the scaling solution it follows with $0 < \kappa < 1$ and $\kappa \neq 1/2$. For the decoupling solution the divergence originates in the logarithm $\ln p^2$. Moreover, from (6.56) it follows that it is

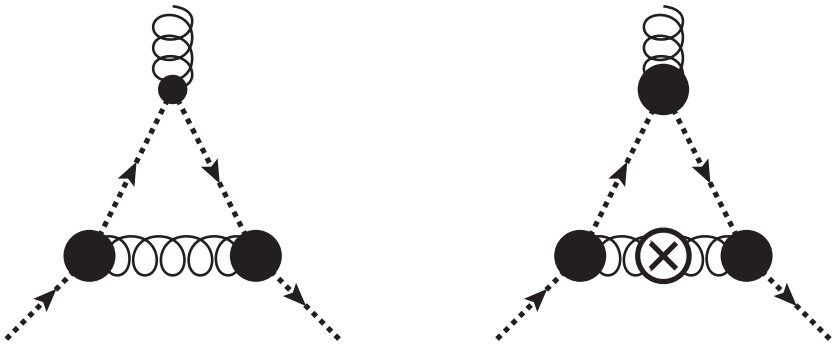

Figure 6.11.: Typical diagrams that contribute to the ghost-gluon vertex DSE (left), see e.g. [297] and FRG (right), see e.g. [66]. The presence of the gapped gluon propagator ensures that the ghost-gluon vertex is constant in the infrared. It can be shown that this behaviour is present at every finite truncation level.

precisely the sign of the p^2-derivative in (6.69) which determines the sign of the spectral function for low frequencies

$$\operatorname{sgn}\left[\lim_{\omega\to 0}\rho_A(\omega)\right] = -\operatorname{sgn}\left[\lim_{p^2\to 0}\partial_{p^2}G_A(p^2)\right], \tag{6.70}$$

where we used that the sign of the spectral function and its derivative are identical at low frequencies. This follows from the expansion of the spectral function around zero

$$\rho_A(\omega) = \omega\,\partial_\omega\rho_A(\omega) \tag{6.71}$$

for positive frequencies. In (6.71) the vanishing of the zeroth order, i.e. $\rho_A(0) = 0$, is one of our basic assumptions, c.f. the discussion in Section C.2. Equation (6.70) entails that the backbending of the propagator leads to a negative spectral function at low frequencies. Note that a backbending implies the existence of a gluon propagator maximum at a finite momentum which indicates positivity violation, see e.g. [45].

Apart from the low frequency behaviour we are also interested in the analytic structure of the gluon propagator. The latter is relevant for an accurate determination of the quasi-particle peak we expect at frequencies related to the physics scale Λ_{QCD}: The analytic form of (6.67) is exact for the scaling solution, see e.g. [109–117], and the discussion in Section 6.4.3.1. For the decoupling solution (6.67) has to be seen as an ansatz. In particular, it is one that is motivated from an Euclidean perspective and it may introduce ambiguities regarding the analytic structure of the propagator in the complex plane. Different proposals for the analytic structure of the gluon propagator have already been made in [296], one of which is compatible with the scenario discussed here. We postpone the thorough discussion of the parametrization to Section 6.4.3.2 and Section 6.4.3.3.

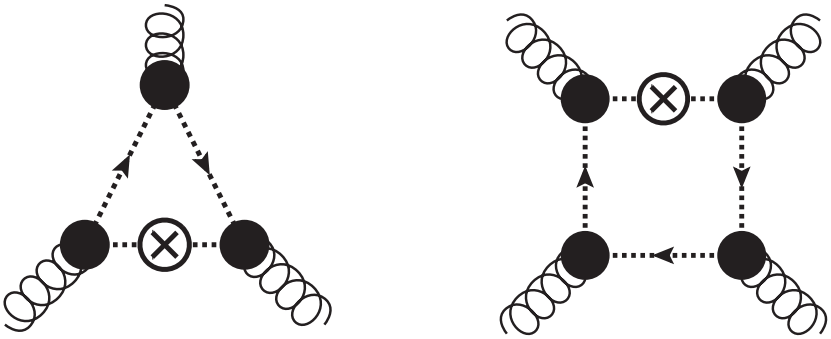

Figure 6.12.: Ghost triangle (left) and ghost box (right) diagrams as they appear in the three- and four-gluon vertex flow equations [66]. As is well known, these ghost loops generate logarithmic divergences in the vertices. Similar diagrams contribute to the respective vertex DSEs, see e.g. [82, 84, 298–300].

6.4.3.1. Scaling solution

The scaling solution is obtained by setting $\gamma_G = 0$ in (6.67). The asymptotic behaviour of the gluon propagator then reads

$$\hat{G}_{\mathrm{A}}^{(\mathrm{sca})}(p) = Z_{\mathrm{IR}}\,(\hat{p}^2)^{-1+2\kappa}\,. \tag{6.72}$$

The scaling coefficient κ is constrained by $1/2 < \kappa < 1$ and recent numerical calculations suggest $\kappa \approx 0.58$ [66] in Yang-Mills theory.

Combining (6.56) and (6.72) we obtain the following low frequency asymptotics of the gluon spectral function for the scaling solution

$$\hat{\rho}_{\mathrm{A}}^{(\mathrm{sca})}(\omega) = -2\,Z_{\mathrm{IR}}\,\mathrm{sgn}(\hat{\omega})\,(\hat{\omega}^2)^{-1+2\kappa}\,. \tag{6.73}$$

Most notable is the negative sign, i.e. the spectral function is negative for small positive frequencies. The functional similarity between (6.72) and (6.73) is not very surprising since the scaling solution has a rather simple complex structure, a single branch cut at $\mathrm{Re}\,p_0 = 0$.

6.4.3.2. Decoupling Solution

In this section we discuss in detail the infrared behaviour of the decoupling solution. In contradistinction to the scaling solution where the analytic structure follows directly from scaling in the Euclidean regime, in the decoupling case this necessitates to monitor the infrared leading logarithms. While the leading logarithms are fully accessible, a complete analysis requires to take into account the back-coupling of the quantum corrections in the functional equations.

To begin with, the leading behaviour for the decoupling solution strictly speaking reads

$$\hat{G}_{\mathrm{A}}^{(\mathrm{dec})}(p_0) \sim \frac{1}{x}\,, \tag{6.74}$$

with x given by (6.68) and $\hat{G}_{\mathrm{A}} = \Lambda_{\mathrm{QCD}}^2 G_{\mathrm{A}}$. (6.74) is the leading term of (6.67) in an expansion around $p_0 = 0$. The log-term in (6.68) arises naturally from the momentum

integration of the ghost loop in the IR, see Figure 6.10. There we have depicted the ghost loop in both the functional renormalization group (FRG) equation for the gluon propagator, see e.g. [66] for more diagrammatic details, and the Dyson-Schwinger equations (DSE), see e.g. [45] for more diagrammatic details. Both depend on the ghost propagator and the ghost-gluon vertex. In the decoupling case the ghost propagator has a trivial infrared behaviour proportional to $1/p^2$.

As a side remark we mention that the ghost propagator is not augmented with a leading order logarithmic IR running, even though this would not change the present analysis. The absence of a leading order logarithmic IR running in the ghost propagator can be shown along a similar line of arguments as done here for the gluon propagator.

6.4.3.2.1. Sources for infrared logarithms

We now proceed with the discussion of the IR behaviour of the gluon propagator. The ghost-gluon vertex dressing tends towards a constant value with a small angular dependence for small momenta, while the ghost propagator dressing also tends towards a constant. The low momentum triviality of the ghost-gluon vertex is related to the non-renormalization theorem for the ghost-gluon vertex in the Landau gauge. It also can be seen from Figure 6.11 which features the gapped gluon propagator and hence is infrared suppressed. This property holds for all mixed ghost-gluon correlations. For a very detailed and extensive discussion in the context of a perturbative one-loop analysis of the Curci-Ferrari set-up we refer to [301]. In summary the ghost loop depicted in Figure 6.10 gives rise to a $p^2 \ln p^2$ contribution with a negative prefactor in the IR. This is reflected by $z_G > 0$ in (6.68). The other diagrams contain the gapped gluon propagator or non-classical vertices. Consequently these diagrams cannot contributed to the logarithmic running at one-loop.

Beyond one-loop further contributions to the IR logarithm could originate from the logarithmic running of the vertices. This scenario was behind the discussion of the Higgs phase for large explicit gluon masses in [66]. These contributions would have the potential of switching the sign of z_G. Again such a running can only be triggered by ghost loops due to the gapping of the gluon. Hence, from an iterative point of view, they first can only occur for purely gluonic vertices triggered by the massless ghost loops contributing to these vertices. If created, they can propagate to all correlation functions via diagrams with at least one purely gluonic vertex. For the propagator the three- and four-gluon vertices are relevant, for the respective diagrams see Figure 6.12. Indeed these vertices feature logarithmic terms at one loop, see e.g. [66, 82, 84, 298–300].

The mere occurrence of logarithmic terms in the vertices is not sufficient for triggering an additional logarithmic running of the gluon propagator. Consider for example a logarithm of the form $\ln(p^2 + q^2)$, where q is the loop momentum of a given diagram for the gluon propagator $G_A(p)$. Then the loop integration effectively removes this logarithm as the gluon in the diagram is gapped. Consequently only logarithmic terms of the form $(p_i)_\mu f_i(p_1, p_2) \ln p^2$ for the three gluon vertex, and $f(p_1, p_2, p_3) \ln p^2$ for the four-gluon vertex would trigger $p^2 \ln p^2$-terms in the propagator. Here p is one of the momenta $p_1, ..., p_n$ with $p_n = -(p_1 + \cdots + p_{n-1})$ in an n-gluon vertex.

Even though the presence of such terms would be of great interest for the effective detection of a possible Higgs phase [66], a complete analysis is beyond the scope of the present work. Here we simply remark that the terms of the required form are singled out

by the infrared limit of one momentum $p \in (p_1, ..., p_n)$ with

$$\lim_{\hat{p}^2 \to 0} |\partial_{p^2} \Gamma^{(n)}_{\text{gluonic}}(p_1, ..., p_n)| \to \infty \,, \tag{6.75}$$

for the three- and four gluon vertices, $n = 3, 4$, at fixed other momenta. For this limit one can concentrate on the propagators attaching the ghost-gluon vertex with the momentum p. In the above limit they only carry the loop momentum, but are multiplied by q_{μ_i} from the respective ghost-gluon vertices. Hence they diverge as $1/q^2$. The derivative w.r.t. p^2 triggers another $1/q^2$: Applied to th ghost propagator G_c that carries the external momentum p, we are led to $\partial_{p^2} G_c(q+p)^2 \propto (1/q^2)^2$ in the limit $p \to 0$. In summary this leaves us with a logarithmic singularity due to $d^4q\, 1/q^4$. The other propagators in the diagrams still carry other external momenta and do not add to the singularity.

In summary, the kinematic analysis above hints at the existence of the logarithmic terms in the gluonic vertices that act as additional sources for the logarithmic running of the propagator. Note however, that a decisive answer requires an analysis that also takes into account the underlying gauge symmetry: first of all the Slavnov-Taylor identities (STIs) connect the different diagrams in the functional equations for the gluon propagator, cf. the discussion in Section 3.4. Second, the STIs also restrict the vertex structures themselves and the prefactors of the logarithmic vertex corrections may even vanish for fully dressed vertices. It goes without saying that even for being indicative such an analysis requires at least a full two-loop analysis of the gluon propagator in the presence of a mass gap. In this context we mention a very careful complete and illuminating perturbative analysis at one-, two and three loops in [302–304] in QCD and [305, 306] in Curci-Ferrari-type models, and also references therein.

Accordingly, the logarithms produced always depend on sums of combinations of external momenta squared. This kinematic argument entails that vertex logarithms always depend on loop momenta and hence do not contribute to z_G. Note that this argument, upon iteration, holds for fully non-perturbative resummations as done within functional methods. We emphasize that evidently this proof necessitates both the logarithmic corrections of vertices as well as the logarithmic corrections that originates from the massless propagators in the loop. Hence, conclusive arguments should at best make systematic use of the full iterative structure of resummation schemes as done here, or exploit perturbation theory at two loop and beyond. The latter ensures in most cases that the perturbative structure mimics of the iterative structure of non-perturbative resummations.

6.4.3.2.2. Potential Higgs branch

For its relevance we come back to the Higgs-phase argument in [66], even though it is a bit outside the line of arguments here. The existence and properties of such a Higgs phase are not only important for the Standard model but also for finite temperature QCD, where the temporal gauge field plays the role of a Higgs field. In [66] the dynamics of such a Higgs field was trivially mimicked by an explicit mass term of the gluon despite of its dynamical structure. The present analysis makes it apparent why such an argument falls short. In the presence of a Higgs mechanism one resorts to R_ξ-gauges that leads to massive ghosts in the Higgs phase with the ghost mass proportional to the expectation value of the Higgs. Within the present set-up this has been discussed in [95]. There it has been also shown that this mechanism has an equivalent in the standard Landau gauge. In Landau gauge the Higgs-Kibble dinner is not apparent. Still, the effect of the massless ghosts is more

than balanced by that of the Goldstone modes. In [95] it has been shown that this leads to a deconfining Polyakov loop potential in the Higgs phase. In the present context it entails that the Goldstone contributions to the gluon in Landau gauge are an additional source of the $p^2 \ln p^2$ running of the gluon propagator, that can turn the sign of z_G: this simply follows from the similarity of the Higgs-gluon vertex to that of the ghost-gluon vertex and a respective perturbative analysis. A more detailed analysis is far beyond the scope of the present work and deferred to future work.

6.4.3.3. Scenarios for analytic structures of the decoupling solution

Now we proceed with our main line of arguments. Even though sufficiently smooth, the non-trivial angular dependence and the sub-leading momentum-dependence will still almost certainly modify the complex structure. Nonetheless (6.68) still provides a very good parametrization in the infrared. Accordingly, in contradistinction to the scaling solution it is not possible for the decoupling solution to determine its analytic structure from the IR asymptotics. The difference between parameterizations cannot be resolved in currently available Euclidean data as the effects are sub-leading in the Euclidean IR domain. Nevertheless, the basic form and generation of terms is well motivated and an investigation of the IR behaviour is still sensible for the case of the decoupling solutions. It allows us to classify two likely scenarios for the analytic structure of the decoupling type gluon propagator:

6.4.3.3.1. Scenario I

We start with the parametrization given in (6.67) since it is the simplest one capturing the Euclidean behaviour. Keeping a finite γ_G in (6.67) this parametrization of the decoupling propagator can be reduced to

$$\hat{G}_{\mathrm{A}}^{(\mathrm{dec})}(p) = \tilde{Z}_{\mathrm{IR}} \left(\tilde{m}_{\mathrm{gap}}^2 + \hat{p}^2 \ln \hat{p}^2 \right)^{-1} , \tag{6.76}$$

after absorbing γ_g and z_G by appropriate redefinitions of $Z_{\mathrm{IR}} \to \tilde{Z}_{\mathrm{IR}}$ and $m_{\mathrm{gap}}^2 \to \tilde{m}_{\mathrm{gap}}^2$. The parametrization (6.76) admits complex conjugated poles, which lead to a modification of the simple spectral representation (6.51). Allowing for additional poles, we make use of the extended spectral representation (6.61). This enables us to separate cut and pole contributions of (6.76), a detailed description of the analytic structure can be found in Section B.9. Specializing (6.76) to the contribution of the cut, i.e. the one contributing to $\rho_{\mathrm{A}}^{(\mathrm{dec})}$ we obtain with (6.56)

$$\hat{\rho}_A^{(\mathrm{dec})}(\omega) = -\hat{Z}_{\mathrm{IR}} \mathrm{sgn}(\hat{\omega}) \frac{2\pi}{\hat{m}_{\mathrm{gap}}^4} \hat{\omega}^2 + \mathcal{O}(\hat{\omega}^4 \ln \hat{\omega}) . \tag{6.77}$$

Again, most notable is the negative sign in front of (6.77), leading to a negative spectral function at low frequencies for the parametrization (6.76) of the decoupling solution.

6.4.3.3.2. Scenario II

As already mentioned above, the form (6.76) is not unique, and cannot be fixed by presently available data. Indeed, another admissible parametrization removes the additional poles in (6.76). Then the propagator exhibits a single cut. We keep the same leading

order expansion in $p_0 = 0$, which renders all differences sub-leading in the Euclidean data in the IR. A possible parametrization with these properties is given by

$$\hat{G}^{(\mathrm{dec})}(p) = \tilde{Z}_{\mathrm{IR}} \tilde{m}_{\mathrm{gap}}^{-2} \left(1 + \tilde{m}_{\mathrm{gap}}^{-2} \ln\Gamma(\hat{p}^2)\right) . \tag{6.78}$$

Here, $\ln\Gamma$ is the logarithmic Γ function (not the logarithm of the Γ function). The logarithmic Γ function has a branch cut for $\mathrm{Re}\, z = 0$ and is analytic everywhere else. It is defined by

$$\ln\Gamma(z) = \sum_{k=1}^{\infty} \left(\frac{z}{k} - \ln\left(1 + \frac{z}{k}\right)\right) - \gamma_{\mathrm{E}}\, z - \ln(z) , \tag{6.79}$$

with the Euler-Mascheroni constant γ_{E}. Both parameterizations lead to the same leading order term in the propagator,

$$\hat{G}^{(\mathrm{dec})}(p) = \tilde{Z}_{\mathrm{IR}} \tilde{m}_{\mathrm{gap}}^{-2} \left(1 - \tilde{m}_{\mathrm{gap}}^{-2}\, \hat{p}^2 \ln(\hat{p}^2)\right) + \mathcal{O}(\hat{p}^4) . \tag{6.80}$$

This implies the same low frequency behaviour of the spectral function as in (6.77) and demonstrates explicitly the remaining freedom in parametrizing the decoupling solution while possibly modifying the corresponding spectral function. It is important to note however that the leading term in $\partial_{p^2} G$ is the one containing the logarithm, whose sign cannot be flipped and from which the non-positivity of the small frequency spectrum arises. More details regarding the propagator at zero can be found in Section C.2. We close this section with a word of caution: While a large class of parameterizations may yield the same spectral function, as it is the case here, this is by no means guaranteed.

6.4.3.4. Realizations of decoupling solutions

In the following subsections several approaches or models that feature decoupling type solutions are discussed. In most cases the gluon propagators results in the approaches are worked out in specific expansion schemes that allow us assigning one the above scenarios described in Paragraph 6.4.3.3.1, Paragraph 6.4.3.3.2 to it. Note that this does not necessarily entail the correct analytic structure of the gluon propagator in the given approach but certainly that of the given expansion order. Note also, that the systematics of generic expansion schemes in the analytic functional approaches suggests the persistence of the analytic structure if resummed vertices are taken into account. However, a detailed analysis is beyond the scope of the present work.

6.4.3.4.1. Lattice

Our discussion is based on the plethora of lattice results for decoupling gluon propagators at vanishing and finite temperature [107, 307–325], for recent analytic fits to high precision data see e.g. [326–328]. However, in our opinion the distinction between the different scenarios Paragraph 6.4.3.3.1, Paragraph 6.4.3.3.2 still requires a far higher precision. Accordingly, without additional information it is not possible to differentiate between any of the possible parameterizations of the decoupling scenario. Therefore statements about the analytic structure of the gluon propagator based on lattice data is currently not possible. Several reconstructions based on lattice data have been performed in the past years. In [272] a reconstruction was presented using simulations results from low

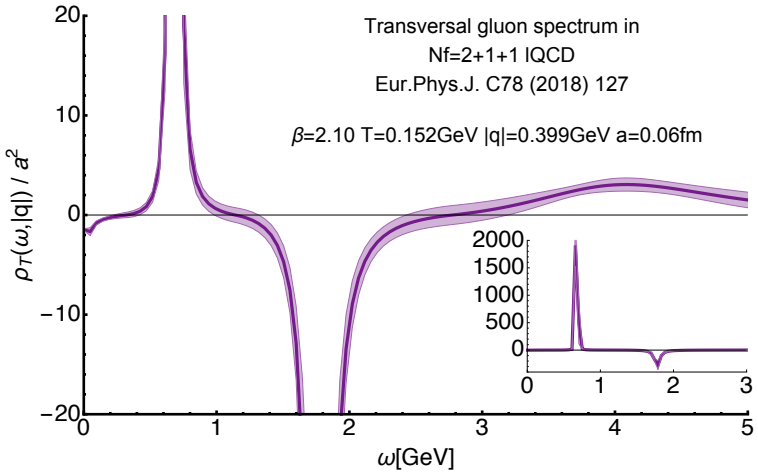

Figure 6.13.: Example of a gluon spectral function in the confined phase $T = 152\,\mathrm{MeV} < T_C$ extracted from lattice QCD simulations by the tmft collaboration including $N_f = 2 + 1 + 1$ flavours of quarks. Note that while the higher lying negative feature at around 1.75 GeV is strongly pronounced, we also find indications for a residual negative contribution at small frequencies. The overshoot into positive values at higher frequencies originally thought of as a Bayesian artefact also emerges in our reconstruction presented below. Error bars include both statistical and systematic errors, for details see [275].

temperature quenched lattice QCD. The authors deployed the Tikhonov regularization to extract the spectral function and observed a negative contribution at low frequencies.

Finite temperature studies have also been carried out. A reconstruction including finite temperature gluon propagators in quenched QCD based on a modified Maximum Entropy Method (MEM) was presented in [224]. The results were mostly positive for small frequencies by construction, due to the modified MEM approach for non-positive spectra. This method has also been applied to decoupling FRG data, see Paragraph 6.4.3.4.2, and the two reconstructions give similar results. Another reconstruction based on a Bayesian

approach has been performed in [275] using finite temperature lattice QCD data, featuring $N_f = 2 + 1 + 1$ quark flavours. The generalized Bayesian Reconstruction (gBR) approach [274] deployed in that study revealed that in the confined phase the gluon spectrum exhibits a small residual negative contribution at small frequencies, see Figure 6.13. Any sign of this negative structure disappeared at higher temperatures, however the systematic uncertainties in the study precluded a definite statement, whether that was a genuine finite temperature effect. We see the finding of a negative low frequency part as a strong indication that the Bayesian reconstruction method (gBR) in [275] recognizes the low frequency relation derived in this work.

In summary, the discussion of the low frequency limit of the gluon spectral function and of the analytic structure suggests to revisit the spectral reconstruction of the gluon spectral function based on improved analytic models that incorporate the logarithmic corrections of the gluon propagator. As the logarithmic terms might be difficult to extract directly even from the high precision lattice data, it calls for a combined lattice-functional methods approach: the logarithmic terms could be constrained by using combined propagator and

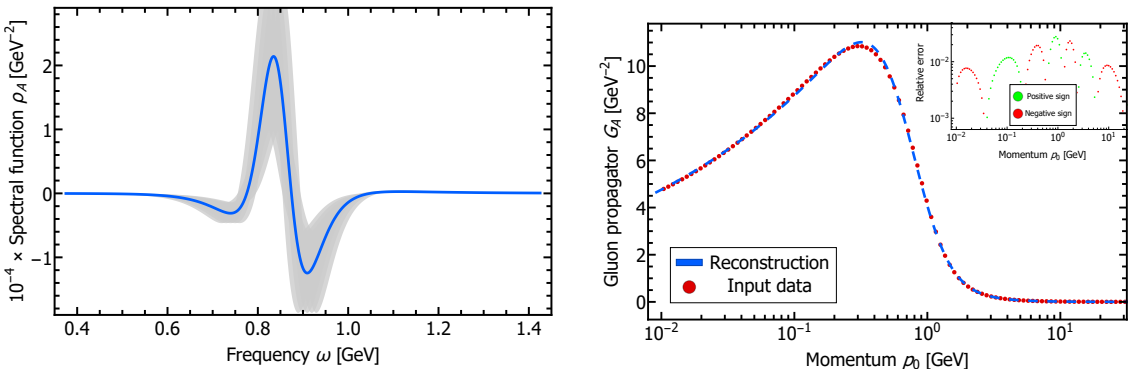

Figure 6.14.: Left: Gluon spectral function. The solid blue line shows our best result. The gray band around it indicates our estimate for the systematic error. Right: Gluon propagator reconstructed from the spectral function shown in Figure 6.16 in comparison to the original propagator.

vertices lattice data and lattice consistent results from functional methods. In the latter the logarithmic infrared terms can easily be extracted.

6.4.3.4.2. DSE & FRG

Decoupling-type propagators have been computed in both DSE and in FRG calculations in good agreement with the corresponding lattice results, see e.g. [105, 118, 119] and [66, 105], respectively. Within the DSEs a direct solution has been computed in the complex plane in [329], where a single branch cut along the $\mathrm{Re}\, p_0 = 0$ axis was found. The spectral function found there stays positive for very small frequencies. Hence the analytic structure has to violate implicitly our smoothness condition, which is very interesting and requires a more detailed investigation.

As mentioned already in the previous Paragraph 6.4.3.4.1, decoupling FRG data as well as lattice data for the finite temperature gluon propagator have been used for a reconstruction of the gluon spectral function for temperatures $T \geq 100\,\mathrm{MeV}$ in [224]. Both, the reconstruction of the lattice data and that of the FRG data have been in very good agreement with each other.

Moreover, the results are in qualitative agreement with that of the direct DSE computation of [329]: The finite temperature data show a thermal broadening. The MEM-type method used in [224] run into accuracy problems for smaller temperatures. This is a typical sign of a sharp peak in the spectral function. A low temperature extrapolation of the thermal spectral functions gives rise to a sharper peak at $T = 0$, but no quantitative statement was possible due to the missing small temperature accuracy. Note also, that the reconstruction method used in [224] leads to a positive low frequency tail almost by construction. Apart from this disagreement the results there are also in qualitative agreement with the reconstruction of the scaling spectral function presented in Section 6.4.4.4 shown in Figure 6.14.

In summary, as already mentioned at the end of Paragraph 6.4.3.4.1, the situation calls for a combined lattice-functional methods approach in order to minimize the systematic error of the reconstruction.

6.4.3.4.3. Gribov-Zwanziger approach

The complex structure arising in the Gribov-Zwanziger approach has been discussed in [330] at the example of a toy model with complex conjugated poles. The current state of the art comparison with lattice data [327] resorts to a tree-level propagator with a perturbative RG improvement that captures the ultraviolet running. It reads

$$G_A(p^2) = \frac{p^2 + M_1^2}{p^4 + M_2^2 p^2 + M_3^4} \left[\ln \frac{p^2 + m_g(p^2)}{\Lambda_{\rm QCD}^2} \right]^\gamma , \tag{6.81}$$

with the one-loop anomalous dimension $\gamma = 13/22$ introduced in (6.65). The regularization mass $m_g(p^2)$ is finite in the IR for $p^2 \to 0$ and either decays or also stays finite in the UV for $p^2 \to \infty$. Equation (6.81) is sufficient to capture the high frequency behaviour as well as the non-perturbative gapping of the gluon. Its complex structure features the perturbative cut as well as complex conjugated poles. The spectral function that follows from the propagator (6.81) is subject to the infrared relation (6.56). Evidently, the sign of the spectral function depends on the combination of parameters chosen in (6.81), for the best fits provided in [327] it is negative.

A one-loop analysis of the GZ approach reveals a logarithmic IR momentum scaling that originates in the gauge-fixing contributions similar to the ghost contribution in the Landau gauge. (6.81) lacks this logarithmic IR running that leads to the negative sign of the spectral function for low frequencies. As it is not built in naturally in (6.81) it suggests to simply restrict the range of allowed parameters by

$$\lim_{p^2 \to 0} \partial_{p^2} G(p^2) > 0 \,, \tag{6.82}$$

which mimics the divergent limit (6.69) insofar that it reproduces (6.70), and hence the correct sign of the spectral function at low frequencies. Alternatively the propagator model (6.81) can be amended by an cut. In either case this enhances the predictive power of the reconstruction.

6.4.3.4.4. Curci-Ferrari model

The Curci-Ferrari model [331] is a massive version of Yang-Mills theory. As such it features an additional relevant coupling, the gluon mass, and reduces to Yang-Mills theory in the -appropriate- massless limit. In recent years, the model has seen revived interest in the context of modeling the non-perturbative mass gap of QCD with a respective choice of the Curci-Ferrari mass parameter. Then, a perturbative treatment of fluctuations may be possible. This reasoning has been introduced in [332–334] where QCD correlation functions have been modelled using perturbation theory, for a recent work see [301]. In the present context this is particularly interesting, as it also allows analytically accessing the kinematic arguments given in Section 6.4.3.2. The one-loop contribution to the gluon

propagator has been calculated and discussed in [301, 332]. It features an asymptotic IR behaviour of the form (6.76), its infrared properties and the relation to positivity violation have been discussed extensively in [301]. We are led to a negative low frequency spectral function of the form (6.77). Higher loop considerations may change the global cut form as discussed in Section 6.4.3.2, but are not relevant for the question of the low frequency behaviour. A very detailed analysis of the complex structure of the Curci-Ferrari model

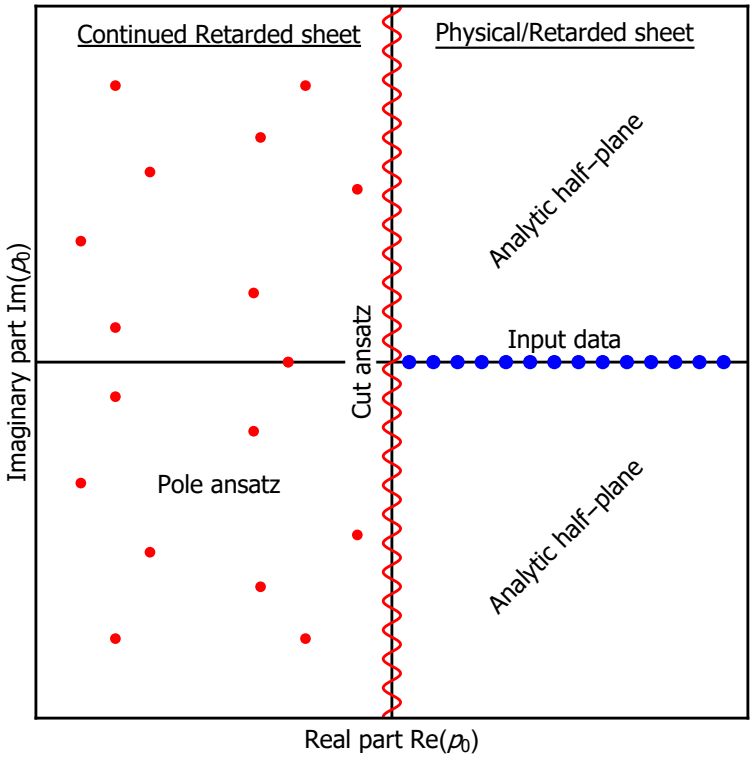

Figure 6.15.: Schematic analytic structure of a retarded propagator. All non-analytic structures are in the $\mathrm{Re}\, p_0 < 0$ half-plane, reflecting the analyticity constraints from the existence of a spectral representation.

is also found in [335–337]. In particular in [337] the gluon propagator in the CF-model is worked out at one loop, leading to a low frequency spectral function with (6.77).

In summary, the detailed one loop analysis in [301, 337] shows the low frequency properties of the spectral function derived here, (6.56). Concerning the global complex structure a two-loop analysis in the CF-framework with respect to its complex structure would be very interesting as it features both one-loop dressed propagators and vertices. In this context we refer the reader to [305, 306] where Curci-Ferrari-type models have been studied up to three loop. A respective analysis should also provide valuable additional information for the reconstruction of Landau gauge spectral function in general.

6.4.4. Extracting the spectral function from the Euclidean propagator

The aim of this section is to reconstruct the gluon spectral function from numerical data of the gluon propagator obtained in the scaling scenario [66]. The final result for the spectral functions is shown in the left panel of Figure 6.14. We would like to emphasize that it exhibits all the analytic properties discussed above up to numerical uncertainties. If used to compute the propagator via (6.51) it reproduces the original input with a precision of $\sim 2\%$, as shown in the right panel of Figure 6.14.

To arrive at the spectral function we use a novel approach based on an explicitly constructed set of basis functions that is carefully derived from the analytic properties of two-point correlation functions, see Figure 6.15 for an illustration. First, we discuss the

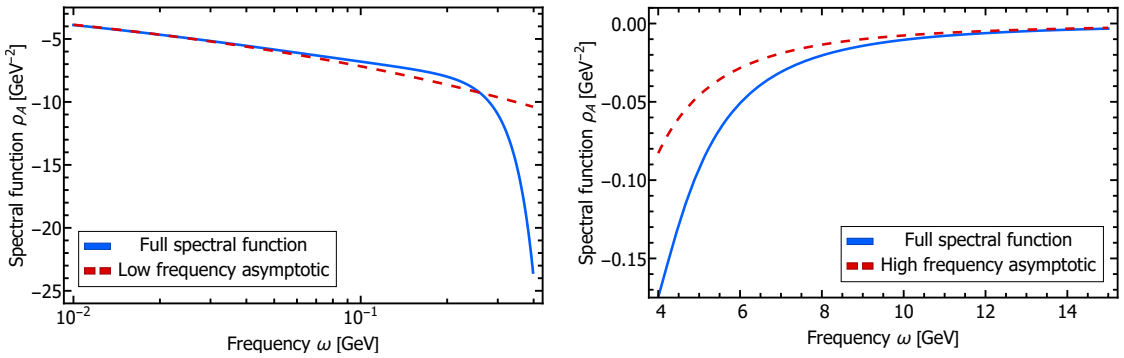

Figure 6.16.: Low (left) and high (right) frequency behaviour of our result for the spectral function shown in Figure 6.14. The dashed red lines show the asymptotic limits given by (6.73) and (6.66).

underlying analytic structure. Next, we introduce the explicit form of the basis and finally describe how it is applied to extract the gluon spectral function.

6.4.4.1. Analytic structure of the retarded propagator

The picture we have used in the preceding sections assumes a specific analytic structure for the gluon propagator, i.e. that it contains a single branch cut at $\mathrm{Re}\, p_0 = 0$ (for more details see Section C.2 and Section 6.1). Therefore, we have two analytic patches in the complex plane, the retarded propagator for $\mathrm{Re}\, p_0 > 0$ and the advanced one for $\mathrm{Re}\, p_0 < 0$. They are related by the well-known relation

$$G^{(\mathrm{ret})}(-\mathrm{i}(\omega + \mathrm{i}\varepsilon)) = \left[G^{(\mathrm{adv})}(-\mathrm{i}(\omega - \mathrm{i}\varepsilon))\right]^* . \tag{6.83}$$

In the following we focus on the retarded propagator. However, all statements hold equivalently for the advanced propagator due to (6.83).

The finite imaginary part in the retarded propagator at $\mathrm{Re}\, p_0 = 0$ signals a branch cut and therefore a finite value of the spectral function, which is defined as the discontinuity of the propagator, c.f. (6.53). Being a holomorphic function for $\mathrm{Re}\, p_0 > 0$, the retarded correlation function can be analytically continued to the entire complex plane, where it is a meromorphic function since the propagator must vanish sufficiently fast for $p \to \infty$.

Our reconstruction approach is based on an ansatz for the complex structure of the analytically continued retarded propagator. This has the advantage that (6.51) holds trivially and it is possible to enforce (6.62) analytically. Furthermore, the branch cuts describing the IR and UV asymptotics can be implemented explicitly and in a straightforward manner.

The ansatz is build up from poles and polynomials. This is possible since the most important, i.e. physically relevant branch cuts, e.g. logarithms and square roots, can be constructed from a series of poles. Of course, branch cuts can also be taken into account directly. If one is only interested in the reconstruction of a spectral function itself, there is an additional freedom to choose the branch cut of e.g. logarithms, as long as they are in the meromorphic half-plane since it does not alter the result. Therefore a rather generic ansatz is the one depicted in Figure 6.15, where all cuts are chosen to be on the $\mathrm{Re}\, p_0 = 0$ axis.

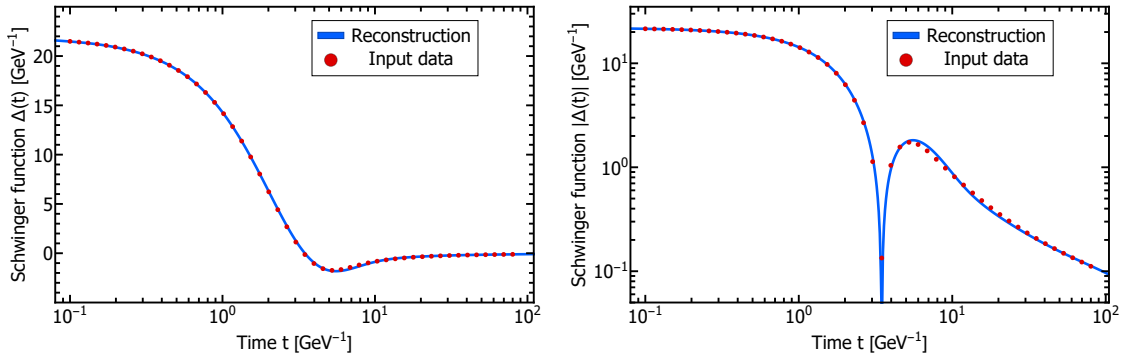

Figure 6.17.: Schwinger function obtained from the reconstruction, blue line, and from the Euclidean input, red dots, in a semi-log (left) and log-log (right) depiction. See Figure 6.14 for the corresponding Euclidean propagators in momentum space.

6.4.4.2. Reconstruction method

Our approach is based on the ability to explicitly select an appropriate basis. As a direct consequence, prior knowledge about the spectral function, e.g. its asymptotics and its functional form in general, can and should be included into the basis. In turn, analytic calculations can serve as a guiding principle for choosing a suitable basis. Importantly, this does not fix the method used to determine the coefficients of the basis. Note that the functional bases deployed in most reconstruction procedures are chosen implicitly, such as e.g. in Bryan's MEM.

One might naively expect that by selecting a basis a priori the ill-conditioned problem of reconstructing the spectral function from Euclidean data becomes artificially regularized. In general this is not the case, as the number of different structures can be chosen arbitrarily large, as is also the case in most other reconstruction procedures. Our specific choice of basis only ensures that the asymptotic and analytic properties discussed above are met.

If the number of structures permitted by the basis function is larger than those actually encoded in the Euclidean correlator data, the problem remains ill-conditioned and Bayesian inference needs to be carried out, assigning a prior probability to the individual basis parameters. The state-of-the-art implementation of Bayesian inference, which provides insight into the full posterior probability distribution and not simply a maximum a posteriori estimate, rests on Hamiltonian Monte Carlo (HMC) techniques (for the industry standard see MC-STAN [338]).

On the other hand one may systematically reduce the number of allowed structures in the basis ansatz until an ordinary χ^2 fit becomes stable. If at the same time such a restricted basis still allows the Euclidean data to be reasonably well reproduced the corresponding basis parameters constitute a valid solution. This issue is discussed in a simple mock example in Section C.3.

6.4.4.3. Construction of a gluon propagator basis

We now introduce the explicit functional form of the basis used in the subsequent reconstruction of the spectral function. It consists of the several modular, dimensionless

building blocks. We start with a set of generalized Breit-Wigner structures,

$$\hat{G}^{\text{pole}}_{\text{Ans}}(p_0) = \sum_{k=1}^{N_{\text{ps}}} \prod_{j=1}^{N^{(k)}_{\text{pp}}} \left(\frac{\hat{\mathcal{N}}_k}{(\hat{p}_0 + \hat{\Gamma}_{k,j})^2 + \hat{M}^2_{k,j}} \right)^{\delta_{k,j}} . \tag{6.84}$$

In addition, we introduce a polynomial-like structures

$$\hat{G}^{\text{poly}}_{\text{Ans}}(p_0) = \sum_{j=1}^{N_{\text{poly}}} \hat{a}_j \left(\hat{p}_0^2\right)^{\frac{j}{2}} . \tag{6.85}$$

To capture the asymptotic IR and UV behaviors, we introduce the following factor,

$$\hat{G}^{\text{asy}}_{\text{Ans}}(p_0) = (\hat{p}_0^2)^{-1-2\alpha} \left[\log\left(1 + \frac{\hat{p}_0^2}{\hat{\lambda}^2}\right) \right]^{-1-\beta} . \tag{6.86}$$

The final ansatz is then given by the product of the three individual contributions (6.84), (6.85) and (6.86):

$$G_{\text{Ans}}(p_0) = \mathcal{K}\, \hat{G}^{\text{pole}}_{\text{Ans}}(p_0) \hat{G}^{\text{poly}}_{\text{Ans}}(p_0) \hat{G}^{\text{asy}}_{\text{Ans}}(p_0) , \tag{6.87}$$

where $\mathcal{K}$ only carries the appropriate dimension. The coefficients are constraint such that (6.51) holds analytically. The superconvergence (6.62) is not included analytically, however it is realized with high accuracy, we get back to this in Section 6.4.4.4.

6.4.4.4. Gluon spectral function reconstruction and benchmarking

With the explicit form of the basis laid out above, we can continue to extract the gluon spectral function from gluon propagator data obtained in the scaling scenario [66].

As a full HMC analysis of the gluon propagator data is beyond the scope of this paper. Instead, we choose the simpler strategy of systematically reducing the number of possible structures allowed by the ansatz. We arrive at a functional form, which permits us to reproduce the Euclidean data of the scaling scenario within $\sim 2\%$ relative deviation, as shown in the right panel of Figure 6.14. At the same time this restricted basis is simple enough that its parameters can be fixed by a standard χ^2 fit. Our best fit uses $N_{\text{ps}} = 1$, $N^{(1)}_{\text{pp}} = 6$ and $N_{\text{poly}} = 5$ and leads to our final result, the gluon spectral function shown in the left panel of Figure 6.14. The shape of the result is stable against a small variation of $N^{(1)}_{\text{pp}}$ and N_{poly}. Nevertheless, we find degenerate solutions varying in their peak height, this is indicated by the grey band in the left panel of Figure 6.14.

The red dots in the right panel of Figure 6.14 denote the numerically evaluated input data from [66], while the dashed line represents the the Euclidean correlator corresponding to our reconstructed spectral function. The inset shows the relative error on a logarithmic scale where deviations with positive sign are coloured green, those with negative sign are coloured red. While the coefficients α and β in the asymptotic part of the basis functions are related to κ and γ of the IR and UV asymptotics, respectively, we note that they do not need to match exactly, since the former may be partially absorbed by some of the $\delta_{k,j}$'s. We list their values in Table 6.1 for completeness. The fit is heavily constraint, as we must enforce the complex structure as well as the correct asymptotics. As a consequence a useful and reliable error estimation is not possible.

Let us inspect the behaviour of the reconstructed spectrum in more detail. From Figure 6.14 we infer that the fitted propagator, by construction, is able to reproduce the asymptotics of the UV and the IR very well. This directly translates into the correct asymptotic behaviour of the spectral function in the IR and the UV, as shown in the left and right panel of Figure 6.16, respectively. The asymptotics are closely reproduced either below $\omega \approx 20\,\mathrm{MeV}$ and above $\omega \approx 12\,\mathrm{GeV}$.

Note that the well pronounced negative trough above the main positive peak in Figure 6.14 does not connect directly to the negative asymptotics but instead the spectrum returns into the positive once more before eventually becoming negative for good, i.e. approaching the frequency axis from below asymptotically. This behaviour is reminiscent to what has been found in a previous lattice QCD study [275]. While the data there was not precise enough to capture the asymptotic behaviour reliably, indications for a similar positive bump structure above a deep negative trough were found (see Figure 6.13).

Superconvergence (6.62) is not enforced analytically as it would unnecessarily complicate our ansatz while being realized already very well on a numerical level as it is only violated by the branch point of the perturbative cut

$$\left(\int_0^\infty \mathrm{d}\eta\ |\eta\rho_\mathrm{A}(\eta)|\right)^{-1}\left(\int_0^\infty \mathrm{d}\eta\ \eta\rho_\mathrm{A}(\eta)\right) \approx 10^{-4}\,. \tag{6.88}$$

The height of the main positive and negative structure still show rather sizeable uncertainties, which is related to our fit having been applied only to a precision of $\sim 2\%$.

The Schwinger function

$$\Delta(t) = 2\int_0^\infty \mathrm{d}p_0\ e^{\mathrm{i}p_0 t}G(p_0) \tag{6.89}$$

is potentially more sensible to differences in the peak height of the spectral function as it corresponds to a Laplace transform of the spectral function, see e.g. [1]. The Schwinger functions from the reconstruction and the input data are shown in Figure 6.17. The point of the zero crossing between both result matches very well and the overall agreement is of the same level as for the Euclidean propagator. We interpret this as further evidence for our successful reconstruction of the gluon spectral function.

Performing a full Bayesian analysis, which allows for a robust reconstruction including more analytic structures in the basis, we expect the uncertainties of the reconstruction to reduce further. This is however postponed to future work.

$\hat{\mathcal{N}}_1$	α	β	$\hat{\lambda}$		
1.33678	-0.428714	-0.777213	1.75049		
$\hat{a}_1$	$\hat{a}_2$	$\hat{a}_3$	$\hat{a}_4$	$\hat{a}_5$	
0.454024	0.241017	3.10257	-1.30804	0.63701	
$\hat{\Gamma}_{1,1}$	$\hat{\Gamma}_{1,2}$	$\hat{\Gamma}_{1,3}$	$\hat{\Gamma}_{1,4}$	$\hat{\Gamma}_{1,5}$	$\hat{\Gamma}_{1,6}$
0.100169	0.100141	2.36445	1.5564	1.22013	1.15102
$\hat{M}_{1,1}$	$\hat{M}_{1,2}$	$\hat{M}_{1,3}$	$\hat{M}_{1,4}$	$\hat{M}_{1,5}$	$\hat{M}_{1,6}$
0.849883	0.849902	2.52171	2.44035	3.6016	2.36723
$\delta_{1,1}$	$\delta_{1,2}$	$\delta_{1,3}$	$\delta_{1,4}$	$\delta_{1,5}$	$\delta_{1,6}$
1.61116	1.94095	-2.54586	1.89765	0.168592	0.296215

Table 6.1.: Parameters obtained in our best fit for the ansatz (6.87).

6.4.5. Conclusion

In this section we discussed the reconstruction of the gluon spectral function in Landau gauge QCD from numerical Euclidean data, as well as its analytic properties. In particular, we have put forward a novel reconstruction approach, which possesses these analytic properties. It satisfies the Oehme-Zimmermann superconvergence relation, has the correct low and high frequency asymptotics, and reproduces the Euclidean gluon propagator data with $\sim 2\%$ accuracy. The key to this successful reconstruction lies in two novel ingredients:

The first one is the use of the analytic low frequency asymptotics of the gluon spectral function in the reconstruction. The latter is related to the IR asymptotics of the Euclidean propagator through the novel general relation (6.56) that has been derived in Section 6.4.1. The analytic knowledge of the spectral function for $\omega \to 0$ eliminates the typically large systematic uncertainty in reconstruction methods at low frequencies, and hence may significantly improve the spectral reconstruction, independently of the used method.

The second novel ingredient in our approach originates in the careful analysis of the analytic structure of two-point correlation functions, and is described in Section 6.4.4. This analysis leads to an ansatz for the propagator in the complex plane that takes into account the generic pole and cut structure. The parameters of our quite general ansatz can then be determined from Euclidean data.

In our opinion these two novel ingredients will improve the accuracy of spectral reconstructions in general, and should be incorporated into existing Bayesian and non-Bayesian frameworks. This is briefly discussed in Section C.3.

We currently extent the present analysis to the finite temperature Euclidean data from [339], and the QCD correlation functions from [64]. This allows for an improved determination of transport coefficients following up on [224, 273] as well as an access to hadronic observables.

6.5. Spectral Reconstruction with Deep Neural Networks

This section is in parts based on [6].

In this section we explore artificial neural networks as a tool for the reconstruction of spectral functions from imaginary time Green's functions, a classic ill-conditioned inverse problem, cf. Section 6.4. Our ansatz is based on a supervised learning framework in which prior knowledge is encoded in the training data and the inverse transformation manifold is explicitly parametrised through a neural network. We systematically investigate this novel reconstruction approach, providing a detailed analysis of its performance on physically motivated mock data, and compare it to established methods of Bayesian inference. The reconstruction accuracy is found to be at least comparable, and potentially superior in particular at larger noise levels. We argue that the use of labelled training data in a supervised setting and the freedom in defining an optimisation objective are inherent advantages of the present approach and may lead to significant improvements over state-of-the-art methods in the future. Potential directions for further research are discussed in detail.

6.5.1. Introduction

Machine Learning has been applied to a variety of problems in the natural sciences. For example, it is regularly deployed in the interpretation of data from high-energy physics detectors [340, 341]. Algorithms based on learning have shown to be highly versatile, with their use extending far beyond the original design purpose. In particular, deep neural networks have demonstrated unprecedented levels of prediction and generalisation performance, for reviews see e.g. [342, 343]. Machine Learning architectures are also increasingly deployed for a variety of problems in the theoretical physics community, ranging from the identification of phases and order parameters to the acceleration of lattice simulations [344–354].

Ill-conditioned inverse problems lie at the heart of some of the most challenging tasks in modern theoretical physics. One pertinent example is the computation of real-time properties of strongly correlated quantum systems. Take e.g. the phenomenon of energy and charge transport, which so far has defied a quantitative understanding from first principles. This universal phenomenon is relevant to systems at vastly different energy scales, ranging from ultracold quantum gases created with optical traps to the quark-gluon plasma born out of relativistic heavy-ion collisions.

While static properties of strongly correlated quantum systems are by now well understood and routinely computed from first principles, a similar understanding of real-time properties is still subject to ongoing research. The thermodynamics of strongly coupled systems, such as the quark gluon plasma, has been explored using the combined strength of different non-perturbative approaches, such as functional Methods and lattice field theory calculations. There are two limitations affecting most of these approaches: Firstly, in order to carry out quantitative computations, time has to be analytically continued into the complex plane, to so-called Euclidean time. Secondly, explicit computations are either fully numerical or at least involve intermediate numerical steps.

This leaves us with the need to eventually undo the analytic continuation of Euclidean correlation functions, which are known only approximately The most relevant examples are two-point functions, the Euclidean propagators. An issue that we have already dis-

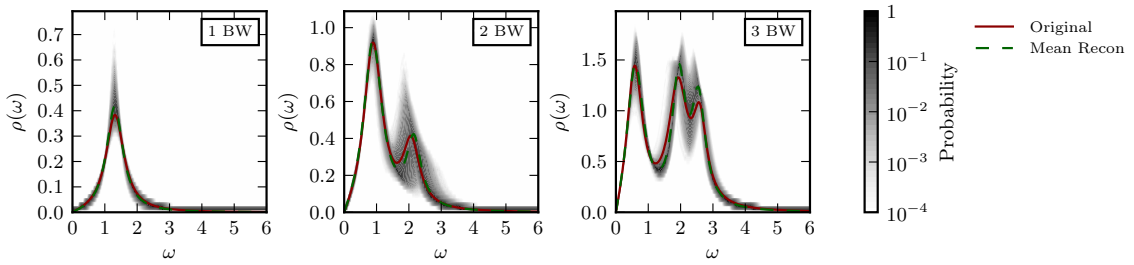

Figure 6.18.: Examples of mock spectral functions reconstructed via our neural network approach for the cases of one, two and three Breit-Wigner peaks. The chosen functions mirror the desired locality of suggested reconstructions around the original function (red line). Additive, Gaussian noise of width 10^{-3} is added to the discretized analytic form of the associated propagator of the same original spectral function multiple times. The shaded area depicts for each frequency ω the distribution of resulting outcomes, while the dashed green line corresponds to the mean. The results are obtained from the FC parameter network optimised with the parameter loss. The network is trained on the largest defined parameter space which corresponds to the volume Vol O. The uncertainty for reconstructions decreases for smaller volumes as illustrated in Figure 6.22. A detailed discussion on the properties and problems of a neural network based reconstruction is given in Section 6.5.5.1.

cussed at length within this chapter. In practice, the limitation of having to approximate correlator data (e.g. through simulations) turns the computation of spectral functions into an ill-conditioned problem. The most common approach to give meaning to such inverse problems is Bayesian inference. It incorporates additional prior domain knowledge we possess on the shape of the spectral function to regularise the inversion task. The positivity of hadronic spectral functions is one prominent example. The Bayesian approach has seen continuous improvement over the past two decades in the context of spectral function reconstructions. While originally it was restricted to maximum a posteriori estimates for the most probable spectral function given Euclidean data and prior information [286, 287, 355], in its most modern form it amounts to exploring the full posterior distribution [356]. An important aspect of the work is to develop appropriate mock data tests to benchmark the reconstruction performance before applying it to actual data. Generally, the success of a reconstruction method stands or falls with its performance on physical data. While this seems evident, it was in fact a hard lesson learned in the history of Bayesian reconstruction methods, a lesson which we want to heed.

Inverse problems of this type have also drawn quite some attention in the machine learning (ML) community [357–360]. In the present work we build upon both the recent progress in the field of ML, particularly deep learning, as well as results and structural information gathered in the past decades from Bayesian reconstruction methods. We set out to isolate a property of neural networks that holds the potential to improve upon the standard Bayesian methods, while retaining their advantages, utilising the already gathered insight in their study.

Consider a feed-forward deep neural network that takes Euclidean propagator data as input and outputs a prediction of the associated spectral function. Although the reasoning

behind this ansatz is rather different, one can draw parallels to more traditional methods. In the Bayesian approach, prior information is explicitly encoded in a prior probability functional and the optimisation objective is the precise recovery of the given propagator data from the predicted spectral function. In contrast, the neural network based reconstruction is conditioned through supervised learning with appropriate training data. This corresponds to implicitly imposing a prior distribution on the set of possible predictions, which, as in the Bayesian case,regularises the reconstruction problem. Optimisation objectives are now expressed in terms of loss functions, allowing for greater flexibility. In fact, we can explicitly provide pairs of correlator and spectral function data during the training. Hence, not only can we aim for the recovery of the input data from the predictions as in the Bayesian approach, but we are now also able to formulate a loss directly on the spectral functions themselves. This constitutes a much stronger restriction on potential solutions for individual propagators, which could provide a significant advantage over other methods. The possibility to access all information of a given sample with respect to its different representations also allows the exploration of a much broader set of loss functions, which could benefit not only the neural network based reconstruction, but also lead to a better understanding and circumvention of obstacles related to the inverse problem itself. Such an obstacle is given, for example,by the varying severity of the problem within the space of considered spectral functions. By employing adaptive losses, inhomogeneities of this type could be neutralised.

Similar approaches concerning spectral functions that consist of normalised sums of Gaussian peaks have already been discussed in [361, 362]. In this work, we investigate the performance of such an approach using mock data of physical resonances motivated by quantum field theory, and compare it to state-of-the-art Bayesian methods. The data are given in the form of linear combinations of unnormalised Breit-Wigner peaks, whose distinctive tail structures introduce additional difficulties. Using only a rather naive implementation, the performance of our ansatz is demonstrated to be at least comparable and potentially superior, particularly for large noise levels. We then discuss potential improvements of the architecture, which in the future could establish neural networks to a state-of-the-art approach for accurate reconstructions with a reliable estimation of errors.

The section is organised as follows. The spectral reconstruction problem is defined in Section 6.5.2.1. State-of-the-art Bayesian reconstruction methods are summarised in Section 6.5.2.2. In Section 6.5.2.3 we discuss the application of neural networks and potential advantages. Section 6.5.3 contains details on the design of the networks and defines the optimisation procedure. Numerical results are presented and compared to Bayesian methods in Section 6.5.5. We summarise our findings and discuss future work in Section 6.5.6.

6.5.2. Spectral reconstruction and potential advantages

6.5.2.1. Defining the problem

Typically, correlation functions in equilibrium quantum field theories are computed in imaginary time after a Wick rotation $t \to it \equiv \tau$, which facilitates both analytical and numerical computations. In strongly correlated systems, a numerical treatment is in most cases inevitable. Such a set-up leaves us with the task to reconstruct relevant information, such as the spectrum of the theory, or genuine real-time quantities such as transport coefficients, from the Euclidean data. This is in complete analogy to the previous Section 6.4.

Nevertheless, we will recap some things here in order to give a consistent representation of the problem from the perspective of Bayesian Inference.

The information we want to access is encoded in the associated spectral function ρ. For this purpose it is most convenient to work in momentum space both for ρ and the corresponding propagator G. The relation between the Euclidean propagator and the spectral function is given by the well known Källen-Lehmann spectral representation, cf. (6.1)

$$G(p) = \int_0^\infty \frac{\mathrm{d}\omega}{2\pi} \frac{2\omega\,\rho(\omega)}{\omega^2 + p^2} \equiv \int_0^\infty \mathrm{d}\omega\, K(p,\omega)\rho(\omega)\,, \tag{6.90}$$

which defines the corresponding Källen-Lehmann kernel. The propagator is usually only available in the form of numerical data, with finite statistical and systematic uncertainties, on a discrete set of N_p points, which we abbreviate as $G_i = G(p_i)$. The most commonly used approach is to work directly with a discretized version of (6.90). We utilise the same abbreviation for the spectral function, i.e. $\rho_i = \rho(\omega_i)$, discretized on N_ω points. This lets us state the discrete form of (6.90) as

$$G_i = \sum_{j=1}^{N_\omega} K_{ij}\,\rho_j\,, \tag{6.91}$$

where $K_{ij} = K(p_i,\omega_j)\Delta\omega_j$. This amounts to a classic ill-conditioned inverse problem, similar in nature to those encountered in many other fields, such as medical imaging or the calibration of option pricing methods. Typical errors on the input data $G(p_i)$ are on the order of 10^{-2} to 10^{-5} when the propagator at zero momentum is of the order of unity.

To appreciate the problems arising in such a reconstruction more clearly, let us assume we have a suggestion for the spectral function ρ_{sug} and its corresponding propagator G_{sug}. The difference to the measured data is encoded in

$$\|G(p) - G_{\text{sug}}(p)\| = \left\| \int_0^\infty \frac{\mathrm{d}\omega}{\pi} \frac{\omega}{\omega^2 + p^2} \Big[\rho(\omega) - \rho_{\text{sug}}(\omega)\Big] \right\|, \tag{6.92}$$

with a suitable norm $\|.\|$. Evidently, even if this expression vanishes point-wise, i.e. $\|G(p_i) - G_{\text{sug}}(p_i)\| = 0$ for all p_i, the spectral function is not uniquely fixed. Experience has shown that with typical numerical errors on the input data, qualitatively very different spectral functions can lead to in this sense equivalent propagators. This situation can often be improved on by taking more prior knowledge into account, c.f. the discussion in [2] and Section 6.4. This includes properties such as:

1. Normalisation and positivity of spectral functions of asymptotic states. For gauge theories, this may reduce to just the normalisation to zero, expressed in terms of the Oehme-Zimmermann superconvergence [292, 363].

2. Asymptotic behaviour of the spectral function at low and high frequencies.

3. The absence of clearly unphysical features, such as drastic oscillations in the spectral function and the propagator.

Additionally, the parametrisation of the spectral function in terms of frequency bins is just one particular basis. In order to make reconstructions more feasible, other choices, and in particular physically motivated ones, may be beneficial, c.f. again the discussion in [2] and Section 6.4. In this work, we consider a basis formulated in terms of physical resonances, i.e. Breit-Wigner peaks.

6.5.2.2. Existing methods

The inverse problem as defined in (6.90) has an exact solution in the case of exactly known, discrete correlator data [195]. However, as soon as noisy inputs are considered, this approach turns out to be impractical [235]. Therefore, the most common strategy to treat this problem is via Bayesian inference. This approach is based on Bayes' theorem, which states that the posterior probability is essentially given by two terms, the likelihood function and prior probability:

$$P(\rho|D, I) \propto P(D|\rho, I)\, P(\rho|I)\,. \tag{6.93}$$

It explicitly includes additionally available prior information on the spectral function in order to regularise the inversion task. The likelihood $P(D|\rho)$ encodes the probability for the input data D to have arisen from the test spectral function ρ, while $P(\rho)$ quantifies how well this test function agrees with the available prior information. The two probabilities fully specify the posterior distribution in principle, however they may be known only implicitly. In order to gain access to the full distribution, one may sample from the posterior, e.g. through a Markov Chain Monte Carlo process in the parameter space of the spectral function. However, in practice one is often content with the maximum a posteriori (MAP) solution. Given a uniform prior, the Maximum Likelihood Estimate (MLE) corresponds to an estimate of the MAP.

6.5.2.3. Advantages of neural networks

In order to make genuine progress, we set out in this study to explore methods in which our prior knowledge of the analytic structure can be encoded in different ways. To this end, our focus lies on the use of Machine Learning in the form of artificial neural networks. These feature a high flexibility in the encoding of information by learning abstract internal representation. They possess the advantageous properties that prior information can be explicitly provided through the training data, and that the solution space can be regularised by choosing appropriate loss functions.

Minimising (6.92), while respecting the constraints discussed in Section 6.5.2.1, can be formulated as minimising a loss function

$$L_G(\rho_{\text{sug}}) = \|G[\rho_{\text{sug}}] - G[\rho]\|\,. \tag{6.94}$$

This corresponds to indirectly working on a norm or loss function for ρ,

$$L_\rho(\rho_{\text{sug}}) = \|\rho_{\text{sug}} - \rho\|\,. \tag{6.95}$$

Of course, the optimisation problem as given by (6.95) is intractable, since it requires the knowledge of the true spectral function ρ. Minimising $L_\rho(\rho_{\text{sug}})$ for a given set of $\{\rho_{\text{sug}}\}$ also minimises L_G, since the Källén–Lehmann representation (6.90) is a linear map. In turn, however, minimising L_G does not uniquely determine the spectral function, as has already been mentioned. Accordingly, the key to optimise the spectral reconstruction is the ideal use of all known constraints on ρ, in order to better condition the problem. The latter aspect has fueled many developments in the area of spectral reconstructions in the past decades.

Given the complexity of the problem, as well as the interrelation of the constraints, this calls, in our opinion, for an application of supervised machine learning algorithms for an

optimal utilisation of constraints. To demonstrate our reasoning, we generate a training set of known pairs of spectral functions and propagators and train a neural network to reconstruct ρ from G by minimising a suitable norm, utilising both L_G and L_ρ during the training. When the network has converged, it can be applied to measured propagator data G for which the corresponding ρ is unknown.

Estimators learning from labelled data provide a potentially significant advantage due to the employed supervision, because the loss function is minimised a priori for a whole range of possible input/output pairs. Accordingly, a neural network aims to learn the entire set of inverse transformations for a given set of spectral functions. After this mapping has been approximated to a sufficient degree, the network can be used to make predictions. This is in contrast to standard Bayesian methods, where the posterior distribution is explored on a case by case basis. Both approaches may also be combined, e.g. by employing a neural network to suggest a solution ρ_{sug}, which is then further optimised using a traditional algorithm.

The given set-up forces the network to regularise the ill-conditioned problem by reproducing the correct training spectrum in accord with our criteria for a successful reconstruction. It is the inclusion of the training data and the free choice of loss functions that allows the network to fully absorb all relevant prior information. This ability is an outstanding property of supervised learning methods, which could yield potentially significant improvements over existing frameworks. Examples for such constraints are the analytic structure of the propagator, asymptotic behaviors and normalisation constraints.

The parametrisation of an infinite set or manifold of inverse transformations by the neural network also enables the discovery of new loss functions which may be more appropriate for a reliable reconstruction. This includes, for example, the exploration of correlation matrices with adapted elements, in order to define a suitable norm for the given and suggested propagators. Existing, iterative methods may also benefit from the application of such adaptive loss functions. These may include parameters, point-like representations and arbitrary other characteristics of a given training sample.

Formulated in a Bayesian language, we set out to explicitly train the neural network to predict MAP estimates for each possible input propagator, given the training data as prior information. By salting the input data with noise, the network learns to return a denoised representation of the associated spectral functions.

6.5.3. A neural network based reconstruction

Neural networks provide high flexibility with regard to their structure and the information they can process. They are capable of learning complex internal representations which allow them to extract the relevant features from a given input. A variety of network architectures and loss functions can be implemented in a straightforward manner using modern Machine Learning frameworks. Prior information can be explicitly provided through a systematic selection of the training data. The data itself provides, in addition to the loss function, a regularisation of possible suggestions. Accordingly, the proposed solutions have the advantage to be similar to the ones in the training data.

The section starts with notes on the design of the neural networks we employ and ends with a detailed introduction of the training procedure and the utilised loss functions.

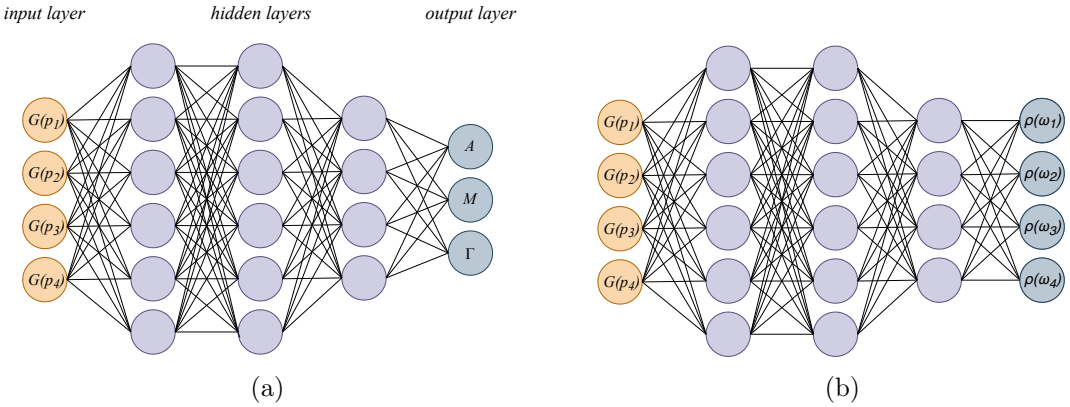

(a) (b)

Figure 6.19.: Sketches of the (a) PaNet, shown here for the case of predicting the parameters A, M, Γ of a single Breit-Wigner peak, as well as the (b) PoNet (and by extension also the PoVarNet). The specific network dimensions in this figure serve a purely illustrative purpose, explicit details on the employed architectures are given in Section C.4.

6.5.3.1. Design of the neural networks

We construct two different types of deep feed-forward neural networks. The input layer is fed with the noisy propagator data $G(p)$. The output for the first type is an estimate of the parameters of the associated ρ in the chosen basis, which we denote as *parameter net (PaNet)*. For the second type, the network is trained directly on the discretised representation of the spectral function. This network will be referred to as *point net (PoNet)*. A consideration of a variable number of Breit-Wigners is feasible per construction by the point-like representation of the spectral function within the output layer. This kind of network will in the following be abbreviated by *PoVarNet*. See Figure 6.19 for a schematic illustration of the different network types. Note that in all cases a basis for the spectral function is provided either explicitly through the structure of the network or implicitly through the choice of the training data. If not stated otherwise, the numerical results presented in the following always correspond to results from the PaNet.

We compare various types of hidden layers and the impact of depth and width within the neural networks. In general, choosing the numbers of layers and neurons is a trade-off between the expressive power of the network, the available memory and the issue of overfitting. The latter strongly depends on the number of available training samples w.r.t. the expressivity. For fully parametrised spectral functions, new samples can be generated very efficiently for each training epoch, which implies an, in principle, infinite supply of data. Therefore, in this case, the risk of overfitting is practically non-existent. The specific dimensions and hyperparameters used for this work are provided in Section C.4. Numerical results can be found in Section 6.5.5.

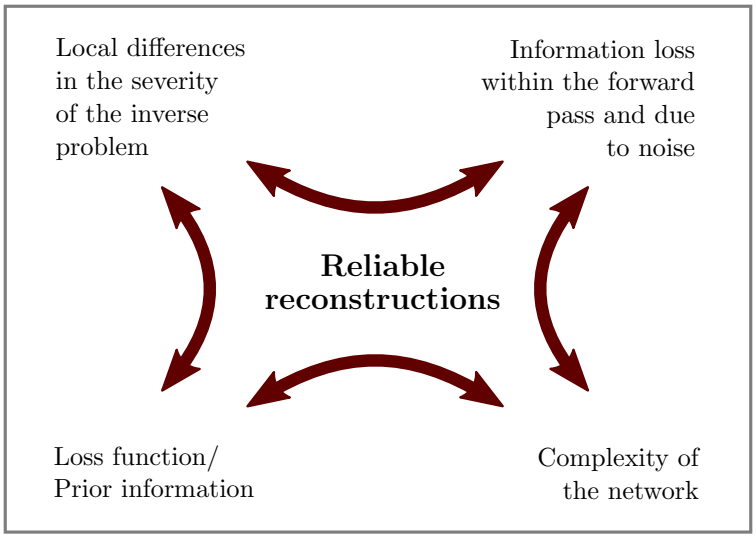

Figure 6.20.: This figure serves to illustrate the impact which the details of the training procedure and of the inverse problem itself have on the quality of the reconstructions. The term *reliable reconstruction* refers to a homogeneous distribution of losses within the parameter space. This involves a reliable error estimation on the given reconstruction and ensures locality of proposed solutions. In essence, we want to emphasise the importance of realising that aiming for reliable reconstructions is a complicated, multifactorial problem whose facets need to be sufficiently disentangled in order to understand all contributions to systematic errors.

6.5.4. Training strategy

The neural network is trained with appropriately labelled input data in a supervised manner. This approach allows to implicitly impose a prior distribution in the Bayesian sense. The challenge lies in constructing a training dataset that is exhaustive enough to contain the relevant structures that may constitute the actual spectral functions in practical applications.

From our past experience with hadronic spectral functions in lattice QCD and the functional renormalization group, the most relevant structures are peaks of the Breit-Wigner type, as well as thresholds. The former present a challenge from the point of view of inverse problems, as they contain significant tail contributions, contrary e.g. to Gaussian peaks, which approach zero exponentially fast. Thresholds on the other hand set in at finite frequencies, often involving a non-analytic kink behaviour. In this work, we only consider Breit-Wigner type structures as a first step for the application of neural networks to this family of problems.

Mock spectral functions are constructed using a superposed collection of Breit-Wigner peaks based on a parametrisation obtained directly from one-loop perturbative quantum field theory. Each individual Breit-Wigner is given by

$$\rho^{(\mathrm{BW})}(\omega) = \frac{4A\Gamma\omega}{(M^2+\Gamma^2-\omega^2)^2+4\Gamma^2\omega^2}\,. \tag{6.96}$$

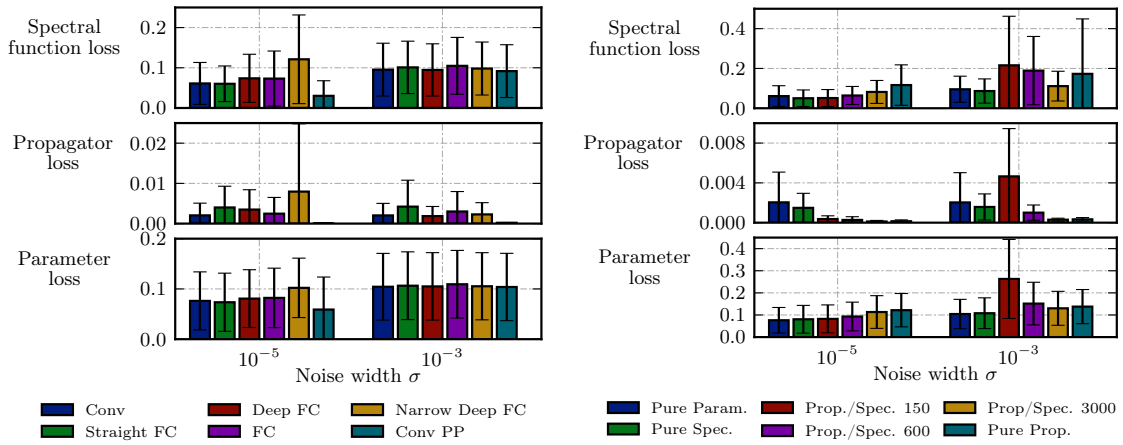

(a) Comparison of different net architectures. All networks are trained based on the parameter loss. The associated architures can be found in Table C.3.

(b) Comparison of different loss functions. Details on the loss functions are described at the end of Section 6.5.4. All results are based on networks with the architecture Conv.

Figure 6.21.: The performance of different net architectures and loss functions is compared for additive Gaussian noise with widths of 10^{-3} and 10^{-5} on the given input propagator. Shown here are the respective losses for the predicted parameters, for the discretised reconstructed spectral function and for the reconstructed propagator to the true, noise-free propagator. For both figures, the performance measures and the training of the neural networks are based on the training and test set of the largest volume in parameter space, Vol O. The definitions of the performance measures are given at the end of Section C.4. The results on the left hand side imply that for larger errors, the choice of a specific network architecture has negligible impact on the quality of the reconstructions. All performance measures can be lowered for the given noise widths by applying a post-processing procedure on the suggested parameters of the network. In particular, the propagator loss can be minimised. The comparison on the right hand side shows that the choice of the loss function has major impact on the resulting performance of the network. The results underpin the importance of an appropriate loss function and support our argument of potential advantages of neural networks compared to existing approaches in Section 6.5.2.3. Contour plots in parameter space are illustrated for the respective measures in Figure 8.8 and Figure 8.9.

Here, M denotes the mass of the corresponding state, Γ its width and A amounts to a positive normalisation constant.

Spectral functions for the training and test set are constructed from a combination of at most $N_{\mathrm{BW}} = 3$ different Breit-Wigner peaks. Depending on which type of network is considered, the Euclidean propagator is obtained either by inserting the discretized spectral function into (6.91), or by a computation of the propagator's analytic representation from the given parameters. The propagators are salted both for the training and test set with additive, Gaussian noise

$$G_i^{\mathrm{noisy}} = G_i + \epsilon\,. \tag{6.97}$$

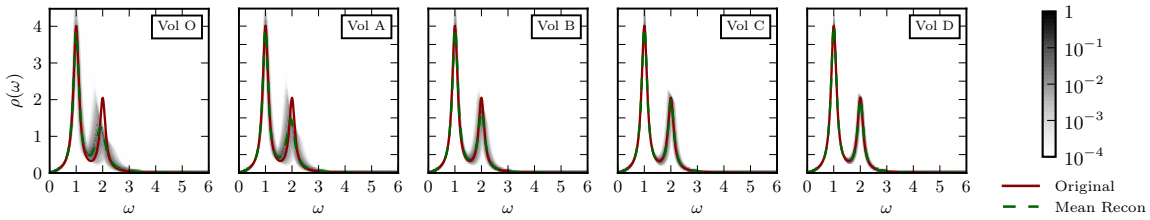

Figure 6.22.: The uncertainties of reconstructions of spectral functions on the same original propagator are illustrated in the same manner as described in Figure 6.18 for different volumes of the parameter space, again using a noise width of 10^{-3}. The plots demonstrate how the quality of the reconstruction improves if the parameter space which the network has to learn is decreased. The volumes of the corresponding parameter spaces are listed in Table C.1. The results are computed from the Conv PaNet. The systematic deviation of the distribution of reconstructions for large volumes shows that the network has not captured the manifold of inverse transformations completely for the entire parameter space. This is in concordance with the results discussed in Figure 8.8 and Figure 8.10.

This is a generic choice which allows to quantify the performance of our method at different noise levels.

The advantage of neural networks to have direct access to different representations of a spectral function implies a free choice of objective functions in the solution space. We consider three simple loss functions and combinations thereof. The (pure) propagator loss $L_G(\rho_{\text{sug}})$ defined in (6.94) represents the most straightforward approach. This objective function is accessible also in already existing frameworks such as the BR or GrHMC methods and is implemented in this work to facilitate a quantitative comparison. In contrast, the loss functions that follow are only accessible in the neural network based reconstruction framework. This unique property is owed to the possibility that a neural network can be trained in advance on a dataset of known input and output pairs. As pointed out in Section 6.5.2.3, a loss function can e.g. be defined directly on a discretized representation of the spectral function ρ. This approach is implemented through $L_\rho(\rho_{\text{sug}})$, see (6.95). The optimisation of the parameters $\theta = \{A_i, M_i, \Gamma_i \,|\, 0 \leq i < N_{\text{BW}}\}$ of our chosen basis is an even more direct approach. In principle, the space of all possible choices of parameters is $\mathbb{R}_+^{3 \cdot N_{BW}}$, assuming they are all positive definite. Of course, only finite subvolumes of this space ever need to be considered as target spaces for reconstruction methods. Therefore, we will often refer to a finite target volume simply as the parameter space for a specific setting. The respective loss function defined in this space is given by:

$$L_\theta(\theta_{\text{sug}}) = \|\theta_{\text{sug}} - \theta\| \,. \tag{6.98}$$

All losses are evaluated using the 2-norm. In the case of the parameter net, we have $\rho_{\text{sug}} \equiv \rho(\theta_{\text{sug}})$. Apart from the three given loss functions, we also investigate a combination of the propagator and the spectral function loss

$$L_{G,\rho}(\rho_{\text{sug}}, \alpha) = L_\rho(\rho_{\text{sug}}) + \alpha L_G(\rho_{\text{sug}}) \,. \tag{6.99}$$

The type of loss function that is employed as well as the selection of the training data have major impact on the resulting performance of the neural network. Given this observation,

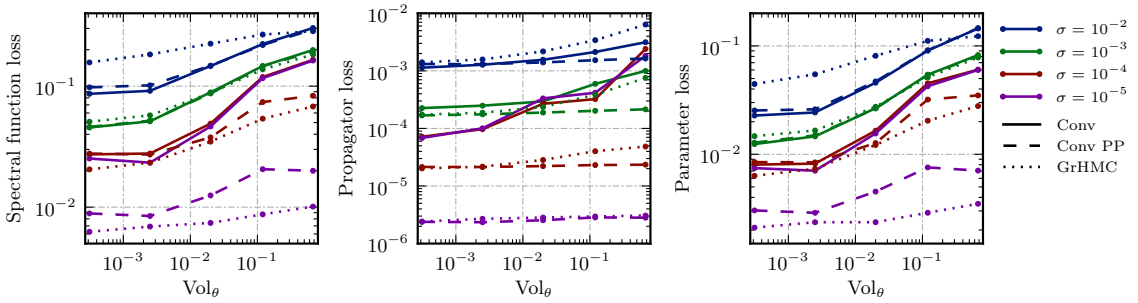

Figure 6.23.: The plots in this figure quantify the impact of the parameter space volume used for the training on the performance of the network. The performance measures are computed based on the test set of the smallest volume, Vol D. The parameter ranges in the training set are gradually reduced to analyse different levels of complexity of the problem. A network is trained separately for each volume, which are listed in Table C.1. The results demonstrate the potential advantage of an iterative restriction of the parameter ranges of possible solutions. The contour plots in Figure 8.10 depict changes of the performance measures within the parameter space. More strongly peaked prior distributions lead to better reconstructions. The comparison with results of the GrHMC approach illustrates the improvement of the performance of neural networks for larger errors and smaller volumes. These observations confirm the discussions of Figure 6.22 and Figure 6.25. Adding a post-processing step leads in particular for the propagator loss and for smaller noise widths to an improvement of the reconstruction, as has also been discussed in Figure 6.21.

it seems likely that a further optimisation regarding the choice of the loss function can significantly enhance the prediction quality. However, for the time being, we content ourselves with the types given above and postpone the exploration of more suitable training objectives to future work.

In the following section, we continue with a thorough assessment of the performance of the neural network based approach and compare numerical results with the existing methods introduced in Section 6.5.2.2.

6.5.5. Numerical results

In this section we present numerical results for the neural network based reconstruction and validate the discussed potential advantages by comparing to existing methods. Details on the training procedure as well as the training and test datasets can be found in Section C.4, together with an introduction to the used performance measures. We start now with a brief summary of the main findings for our approach. Furthermore, a detailed numerical analysis and discussion of different network set-ups with respect to performance differences are provided. Subsequently, additional post-processing methods for an improvement of the neural network predictions are covered. The section ends with a discussion of results from the PoNet. Readers who are interested in a comparison of the neural network based reconstruction to existing methods may proceed directly with Section 6.5.5.2.

6.5.5.1. Reconstruction with neural networks

Our findings concerning the optimal set-up of a feed-forward network can be summarised as follows. As pointed out in Section 6.5.2.3, the network aims to learn an approximate parametrisation of a manifold of (matrix) inverses of the discretized Källén-Lehmann transformations. The inverse problem grows more severe if the propagator values are afflicted with noise. In Bayesian terms, this is caused by a wider posterior distribution for larger noise. The network needs to have sufficient expressivity, i.e. an adequate number of hyperparameters, to be able to learn a large enough set of inverse transformations. We assume that for larger noise widths a smaller number of hyperparameters is necessary to learn satisfactory transformations, since the available information content about the actual inverse transformation decreases for a respective exact reconstruction. A varying severity of the inverse problem within the parameter space leads to an optimisation of the spectral reconstruction in regions where the problem is less severe. This effect occurs naturally, since there the network can minimise the loss more easily than in regions where the problem is more severe. Besides the severity of the inverse problem, the form of the loss function has a large impact on global optima within the landscape of the solution space. Based on these observations, an appropriate training of the network is non-trivial and demands a careful numerical analysis of the inverse problem itself, and of different set-ups of the optimisation procedure. A sensible definition of the loss function or a non-uniform selection of the training data are possible approaches to address the disparity in the severity of the inverse problem. A more straightforward approach is to iteratively reduce the covered parameter ranges within the learning process, based on previous suggested outcomes. This amounts to successively increasing the prediction accuracy by restricting the network to smaller and smaller subvolumes of the original solution space. However, one should be aware that this approach is only sensible if the reconstructions for different noise samples on the original propagator data are sufficiently close to each other in the solution space. A successive optimisation of the prediction accuracy in such a way can also be applied to existing methods. All approaches ultimately aim at a more homogeneous reconstruction loss within the solution space. This allows for a reliable control of systematic errors, as well as an accurate estimation of statistical errors. The desired outcome for a generic set of Breit-Wigner parameters is illustrated and discussed in Figure 6.18. The essence of our discussion here is summarised pictorially in Figure 6.20.

The impact of the net architecture and the loss function on the overall performance within the parameter space is illustrated in Figure 6.21. Associated contour plots can be found in Figure 8.8 and Figure 8.9. These plots demonstrate that the minima in the loss landscape highly depend on the employed loss function. In turn, this leads to different performance measures. This observation confirms our previous discussion and the necessity of an appropriate definition of the loss function. It also reinforces our arguments regarding potential advantages of neural networks in comparison to other approaches for spectral reconstruction. The comparison of different feed-forward network architectures shows that the specific details of the network structure are rather irrelevant, provided that the expressivity is sufficient.

Differences in the performance of the networks that are trained with the same loss function become less visible for larger noise. This is illustrated by a comparison of contour

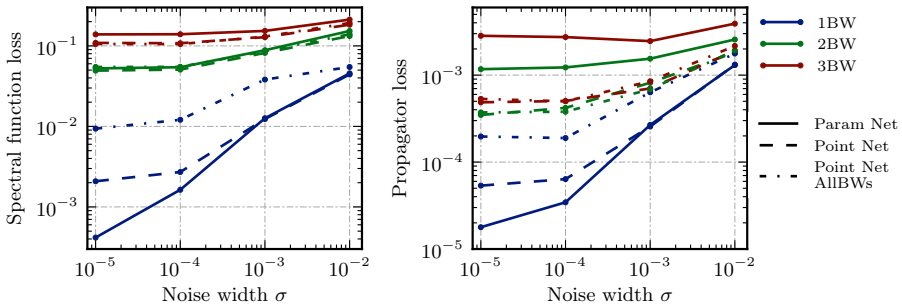

Figure 6.24.: Comparison of reconstruction errors of the PaNet and PoNet. The performance measures are computed based on the test set of the largest parameter space volume Vol O for one, two and three Breit-Wigners. The overall smaller losses for the point nets are due to the large number of degrees of freedom for the point-like representation of the spectral function. The partly competitive performance of the PoVarNet compared to the results of the PoNet encourage the further investigation of networks that are trained using a more exhaustive set of basis functions to describe physical structures in the spectral functions.

plots with different noise widths, see e.g. Figure 8.8. The severity of the inverse problem grows with the noise and the information content about the actual matrix transformation decreases. These properties lead to the observation of a generally worse performance for larger noise widths, as can be inferred from Figure 6.22, Figure 6.25 and Figure 6.26, for example. They also imply that for specific noise widths, the neural network possesses enough hyperparameters to learn a sufficient parametrisation of the inverse transformation manifold. Furthermore, the local optima into which the network converges are mainly determined by differences in the local severity of the inverse problem. Hence, the issue remains that generic loss functions are inappropriate to address the varying local severity of the inverse problem. This issue implies the existence of systematic errors for particular regions within the parameter space, as can be seen e.g. in the left plot of Figure 6.22.

The results shown in Figure 6.22, Figure 6.23 and Figure 8.10 confirm our discussion regarding the expressive power of the network w.r.t. the complexity of the solution space and the decreasing information content for larger errors. The parameter space is gradually reduced, effectively increasing the expressivity of the network relative to the severity of the problem and improving the behavior of the loss function for a given fixed parameter space. The respective volumes are listed in Table C.1. Shrinking the parameter space leads to a more homogeneous loss landscape due to the increased locality, thereby mitigating the issue of inappropriate loss functions. The necessary number of hyperparameters decreases for larger noise widths and smaller parameter ranges in the training and test dataset. The arguments above imply a better performance of the network for smaller parameter spaces. A reduction of the parameter space effectively corresponds effectively to a sharpening of the prior information, which also has positive effects on the spread of the posterior distribution. More detailed discussions on the impact of different elements of the training procedure can be found in the captions of the respective figures.

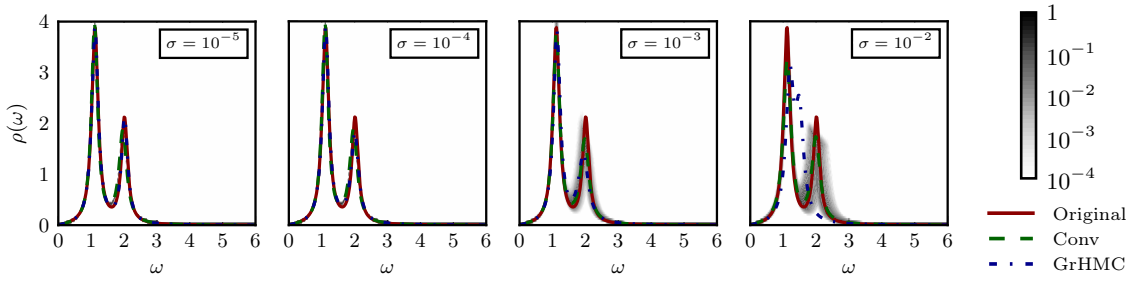

Figure 6.25.: The quality of the reconstruction of two Breit-Wigner peaks is compared for different strength of additive noise on the same propagator. The labels indicate the noise width on the original propagator. It can be seen that the reconstructed spectral function of the neural network exhibits in particular for larger errors a lower deviation to the original spectral function than the GrHMC method. This mirrors the in general observable better performance of the neural network for larger errors, as can be seen in Figure 6.23 and in Figure 6.26. The green and the red curve correspond to reconstructions of the Conv PaNet and the GrHMC method for the same given noisy propagator. The prior is in both cases given by the parameter range of volume Vol B. The uncertainty of the reconstructions for the neural network is depicted by the grey shaded areas as described in Figure 6.18. For small errors, this area is covered by the corresponding reconstructed spectral functions.

Since increasing the expressivity of the network is limited by the computational demand required for the training, one can also apply post-processing methods to improve the suggested outcome with respect to the initially given, noisy propagator. These methods are motivated by the in some cases large observed root-mean-square deviation of the reconstructed suggested propagator to the input, see for example Figure 6.21. The application of standard optimisation methods on the suggested results of the network represents one possible approach to address this problem. Here, the network's prediction is interpreted as a guess of the MAP estimate, which is presumed to be close to the true solution. For the PaNet, we minimise the propagator loss a posteriori with respect to the following loss function:

$$\min_{\theta_{\text{sug}}} L_{\text{PP}}[\theta_{\text{sug}}] = \min_{\theta_{\text{sug}}} \left\| G_{\text{noisy}} - G\left[\rho\left(\theta_{\text{sug}}\right)\right] \right\| . \tag{6.100}$$

This ensures that suggestions for the reconstructed spectral functions are in concordance with the given input propagator. Results obtained with an additional post-processing are marked by the attachment PP in this work. The numerical results in Figure 6.26 and Figure 6.22 show that the finite size of the neural network can be partially compensated for small errors. The resulting low propagator losses are noteworthy, and are close to state-of-the-art spectral reconstruction approaches. One reason for this similarity is the shared underlying objective function. However, the situation is different for larger noise widths. For our choice of hyperparameters, the algorithm quickly converges into a local minimum. For large noise widths, the optimisation procedure may even lead to worse results than the initially suggested reconstruction. This is due to the already mentioned systematic deviations which are caused by the inappropriate choice of the loss function for large parameter spaces. This kind of post-processing should therefore be applied with

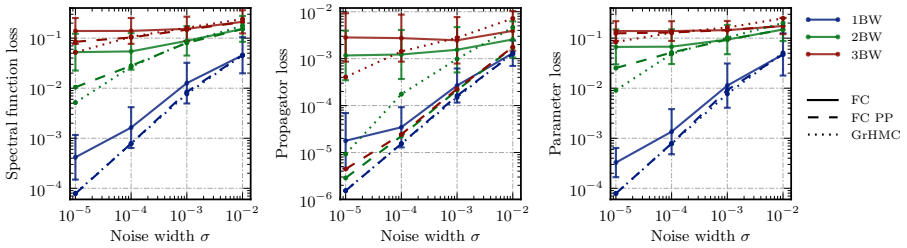

Figure 6.26.: The performance of the reconstruction of spectral functions is benchmarked for the neural network approach with respect to results of the GrHMC method. The neural network approach is in particular for large noise widths competitive. The worse performance for smaller noise widths is a result of an inappropriate training procedure and a too low expressive power of the neural network. The problems are caused by a varying severity of the inverse problem and by a too large parameter space that needs to be covered by the neural network, as discussed in Section 6.5.5.1. The error bars of the results for the FC network are representative for typical errors within all methods and plots of this kind.

caution, since it may cancel out the potential advantages of neural networks with respect to the freedom in the definition of the loss function.

The following alternative post-processing approach preserves the potential advantages of neural networks while nevertheless minimising the propagator loss. The idea is to include the network into the optimisation process through the following objective:

$$\min_{G_{\text{input}}} \; L_{\text{input}}[G_{\text{input}}] = \min_{G_{\text{input}}} \; \left\| G_{\text{noisy}} - G\left[\rho\left(\theta_{\text{sug}}\right)\right] \right\| , \tag{6.101}$$

where G_{input} corresponds to the input propagator of the neural network and θ_{sug} to the associated outcome. This facilitates a compensation of badly distributed noise samples and allows a more accurate error estimation. The approach is only sensible if no systematic errors exist for reconstructions within the parameter space, and if the network's suggestions are already somewhat reliable. We postpone a numerical analysis of this optimisation method together with the exploration of more appropriate loss functions and improved training strategies to future work, due to a currently lacking setup to train such a network.

In Figure 6.24 and Figure 8.11, results of the PoNet and the PaNet are compared. We observe that spectral reconstructions based on the PoNet structure suffer from similar problems as the PaNet, cf. again Figure 6.20. The point-like representation of the spectral function introduces a large number of degrees of freedom for the solution space. The training procedure implicitly regularises this problem, however, a visual analysis of individual reconstructions shows that in some cases the network struggles with common issues known from existing methods, such as partly non-Breit-Wigner like structures and wiggles. An application of the proposed post-processing methods serves as a possible approach to circumvent such problems. An inclusion of further regulator terms into the loss function, concerning e.g. the smoothness of the reconstruction, is also possible.

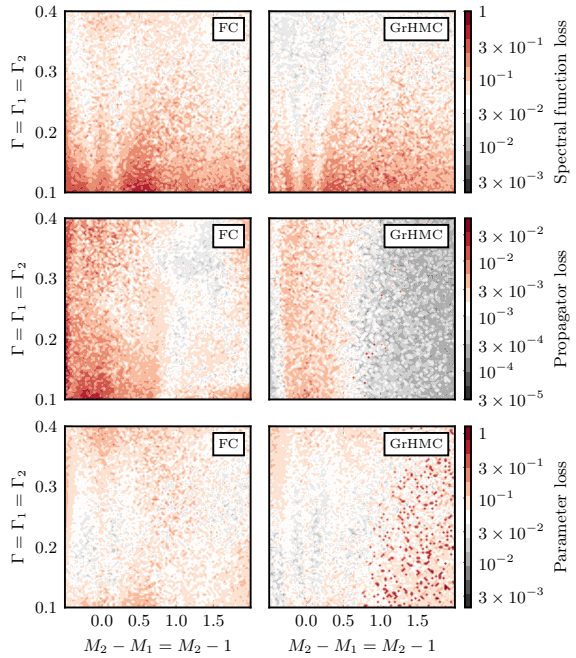

Figure 6.27.: Comparison of performance measures for the reconstruction of two Breit-Wigners with neural networks and with the GrHMC method for input propagators with noise width 10^{-3} within the parameter space volume Vol O. The similar loss landscape emphasises the high impact of variations of the severity of the inverse problem within the parameter space on the quality of reconstructions. Contrary to expectations, the parameter network mimics, despite an optimisation based on the parameter loss L_θ, the reconstruction of the GrHMC method which relies on an optimisation of the propagator loss L_G with respect to the parameters. A reconstruction resulting in an averaged peak with the other parameter set effectively removed, as outlined in [2], results in the spiking parameter losses for the GrHMC reconstructions with large errors.

6.5.5.2. Benchmarking and discussion

In this subsection, we want to emphasise differences of our proposed neural network approach to existing methods. Our arguments are supported by an in-depth numerical comparison.

Within all approaches the aim is to map out, or at least to find the maximum of, the posterior distribution $P(\rho|G)$ for a given noisy propagator G. The BR and GrHMC methods represent iterative approaches to accomplish this goal. The algorithms are designed to find the maximum for each propagator on a case-by-case basis. The GrHMC method additionally provides the possibility to implement constraints on the functional basis of the spectral function in a straightforward manner. In contrast, a neural network aims to learn the full manifold of inverse Källen-Lehman transformations for any noisy propagator (at least within the chosen parameter space). In this sense, it needs to propose for each given propagator an estimate of the maximum of $P(\rho|D)$. A complex parametrisation, as given by the network, an exhaustive training dataset and the optimisation procedure itself are

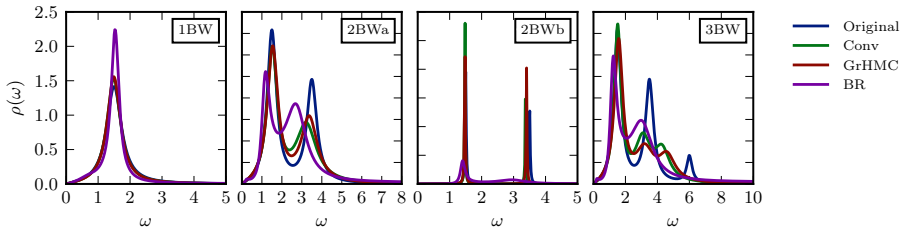

Figure 6.28.: Reconstructions of one, two and three Breit-Wigners are compared for our proposed neural network approach, the GrHMC method and the BR method. The reconstructions of the first two methods are based on a single sample with noise width 10^{-3}, while the results of the BR method are obtained from multiple samples with larger errors, but an average noise width of 10^{-3} as well. In contrast to the previous plots, the neural network and the GrHMC method now use different priors for each case in order to allow for a reasonable comparison with the BR method, see Table C.2. We observe that all approaches qualitatively capture the features in the spectral function. Due to the comparably large error on the input data, all methods are expected to face difficulties in finding an accurate solution. The reconstructions of the neural network approach and the GrHMC method are comparable, whereas the BR method struggles in particular with thin peaks and the three Breit-Wigner case. The results demonstrate that, generally, using suitable basis functions and incorporating prior information lead to a superior reconstruction performance.

essential features of this approach for tackling this tough challenge. The computational effort to find a solution in an iterative approach is therefore shifted to the training process as well as the memory demand of the network. Accordingly, the neural network based reconstruction can be performed much faster after training has been completed, which is in particular advantageous when large sets of input propagators are considered.

The numerical results in Figure 6.23, Figure 6.25, Figure 6.26, Figure 6.27 and Figure 6.28 demonstrate that the formal arguments of Section 6.5.2.3 apply, particularly for comparably large noise widths as well as smaller parameter ranges. For both cases, the network successfully approximates the required inverse transformation manifold. Smaller noise widths and a larger set of possible spectral functions can be addressed by increasing the number of hyperparameters and through the exploration of more appropriate loss functions, as was already discussed previously.

6.5.6. Conclusion

In this study we have explored artificial neural networks as a tool to deal with the ill-conditioned inverse problem of reconstructing spectral functions from noisy Euclidean propagator data. We systematically investigated the performance of this approach on physically motivated mock data and compared our results with existing methods. Our findings demonstrate the importance of understanding the implications of the inverse problem itself on the optimisation procedure as well as on the resulting predictions.

The crucial advantage of the presented ansatz is the superior flexibility in the choice of the objective function. As a result, it can outperform state-of-the-art methods such as the

hybrid Monte Carlo algorithm if the network is trained appropriately and exhibits sufficient expressivity in order to be able to approximate the inverse transformation manifold. The numerical results demonstrate that defining an appropriate loss function grows increasingly important for an increased variability of considered spectral functions and of the severity of the inverse problem.

In future work, we aim to further exploit the advantage of neural networks that local variations in the severity of the inverse problem can be systematically compensated. The goal is to eliminate systematic errors in the predictions in order to facilitate a reliable reconstruction with an accurate error estimation. This can be realised by finding more appropriate loss functions with the help of implicit and explicit approaches [364, 365]. A utilisation of these loss functions in existing methods is also possible if they are directly accessible. Varying the prior distribution will also be investigated, by sampling non-uniformly over the parameter space during the creation of the training data. Furthermore, we aim at a better understanding of the posterior distribution through the application of invertible neural networks [360]. This novel architecture provides a reliable estimation of errors by mapping out the entire posterior distribution by construction.

In conclusion, we believe that the suggested improvements will boost the performance of the proposed method to an as of yet unprecedented level and that neural networks will eventually replace existing state-of-the-art methods for spectral reconstruction.

7. Extracting observables from elementary correlation functions

In the previous chapters we discussed the determination of elementary correlation functions in Euclidean space-time, Chapter 5, and Minkowski space-time, Chapter 6. Quite a lot of physics can already be extracted from these, as seen in the corresponding chapters. However, in order to make contact with experiments, usually the knowledge of composite operators is required, for technical aspects cf. the discussion around (2.13) and (2.72). This is particularly obvious in gauge theories, where the elementary correlation functions are not gauge invariant and hence not observable at all.

At first sight, this might seem like a disadvantage of Function Methods, a formulation based on elementary correlation functions is actually extremely powerful. In this chapter we demonstrate the aforementioned powerfulness at a variety of examples, ranging from thermodynamic quantities to non-equilibrium descriptions.

7.1. Trace anomaly

This section is in parts based on [13].

Here we discuss the determination of the thermodynamic properties of a system while working with the Functional Renormalization Group. Properties like the pressure, entropy density or the trace anomaly have usually been extracted by using the analogy of the QEA to the grand canonical ensemble, see e.g. [62, 189, 366–371]. This works well in effective theories, such as the Quark-Meson model, cf. Section 4.3 and Section 5.2, but not in gauge theories. Overcoming these problems is our main motivation for the work at hand. In this section we'll take an approach based on a non-perturbative definition of the Energy-Momentum Tensor (EMT).

We start by recalling the definition Energy-Momentum Tensor in a curved space-time

$$\mathcal{T}_{\mu\nu}(x) = \frac{2}{\sqrt{-g(x)}} \frac{\delta\Gamma[\Phi, g]}{\delta g^{\mu\nu}(x)} , \tag{7.1}$$

where Γ is again the QEA, Φ a superfield and g the metric. In equilibrium we can now access all thermodynamic quantities by calculating the trace anomaly in flat space-time, which is defined as the trace of (7.1)

$$\mathcal{A} = \int_x g^{\mu\nu}(x) \mathcal{T}_{\mu\nu}(x) \Big|_{g=\eta} , \tag{7.2}$$

where η is the flat metric of Minkowski space-time. In principle, the definitions (7.1) and (7.2) are straightforwardly accessible for a given QEA, if the metric dependence is known.

In the FRG we can essentially trivially write down the corresponding flow equation for the Energy-Momentum Tensor (7.1), and hence the anomaly (7.2). Taking an RG-time

derivative of (7.1) leads to

$$\partial_t \mathcal{T}_{\mu\nu}(x) = \frac{2}{\sqrt{-g(x)}} \frac{\delta \partial_t \Gamma[\Phi, g]}{\delta g^{\mu\nu}(x)} = \frac{2}{\sqrt{-g(x)}} \frac{\delta}{\delta g^{\mu\nu}(x)} \left[\frac{1}{2} \operatorname{Tr} G_{ab}\, \partial_t R^{ab} \right], \tag{7.3}$$

where we have used the Wetterich equation (2.74) to obtain the last expression. In particular, we obtain the flow of the Energy-Momentum Tensor by taking a metric variations of the right-hand side of the Wetterich equation. This way of approaching the Energy-Momentum Tensor comes with the added benefit of mapping the renormalization thereof to the renormalization of the QEA, which is, at least partially, discussed in Chapter 2.

In practice, the right-hand side of the Wetterich equation is usually a function of the scalar Laplacian

$$\Delta_g = g^{\mu\nu} \partial_\mu \partial_\nu \,. \tag{7.4}$$

Please note that this is by no means a complete representation of the potential dependence on the metric, for this one has to consider the Casimir invariants of the Poincaré group. We postpone this discussion to future work. With the right-hand side only depending on the Laplacian we can carry out the variation with respect to the metric explicitly, go to momentum space and arrive at the flow for the trace anomaly

$$\partial_t \mathcal{A} = \operatorname{Tr} p^2 \partial_{p^2} \left[G_{ab}\, \partial_t R^{ab} \right] (p^2) \,. \tag{7.5}$$

Equation (7.5) is one of the central results of this section, it expresses the flow of the trace anomaly as a (dimensionless) momentum derivative of the right-hand side of the Wetterich equation, which is a very convenient object to compute.

Throughout the remainder of this section we will be interested in the thermal part of the anomaly, i.e.

$$\mathcal{A}_{\mathrm{T}}(T) = \mathcal{A}(T) - \mathcal{A}(T=0) \,, \tag{7.6}$$

with the temperature T.

The procedure presented above generalizes naturally to the Energy-Momentum Tensor and correlations functions thereof.

7.1.1. Thermodynamics of a free, massive scalar theory

To illustrate the discussion above, and also to explore its technical realisation, we investigate a free scalar theory. The first part of the following investigation can be found in a similar fashion in [189], where the pressure in the conventional formulation has been considered. The quantum effective action is given by

$$\Gamma[\phi] = \int_p \phi(p) \left(p^2 + m^2 \right) \phi(-p) \,. \tag{7.7}$$

The exact result for the thermal trace anomaly is easily calculated and reads

$$\begin{aligned} \mathcal{A}_{\mathrm{T}}(T) = \sum_{n=1}^{\infty} \Bigg\{ & 4 \frac{-m^2 T^2}{2\pi^2} \frac{K_2\left(\frac{nm}{T}\right)}{n^2} \\ & + T m^2 \frac{mn\, K_1\left(\frac{nm}{T}\right) + 4T\, K_2\left(\frac{nm}{T}\right) + mn\, K_3\left(\frac{nm}{T}\right)}{(2\pi n)^2} \Bigg\} , \end{aligned} \tag{7.8}$$

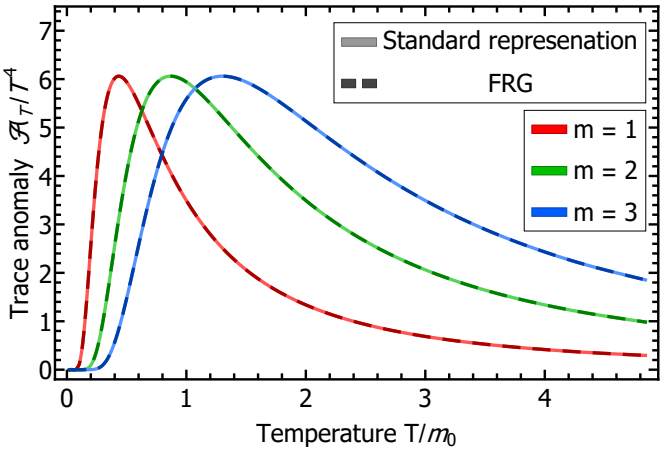

Figure 7.1.: Thermal trace anomaly of a free, massive scalar theory.

where $K_n(z)$ is the modified Bessel function of the second kind.

Based on (7.7), the (regularized) propagator is propagator is simply given by

$$G(p) = \frac{1}{p^2 + m^2 + R_k(p)} \,. \tag{7.9}$$

It turns out that the choice of regulator is rather important. Using a regulator that also regulates the frequency direction leads to an oscillatory flow of the trace anomaly. The possibility for positive and negative contributions can be seen from the flow, which is apart from this not very illuminating and will therefore be skipped here as it is straightforward to write down in addition. Since we are dealing with arbitrary regulators, the Matsubara sum and the momentum integration have to be calculated numerically, which is a straightforward task. Being a trivial theory, the integrated flow is independent from the regulator choice. However, as aforementioned, the flow itself is not. Before discussing further details of the flow, the thermal trace anomaly of this theory is shown in Figure 7.1.

As expected, the standard the textbook representation and the result from the metric variation of the QEA agree to numerical precision. The three curves can be scaled on top each other, since the result is a function fo m/T only. The thermal trace anomaly, divided by appropriate powers of the temperature, shows the expected bump at $T \approx m$ and is described at low and high temperatures by well known asymptotics, see e.g. [372].

Turning back to the question of efficiently calculating the thermal trace anomaly via its flow. Ideally, the flow should have a definite sign, and hence avoid cancellations. Additionally, the regulator should restrict the thermal range to a small domain of roughly $\lesssim 4\pi T$. Turns out this question is closely related to the sharpness of the regulator, cf. Section 2.3.3. The flow for several regulators introduced in Section 2.3.3 is shown in Figure 7.2.

The dependence on the sharpness of the regulator can be explained pictorially rather easily. It probes how well the peak of the integrand aligns with the discrete Matsubara modes. If the kernel is sufficiently non-local the discrete modes probe roughly equal contributions, while in a very peaked integrand slight shifts see rather different values. Unfortunately, for the thermodynamic quantities it turns out that this doesn't result in

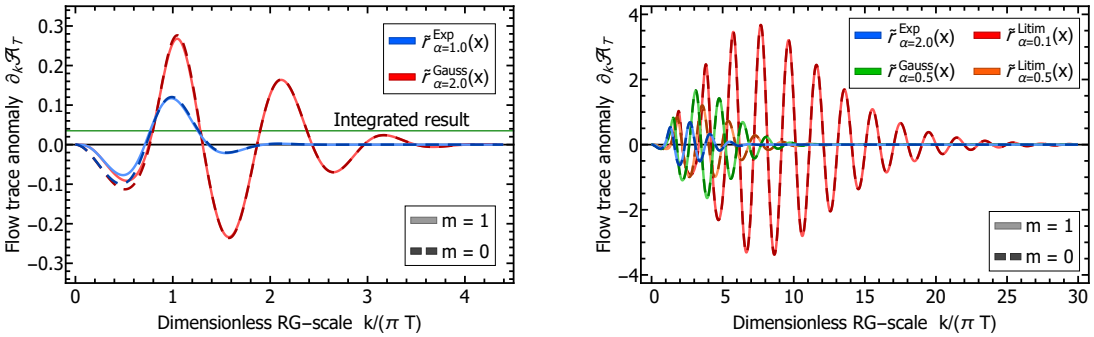

(a) Good regulator choices.

(b) Bad regulator choices.

Figure 7.2.: Flow of the thermal trace anomaly for different regulators introduced in Section 2.3.3 at an arbitrary temperature. The flow of a massive theory, as well as of a massless theory are shown together, underlining the spurious nature of the oscillations in the massive case.

a peaked flow, but rather in an oscillatory one. For reference we have also included the integrated result in the plot with the better regulator choices Figure 7.2a. Please note that even for these rather non-local regulators, cf. Section 2.3.3, the peaks of the flow are several times larger than the integrated result. In the figure shown bad choices for the regulator, Figure 7.2b, the line for the integrated result would not be distinguishable from zero. Please note that the regulators shown in Figure 7.2b are rather popular in the FRG. In particular the "optimized" Limit regulator amounts to a maximally bad choice for thermodynamics. Please note that this drastically changes when considering regulators that do not regulate frequencies, cf. the discussion above and [189].

The plots shown in Figure 7.2 show a striking, but expected, feature. Namely, that the flow for a massless theory is almost identical to that in a massive theory. After all, we do neither expect nor want the flow to be modified by mass scales $m \lesssim a\,k$ with a being a constant of order unity. Consequently, the only deviation between the two cases can be seen in Figure 7.2a for very small RG-scales k. While nothing about this so far is surprising, keep in mind that the thermal trace anomaly of a free, massless theory is trivial, i.e. it's zero. Hence, the oscillations in the massless case have to integrate to zero, shown the entirely spurious nature of these oscillations. While one might think that these oscillations only introduce a minor technical inconvenience, they are actually more deeply problematic. This already starts in pure gauge theories and QCD, where only results with limited precision are available. Furthermore, in these calculation so far an exponential regulator with $\alpha = 2$ or a Litim regulator way sharper than anything shown here has been used, cf. [64, 66, 339], making the subsequent determination of the thermal trace anomaly practically impossible.

It turns out, we can use the triviality of the thermal trace anomaly of a free, massless theory in order to improve the situation. This is done by simply subtracted the the part that trivially integrates to zero, i.e. the flow of a free, massless scalar field. Practically, this can be done by replacing the regularized propagator

$$\frac{1}{p^2 + m^2 + R_k(p)} \longrightarrow \frac{1}{p^2 + m^2 + R_k(p)} - \frac{1}{p^2 + R_k(p)}\,. \tag{7.10}$$

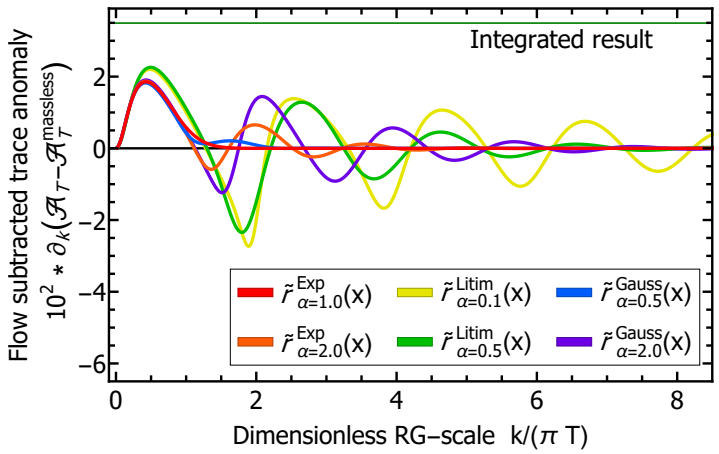

Figure 7.3.: Flow of the thermal trace anomaly after subtracting the part of a free, massless theory that integrates non-trivially to zero.

After doing so, the flows shown in Figure 7.2 improve significantly. The subtracted flows are shown in Figure 7.3. The first notable observation is that no amplitudes exceed now the integrated result. Furthermore, the two regulators that are the most non-local, cf. Figure 7.2a, now generate strictly positive flows, where all seizable contributions are limited to a acceptably small thermal range. The thermal range of the regulators shown in Figure 7.2b is reduced and their amplitudes decreased significantly. This gives hope that such an approach might work successfully in gauge theories, even in cases where the underlying elementary correlation functions have been obtained with regulators that are naively far from optimal for an application in thermodynamics. Please note that an exception to this is the Litim regulator without any smearing whose thermal range does not even decay after subtracting the massless case. To this day it is not know whether or not Lorentz invariant regulators exist that do not have the drawback of introducing oscillations.

7.1.2. Conclusion

In this section we have introduced a novel way of computing thermodynamic quantities in the FRG, namely via the flow of the trace anomaly. Furthermore, we discussed the necessary efficiency gain from subtracting the non-trivial oscillations already present for a trivially vanishing trace anomaly. The presented procedure should yield a robust procedure in gauge theories, which will be our next application.

The presented way of accessing the trace of the Energy-Momentum Tensor can be generalized to correlation functions thereof. This provides a fruitful perspective on the calculation of these correlation functions in the FRG. These correlation functions are need in order to access the full spectrum of the theory or extracting e.g. transport coefficients.

7.2. Transport coefficients of Yang-Mills

This section is in parts based on [14].

The modern phenomenological description of heavy ion collisions heavily relies on the use of viscous relativistic hydrodynamics, see e.g. [373–377]. A detailed description of relativistic hydrodynamics goes far beyond the scope of this work and we refer to the aforementioned references, as well as references therein. Hydrodynamics makes, of course, only up a part of the full dynamical evolution in such a collision. For reviews describing the entire tool chain employed see e.g. [378, 379] and references therein.

Focusing only on the hydrodynamical part, such a description allows to bridge, in principle, the gap between heavy ion experiments and calculations from first principles in QCD. A hydrodynamic description requires local thermal equilibrium, and consequently depends on the input from the underlying microscopic theory in equilibrium. This includes in particular the equation of state at leading order and the shear and bulk viscosity and next to leading order. Whereas, the latter are the leading order transport coefficients. The equation of state is already necessary at the level of ideal hydro and is closes the set of equations, see e.g. [139]. The transport coefficients enter the equations when going from ideal hydrodynamics to viscous hydrodynamics. They encode the linear deformability of the medium. In this section we want to present the calculation of the shear and bulk viscosity in Yang-Mills theory, based on a formulation in QFTs. Our general setting is very similar to [273], where the shear viscosity was obtained via the same approach.

7.2.1. Theoretical set-up

Transport coefficients can be accessed in QFTS via Kubo relations, which are intuitively easy to understand. Since we are coming from a hydrodynamic description, we are interested in the long-range behaviour of the system. Hence these relations should naturally be related to correlation functions in the vanishing momentum and frequency limit. Since hydrodynamics describes the evolution of collective modes, i.e. conserved quantities, we should also look at the corresponding correlation function, in particular correlation functions of the Energy-Momentum Tensor, which plays a central role in the hydrodynamic descriptions.

The shear viscosity η and the bulk viscosity ζ are related to the Energy-Momentum Tensor via, see e.g. [372, 380–382]

$$\begin{aligned} \eta &= \lim_{\omega\to 0} \frac{1}{20} \frac{\rho_{\pi\pi}(\omega, \boldsymbol{p}=0)}{\omega} \\ \zeta &= \lim_{\omega\to 0} \frac{1}{2} \frac{\rho_{\mathcal{P}\mathcal{P}}(\omega, \boldsymbol{p}=0)}{\omega} \,. \end{aligned} \tag{7.11}$$

Regarding the notation in (7.11), the symbol ρ symbolizes a spectral function, here the propagator of the indices. $\pi^{im} = \mathcal{T}^{im} - \delta^{im}\mathcal{P}$ is the traceless part of the spatial components of the Energy-Momentum Tensor, and correspondingly, $\mathcal{P} = \frac{1}{3}\mathcal{T}^{j}_{\ j}$ is proportional to the trace of the Energy-Momentum Tensor.

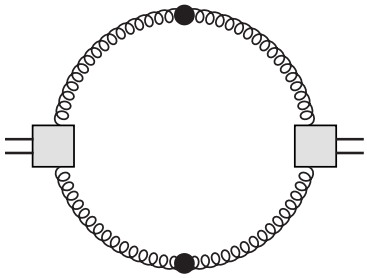

Figure 7.4.: One-loop representation of the Energy-Momentum Tensor correlation function from which the transport coefficients are extracted. The propagators are full gluon propagators and the grey boxes are EMT vertices.

The spectral function associated to an operator is given by the Fourier transformation of the commutator, cf. Section 6.1

$$\rho_{\mathcal{B}\mathcal{B}}(p) = \int \mathrm{d}^4x \, e^{\mathrm{i}\,px} \, \langle [\mathcal{B}(x), \mathcal{B}(0)] \rangle \ . \tag{7.12}$$

In the following we will not use an alternative way to Section 7.1 to calculate the correlation function of the Energy-Momentum Tensor, instead of taking variations of the QEA with respect to the metric, we use the Dyson-Schwinger representation of composite operators, cf. (2.13) and (2.72).

Doing so we arrive at a diagrammatic representation of the Energy-Momentum Tensor. Having eight field insertions in Yang-Mills, twice the number of fields appearing in the Energy-Momentum Tensor, the resulting expression contains terms with up to six loops. This requires truncation since a full numerical calculation thereof is beyond the current technical capabilities. Luckily, for our purposes, i.e. extracting the temperature dependence of transport coefficients, the connected subset of the diagrams is sufficient. It can be argued [273, 383, 384] that the disconnected pieces can be absorbed by dressing the EMT vertex appearing in the diagrams. The argument relies on the fact that the left-hand side is RG-invariant, while the right-hand side can only be RG-invariant if it can be expressed by fully dressed quantities. However, the only quantity that is not dressed by construction are the EMT vertices. As a result, the diagrammatic is reduced to the three-loop level. The aforementioned papers have found that the qualitative structure of the temperature dependence is already captured by one-loop contribution. Since we do not care for the purpose of our investigate about the asymptotic running and can live without knowing the normalization, we truncate the diagrammatic expression at the one-loop level. The only diagram contributing at the one-loop level is the polarization diagram, discussed at length throughout this work, see e.g. Section 6.1.3 and shown in Figure 7.4.

The equations are simple to derive, where the spectral function can either be obtained by analytically continuing the expression from Euclidean space-time or by directly working in Minkowski space-time. We have chosen the latter, following [273]. Due to the length of the equations we do not display them explicitly here, as there is no further insight gained.

As mentioned above, our calculation does not fix the multiplicative normalization of the Energy-Momentum Tensor, i.e. both transport coefficients are only determined up to a temperature independent multiplicative factor, which is the same for both. We will fix

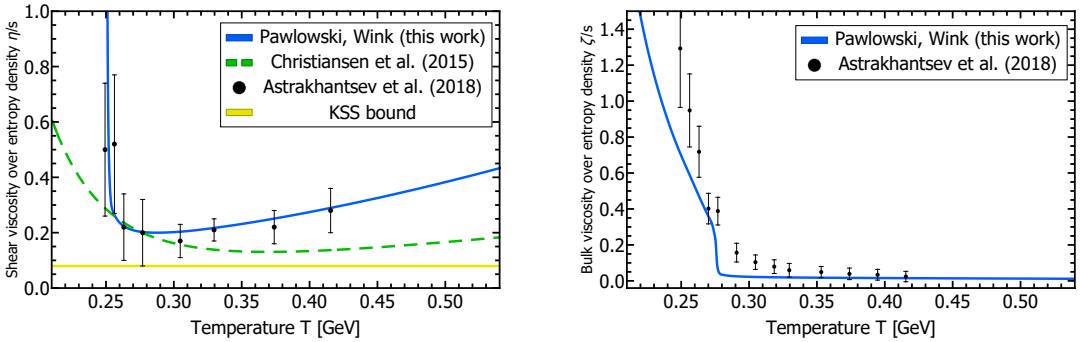

(a) Shear viscosity over entropy density.

(b) Bulk viscosity over entropy density.

Figure 7.5.: Shear and bulk viscosity of $SU(3)$ Yang-Mills theory. The phase transition is at $T_c \approx 277\,\mathrm{MeV}$ and of first order. The result for the shear viscosity is compared to the result our study is based upon, [273] and the more recent result of [279]. Whereas the bulk viscosity is only compared to the latter. A detailed discussion of the result can be found in the main text.

this factor by matching our result of the shear viscosity at one temperature to the results of a recent reconstruction from Lattice simulations [279]. We would like to note again that there is no additional value fixed for the bulk viscosity, but the same multiplicative prefactor enters.

7.2.2. Results

The diagrammatic representation, Figure 7.4, already shows, that the only elementary correlation function we require is the gluon propagator, or equivalently, the gluon spectral function. For the gluon spectral function we use the one presented and discussed in Section 6.4. While this spectral function was obtained from the vacuum propagator, we do not expect this approximation to be too bad. The argument is that the main change should be induced by an effective shift of the Debye mass. However, the mass gapping, which is around 850 MeV in vacuum, only lowers to about 500 MeV at the phase transition, as it can be extracted from Figure 3 in [339]. This means that there is a not too big shift in the effective mass entering the loop at scales above the temperature scales of interest. Hence we expect the resulting approximation of a vacuum spectral function to be sufficient for our calculation. The last ingredient we require is the strong coupling, appearing in the expressions of the vertices. Here we use the parametrization given in [273, 385], namely

$$\alpha_s(z) = \frac{1}{\beta_0}\frac{z^2-1}{z^2\log z^2}\,, \tag{7.13}$$

where z is a momentum variable, appropriately made dimensionless, and $\beta_0 = \frac{33}{12\pi}$ is the coefficient of the one-loop beta function of $SU(3)$ Yang-Mills.

Transport coefficients are usually best displayed as dimensionless ratio with the entropy density as reference quantity. This is because the transport coefficients only appear in ratios in the hydrodynamic equations, either with the entropy density or as ratio of transport coefficients. Here, we also choose the entropy density as normalization, as its customary, and use the result from Lattice calculations presented in [386].

Our results for the transport coefficients are shown in Figure 7.5. In both cases the position of the phase transition is clearly identifiable, which is located at $T_c \approx 277\,\mathrm{MeV}$.

In the shear viscosity over entropy density, Figure 7.5a, a minimum is located. This has the nice physical interpretation that the resistance to flow is lowest in the vicinity of the phase transition. Note however, that there is no strong argument that the phase transition should be located at precisely the minimum. Our result agrees nicely with the recent determination of the shear viscosity in [279]. There, the transport coefficients were extracted from a spectral reconstruction of the Euclidean EMT correlator, cf. Section 6.4. A comparison with the Kovtun-Son-Starinet (KSS) bound [387], which should provide a lower bound to η/s if the conjecture holds, with our result is rather pointless, since we fixed our normalization with one of the data points from [279]. Very interesting is also the comparison with the result from [273], which calculates the shear viscosity with the same diagrammatic representation of the EMT correlator, but uses a different spectral function as input. Namely, the one obtained via spectral reconstruction in [224]. The main difference between the spectral function obtained in that work, and the one we used here, cf. Section 6.4, is the sharpness of the peak. This reflects itself in a more pronounced minimum in the vicinity of the phase transition.

Turning to the bulk viscosity, Figure 7.5b, there's a rapid increase at the phase transition. Phenomenologically, transitioning from the high temperature phase to the low temperature phase would lead to cavitation in an hydrodynamical simulation. Apart from this our result is in good qualitative agreement with the reconstruction of [279] and it will be exciting to see if such a bulk viscosity, after extension to full QCD, can be used in a relativistic hydrodynamics simulation, while still describing the data.

7.2.3. Conclusion

In this section we put forward results for the leading order transport coefficients, the shear and bulk viscosity, in $SU(3)$ Yang-Mills theory. For the shear viscosity our result constitutes an improvement over a previous calculation [273] within Functional Methods, while its the first determination of the bulk viscosity in such a setting. Both transport coefficients clearly show the phase transition and it will be interesting to explore their phenomenological implications in hydrodynamic simulations in the future.

7.3. Effective transport descriptions of QCD

This section is in parts based on [3].

In the previous section we have discussed the calculation of equilibrium coefficients for use in relativistic hydrodynamic simulations. Here we would like to go one step further and start investigate the non-equilibrium evolution from a QFT inspired perspective. In particular, we want to use the fact that the linear response function encode, like their name suggests, the response from a perturbation away from equilibrium. Such a study for the chiral dynamics can be seen as complementary to a relativistic hydrodynamics simulation. Both approaches can be coupled together and can be seen as a precursor before true non-equilibrium calculations from first principles in QFTs become available.

In order to verify the existence of a possible critical endpoint in the phase diagram of QCD, a more detailed understanding of the connection between the equilibrium phase structure and the highly dynamical non-equilibrium situation created in heavy-ion collisions needs to be established. Only then firm conclusions can unambiguously be drawn from fluctuation measurements, see e.g. [388–395], which are currently the main experimental tool to study the phase structure of QCD. For recent theoretical works see e.g. [396–400] and references therein. The basic assumption when looking for a critical endpoint with the use of fluctuation measurements is that the fluctuations of the net baryon density are expected to be enhanced in the critical region [401, 402]. In this section we want to investigate the embedding of such critical fluctuations, relative to the non-critical fluctuations. This question is closely related to the size of the critical region, which is to date unknown, if even present, but might be rather small [403].

First attempts in this direction were based on non-equilibrium chiral fluid dynamics studies connected with an effective mean-field model for QCD [404–406]. A recent approach [407] studies a fully interacting stochastic description of the non-equilibrium evolution of fluctuation observables, see also [7, 408–410]. In the present work, we explore a novel method which is capable of connecting the equilibrium physics of QCD, obtained beyond mean field within the FRG framework applied to QCD, with the non-equilibrium evolution around an equilibrium state in a systematic manner. In a first study, we apply this method to the time-evolution of the critical mode around the various equilibrium states in the phase diagram of a 2+1 flavour Quark-Meson model. This is achieved by solving a transport equation with the corresponding linear response functions of a given equilibrium state as input.

In Section 7.3.1, we describe the calculation of the necessary equilibrium input, i.e. the effective potential and the spectral functions of the sigma meson. In Section 7.3.2, the dynamical evolution of the critical mode around this equilibrium result is described.

7.3.1. Equilibrium linear response functions

The calculation of equilibrium correlation functions needed as input for the transport evolution utilizes the Functional Renormalization Group, the setting is quite similar to the one presented in Section 6.2. The advantage of the FRG in the present context is that it allows for the computation of the phase structure, i.e. the effective potential, and momentum dependent correlation functions within a unified framework.

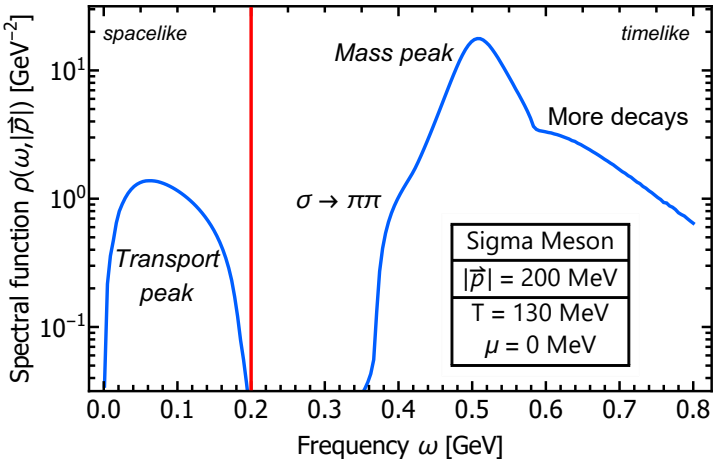

Figure 7.6.: Spectral function of the sigma meson at $T = 130$ MeV, $\mu = 0$ MeV in the phase diagram. The transport peak and the mass peak are associated with the diffusion in the transport equation. A detailed discussion of the seen structures can be found in e.g. [1].

The equilibrium part of our work, i.e. the equation of state and the equilibrium correlation functions, is based on a 2+1 flavour study of a low-energy effective description of QCD presented in [193], where the dynamics of constituent quarks as well as the lowest scalar- and pseudoscalar meson nonets are taken into account. For other works exploring the 2+1 flavour Quark-Meson model and extensions thereof, see [28, 369, 411–413]. It captures, by design, the relevant physical effects at small chemical potential μ and temperatures $T \lesssim T_c$. Additionally, it features a critical endpoint which is in the same static universality class as the one potentially present in QCD. Therefore this model provides a well-suited base for studying how dynamical non-equilibrium effects manifest themselves in observables.

In general, spectral functions can be obtained either via analytically continuing numerical data, see e.g. [2] or via a direct computation from analytically continued equations, see e.g. [217, 219]. If possible, the latter is preferred and also the option utilized in this work. The spectral functions of the sigma meson are calculated similarly to [1, 165]/Section 6.2 with suitable modifications in order to take non-trivial wave-function renormalizations into account. As a result we have access to the two-point correlator $\Gamma^{(2)}_{\sigma\sigma}(\omega, |\vec{p}|)$, depending on an external frequency ω and an external momentum $\vec{p}$, as well as momentum independent vertices $\Gamma^{(n)}_{\sigma^n}$ which are extracted from the full effective potential computed in [193]. An exemplary spectral function is shown in Figure 7.6. The two main features that influence the behaviour of the dynamical evolution are the transport peak and the mass peak. The transport peak, if present at small frequencies $\omega < |\vec{p}|$, dominates the long range behaviour of the sigma field. The mass peak, instead, becomes the driving force for the evolution dynamics when the transport peak is absent, e.g. in the vacuum. In total, the appearing structures and features are the same as discussed in Section 6.2 and we refer to this section for a discussion. The only difference is a modification of the scales and more decay channels due to working in 2+1 flavours and not only the $O(4)$-model sub-part.

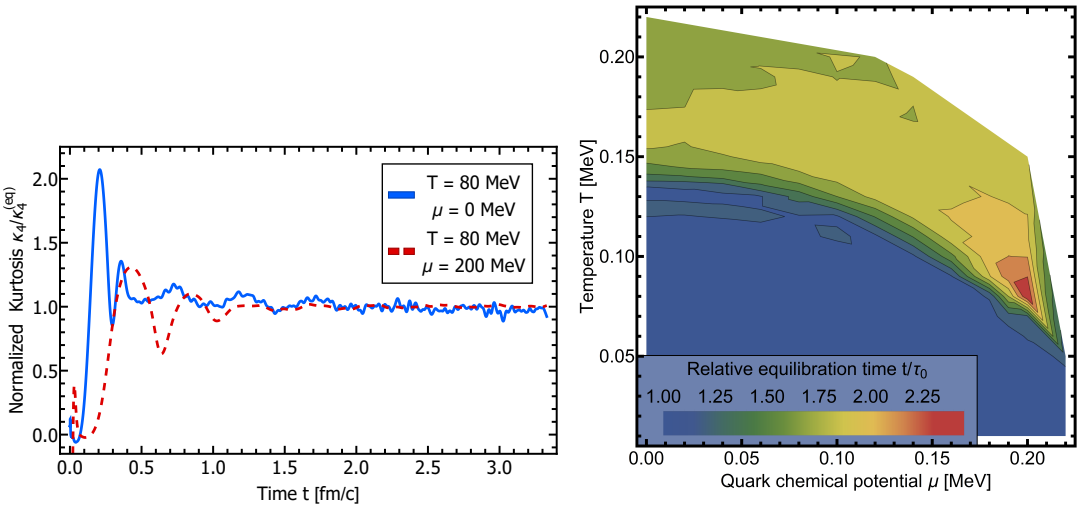

Figure 7.7.: Left: Scaled kurtosis as a function of time for a quench from high T to two different points in the phase diagram. Within statistical deviations, the equilibration time is found to be significantly increased near the critical endpoint (red, dashed curve) compared to a quench far away from it (blue, solid curve). Right: Equilibration time t in units of $\tau_0 \simeq 0.4$ fm/c in the QCD phase diagram based on the analysis of the scaled kurtosis in the quench scenario (see left panel).

7.3.2. Time-evolution of fluctuation measures

We are now in the position to study the time-evolution of the critical mode and its event-by-event fluctuations. For this purpose, we solve the Langevin-type transport equation

$$\frac{\mathrm{d}\Gamma}{\mathrm{d}\sigma} = \xi \,. \tag{7.14}$$

In (7.14), the equation of motion contains a kinetic term related to the real part of $\Gamma^{(2)}_{\sigma\sigma}$, a diffusion term sensitive to the imaginary part of $\Gamma^{(2)}_{\sigma\sigma}$, and the effective potential, discussed in Section 7.3.1, while ξ represents the noise field chosen such that the fluctuation-dissipation balance is guaranteed, see (7.15).

For the numerical results presented in the following we consider the critical mode to be spatially isotropic, i.e. $\sigma(\vec{x},t) = \sigma(r,t)$, where we split $\sigma = \sigma_0 + \delta\sigma$. We study the time-evolution of the critical fluctuations for a system subject to a sudden quench from high temperatures to a specific point in the QCD phase diagram. Accordingly, the system is initialized such that $\sigma(r, t=0) = 0$ and $\partial_t\sigma(r, t=0) = 0$ which implies that the initial fluctuations $\delta\sigma(t=0)$ are of the magnitude of the equilibrium value σ_0 after the quench. Moreover, we consider spatially constant Gaussian white noise, with zero mean and a variance given as [404]

$$\langle \xi(t)\xi(t')\rangle = \frac{1}{V}\delta(t-t')m_\sigma\eta\coth\left(\frac{m_\sigma}{2T}\right) \,, \tag{7.15}$$

where the diffusion coefficient η is extracted from the imaginary part of $\Gamma^{(2)}_{\sigma\sigma}$, such that

the fluctuation-dissipation theorem is recovered. To be more precise, η is given by the height of the transport peak bump in the imaginary part of the two-point function.

In Figure 7.7 (left panel), we show, as an example, the time-evolution of the kurtosis scaled by its late-time equilibrium limit for the quench to two different points in the phase diagram. Far away from the critical endpoint the scaled kurtosis exhibits a rather quick equilibration while close to it the corresponding time scale is clearly increased. For the quench through the phase boundary we furthermore observe that the equilibrium value is approached from above as the equilibrium kurtosis is larger near the phase boundary than in the low-temperature phase.

Based on our preliminary results for the scaled kurtosis in the quench scenario, we may estimate the equilibration time of the critical fluctuations within the QCD phase diagram. This is shown in Figure 7.7 (right panel). One can clearly identify both the phase boundary and the region near the critical endpoint and observe the expected increase of the equilibration time in that region. Nevertheless, we find this increase to be rather moderate suggesting that phenomena associated with critical slowing down are only moderately pronounced. This hints towards equilibrium dominated measurements and, thus, to the feasibility of studying the QCD phase diagram by means of heavy-ion collisions.

7.3.3. Conclusion

In this section we developed a novel method to study dynamical non-equilibrium effects in the phase diagram of the 2+1 flavour Quark-Meson model. This method is valid not only in the scaling region but across the entire region of the phase transition in QCD because it contains critical and non-critical contributions to fluctuation observables in a single framework. It builds upon the dynamics of a quantum field around an equilibrium state with an appropriate Langevin-type transport equation. We study the time-evolution of the critical mode from a quench at high temperatures to different points within the phase diagram. The time-evolution of different cumulants of the sigma field was calculated, and an equilibration time was extracted from the kurtosis. We find a moderate increase of the equilibration time near the phase boundary and when approaching the critical point. A region of critical slowing down is clearly identifiable, but even close to the critical point only an enhancement of roughly a factor of two is found.

In order to connect even closer to the full dynamics of a heavy-ion collision, the scenario of a temperature quench will be subsequently improved towards the full dynamics of the underlying quantum field theory.

8. Summary & Conclusion

In this work we have explored connections between first principle descriptions of QFTs and the phenomenology of experiments of strongly correlated systems. This concerns particularly quantum chromodynamics and the long-term goals of uncovering the mechanism of confinement, as well as exploring the phase structure. The main experimental tool currently available to explore both questions are heavy-ion collisions. Here we explored several aspects of bridging the gap between first principle descriptions of QCD using Functional Methods and phenomenologically interesting observables. Throughout we outlined how these calculations can be split into two distinct parts: Firstly, the determination of the elementary correlation functions of the system, i.e. the moments of the Quantum Effective Action. Secondly, the extraction of observables from said correlation functions. This splitting occurs naturally in Functional Methods, since these approaches are fundamentally formulated in terms of the elementary correlation functions, this is explained in great detail in Chapter 2.

Turning to QCD, the second steps necessity of accessing observables, i.e. gauge invariant correlation functions, subsequently becomes obvious, since the elementary correlation functions are gauge dependent in QCD. In Chapter 3 we introduced the application of Functional Methods to QCD. Here we did not only recap the required technical prerequisites for the remainder of this work, but also entered into an extended of the (modified) Slavnov-Taylor Identities in Section 3.4, which ensure the gauge invariance of observables. The modern formulation presented in this section nicely fits the language of elementary correlation functions and was the basis for the development of the software package *QMeS : Derivation*. It's designed to expand quantum master equations in terms of moments, the elementary correlation functions. Its strength is a theory independent formulation, working in the superfield formalism introduced in Section 2.4.

The following three Chapters, Chapters 4 to 6, concerned the calculation of elementary correlation functions in QCD and low energy effective theories thereof.

In Chapter 4 we discussed the field dependence of said correlation functions, which is the dominant dynamical dependence in applications of derivative expansions. Physics wise, this is of enormous in the vicinity of phase transitions. We introduced the use of Discontinuous Galerkin methods to the flow equations arising in the FRG. This comes with some major advantages: The first is the adaptation of a hydrodynamic language, which comes naturally, since the applicability of Discontinuous Galerkin methods was achieved by casting the flow equation into a form that's form equivalent to hydrodynamic equations. Terms such as flow, which are being used a lot in the context of RG flow equations are naturally given a precise meaning. Additionally, this can be used to make numerics unconditionally stable, which has previously been a problem. Applying these methods to the O(N)-model in the large N limit, we confirmed the expected, excellent numerical performance and found the formation of discontinues in the vicinity of first order phase transitions. In particular, we found that the position of the discontinuity in the effective potential shows a scaling behaviour, a very exciting discovery. Furthermore, we demonstrated that the numerical advantages carry over to the case of finite N and

fermions by calculating the well known phase diagram of the Quark-Meson model in LPA.

In Chapter 5 we covered the Euclidean momentum dependence of the elementary correlation functions. In particular, in Section 5.1 we studied the O(N)-model at finite temperature, exploring the use of Lorentz invariant regulators in such a setting, as well as resolving the elementary correlation function between the Matsubara modes, requiring analytic continuation of the flow equations. In Section 5.2 we explored the range of validity of the Euclidean momentum dependence in the Quark-Meson model, as low energy effective theory of QCD. Hereby, we focused on the systematic determination of bound state masses and their properties by utilizing dynamical bosonisation.

Chapter 6 extends the resolution of momentum dependencies to Minkowski space-time, a topic of utmost importance for accessing experiment relevant observables. The chapter starts by reviewing spectral representations and extending the very well known Källén-Lehmann spectral representation to the case of three-point functions in Section 6.1.2.2. In the same section we discussed how spectral representations can be used to make calculations in Minkowski space-time numerically feasible in Functional Methods. Using this methodology we also explored the spectral functions of a O(4)-theory as a function of temperature across a phase transition, in the same setting as the aforementioned Euclidean one. It also allowed us in Section 6.3 to solve Dyson-Schwinger equations for the two-point function of a scalar theory in Minkowski space-time. Using spectral representations enabled the use of dimensional regularization, a highly desirable regularization scheme.

Apart from directly calculating in Minkowski space-time, we also developed additional spectral reconstruction techniques, based on the insight from doing calculations, to gain access to spectral functions. In Section 6.4 we based the reconstruction on a suitable ansatz of the complex structure of the analytically continued retarded propagator. This resulted in a reconstruction of the gluon spectral function in Landau gauge Yang-Mills theory, featuring a very pronounced peak at $\approx 850\,\mathrm{MeV}$. Additionally, our result for the spectral function is negative in the deep IR, a fact that has not been seen before. We obtained an analytical expression, connecting the deep IR of the Euclidean propagator and of the spectral function, showing that it even has to be negative. In a further development we made use of neural nets for the Bayesian inference step of obtaining the coefficients of the basis of the propagator., which we benchmarked and compared against more conventional methods extensively in Section 6.5.

Finally, we made use of the elementary correlation functions and discussed the determination of observables based on them in Chapter 7. In this thesis we explored three different applications thereof. Firstly, the calculation of the thermodynamic properties, or the be more precise, the trace anomaly. The calculation in Section 7.1 is directly based on a metric variation of the Quantum Effective Action and can therefore be extended to correlations of the Energy-Momentum Tensor. We discussed the numerical feasibility using different regulators in the FRG in this context and showed how such calculations can be made significantly more efficient. Secondly, we calculated the shear and bulk viscosity of Yang-Mills theory in Section 7.2. The results for both transport coefficients are in agreement with expectations and other recent results. Lastly, we used the Quantum Effective Action the sense of a collection of linear response function in order to access the non-equilibrium evolution of the 2+1 flavour Quark-Meson model in Section 7.3. Here we extracted the equilibration time of the critical mode from a quench from high temperatures to points in the phase diagram. While we clearly find critical slowing down in the vicinity of the critical point, the region of critical slowing down seem to be very small.

This, coupled with the equilibration time scale of $\sim 1\,\mathrm{fm/c}$, is very positive in the light of investigating the phase structure of QCD with heavy-ion collisions.

To conclude, we explored the full tool chain of Function Methods, from first principles in QFTs to phenomenologically relevant observables in this thesis. This demonstrates the impressive power of such approaches. This feature, of accessing not only Euclidean correlation functions, but also the Minkowski space-time once and even out-of-equilibrium correlation functions, all within the same framework is particularity appealing. Utilizing the development of the underlying methods achieved, among other things, in this thesis: unravelling discontinuities in the solution of the effective potential in the vicinity of first order phase transitions; showed that the gluon spectral function has to be negative in the deep IR and is most likely sharply peaked; calculated the shear and bulk viscosity in Yang-Mills based on this spectral function; estimated the equilibration time of the critical mode in heavy-ion collisions.

A. Conventions

A.1. Legendre polynomials

In Section 4.1 we have introduced a dual expansion basis: $\psi_n(x)$ for the modes and $l_i^k(x)$ for the nodes, c.f. (4.3). The simplest, practical choice for the mode basis $\psi_n(x)$ is the set of orthogonal Legendre polynomials P_n, which are part of the large family of Jacobi polynomials $P^{(\alpha,\beta)}$.

The Jacobi polynomials $P_n^{(\alpha,\beta)}(x)$ are the solution to the singular Sturm-Liouville problem

$$\frac{\mathrm{d}}{\mathrm{d}x}\left[(1-x^2)\omega(x)\frac{\mathrm{d}}{\mathrm{d}x}P_n^{(\alpha,\beta)}(x)\right] = -\lambda_n\omega(x)P_n^{(\alpha,\beta)}(x)\,, \tag{A.1}$$

defined on the interval $[-1,1]$. In (A.1) $\omega(x) = (1-x)^\alpha(1+x)^\beta$ is the weight function and $\lambda_n = n(n+\alpha+\beta+1)$ are the eigenvalues. The Jacobi polynomials satisfy the weighted orthonormality relation

$$\int_{-1}^{1}\mathrm{d}x\;\omega(x)P_n^{(\alpha,\beta)}(x)P_m^{(\alpha,\beta)} = \delta_{nm}\,. \tag{A.2}$$

To construct the polynomials, it is convenient to use their recurrence relation, see e.g. [136], which relates the higher order P_n to the lower ones,

$$xP_n^{(\alpha,\beta)}(x) = a_nP_{n-1}^{(\alpha,\beta)}(x) + b_nP_n^{(\alpha,\beta)}(x) + a_{n+1}P_{n-1}^{(\alpha,\beta)}(x)\,, \tag{A.3}$$

where the coefficients are defined as

$$\begin{aligned} a_n &= \frac{2}{2n+\alpha+\beta}\sqrt{\frac{n(n+\alpha+\beta)(n+\alpha)(n+\beta)}{(2n+\alpha+\beta-1)(2n+\alpha+\beta+1)}} \\ b_n &= -\frac{\alpha^2-\beta^2}{(2n+\alpha+\beta)(2n+\alpha+\beta+2)}\,. \end{aligned} \tag{A.4}$$

The recurrence relation can be used once the initial polynomials are defined,

$$\begin{aligned} P_0^{(\alpha,\beta)}(x) =& \sqrt{2^{-\alpha-\beta-1}\frac{\Gamma(\alpha+\beta+2)}{\Gamma(\alpha+1)(\beta+1)}} \\ P_1^{(\alpha,\beta)}(x) =& \frac{1}{2}P_0^{(\alpha,\beta)}(x)\sqrt{\frac{\alpha+\beta+3}{(\alpha+1)(\beta+1)}} \\ & [(\alpha+\beta+2)x + (\alpha-\beta)]\,. \end{aligned} \tag{A.5}$$

Derivatives can be computed form the lower order polynomials using the important relation

$$\frac{\mathrm{d}}{\mathrm{d}x}P_n^{(\alpha,\beta)}(x) = \sqrt{n(n+\alpha+\beta+1)}P_{n-1}^{(\alpha+1,\beta+1)}(x). \tag{A.6}$$

The Legendre polynomials are the special case $\alpha = \beta = 0$, i.e. $P_n(x) = P_n^{(0,0)}$ and their properties and relations are easily obtained from the ones for the Jacobi polynomial.

In our implementation of the DG discretization method we used the following convention for $\psi_n(x)$,

$$\psi_n(x) = \sqrt{\frac{2n-1}{2}} P_{n-1}(x)\,. \tag{A.7}$$

The nodal basis functions are chosen as the standard Lagrange interpolating polynomials,

$$l_i(x) = \prod_{j=1\, j\neq i} \frac{x - x_j}{x_j - x_i}\,, \tag{A.8}$$

which are well define and unique if the nodes x_i are all distinct. It is advantageous to select the nodes such that the transformation matrix between the modal representation $\hat{u}_n$ and the nodal representation $u(x_i)$ is well conditioned. It can be shown, see e.g. [136], that the Legendre-Gauss-Lobatto (LGL) points, defined as the N zeros of the equation

$$(1 - x^2) P_N'(x) = 0\,, \tag{A.9}$$

amount to an optimal choice.

A.2. Additional definitions and technical details for Section 5.2

In this section additional informations regarding our ansatz for the effective action (5.10) and its solution are provided. Furthermore some additional definitions are introduced, used to keep the flow equations as simple as possible.

A.2.1. Regulator and propagators

The momentum independent part of the mesonic two-point function can be obtained from the effective potential

$$\begin{aligned}\Gamma^{(2)}_{\vec{\pi}}(p=0) &= \partial_\rho V(\rho)\,,\\ \Gamma^{(2)}_{\sigma}(p=0) &= \partial_\rho V(\rho) + 2\rho\,\partial^2_\rho V(\rho)\,,\end{aligned} \tag{A.10}$$

which can be obtained from matching the corresponding flow equations. Instead of solving the flow for the full mesonic two-point functions only the momentum dependent part needs to be considered:

$$\Delta\Gamma^{(2)}_{i,k}(p) = \Gamma^{(2)}_{i,k}(p) - \Gamma^{(2)}_{i,k}(0)\,, \quad i \in \{\sigma, \vec{\pi}\}\,. \tag{A.11}$$

For the flows of the momentum dependent part only the polarization diagrams have to be calculated, as the four-point functions do not carry any momentum dependence in our truncation and all tadpoles vanish as a result. The mesonic wave-function renormalizations are directly related to the two-point functions by

$$Z_{i,k}(p) = p^{-2}\Delta\Gamma^{(2)}_{i,k}(p)\,. \tag{A.12}$$

The fermion mass and the Yukawa coupling are related by

$$m^2_{q,k}(p) = \frac{\rho}{N_f} h_k(p,-p)\,. \tag{A.13}$$

As a regulator shape function we are using a standard exponential regulator

$$\begin{aligned}r_B(x) &= \frac{x^{m-1}}{e^{x^m}-1}\\ r_F(x)+1 &= \sqrt{r_B(x)+1}\,,\end{aligned} \tag{A.14}$$

resulting in the following full regulators

$$\begin{aligned}R_{i,k}(p) &= Z_{i,k}(0)p^2\, r_B\left(\frac{p^2}{k^2}\right)\,, \quad i\in\{\sigma,\vec{\pi}\}\\ R_F(p) &= \hat{R}(p)\not{p} \quad \hat{R}(p) = Z_q(0) r_F\left(\frac{p^2}{k^2}\right)\,.\end{aligned} \tag{A.15}$$

We define the following mesonic propagators ($i\in\{\sigma,\vec{\pi}\}$)

$$G_i(p) = \frac{1}{Z_i(p)p^2 + R_{i,k}(p) + \Gamma^{(2)}_i(0)}\,. \tag{A.16}$$

In addition we can define an effective (scalar) quark propagator, entering all loop functions

$$\begin{aligned}G_q(p) &= \frac{1}{[Z_{rq}(p)]^2 + m^2_q(p)}\\ Z_{rq}(p) &= Z_q(p) + \hat{R}(p)\,.\end{aligned} \tag{A.17}$$

A.2.2. Effective potential

The effective potential $V_k(\rho)$ is solved using a Taylor expansion about the IR minimum of the potential including the explicit symmetry breaking term. The bare expansion point is kept fix, therefore greatly increasing the stability of the equations [185]. It has been verified that the results are independent of the order of the Taylor expansion. The use of a Taylor expansion can loosely be justified with the results of Section 4.2.

A.2.3. Initial values

Our initial values are chosen such that the physical values for the quark mass $\bar{m}_q = 298\,\text{MeV}$, the expectation value of the chiral condensate $\sigma_{\text{min}} = 93\,\text{MeV}$, the pion mass $\bar{m}_{\vec{\pi}} = 139\,\text{MeV}$ and the curvature mass of the sigma meson $\bar{m}_\sigma = 495\,\text{MeV}$ are obtained. Since the sigma meson is a scattering state in this model, it is not possible to directly assign it a pole mass, therefore we resorted to the curvature mass, which we fixed slightly higher than the physical mass. More details on the relation between curvature and pole masses, can be found in Section 5.2.6 or e.g. [1]. The flow is initiated at $\Lambda_{\text{UV}} = 950\,\text{MeV}$, in accordance with our discussion in Section 5.2.3.2. The initial potential is assumed to be quadratic

$$V_{k=\Lambda_{\text{UV}}} = a_1(\rho - \rho_0) + \frac{a_2}{2}(\rho - \rho_0)^2\,, \tag{A.18}$$

where ρ_0 is the expansion point. All other orders of the effective potential are zero. The wave-function renormalizations are set to unity at the UV cutoff. For completeness we also state our initial values for our full truncation considered in this work

$$\begin{aligned} a_1 &= (2638\,\text{MeV})^2 \\ a_2 &= 50 \\ h_\Lambda &= 18.085 \\ \rho_0 &= 28.32\,\text{MeV}\,. \end{aligned} \tag{A.19}$$

A.2.4. Dynamical Hadronization

Our dynamical hadronization procedure follows [64]. To this end we parametrize the scale dependence of the auxiliary field as

$$\begin{aligned} \dot{\sigma}(p) =& \frac{1}{\sqrt{2N_f}} \int_q \dot{A}\,(p-q,q)\,\bar{q}(p-q)q(q) \\ \dot{\vec{\pi}}(p) =& \int_q \dot{A}\,(p-q,q)\,\bar{q}(p-q)\mathrm{i}\gamma_5\vec{\tau}q(q)\,, \end{aligned} \tag{A.20}$$

where the dot denotes the derivative with respect to the RG-time t. In [64] it was found that a weighted sum between total and relative momenta captures the full momentum dependence quite accurately

$$\dot{A}(p_1,p_2) = \dot{A}\left((p_1+p_2)^2 + \frac{1}{4}(p_1-p_2)^2\right)\,. \tag{A.21}$$

As a result the flow of the corresponding channel in the four-Fermi interaction λ_k is set to zero

$$\begin{aligned} \partial_k \lambda(p,-p,p) =& \text{Flow}\left[\lambda(p,-p,p)\right] - \dot{A}(p^2) h(p^2) \\ \dot{A}(p^2) =& \frac{\text{Flow}\left[\lambda(p,-p,p)\right]}{h_k(p^2)} \,. \end{aligned} \tag{A.22}$$

B. Technicalities

B.1. BRST transformation of the cutoff term

Here we consider (minus) the right hand side of (3.94),

$$\langle \mathfrak{s}\, \Delta S_k \rangle + \frac{\delta \Gamma_k}{\delta \mathcal{Q}} \cdot \frac{\delta \Delta S_k}{\delta \Phi} = \langle \mathfrak{s}\, \Delta S_k \rangle + \mathfrak{s}_\Gamma\, \Delta S_k \,. \tag{B.1}$$

where

$$\mathfrak{s}_\Gamma\, \Phi_i = \frac{\delta \Gamma_k}{\delta \mathcal{Q}^i} = -\frac{\delta W_k}{\delta \mathcal{Q}^i} \,, \tag{B.2}$$

see (3.90). This leads us to

$$\left\langle (\mathfrak{s}\, \Phi_i) R^{ij} \Phi_j \right\rangle + (\mathfrak{s}_\Gamma\, \Phi_i) R^{ij} \Phi_j = \frac{\delta}{\delta Q i} \left\langle R^{ij} \Phi_j \right\rangle = R^{ij} \frac{\delta}{\delta J^j} \frac{\delta}{\delta Q^i} W_k[J, \mathcal{Q}] \,, \tag{B.3}$$

where we have used (B.2) twice. We have also used, that the derivatives w.r.t. to J_j and $\mathcal{Q}_i$, that are contracted with the regulator R^{ij}, commute. Now we use (B.2) again, and arrive at

$$\left\langle (\mathfrak{s}\, \Phi_i) R^{ij} \Phi_j \right\rangle + (\mathfrak{s}_\Gamma\, \Phi_i) R^{ij} \Phi_j = -R^{ij} \frac{\delta}{\delta J^j} \frac{\delta \Gamma_k[\Phi, \mathcal{Q}]}{\delta Q^i} = -R^{ij} G_{jl} \frac{\delta^2 \Gamma_k[\Phi, \mathcal{Q}]}{\delta \Phi_l \delta Q^i} \,, \tag{B.4}$$

where we have used the usual trick for rewriting $\delta / \delta J$ as $G \cdot \delta / \delta \Phi$.

B.2. Method of characteristics

In this appendix we present the analytic solution of Equation (4.22). The PDE is a scalar quasilinear partial differential equation in conservative form, therefore an implicit solution can be obtain using the method of characteristics [414]. The equation in conservative form is

$$\partial_t u(t,\rho) + \partial_\rho \left(A_d \frac{(\Lambda e^{-t})^{d+2}}{(\Lambda e^{-t})^2 + u(t,\rho)} \right) = 0\,, \tag{B.5}$$

and can be express in a quasilinear form performing the derivative on the flux,

$$\partial_t u(t,\rho) - A_d \frac{(\Lambda e^{-t})^{d+2}}{\left[(\Lambda e^{-t})^2 + u(t,\rho)\right]^2} \partial_\rho u(t,\rho) = 0\,, \tag{B.6}$$

combined with the initial condition

$$u(0,\rho) = u_0(\rho)\,. \tag{B.7}$$

The solution can be found by introducing the characteristic curves that are the solution of

$$\begin{aligned} \frac{\mathrm{d}t(s)}{\mathrm{d}s} &= 1 \\ \frac{\mathrm{d}\rho(s)}{\mathrm{d}s} &= -A_d \frac{(\Lambda e^{-t(s)})^{d+2}}{\left[(\Lambda e^{-t(s)})^2 + u(s)\right]^2} \\ \frac{\mathrm{d}u(s)}{\mathrm{d}s} &= 0\,, \end{aligned} \tag{B.8}$$

combined with the initial conditions

$$\begin{aligned} t(0) &= 0 \\ \rho(0) &= \rho_0 \\ u(0) &= u_0(\rho_0)\,. \end{aligned} \tag{B.9}$$

This system of ordinary differential equation is equivalent to the original partial differential equation (B.6) if we define

$$u(s) = u(t(s), \rho(s))\,. \tag{B.10}$$

The system (B.8) can easily be integrated, noting that $u(s)$ is constant along the characteristic and $t(s)$ is the curve parameter. The result can be written as

$$u(s) = u_0(\rho_0) \quad \text{and} \quad t(s) = s = t \tag{B.11}$$

and

$$\rho(t) = \rho_0 - A_d \int_0^t \frac{(\Lambda e^{-s})^{d+2}}{\left[(\Lambda e^{-s})^2 + u_0(\rho_0)\right]^2} \mathrm{d}s\,. \tag{B.12}$$

The integral can be carried out, leading to

$$\begin{aligned}\rho(t) = \rho_0 - \frac{A_d \Lambda^d}{2}\Bigg[&\frac{e^{-dt}}{u_0(\rho_0) + (\Lambda e^{-t})^2} - \frac{1}{u_0(\rho_0) + \Lambda^2} \\ &- \frac{d(\Lambda e^{-t})^{d-2}}{(d-2)\Lambda^d}\, {}_2F_1\left(1, \frac{2-d}{2}, \frac{4-d}{2}, -\frac{u_0(\rho_0)}{(\Lambda e^{-t})^2}\right) \\ &+ \frac{d\Lambda^{-2}}{d-2}\, {}_2F_1\left(1, \frac{2-d}{2}, \frac{4-d}{2}, -\frac{u_0(\rho_0)}{\Lambda^2}\right)\Bigg], \end{aligned} \tag{B.13}$$

where ${}_2F_1$ is the Gaussian or ordinary hypergeometric function, see e.g. [415]. The equation (B.13) is a transcendental equation between ρ_0, the position at the initial RG-time where u has the value $u_0(\rho_0)$ and ρ, which is the position at RG-time t where u has the same value. Formally this can now be inverted obtaining

$$\rho_0 = \rho_0(t, \rho)\,, \tag{B.14}$$

giving the initial position of the value $u_\Lambda(\rho_\Lambda)$ as a function of the final one $\rho(t)$. The solution can be construct using this inverse function as

$$u(t, \rho) = u_0(\rho_0(t, \rho)). \tag{B.15}$$

Practically, except for very simple cases, the solution of the transcendental equation (B.13) cannot be achieved analytically. Therefore, the inversion is performed numerically.

The equation (B.13) can be used to find a simple expression for the RG-time evolution of the minima of the potential, indeed if one use that $u_0(\rho_0) = 0$ and hence ${}_2F_1 = 1$, we obtain

$$\rho_{\min}(t) = \rho_{\min}(0) - \frac{A_d \Lambda^{d-2}}{d-2}\left[1 - e^{-(d-2)t}\right]. \tag{B.16}$$

B.3. Shock propagation and detection

B.3.1. Position of the shock

Consider an interval $[\rho_{\mathrm{L}}, \rho_{\mathrm{R}}]$ that contains the position of the discontinuity at a given RG-time t, namely $\rho_{\mathrm{L}} \leq \xi(t) \leq \rho_{\mathrm{R}}$. Additionally, the interval must be chosen small enough that it only contains a single discontinuity. If this is not the case, it can always be split in to multiple intervals. The integral in $\rho-$space of our equation of interest (4.22) on this interval is

$$\frac{\mathrm{d}}{\mathrm{d}t}\int_{\rho_{\mathrm{L}}}^{\rho_{\mathrm{R}}} \mathrm{d}\rho\; u(\rho,t) - \int_{\rho_{\mathrm{L}}}^{\rho_{\mathrm{R}}} \mathrm{d}\rho\; \partial_\rho f(t,u(\rho)) = 0\,. \tag{B.17}$$

Splitting the integral around the discontinuity results in

$$\begin{aligned}&\frac{\mathrm{d}}{\mathrm{d}t}\int_{\rho_{\mathrm{L}}}^{\xi(t)} \mathrm{d}\rho\; u(\rho,t) + \frac{\mathrm{d}}{\mathrm{d}t}\int_{\xi(t)}^{\rho_{\mathrm{R}}} \mathrm{d}\rho\; u(\rho,t)\\ =&f(t,u(t,\rho_{\mathrm{R}})) - f(t,u(t,\rho_{\mathrm{L}}))\,.\end{aligned} \tag{B.18}$$

The RG-time derivative can be done explicitly and leads to

$$\begin{aligned}&\frac{\mathrm{d}\xi(t)}{\mathrm{d}t}(u(\rho_{\mathrm{R}},t) - u(\rho_{\mathrm{L}},t)) - f(t,u(t,\rho_{\mathrm{R}})) + f(t,u(t,\rho_{\mathrm{L}}))\\ =&-\int_{\xi(t)}^{\rho_{\mathrm{R}}} \mathrm{d}\rho\; \partial_t u(\rho,t) - \int_{\rho_{\mathrm{L}}}^{\xi(t)} \mathrm{d}\rho\; \partial_t u(\rho,t)\,.\end{aligned} \tag{B.19}$$

In the limit $\rho_{\mathrm{L}} \to \xi^-(t)$ and $\rho_{\mathrm{R}} \to \xi^+(t)$ the right-hand side vanishes and we obtain the equation

$$\frac{\mathrm{d}\xi(t)}{\mathrm{d}t}(u_{\mathrm{R}}(t) - u_{\mathrm{L}}(t)) - f_{\mathrm{R}}(t) + f_{\mathrm{L}}(t) = 0\ , \tag{B.20}$$

where we have used the definitions

$$\begin{aligned}u_{\mathrm{R}}(t) &= \lim_{\rho\to\xi^+(t)} u(\rho,t)\\ f_{\mathrm{R}}(t) &= \lim_{\rho\to\xi^+(t)} f(t,u(\rho,t))\\ u_{\mathrm{L}}(t) &= \lim_{\rho\to\xi^-(t)} u(\rho,t)\\ f_{\mathrm{L}}(t) &= \lim_{\rho\to\xi^-(t)} f(t,u(\rho,t))\,.\end{aligned} \tag{B.21}$$

The equation for the position of the discontinuity is described by

$$\frac{\mathrm{d}\xi(t)}{\mathrm{d}t} = \frac{f_{\mathrm{R}}(t) - f_{\mathrm{L}}(t)}{u_{\mathrm{R}}(t) - u_{\mathrm{L}}(t)} = \frac{[\![f]\!]}{[\![u]\!]}\,, \tag{B.22}$$

which can be integrated to obtain the RG-time evolution of the shock.

B.3.2. Shock detection

To determine the position of jump discontinuities in our numerical approximation $u_h(t,\rho)$ we follow the procedure outlined in [416, 417], i.e. the method of concentration.

We briefly summarize here how this procedure is practically applied. While shock capturing schemes are very interesting by itself and are a promising future direction, we restrict ourselves here to the extraction of the position of discontinuities during post processing. Discontinuities, i.e. their position and height can be extracted by folding the function $f(x)$, which is assumed to be piecewise continuous, with a suitable concentration kernel, which acts as

$$K_\varepsilon * f(x) = [\![f]\!](x) + \mathcal{O}(\varepsilon)\,. \tag{B.23}$$

To define the concentration kernel from a numerical point of view, we have to understand how a discontinuous function is expand in our basis. Consider the expansion of a piecewise smooth function $f(x)$ in terms of Jacobi polynomials,

$$\begin{aligned} f(x) &\simeq \sum_{k=0}^{N} \hat{f}_k P_k(x) \\ \text{with} \quad \hat{f}_k &= \int_{-1}^{1} \mathrm{d}x\, \omega(x) f(x) P_k(x)\,. \end{aligned} \tag{B.24}$$

Utilizing the Sturm-Liouville equation (A.1), assuming that the function f has a jump $[\![f]\!](c)$ for $x = c$, it is possible to obtain an estimation for the decay of the spectrum $\hat{f}_k$ with k,

$$\begin{aligned} \hat{f}_k &= \frac{-1}{\lambda_k} \int_{-1}^{1} \mathrm{d}x \left[(1-x^2)\omega(x)P_k'(x)\right]' f(x) \\ &= [\![f]\!](c) \frac{1}{\lambda_k}(1-c^2)\omega(c)P_k'(x) + \mathcal{O}\left(\frac{1}{\lambda_k}\right)\,. \end{aligned} \tag{B.25}$$

This equation expresses the fact that next to a jump the coefficients of the mode expansion decays like $\frac{1}{\lambda_k}$, which is substantially slower than far away from a jump. In (B.25) λ_k refers to the eigenvalue of the associated Sturm-Liouville equation, c.f. (A.1). Motivated by this characteristic property of the spectrum of a particular polynomial expansion it is possible to define a quantity that detects the discontinuity from the mode expansion of the function. The concentration kernel for Legendre polynomial was obtain in [416] and is define as

$$K_N^\sigma * f = \sqrt{2}\frac{\pi}{N}\sqrt{1-x^2}\sum_{k=1}^{N} \sigma\left(\frac{|k|}{N}\right) \hat{f}_k \psi_k'(x)\,, \tag{B.26}$$

where $\sigma(\xi)$ is an adequate concentration factor. There are different possibility for this function and an extensive discussion can be found in [416]; for our implementation we have made the simple choice of $\sigma(\xi) = 1$. In the vicinity of the discontinuity, and away from it, this kernel behaves as

$$K_N^\sigma * f = \begin{cases} \mathcal{O}(\frac{1}{N}) & x \neq c \\ [\![f]\!](c) + \text{const.}\frac{\log N}{N} & x = c \end{cases}\,. \tag{B.27}$$

Consequently, is possible to pin-point the discontinuity, when examining the scaling of this operator with the number of nodes. However, is more convenient to enhance the separation of scale between the smooth part and the discontinuity, namely

$$N^{\frac{p}{2}}(K_N^\sigma * f)^p = \begin{cases} \mathcal{O}(N^{-\frac{p}{2}}) & x \neq c \\ [\![f]\!](c)N^{\frac{p}{2}} & x = c \end{cases}, \tag{B.28}$$

where p is the enhancement exponent. Using this operator is possible to construct an operator that is non vanishing only in a presence of the jump,

$$K_{N,J}^p * f = \begin{cases} K_N * f & \text{if } |N^{\frac{p}{2}}(K_N^\sigma * f)^p| > J \\ 0 & \text{otherwise} \end{cases}, \tag{B.29}$$

where J is an appropriately chosen threshold. This additional definition becomes very important for smaller values of N if we want to achieve a good separation of scales between shocks and smooth parts of the solution. In our implementation we have chosen the heuristic values $p = 2$ and $J = 5.0 \times 10^{-8}$. With this set of parameters we were able to detect the discontinuities in Section 4.2.3 efficiently.

B.4. Calculation of Matsubara sums

We review the calculation of series frequently encountered in the Matsubara formalism. As an example consider the flow equation for the effective potential in a scalar theory at temperature T

$$\partial_t V_k(\rho) = \frac{T}{2} \sum\!\!\!\!\!\!\int_q G(q_0, \vec{q}) \partial_t R_k(q_0, \vec{q}) \,, \tag{B.30}$$

with $q_0 = 2\pi n T$ and the notation $\sum\!\!\!\!\!\!\int$ denotes both integration and summation

$$\sum\!\!\!\!\!\!\int_q = \sum_{n=-\infty}^{\infty} \int_{\vec{q}} \,. \tag{B.31}$$

For the beginning we will restrict ourselves to bosonic Matsubara sum, the generalization to fermions is obvious and will be stated at the end. Technically, it is easier to start with the summation in (B.30) and therefore we consider problems of the form

$$\mathcal{M}_{\text{bos}} = T \sum_{n=-\infty}^{\infty} f(2n\pi T) \,, \tag{B.32}$$

where the generic function f is assumed to be sufficiently well behaved, analytic on the real axis and decays sufficiently fast at infinity, this is usually the case for integrands encountered in flow equations. Recalling the residue theorem

$$\oint_\gamma \mathrm{d}z \; g(z) = 2\pi \mathrm{i} \sum_{k=1}^{N} \mathrm{ind}_\gamma(a_k) \mathrm{res}(g, a_k) \,, \tag{B.33}$$

where a_k are the poles of $g(z)$ contained in the closed path γ, $\mathrm{ind}_\gamma(a)$ is the winding number of γ with respect to a and $\mathrm{Res}(g, a)$ is the residue of g at a. Utilizing the requirement of analyticity on the real axis, the sum in (B.32) can be rewritten to an integral by means of the residue theorem (B.33), by introducing an additional function that has poles at $q_0 = 2\pi n T$

$$\mathcal{M}_{\text{bos}} = \frac{\mathrm{i}}{2} \oint_\gamma \mathrm{d}z \; f(z) \left[1 + 2n_{\text{B}}(\mathrm{i}z)\right] \,, \tag{B.34}$$

where the path γ encloses the real axis without enclosing any additional non-analyticities of $f(z)$ in positive direction and n_{B}. In (B.34) we have used that the poles of n_{B} are located at the Matsubara modes $2n\pi T$ and contribute with a residue of $\mathrm{i}T/2$. It would have been sufficient to use $\mathrm{i}\, n_{\text{B}}(\mathrm{i}z)$, the bosonic occupation number defined in (4.46), as factor to achieve this, but we are using $\mathrm{i}/2\left[1 + 2n_{\text{B}}(\mathrm{i}z)\right]$ because it makes successive calculations often more convenient. Turning back to (B.34) we can cut the contour γ open at $\pm\infty$ and close them individually at infinity by means of Jordan's lemma in the complex plane. As a result we can express the Matsubara sum in (B.32) as

$$\mathcal{M}_{\text{bos}} = T \sum_{n=-\infty}^{\infty} f(2n\pi T) = \frac{1}{2\mathrm{i}} \sum_{k=1}^{N} \mathrm{res}(f, z_k) \left[1 + 2n_{\text{B}}(\mathrm{i}z_k)\right] \,, \tag{B.35}$$

where the z_k are the poles of $f(z)$ and the additional minus sign comes from the winding number when closing the paths at infinity.

Turning to fermions, it turns out that it only necessary to replace the thermal kernel in (B.34)

$$\mathcal{M}_{\text{fer}} = T \sum_{n=-\infty}^{\infty} f((2n+1)\pi T) = \frac{1}{2\mathrm{i}} \sum_{k=1}^{N} \operatorname{res}(f, z_k) \left[1 - 2n_{\text{F}}(\mathrm{i}z_k)\right] . \tag{B.36}$$

B.5. O(N)-theory regulator & cut-off scale

In order to use a Lorentz invariant regulator $R_k(p^2)$, we need to deal with additional poles/branch-cuts necessarily introduced by the non-trivial analytic structure of $R_k(p^2)$. While the propagator $1/\Gamma^{(2)}$ is restricted to have poles on the Minkowski axis, a Lorentz invariant regulator with non-trivial momentum dependence that leaves all non-analyticities of the regulated propagator $1/(\Gamma^{(2)}(q)+R_k(q))$ on the Minkowski axis is to date not known. As mentioned in section in the beginning of Section 5.1 we use the regulator introduced in [197], i.e.

$$R_k(p^2) = Z_\sigma \left[p^2 + \Delta m_r^2\right] r\left(\frac{q^2 + \Delta m_r^2}{k^2}\right) , \tag{B.37}$$

for the shape function we chose the exponential one

$$r(x) = \frac{x^{m-1}}{e^{x^m} - 1} \tag{B.38}$$

with $m = 2$. In particular, this amounts to the use of a modified regulator, compared to what we have introduced in Section 2.3.3. The mass-like term Δm_r^2 has the effect of pushing regulator poles away from the Euclidean axis, while only having a small impact on the analytic structure of the unregulated propagator. It is parametrised as a smooth theta function

$$\Delta m_r^2 = \alpha \frac{p_{0,\max^2}}{1 + \left(\frac{\beta k}{p_{0,\max}}\right)^n} , \tag{B.39}$$

where we have chosen our parameters according to Table B.1. These parameters are

chosen such that the initial conditions, Γ_Λ, are unchanged compared to the standard case $\Delta m_r^2 = 0$. In the vacuum it is possible to show for LPA that the regulator poles do not contribute to a certain frequency range if $p_{0,\max}$ is sufficiently large and the available frequency range corresponds roughly to its value. For finite temperature this is in not true anymore, as the correction factor for simple poles at position z_0 is proportional to $n_B(z_0 + \mathrm{i}p_0) - n_B(z_0)$, which is only sufficiently suppressed for $|z_0|/T \gg 1$. Therefore we have restricted our frequency range to 720 MeV, where we have checked for explicit independence of the results on the parametrisation of Δm_r^2.

The large value of Δm_r^2, which enables us to resolve a large range of frequencies, comes with the downside that the cut-off scale Λ_{UV} must be sufficiently large. In order to still fulfil the requirement of unchanged initial conditions compared to a vanishing Δm_r^2 we have chosen $\Lambda_{\mathrm{UV}} = 8.28\,\mathrm{GeV}$, therefore the interpretation of our results as an effective theory of low energy QCD is strictly speaking not possible. Nevertheless our results demonstrate the applicability of the method to extract real time correlation functions from the FRG via analytic continuation and the qualitative features stay unchanged compared to the usual

Parameter	$p_{0,\max}$	α	β	n
Value	3.45 GeV	2.5	0.44	150

Table B.1.: Values for the parametrisation of Δm_r^2.

O(N)-model with a lower cut-off. We are unable to fix all values to their physical ones, as we observe a loss of solution similar to [233], restricting us from tuning to arbitrary IR values. Moreover we also observed a smaller and smaller range of initial values that do not lead to a break down of the numerics as we increase our truncation. Therefore we chose $f_\pi/m_\pi = 0.93$ and $m_\sigma/m_\pi = 2.09$, which fulfils the requirement $m_\sigma/m_\pi > 2$, resulting in the sigma being an unstable particle. For all truncations the initial values where chosen such that the curvature masses agree.

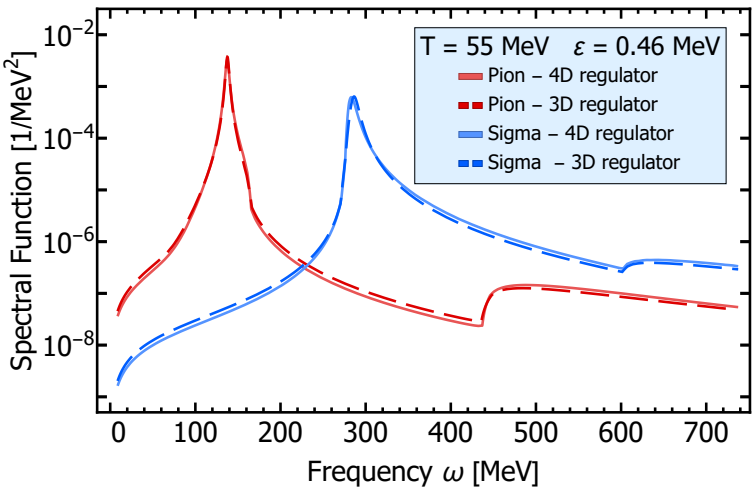

Figure B.1.: Comparison of different regulators in a $O(N)$-theory at finite temperature.

B.6. Comparing regulators in the calculation of spectral functions

In addition to the regulator described in Section B.5 it is also insightful to compare to the Lorentz invariance breaking regulator (B.40), which has been used in most FRG related works so far

$$R_k(p) = \left(k^2 - \boldsymbol{p}\right) \Theta\left(k^2 - \boldsymbol{p}\right) \ . \tag{B.40}$$

This regulator has the advantage that the Matsubara sum and the following analytic continuation can be performed analytically. Therefore we compare our results obtained with the Lorentz invariant regulator (B.37) against the results obtained with (B.40) for the LPA case and vanishing external momenta in Figure B.1. This shows that the difference

between the two regulators is marginal, which can be explained by the small breaking of Lorentz invariance for $\boldsymbol{p} = 0$, c.f. the discussion in Section 6.2.1.3, and the already very similar running of the Euclidean system for the two regulators in this regime. For larger temperatures the difference is dominantly driven by the difference in the condensate, leading to a general mismatch between the spectral functions.

B.7. Details regarding the numerics used in the O(N)-model

We followed the general workflow outlined in [66]. The flow equations are derive using DoFun [103, 104], traced and optimized using the FormTracer [418], utilizing FORM [419], and solved using the *frgsolver*, a c++ framework developed for [1, 63, 64, 66, 197, 339]

In order to implement the procedure outlined in the beginning of Section 5.1, the equations are solved as

$$\begin{aligned}\Gamma^{(2)}(\omega,\vec{p}) = \Gamma^{(2)}_{\Lambda}(\omega,\vec{p}) + \lim_{\varepsilon\to 0}\int_{\Lambda}^{k_{\mathrm{IR}}} \mathrm{d}k \int_0^{\infty} \mathrm{d}^3\vec{q} \left\{ \sum_{q_0=2\pi n T} + \text{Correction} \right\} \times \\ \times \text{Flow}\left[\Gamma^{(2)}_k(q_0,\vec{q},p_0=-\mathrm{i}(\omega+\mathrm{i}\varepsilon),\vec{p})\right] ,\end{aligned} \tag{B.41}$$

where "Correction" term refers to the correction of the occupation numbers arising implicitly from the Matsubara sum. From the study of the flow equation using a 3D regulator it is well known [197, 221] that the equations reduce to delta functions for the imaginary part when the limit $\varepsilon \to 0$ is taken by means of the Sokhotski-Plemelj theorem. Due to our Lorentz invariant regulator (B.37) we are however not able to resolve the Matsubara sum analytically and must take the limit numerically, therefore greatly increasing the numerical cost of the calculation as the delta functions (and derivatives thereof) have to be resolved numerically for very small values of ε. In practice the limit is performed using Richardson extrapolation with several small values of ε, the independence of the result for different sets of ε's has been checked explicitly. From the symmetries of the two-point correlator it is known that the leading term in ε of the imaginary part behaves as $\mathcal{O}(\varepsilon^1)$ and the real part behaves as $\mathcal{O}(\varepsilon^2)$, the exponents in the extrapolation are chosen accordingly.

The correction term can in principle also take branch cuts into account, as described in the beginning of Section 5.1, and therefore allows for a self consistent treatment. With the current methods, this is numerically insurmountable as it introduces a second competing limit for the branch cut integrals.

B.8. Flow equations of the Quark-Meson model

For the derivation of the flow equations DoFun [103] was used. For the subsequent tracing of the equations we have used FormTracer [418]. We do not state the tadpole (TP) contributions explicitly, since we obtain the momentum independent part from (A.11). Let us define the relative momenta between the internal and the external momenta $r = q - p$. For clarity we insert the index k to all RG-scale dependent quantities. The contribution to the $\dot{\Gamma}^{(2)}_{\pi,k}(p)$ and $\dot{\Gamma}^{(2)}_{\sigma,k}(p)$, with the dot denoting the derivative with respect to the RG-time t, from the quark loop is the same, which is given by

$$\begin{aligned}\dot{\Gamma}^{(2),q}_{\phi,k}(p) = \int_q \Big\{ & 12\dot{\hat{R}}^q_k(q) G^2_q(q) G_q(r) h_k(r,-q) h_k(q,-r) \\ & \left[\left(Z^2_{rq,k}(q) q^2 - m^2_{q,k}(q) \right) Z_{rq,k}(r)(p\,q - p^2) \right. \\ & \left. + 2 m_{q,k}(q) m_{q,k}(r) Z_{rq,k}(q) q^2 \right] \Big\} \,.\end{aligned} \tag{B.42}$$

The full flow for the two-point function of the pion is

$$\begin{aligned}\dot{\Gamma}^{(2)}_{\pi,k}(p) = & \dot{\Gamma}^{(2),q}_{\phi,k}(p) + \int_q \Big\{ \left(\Gamma^{(3)}_{\pi\pi\sigma}(0) \right)^2 \Big[\dot{R}_{\pi,k}(q) G^2_\pi(q) \\ & G_\sigma(r) + \dot{R}_{\sigma,k}(q) G^2_\sigma(q) G_\pi(r) \Big] \Big\} + \mathrm{TP} \,,\end{aligned} \tag{B.43}$$

and correspondingly the full flow of the sigma is

$$\begin{aligned}\dot{\Gamma}^{(2)}_{\sigma,k}(p) = & \dot{\Gamma}^{(2),q}_{\phi,k}(p) + \int_q \Big\{ 3 \left(\Gamma^{(3)}_{\pi\pi\sigma}(0) \right)^2 \dot{R}_{\pi,k}(q) G^2_\pi(q) G_\pi(r) \\ & + \left(\Gamma^{(3)}_{\sigma\sigma\sigma}(0) \right)^2 \dot{R}_{\sigma,k}(q) G^2_\sigma(q) G_\sigma(r) \Big\} + \mathrm{tadpole} \,.\end{aligned} \tag{B.44}$$

The mesonic three point vertices are obtained from the effective potential

$$\begin{aligned}\Gamma^{(3)}_{\pi\pi\sigma}(0) &= \sigma V^{(2)}_k[\rho]\Big|_{\rho=\rho_0} \,, \\ \Gamma^{(3)}_{\sigma\sigma\sigma}(0) &= \left[3\sigma V^{(2)}_k[\rho] + \sigma^3 V^{(3)}_k[\rho] \right]\Big|_{\rho=\rho_0} \,.\end{aligned} \tag{B.45}$$

The flow for the wave function part of the quark propagator reads

$$\begin{aligned}\dot{Z}_{q,k}(p) = & -\frac{1}{4p^2} \int_q \Big\{ (p\,q) \dot{\hat{R}}^q_k(q) G^2_q(q) h_k(-p,q) h_k(-q,p) \\ & \left(m^2_{q,k}(q) - Z^2_{rq,k}(q) q^2 \right) \left(3G_\pi(r) + G_\sigma(r) \right) \\ & + 2 G_q(r) Z_{rq,k}(r) (p\,q - p^2) h_k(r,p) h_k(-p,-r) \\ & \left(3\dot{R}_{\pi,k}(q) G^2_\pi(q) + \dot{R}_{\sigma,k}(q) G^2_\sigma(q) \right) \Big\} + \mathrm{tadpole} \,,\end{aligned} \tag{B.46}$$

and finally the flow of the Yukawa coupling:

$$\begin{aligned}\dot{h}_k(p,-p) = -\frac{1}{4}\int_q \Big\{ & 2\dot{\hat{R}}_k^q(q) G_q^2(q) h_k(-p,-q) h_k(q,p) \\ & h_k(q,-q) Z_{rq,k}(q) q^2 \left(3G_\pi(r) - G_\sigma(r)\right) \\ & + G_q(r) h_k(-p,-r) h_k(r,p) h_k(r,-r) \\ & \Big(3\dot{R}_{\pi,k}(q) G_\pi^2(q) - \dot{R}_{\sigma,k}(q) G_\sigma^2(q)\Big)\Big\} \\ & - \dot{A}(p,-p)\frac{\Gamma_\phi^{(1)}(0)}{\sigma}\,.\end{aligned} \tag{B.47}$$

The flow of λ_k has a very lengthy expression and thus is not noted here.

B.9. Poles of decoupling scenario I

More details about the poles of (6.76) are collected here We drop the normalization Z_{IR} and additional notation to keep things simple

$$\hat{G}^{(\mathrm{dec})}(p) = \left(\hat{m}_{\mathrm{gap}}^2 + \hat{p}^2 \ln \hat{p}^2\right)^{-1} . \tag{B.48}$$

Using the Lambert W-Function, with the usual index notation for the different branches, the roots can be expressed as

$$z_{0,\pm}^{(r)} = \pm\sqrt{\psi_0} \tag{B.49}$$

$$z_{-1,\pm}^{(r)} = \pm\sqrt{\psi_{-1}} , \tag{B.50}$$

with

$$\psi_k = e^{W_k(-\hat{m}_{\mathrm{gap}}^2)} . \tag{B.51}$$

There are now three different cases for the additional poles

$\hat{m}_{\mathrm{gap}}^2 < 1/e$

First order poles, located pairwise on the Euclidean axis ($\Im(z_{k,\pm}^{(r)}) = 0$).

$\hat{m}_{\mathrm{gap}}^2 = 1/e$

Two second order poles at $p = \pm 1/\sqrt{e}$

$\hat{m}_{\mathrm{gap}}^2 > 1/e$

Complex first order poles which are linked by complex conjugation (as required by Lorentz invariance)

$$z_{0,\pm}^{(r)} = \left(z_{-1,\pm}^{(r)}\right)^* . \tag{B.52}$$

Introducing the additional function

$$\chi_k = 1 + \ln \psi_k , \tag{B.53}$$

the residues can be computed in a straight forward manner

$$\mathrm{Res}[\hat{G}^{(\mathrm{dec})}, z_{k,\pm}^{(r)}] = (2\chi_k z_{k,\pm}^{(r)})^{-1} \tag{B.54}$$

for $k = -1, 0$. The additional term in (6.61) can then conveniently be written as

$$\text{pole term} = \sum_{k\in=\{-1,0\}} \frac{1}{\chi_k \left(\hat{p} - e^{W_k(-\hat{m}_{\mathrm{gap}}^2)}\right)} . \tag{B.55}$$

B.10. BR method

Different Bayesian methods propose different prior probabilities, i.e. they encode different types of prior information. The well known Maximum Entropy Method e.g. features the Shannon-Jaynes entropy

$$S_{\mathrm{SJ}} = \int d\omega \big(\rho(\omega) - m(\omega) - \rho(\omega)\log\big[\frac{\rho(\omega)}{m(\omega)}\big]\big)\,, \tag{B.56}$$

while the more recent BR method uses a variant of the gamma distribution

$$S_{\mathrm{BR}} = \int \mathrm{d}\omega \big(1 - \frac{\rho(\omega)}{m(\omega)} + \log\big[\frac{\rho(\omega)}{m(\omega)}\big]\big)\,. \tag{B.57}$$

Both methods e.g. encode the fact that physical spectral functions are necessarily positive definite but are otherwise based on different assumptions.

As Bayesian methods they have in common that the prior information has to be encoded in the functional form of the regulator and the supplied default model $m(\omega)$. Note that discretizing ρ by choosing a particular functional basis also introduces a selection of possible outcomes. The dependence of the most probable spectral function, given input data and prior information, on the choice of S, $m(\omega)$ and the discretized basis comprises the systematic uncertainty of the method.

One major limitation to Bayesian approaches is the need to formulate our prior knowledge in the form of an optimisation functional. The reason is that while many of the correlation functions relevant in theoretical physics have very well defined analytic properties it has not been possible to formulate these as a closed regulator functional S. Take the retarded propagator for example (for a more comprehensive discussion see [2] or Section 6.4). Its analytic structure in the imaginary frequency plane splits into two parts, an analytic half-plane, where the Euclidean input data is located, and a meromorphic half-plane which contains all structures contributing to the real-time dynamics. Encoding this information in an appropriate regulator functional has not yet been achieved.

Instead the MEM and the BR method rather use concepts unspecific to the analytic structure, such as smoothness, to derive their regulators. Among others this e.g. manifests itself in the presence of artificial ringing, which is related to unphysical poles contributing to the real-time propagator, which however should be suppressed by a regulator functional aware of the physical analytic properties.

B.11. GrHMC method

The main idea of the setup is already stated in the main text in Section 6.5.2 and was first introduced in [2]. Nevertheless, for completeness we outline the entire reconstruction process here. The approach is based on formulating the basis expansion in terms of the retarded propagator. The resulting set of basis coefficients are then determined via Bayesian inference. This leaves us with two objects to specify in the reconstruction process, the choice of a basis/ansatz for the retarded propagator and suitable priors for the inference.

Once a basis has been chosen it is straightforward to write down the corresponding regression model. As in the reconstruction with neural nets we use a fixed number of Breit-Wigner structures, c.f. (6.96), corresponding to simple poles in the analytically continued retarded propagator. The logarithm of all parameters is used in the model in order to enforce positivity of all parameters. The uniqueness of the parameters is ensured by using an ordered representation of the logarithmic mass parameters.

The other crucial point is the choice of priors, which are of great importance to tame the ill-conditioning practically and should therefore be chosen as restrictive as possible. For comparability to the neural net reconstruction, the priors are matched to the training volume in parameter space. However, it is more convenient to work with a continuous distribution. Hence the priors of the logarithmic parameters are chosen as normal distributions where we have fixed the parameters by the condition that the mean of the distribution is the mean of the training volume and the probability at the boundaries of the trainings volume is equal. Details on the training volume in parameters space can be found in Section C.4.

All calculations for the GrHMC method are carried out using the python interface [420] of Stan [338].

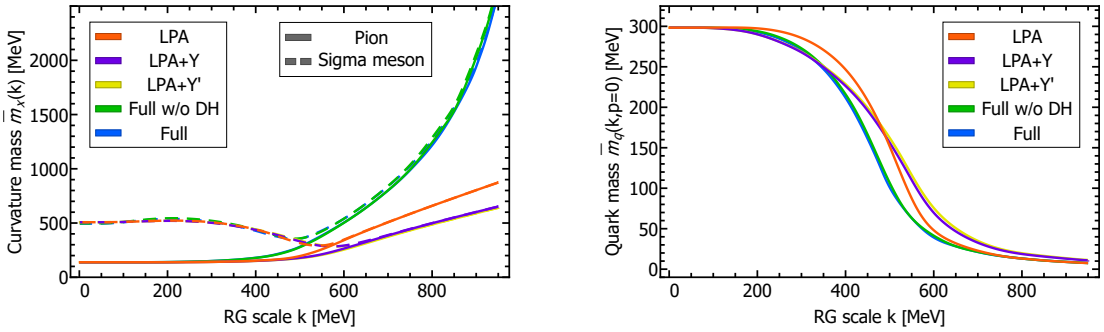

Figure C.1.: Flow of the meson masses (left panel) and quark masses at $p = 0$ (right panel), shown for different truncations.

C. Additional material

C.1. Truncations

In this section of the Appendix we discuss details on the different truncations analysed within the quark-meson model and compare them to the full case. All truncations are set to get the same IR physics. The results are shown in Figure C.1, Figure C.2 and Figure C.3.

In total we consider four additional truncations

- LPA: The wave functions are set to unity, the Yukawa coupling is fixed to a constant and the rebosonisation is ignored.

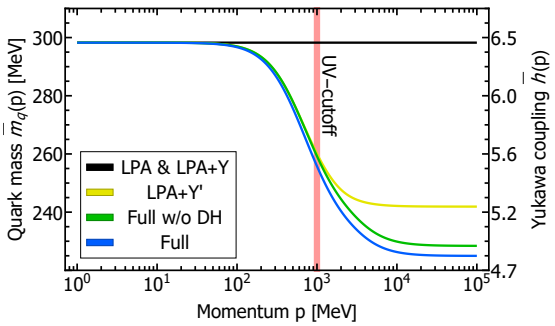

Figure C.2.: The momentum dependence of the quark mass (left axes) and Yukawa coupling (right axes) for $k = 0$ and different truncations is depicted. The vertical red line shows the value of the UV cutoff.

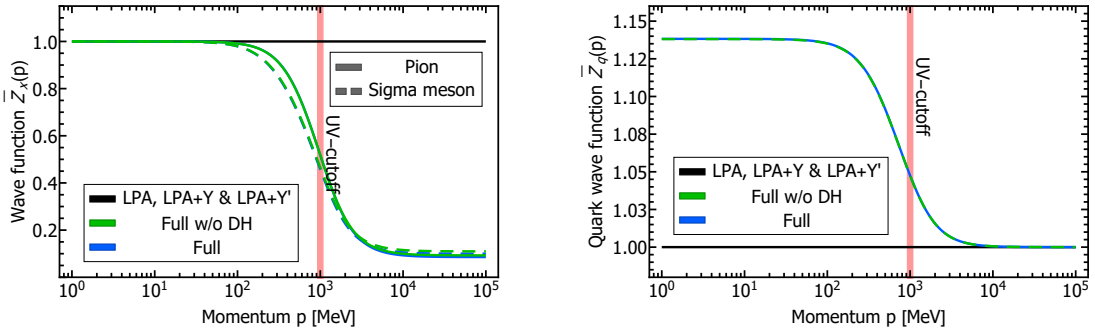

Figure C.3.: The momentum-dependent wave function renormalizations for the meson (left panel) and quarks (right panel) is plotted for $k = 0$ and different truncations.

- LPA + Y: The k-dependence of the Yukawa coupling is additionally taken into account.
- LPA + Y': The momentum dependence of the Yukawa coupling is additionally taken into account.
- Full w/o DH: The full wave functions are taken additionally into account, this corresponds to the full truncation without the rebosonisation procedure.

Turning to the running of the curvature masses, shown in Figure C.1, the most notable effect is the faster decoupling of the mesons at larger scales, hence getting closer to the behaviour in full QCD, while the running of the quark mass is mostly unaffected. The momentum dependence of the Yukawa coupling, shown in Figure C.2, is below the UV-cutoff essentially independent of the truncation as long as it is calculated. A similar result is found for the wave functions, shown in Figure C.3. These findings fit to the discussion about the different contributions generating momentum dependencies in Section 5.2.7.

C.2. Derivation of the IR asymptotics of spectral functions

Our analysis that lead to the derivation of (6.56) in Section 6.4.1 is based on the existence of a spectral representation (6.51). The inverse relation (6.53) together with the existence of a spectral representation (6.51), that holds for the entire complex plane, has strong implications on the analytic structure of the propagator on the left hand side. As a consequence the holomorphicity of the associated retarded and advanced propagators in their respective domain of definition, c.f. Section 6.4.4.1, follows directly from Cauchy's theorem. As we define our spectral function as the cut in the propagator along the $\mathrm{Re}\, p_0$ axis, i.e. (6.53), the spectral representation is sufficient as condition. Having established analyticity in one half-plane, (6.56) holds already by means of the Cauchy-Riemann equations, where the additional factor two comes from (6.53).

In general neither the Minkowski propagator nor the spectral function is a function in the classical sense, but a tempered distribution. Nevertheless, the arguments about the analytic properties hold, see e.g. [194, 195]. Another prerequisite mentioned in the main text is the smoothness of the spectral function at zero. In the absence of truly distributional contribution to the integral for small p_0 in (6.51), the spectral function must go to zero sufficiently fast, otherwise the propagator obtains at least a log-divergence in p_0. On the other hand, if such contributions would be present this argument might not hold. A detailed discussion about the issue of these contributions regarding the gluon and their relation to functional methods can be found in [262, 421]. Mathematically rigorous statements in the context of axiomatic QFT's about this issues and the relation to our derivation are beyond the scope of this work.

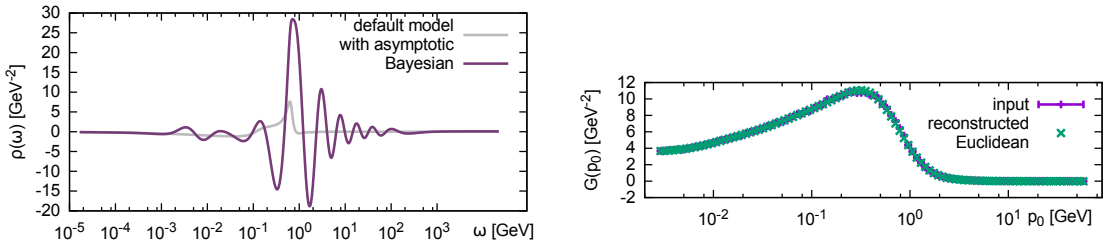

(a) (b)

Figure C.4.: (Figure C.4a): Representative example of a Bayesian reconstruction of the gluon spectral function based on FRG Euclidean data in the scaling scenario. One hundred data points with a relative error of 10^{-2} were supplied, as well as a default model (gray solid), which produces the correct asymptotics of the correlator. We find that while the asymptotics are correctly recovered in the final result (solid violet) eventually, the agreement emerges far later than in our new method. In addition we find that the non-perturbative region at around $\omega \sim 1\,\mathrm{GeV}$ is contaminated by strong ringing artefacts. (Figure C.4b): Comparison between the reconstructed Euclidean correlator (green) and the input data (violet).

C.3. Other reconstruction approaches

In this appendix we discuss two reconstruction strategies, the Bayesian Reconstruction using a quadratic prior (Tikhonov) and the Schlessinger point method, which we had explored previous to developing the method presented in this paper. The reason that a new approach became necessary for the reconstruction of the gluon spectral function lies in the individual shortcomings of the above mentioned methods.

Our goal is to reconstruct a spectral function, which, as discussed in the main part of this paper, should exhibit the following properties:

1. Normalization, as required by Oehme-Zimmermann superconvergence (6.62)
2. Correct low frequency asymptotics, c.f. Section 6.4.3
3. Correct high frequency asymptotics, c.f. Section 6.4.2
4. Respect the Källén–Lehmann spectral representation (6.51)
5. Antisymmetric around $\omega = 0$, c.f. (6.52)
6. A smooth function without drastic oscillations

A successful reconstruction based on Euclidean data should fulfil these requirement. We observed that neither the gBR method nor the Schlessinger point method was able to meet all the requirements in a satisfactory manner. The underlying reason for these difficulties

is related to the fact that both methods indirectly or directly choose a set of basis functions not adapted to the problem at hand.

C.3.0.1. Bayesian reconstruction

The Bayesian reconstruction usually selects a set of basis functions simply by introducing a numerical integration scheme to represent the discretized spectral function. This choice of basis is naturally unaware of the analytic structure of the correlator and thus of the functional form admissible for the spectral function. In particular this basis does not prevent highly oscillatory and thus unphysical structures to manifest themselves in the end result. In the spirit of the Bayesian approach the prior probability then needs to be constructed such that these oscillatory solutions are suppressed. The quadratic prior, we have found is not efficient in doing so and thus unphysical ringing may persists in the end result. Similar ringing also manifests itself in case of the generalized BR method.

We have performed reconstructions based on the Euclidean data in the scaling scenario, using different default models, which were endowed with the correct asymptotic form. One example is shown in Figure C.4, where the green solid line denotes the default model and the solid violet line corresponds to the Bayesian end result. One hundred data points with a relative error of 10^{-2} were used. Due to the asymptotics supplied in the default model, as well as the fact that the Bayesian method uses the Källén–Lehmann representation to translate the spectrum into a Euclidean correlator, items (2-5) from our list are fulfilled here. Item (1) is not fulfilled since the ratio between the area under the curve and the area under the absolute value of the spectrum is around 0.8. The most striking drawback of this reconstruction however is the strong oscillatory behaviour found, which renders an interpretation of the non-perturbative region at intermediate frequencies at best difficult. Note that with currently available lattice QCD data such a strong oscillatory behaviour was not observed when investigating the gluon spectrum.

It will be interesting future work to include the prior information on the analytic structure of the gluon propagator into the prior probability of these Bayesian approaches.

C.3.0.2. Backus-Gilbert reconstruction

The Backus-Gilbert approach to spectral function reconstruction operates [422, 423] with an implicit set of basis functions, which are characterized by the resolution function $\Delta(\omega - \omega')$. Also in this case the basis is not aware of the analytic structure admissible for the correlator under investigation. The naive Backus-Gilbert method in addition requires a regularization prescription, for which we here choose the Tickhonov approach with regulator parameter λ.

No explicit default model enters the BG approach, i.e. the prior information needed to give meaning to the ill-conditioned inverse problem enters through the definition of the optimization functions of which the BG spectrum is an extrema. This functional is designed such that it selects a solution for which the resolution function $\Delta(\omega - \omega')$ is most sharply peaked.

Note that in order to carry out the BG reconstruction the so called response kernels need to be computed. Here in case of the gluon spectrum these correspond to integrals over the Källén–Lehmann without the spectrum multiplied. As these functions are not

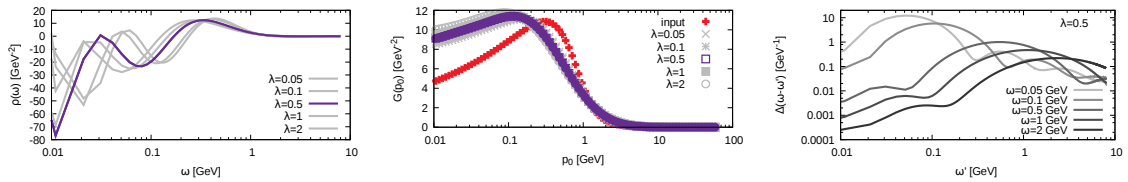

(a) (b) (c)

Figure C.5.: (Figure C.5a): Series of Backus-Gilbert reconstructed spectral functions using the Tickhonov regularization prescription for different regulator parameter $\lambda = [0.05..2]$. Note that the reconstruction identifies the presence of both the negative trough close to the origin and the one above the main peak at around $\omega > 1\,\mathrm{GeV}$. Ringing at small frequencies is not cured by simply increasing the value of λ. The best choice $\lambda = 0.5$ is given in dark violet, while the other values are denoted by light gray curves. (Figure C.5b): Euclidean data of the reconstructed spectra compared to the original input (red). The result corresponding to $\lambda = 0.5$ (dark violet) works relatively well above $p_0 > 1\,\mathrm{GeV}$ but misses the position of the main peak structure and exhibits too weak of a backbending. (Figure C.5c): Resolution function $\Delta(\omega - \omega')$ for the best choice $\lambda = 0.5$ plotted for completeness.

well defined, we instead choose to reconstruct the function $\rho(\omega)\omega$ with the corresponding response Kernel

$$R(p_0) = \int_0^\infty \frac{d\omega}{\pi} \frac{1}{\omega^2 + p_0^2} \tag{C.1}$$

which is finite. The spectrum is the obtained from dividing out ω from the raw reconstruction.

A series of results for the BG spectral reconstruction based on one-hundred ideal Euclidean input data points is shown in the top panel of Figure C.5 for several different values of λ. We find that a main peak close to $\omega = 1\,\mathrm{GeV}$ is consistently found and in addition the reconstructions show a negative trough close to the origin and above the main peak. However it is also clear from the top panel that close to the origin ringing artefacts again impede the physics interpretation of the result.

The BG solution by construction is not required to reproduce the input data, which then also leads to significant deviations as shown in the centre panel of Figure C.5. Thus, we find that the BG approach in case of the gluon spectral function is challenged to meet, in particular, criteria (1-4) that we require for a successful reconstruction.

C.3.0.3. Padé-type approaches

Padé approaches, e.g. Schlessinger's point method, obtain the spectral function from analytically continuing an interpolating or fitted rational function. The nomenclature *Padé* is used here in a loose sense, referring to all approaches based on matching a rational function of arbitrary degree to Euclidean data. Usually, (6.53) is used in order to obtain the spectral function. It has the advantage of being easy to apply and gives reasonable results for the position of the lowest lying resonances, see e.g. [227]. Padé approaches

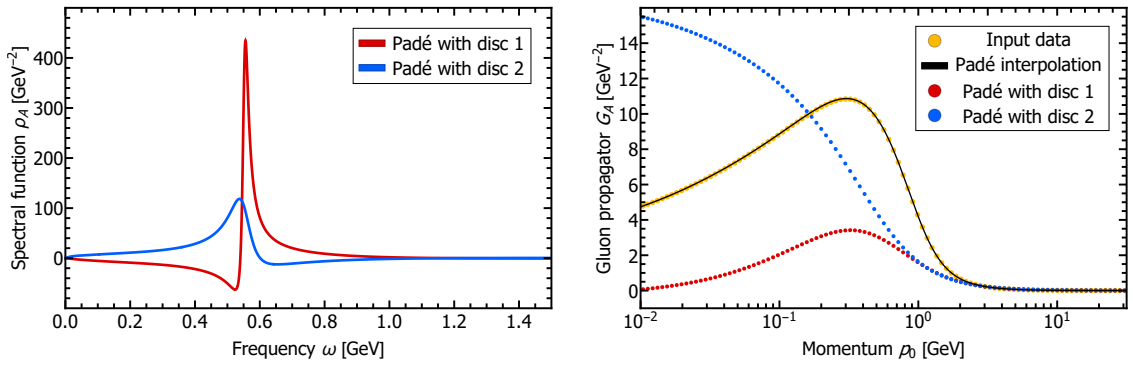

Figure C.6.: Reconstruction of the gluon propagator via Padé, the difference between the two spectral functions is described in the main text. The left panel shows the spectral functions while the right panel shows the input data, the Padé interpolant and the reconstructions obtained from the spectral functions.

describe the analytic structure of the analytically continued retarded propagator in terms of poles and is therefore naturally contained in our approach outlined in Section 6.4.4.

However, it does not respect the holomorphicity of the retarded propagator in the given half-plane, c.f. Figure 6.15 and the corresponding discussion, by design. While Padé approaches will still converge for infinite precision and infinitely many data points, violations of the holomorphicity at finite precision might be severe and make an unambiguous reconstruction impossible. As the spectral function obtained from (6.53) does not respect (6.51) anymore, if the holomorphicity of the right half-plane is violated, the obtained spectral function will fail to reproduce the Euclidean propagator. The violation might be acceptable if the violation is small, suitably defined via the reconstruction. But is most certainly not, if a pole dominantly contributing in (6.51) is missing. A more realistic spectral function can then still be obtained by suitably modifying (6.53), but there is no consistent, unambiguous way of doing so.

This discussion is especially relevant when turning to the reconstruction of the gluon, since here the dominant pole violates the holomorphicity of the retarded propagator. We employed two choices for the reconstruction, "Padé with disc 2", where we keep (6.53) with a flipped sign to account for the dominant pole being in the wrong half-plane, and "Padé with disc 1", but evaluated it at an argument with a finite real part slightly larger than the position of the pole. The corresponding spectral functions are shown in the left panel of Figure C.6. Both methods get the roughly a similar shape which is also loosely compatibly with our main result Figure 6.14. However, "Padé with disc 2" fails to reproduce the general shape in the reconstruction and "Padé with disc 1" gets a significantly too small propagator, but describes the shape correctly. Additionally several other requirements listed above are not fulfilled. While some requirements might be fixed by manipulating poles in the Padé interpolant, any systematic way of doing so will lead to an approach very similar to the one described in the main text in Section 6.4.4.

Please note that after our original publication a sampling based version of the Schlessinger's point method has been applied to the gluon propagator, based on DSE and Lattice data [424]. However, the way this study is performed it is not compatible with the basic assumptions underlying our work outlined in Section 6.1, as it allows for non-

analyticities where we demand the propagator to be holomorphic by construction.

C.3.1. Mock reconstruction benchmark

In this section we demonstrate with the simple example of a two Breit-Wigner spectral function how incorporating our novel approach into a Bayesian framework allows to straight forwardly improve the spectral reconstruction. As mock spectral function we take the parametrization of (6.60) with a direct sum of two Breit-Wigner peaks

$$\rho_{\text{mock}}(\omega) = \rho_1^{(\text{BW})}(\omega) + \rho_2^{(\text{BW})}(\omega) \tag{C.2}$$

and the following values for peak positions and widths

Parameter	A	M	Γ
Peak 1	0.35	1.0	0.25
Peak 2	0.65	3.0	0.25

From this spectrum we evaluate 60 equidistantly spaced Euclidean correlator data points in the imaginary frequency interval between $0 - 45\,\text{GeV}$, which are subsequently salted with Gaussian noise with a strength leading to 10^{-3} relative errors.

In the absence of any prior knowledge about the analytic structure (i.e. the two poles) contained in our example data we may choose to deploy a standard Bayesian method, such as the BR method [355], which only enforces positive definiteness and smoothness. As shown in Figure C.7 as green solid line, with the provided quality of the Euclidean data, this method manages to correctly identify the number of peak present but only achieves an accuracy of the peak positions of around $75 - 80\%$.

Now we can proceed to deploy our novel ansatz for the functional basis in (6.87). Three different cases are possible. Depending on the number N_{ps} of pole structures chosen in the basis, we may either have less structure, exactly the same amount of pole structures, or irrelevant additional structure present compared to what is actually encoded in the Euclidean data.

In the first case, where only one pole is contained in the basis, fitting its parameters is a well posed problem and can be carried out using both a naive χ^2 fit or a full Bayesian analysis, where each parameter is endowed with an additional prior probability. In Figure C.7 we have carried out a full Bayesian estimation of the posterior for the parameters in the single pole basis (purple dashed line) using the Hamiltonian Monte Carlo framework implemented by the MC-STAN [338, 425] library. The used prior only enforces the finiteness of the peak position. As expected this too strongly restricted basis yields a reconstruction, which cannot correctly account for the pole structure and instead positions one peak in between the actual two peaks present.

Increasing the number of available poles in the basis to two, we have the same number of structures in our basis, as we have in our data. This case is still well-posed and again admits a solution both via χ^2 fit and a full Bayesian analysis. Since we are using a parametrization that can exactly match our input data it is not surprising that now the end result from the HMC analysis lies spot on the mock spectrum (orange dashed curve). Note that for the χ^2 fit the result is slightly worse and only reproduces the mock spectrum with around 5% deviation. Please note that as soon as two or more poles are present in

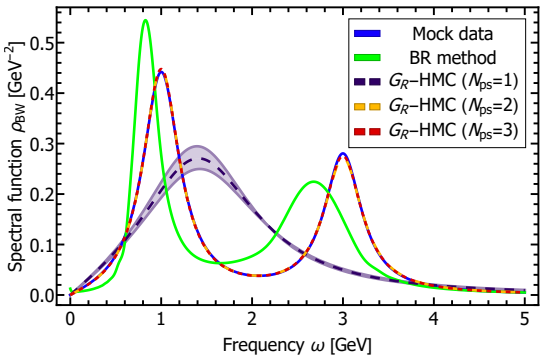

Figure C.7.: Reconstruction benchmark with a double Breit-Wigner peak.

the basis an ordering prescription must be enforced, otherwise the posterior distribution degenerates by means of a simple reparameterization.

The more interesting case, relevant in practice concerns allowing more structure in the basis than encoded in the Euclidean data, which we here tests with a three pole basis ansatz. In view of the χ^2 fit this problem is now ill-conditioned and indeed carrying out a naive fit shows that the obtained parameters become unstable. Here the HMC approach plays out its strength, maintaining stability even if the problem becomes ill-conditioned. Indeed the position and width of the lowest two pole structures is again recovered excellently (red dashed curve), while the posterior of the position of the third peak shows that it is highly unconstrained and thus irrelevant. The pole ordering naturally achieves that any excess pole structure beyond what is encoded in the data is simply pushed to infinity, not contributing to the end result.

We find that incorporating our novel basis may significantly improve the reconstruction result compared to those methods, which do not make any assumptions on the analytic structure of the underlying data. The example used here of course is simplistic but captures a main aspect, a multi pole structure, encountered also in more realistic cases.

Vol	A	M	Γ	ΔM
O	$[0.1, 1.0]$	$[0.5, 3.0]$	$[0.1, 0.4]$	$[0.0, 2.5]$
A	$[0.3, 0.7]$	$[0.5, 3.0]$	$[0.1, 0.3]$	$[0.25, 1.75]$
B	$[0.4, 0.6]$	$[0.5, 3.0]$	$[0.1, 0.2]$	$[0.5, 1.5]$
C	$[0.45, 0.55]$	$[0.5, 3.0]$	$[0.1, 0.15]$	$[0.75, 1.25]$
D	$[0.475, 0.525]$	$[0.5, 3.0]$	$[0.1125, 0.1375]$	$[0.875, 1.125]$

Table C.1.: Parameter ranges of the different volumes in parameter space. Two Breit-Wigner functions are sampled uniformly based on these parameters for the training and test sets. The difference $\Delta M = M_2 - M_1$ is also limited to restrict the minimum possible distance between two peaks. The volumes V_θ in Figure 6.23 are computed based on the ranges of A, M and Γ.

C.4. Mock data, training set and training procedure

We consider three different levels of difficulty for the reconstruction of spectral functions to analyse and compare the performance of the approaches in this work. These levels differ by the number of Breit-Wigners that need to be extracted based on the given information of the propagator. We distinguish between training and test sets with one, two and three Breit-Wigners. A variable number of Breit-Wigners within a test set entails the task to determine the correct number of present structures. This can be done a priori or a posteriori based either on the propagator or on the quality of the reconstruction. We postpone this problem to future work.

The training set is constructed by sampling parameters uniformly within a given range for each parameter. The ranges for the parameters of a Breit-Wigner function of ((6.96)) are as follows: $M \in [0.5, 3.0]$, $\Gamma \in [0.1, 0.4]$ and $A \in [0.1, 1.0]$. In addition, we investigate the impact of the size of the parameter space on the performance of the network for the case of two Breit-Wigner functions. This is done by decreasing the ranges of the parameters Γ and A gradually. We proceed differently for the two masses to guarantee a certain finite distance between the two Breit-Wigner peaks. Instead of decreasing the mass range, the minimum and maximum distance of the peaks is restricted. Details on the different parameter spaces can be found in Table C.1. The propagator function is parametrised by $N_p = 100$ data points that are evaluated on a uniform grid within the interval $\omega \in [0, 10]$. For a training of the point net, the spectral function is discretized by $N_\omega = 500$ data points on the same interval. Details about the training procedure can be

BR Comparison	A	M	Γ
1BW	$[0.1, 1.0]$	$[0.5, 3.0]$	$[0.1, 0.4]$
2BWa	$[0.2, 1.8]$	$[0.8, 3.8]$	$[0.2, 1.0]$
2BWb	$[0.3, 1.2]$	$[0.8, 3.8]$	$[0.002, 0.02]$
3BW	$[0.2, 1.8]$	$[1.0, 6.0]$	$[0.2, 1.0]$

Table C.2.: Parameter ranges for the training of the neural networks for the comparison in Figure 6.28.

found at the end of the section. The parameter ranges deviate for the comparison of the neural network approach with existing methods. The corresponding ranges are listed in Table C.2.

The different approaches are compared by a test set for each number of Breit-Wigners consisting of 1000 random samples within the parameter space. Another test set is constructed for two Breit-Wigners with a fixed scaling $A_1 = A_2 = 0.5$, a fixed mass $M_1 = 1$ and equally chosen widths $\Gamma := \Gamma_1 = \Gamma_2$. The mass M_2 and the width Γ are varied according to a regular grid in parameter space. This test set allows the analysis of contour plots of different loss measures. It provides more insights into the minima of the loss functions of the trained networks and into the severity of the inverse problem. The contour plots are averaged over 10 samples for the noise width of 10^{-3} (except for Figure 6.27).

We investigate three different performance measures and different set-ups of the neural network for a comparison to existing methods. The root-mean-square-deviation of the predicted parameters in parameter space, of the reconstructed spectral function and of the reconstructed propagator are considered. For the latter case, the error is computed based on the original propagator without noise. The measures are denoted as *parameter loss*, *spectral function loss* and *propagator loss* in this work. The spectral function loss and the propagator loss are computed based on the discretized representations on the uniform grid. Representative error bars for all methods are depicted in Figure 6.26.

The training procedure for the neural networks in this work is as follows. A neural network is trained separately for each training set, i.e., for each error and for each range of parameters. The learning rates are between 10^{-5} and 10^{-7}. The batch size is between 128 and 500 and the number of generated training samples per epoch is around 6×10^5. Depending on the kind of network, the nets are trained for 80 to 160 epochs. The used loss functions are described at the end of Section 6.5.4. The implemented net architectures are provided in Table C.3.

Name	CenterModule	Number of parameters
FC	FC(6700) ⇒ ReLU ⇒ FC(12168) ⇒ ReLU ⇒ FC(1024)	95×10^6
Deep FC	FC(512) ⇒ ReLU ⇒ FC(1024) ⇒ ReLU ⇒ (FC(4056) ⇒ ReLU)^3 ⇒ (FC(2056) ⇒ ReLU)^2	50×10^6
Narrow Deep FC	FC(512) ⇒ ReLU ⇒ (FC(1024) ⇒ ReLU)^3 ⇒ (FC(2056) ⇒ ReLU)^5 ⇒ (FC(1024) ⇒ ReLU)^3 ⇒ FC(512) ⇒ ReLU ⇒ FC(256)	96×10^6
Straight FC	(FC(4112) ⇒ BatchNorm1D ⇒ ReLU ⇒ Dropout(0.2))^7	102×10^6
Conv	Conv(64, 10) ⇒ ReLU ⇒ Conv(256, 10) ⇒ ReLU ⇒ (FC(4096) ⇒ ReLU)^2 ⇒ FC(1024)	41×10^6

Table C.3.: Details on the implemented network architectures. The general setup is: Input(100) ⇒ ReLU ⇒ CenterModule ⇒ ReLU ⇒ FC(3/6/9/500) ⇒ Output, whereas the CenterModule is given along with the associated name in the Table. The size of the output layer is determined by the use of a parameter net or a point net and the considered number of Breit-Wigners. An attached PP indicates that a post-processing procedure is applied on the suggested parameters, for more details, see Section 6.5.5.1.

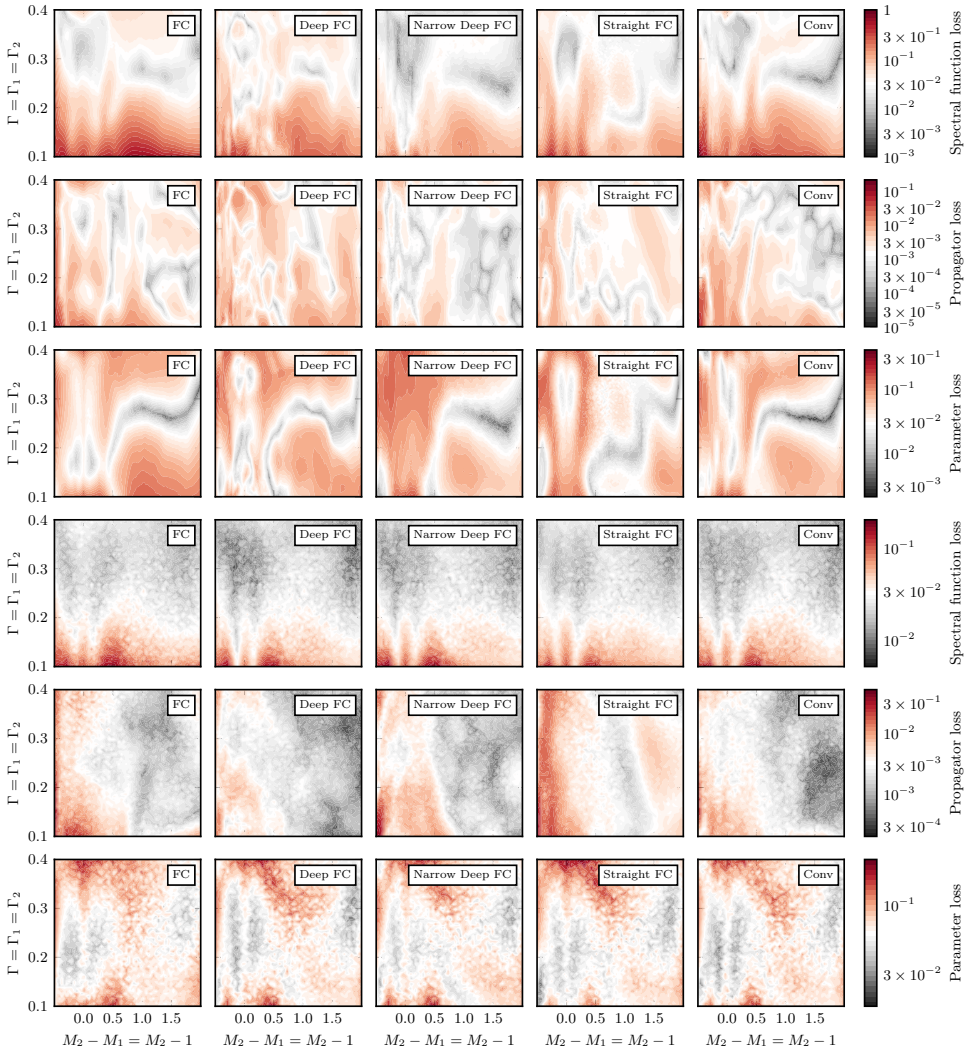

Figure 8.8.: **Comparison of network architectures**: Contour plots of loss measures are shown for different net architectures. The upper three rows correspond to reconstructions of propagators with a noise width of 10^{-5}, the lower ones with 10^{-3}. The plots illustrate the loss measures in a hyperplane within the parameter space whose properties are described in Section C.4. The networks are trained with the parameter loss on the training set of volume Vol O. The contour plots show that the local minima are slightly different for small noise widths, whereas the global structures remain similar for all network architectures. These differences are caused by a slightly differing utilization of the limited number of hyperparameters. The differences between the network architectures become less visible for larger errors due to the growing severity of the inverse problem and a decreasing knowledge about the correct inverse transformations. Interestingly, the loss landscape of the convolutional neural network, which intrinsically operates on local structures, and of the fully connected networks are almost equal. The non-locality of the inverse integral transformation represents a possible reason for why the specific choice of the network structure is largely irrelevant. We conclude that the actual architecture is rather negligible in comparison to other attributes of the learning process, such as the selection of training data and the choice of the loss function.

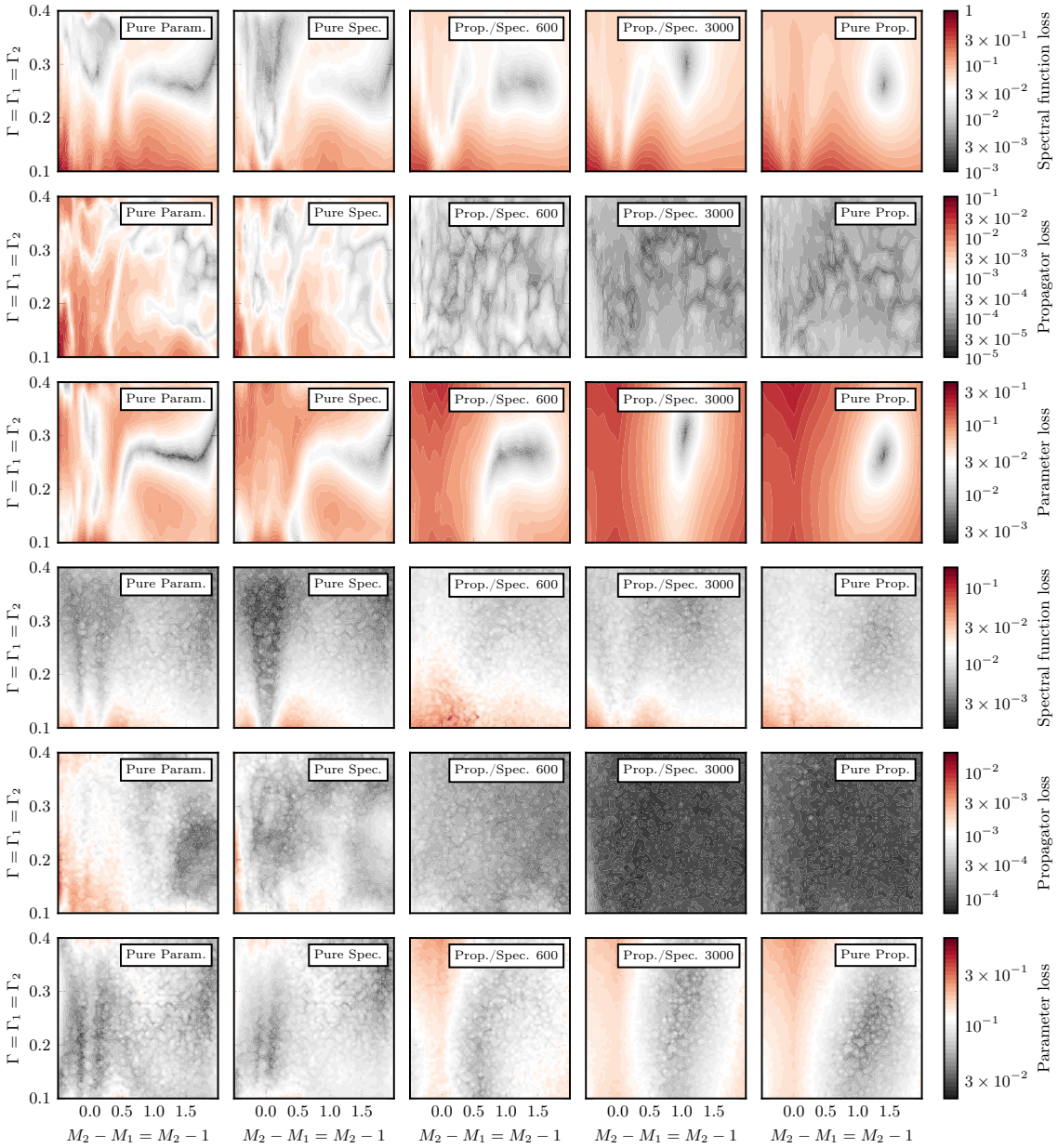

Figure 8.9.: **Comparison of loss functions**: Contour plots of loss measures are illustrated in the same manner as in Figure 8.8, but with a comparison o different loss functions. The considered loss functions are introduced in Section 6.5.4. The results are based on the Conv PaNet that is trained on volume Vol O. The optima in the loss function differ and, consequently, lead to different mean squared errors for the different measures. It is interesting that the network with the pure propagator loss function leads to a rather homogeneous propagator loss distribution. In contrast, the networks with the pure parameter and the pure spectral function loss do not result in homogeneous distributions for their corresponding loss function. The large set of nearly equal propagators for different parameters explains this observation. It confirms also once more the necessity of approaches that can be trained using loss functions with access to more information than just the reconstructed propagator.

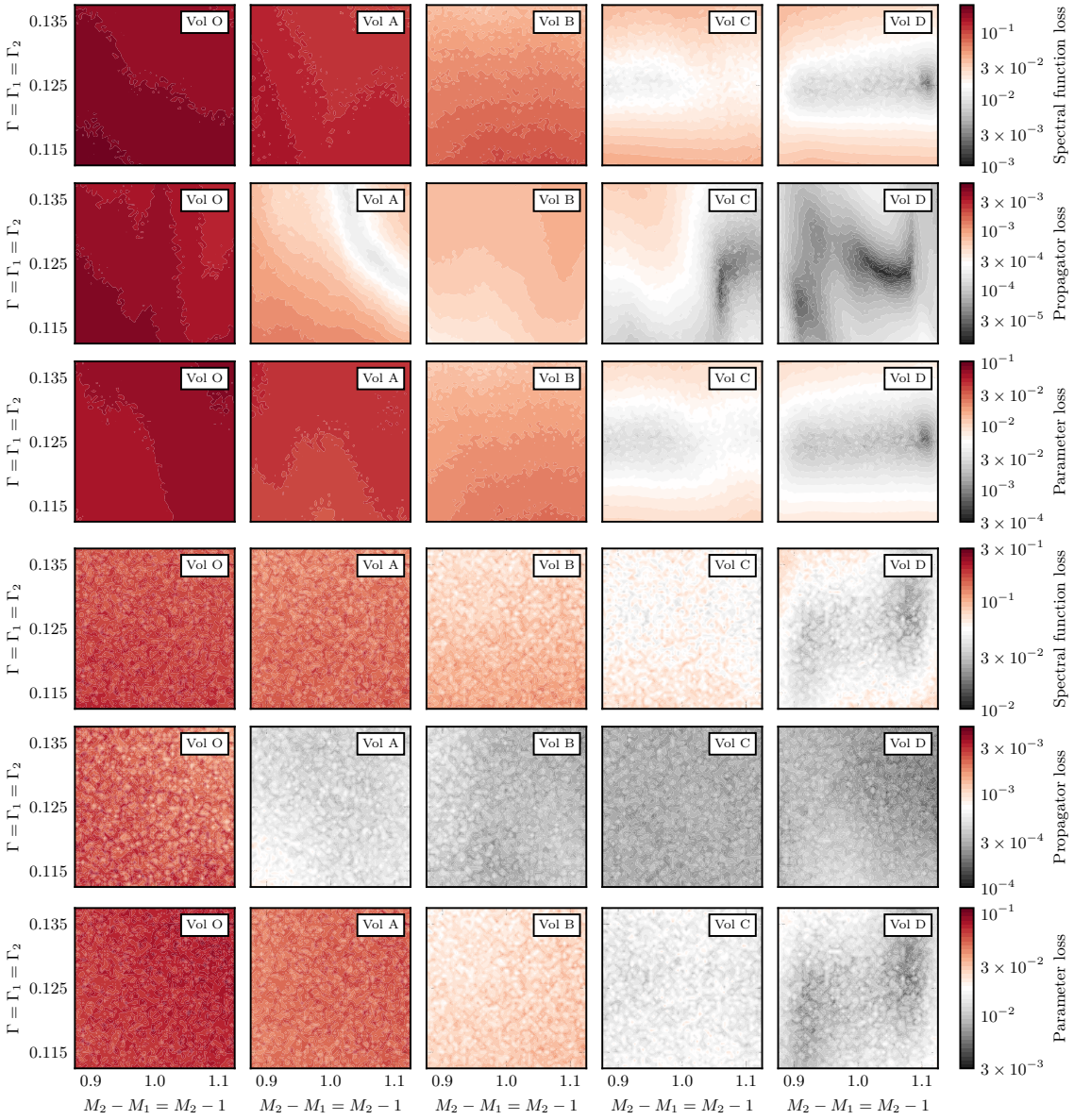

Figure 8.10.: **Analysis of prior information (parameter space of the training data) and of local differences in the severity of the inverse problem**: The evolution of the landscape of different loss measures is shown for networks that are trained on different parameter spaces. All contour plots are based on the same section of the parameter space, namely the range that is spanned by volume D. The upper three and lower rows correspond again to reconstructions of propagators with noise widths 10^{-5} and 10^{-3}. The gradual reduction of the parameter space allows the analysis of different levels of complexity of the problem. A general improvement of performance can be observed besides a shift of the global optima. The more homogeneous loss landscape demonstrates that the problem of a different severity of the inverse problem is still present, but damped.

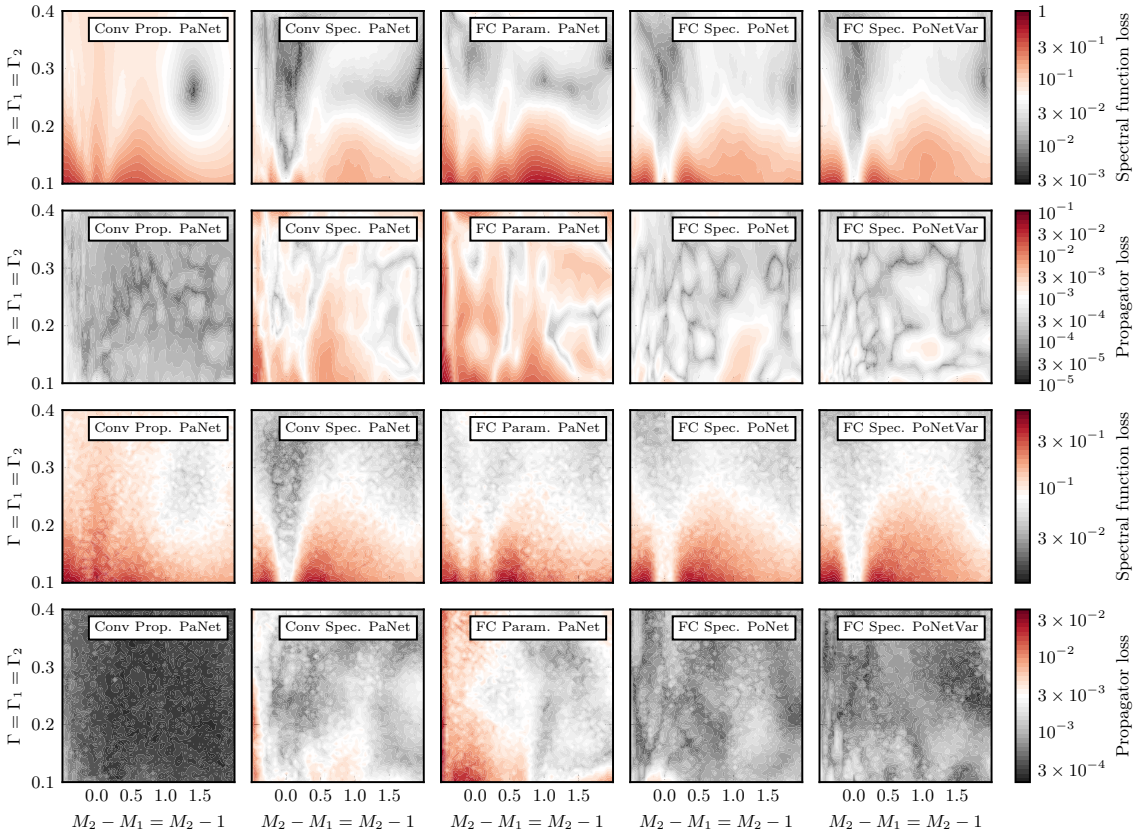

Figure 8.11.: **Comparison of the parameter net and the point net**: Root-mean-squared-deviations are compared between the parameter net and the point net, trained on two Breit-Wigner like structures (PoNet) and trained on a variable number of Breit-Wigners (PoNetVar), with respect to different loss functions. The two upper rows correspond to results from input propagators with a noise width of 10^{-5} and the two lower ones with a noise width of 10^{-3}. Problems concerning a varying severity of the inverse problem and concerning an information loss caused by the additive noise remain independent of the chosen basis for the representation of the spectral function.

Acknowledgments

First and foremost I would like to express my gratitude to Jan M. Pawlowski for an excellent supervision over the past couple of years. The almost infinite number of discussion, covering essentially all aspects of physics, as well as other topics, have always been scientifically fruitful and entertaining. The accompanying open door philosophy and informal atmosphere made working with him a very pleasant experience.

Furthermore, I would like to thank Jörg Jäckel for agreeing to be my second referee.

Special thanks goes to all my collaborators, whom I have worked with over the past couple of years and contributed greatly to my scientific knowledge.

Of great importance were also all the colleagues at the Institute for Theoretical Physics in Heidelberg and the nice working group I was a part of during my PhD. Since there are way to many people I had a wonderful time with to thank personally, I would like restrict myself to the few I spent probably the most time with, namely Eduardo Grossi, Anton K. Cyrol, Jan P. Horak, Coralie S. Schneier, Manuel Reichert and Fabian Rennecke.

Finally, I would like to express my gratitude to my friends and family for always being there for me.

Bibliography

[1] J. M. Pawlowski, N. Strodthoff, and N. Wink, "Finite temperature spectral functions in the O(N)-model," Phys. Rev. D98, 074008 (2018), arXiv:1711.07444 [hep-th].

[2] A. K. Cyrol, J. M. Pawlowski, A. Rothkopf, and N. Wink, "Reconstructing the gluon," SciPost Phys. 5, 065 (2018), arXiv:1804.00945 [hep-ph].

[3] M. Bluhm, Y. Jiang, M. Nahrgang, J. M. Pawlowski, F. Rennecke, and N. Wink, "Time-evolution of fluctuations as signal of the phase transition dynamics in a QCD-assisted transport approach," *Proceedings, 27th International Conference on Ultrarelativistic Nucleus-Nucleus Collisions (Quark Matter 2018): Venice, Italy, May 14-19, 2018*, Nucl. Phys. A982, 871 (2019), arXiv:1808.01377 [hep-ph].

[4] R. Alkofer, A. Maas, W. A. Mian, M. Mitter, J. París-López, J. M. Pawlowski, and N. Wink, "Bound state properties from the functional renormalization group," Phys. Rev. D99, 054029 (2019), arXiv:1810.07955 [hep-ph].

[5] E. Grossi and N. Wink, "Resolving phase transitions with Discontinuous Galerkin methods," (2019), arXiv:1903.09503 [hep-th].

[6] L. Kades, J. M. Pawlowski, A. Rothkopf, M. Scherzer, J. M. Urban, S. J. Wetzel, N. Wink, and F. Ziegler, "Spectral Reconstruction with Deep Neural Networks," (2019), arXiv:1905.04305 [physics.comp-ph].

[7] M. Bluhm *et al.*, "Dynamics of critical fluctuations: Theory – phenomenology – heavy-ion collisions," (2020), arXiv:2001.08831 [nucl-th].

[8] J. M. Pawlowski, J. A. Bonnet, S. Rechenberger, M. Reichert, and N. Wink, "-the functional renormalization group- & applications to gauge theories and gravity," (in preparation).

[9] J. M. Pawlowski, C. Schneider, and N. Wink, "QMeS - Derivation," (in preparation).

[10] E. Grossi, J. M. Pawlowski, and N. Wink, "An upwind Finite Difference scheme for Functional Renormalization Group equations," (in preparation).

[11] J. M. Pawlowski and N. Wink, "Spectral representations of elementary correlation functions," (in preparation).

[12] J. Horak, J. M. Pawlowski, and N. Wink, "Spectral functions in the ϕ^4-theory from DSE using dimensional regularization," (in preparation).

[13] J. M. Pawlowski and N. Wink, "Robust determination of the trace anomaly in gauge theories from the Functional Renormalization Group," (in preparation).

[14] J. M. Pawlowski and N. Wink, "Shear and Bulk viscosity of Yang-Mills from first principles," (in preparation).

[15] C.-N. Yang and R. L. Mills, "Conservation of Isotopic Spin and Isotopic Gauge Invariance," Phys. Rev. 96, 191 (1954).

[16] A. Jaffe and E. Witten, "Quantum yang-mills theory," The millennium prize problems 1 (2006).

[17] Relativistic Heavy Ion Collider (RHIC), https://www.bnl.gov/rhic/.

[18] Large Hadron Collider (LHC), https://home.cern/.

[19] Facility for Antiproton and Ion Research (FAIR), http://www.fair-center.eu/.

[20] Nuclotron-based Ion Collider fAcility (NICA), http://nica.jinr.ru/.

[21] Y. Aoki, G. Endrodi, Z. Fodor, S. D. Katz, and K. K. Szabo, "The Order of the quantum chromodynamics transition predicted by the standard model of particle physics," Nature 443, 675 (2006), arXiv:hep-lat/0611014 [hep-lat].

[22] S. Borsanyi, Z. Fodor, C. Hoelbling, S. D. Katz, S. Krieg, C. Ratti, and K. K. Szabo (Wuppertal-Budapest), "Is there still any Tc mystery in lattice QCD? Results with physical masses in the continuum limit III," JHEP 09, 073 (2010), arXiv:1005.3508 [hep-lat].

[23] S. Borsanyi *et al.*, "Calculation of the axion mass based on high-temperature lattice quantum chromodynamics," Nature 539, 69 (2016), arXiv:1606.07494 [hep-lat].

[24] A. Bazavov *et al.*, "The QCD Equation of State to $\mathcal{O}(\mu_B^6)$ from Lattice QCD," Phys. Rev. D95, 054504 (2017), arXiv:1701.04325 [hep-lat].

[25] M. Troyer and U.-J. Wiese, "Computational complexity and fundamental limitations to fermionic quantum Monte Carlo simulations," Phys. Rev. Lett. 94, 170201 (2005), arXiv:cond-mat/0408370 [cond-mat].

[26] P. de Forcrand, "Simulating QCD at finite density," *Proceedings, 27th International Symposium on Lattice field theory (Lattice 2009): Beijing, P.R. China, July 26-31, 2009*, PoS LAT2009, 010 (2009), arXiv:1005.0539 [hep-lat].

[27] C. S. Fischer, "QCD at finite temperature and chemical potential from Dyson–Schwinger equations," Prog. Part. Nucl. Phys. 105, 1 (2019), arXiv:1810.12938 [hep-ph].

[28] W.-j. Fu, J. M. Pawlowski, and F. Rennecke, "The QCD phase structure at finite temperature and density," (2019), arXiv:1909.02991 [hep-ph].

[29] F. Gao and J. M. Pawlowski, "QCD phase structure from functional methods," (2020), arXiv:2002.07500 [hep-ph].

[30] S. Schlichting and D. Teaney, "The First fm/c of Heavy-Ion Collisions," Ann. Rev. Nucl. Part. Sci. 69, 447 (2019), arXiv:1908.02113 [nucl-th].

[31] F. J. Dyson, "The S matrix in quantum electrodynamics," Phys. Rev. 75, 1736 (1949).

[32] J. S. Schwinger, "On the Green's functions of quantized fields. 1." Proc. Nat. Acad. Sci. 37, 452 (1951).

[33] J. S. Schwinger, "On the Green's functions of quantized fields. 2." Proc. Nat. Acad. Sci. 37, 455 (1951).

[34] C. Wetterich, "Exact evolution equation for the effective potential," Phys. Lett. B301, 90 (1993), arXiv:1710.05815 [hep-th].

[35] U. Ellwanger, "FLow equations for N point functions and bound states," *Proceedings, Workshop on Quantum field theoretical aspects of high energy physics: Bad Frankenhausen, Germany, September 20-24, 1993*, Z. Phys. C62, 503 (1994), [,206(1993)], arXiv:hep-ph/9308260 [hep-ph].

[36] T. R. Morris, "The Exact renormalization group and approximate solutions," Int. J. Mod. Phys. A9, 2411 (1994), arXiv:hep-ph/9308265 [hep-ph].

[37] J. Berges, N. Tetradis, and C. Wetterich, "Nonperturbative renormalization flow in quantum field theory and statistical physics," Phys. Rept. 363, 223 (2002), arXiv:hep-ph/0005122 [hep-ph].

[38] J. M. Pawlowski, "Aspects of the functional renormalisation group," Annals Phys. 322, 2831 (2007), arXiv:hep-th/0512261 [hep-th].

[39] H. Gies, "Introduction to the functional RG and applications to gauge theories," *Renormalization group and effective field theory approaches to many-body systems*, Lect. Notes Phys. 852, 287 (2012), arXiv:hep-ph/0611146 [hep-ph].

[40] O. J. Rosten, "Fundamentals of the Exact Renormalization Group," Phys. Rept. 511, 177 (2012), arXiv:1003.1366 [hep-th].

[41] J. Braun, "Fermion Interactions and Universal Behavior in Strongly Interacting Theories," J. Phys. G39, 033001 (2012), arXiv:1108.4449 [hep-ph].

[42] L. von Smekal, "Universal Aspects of QCD-like Theories," *Physics at all scales: The Renormalization Group. Proceedings, 49. Internationale Universitätswochen für Theoretische Physik, Winter School: Schladming, Austria, February 26-March 5, 2011*, Nucl. Phys. Proc. Suppl. 228, 179 (2012), arXiv:1205.4205 [hep-ph].

[43] C. Wetterich, "Quantum scale symmetry," (2019), arXiv:1901.04741 [hep-th].

[44] C. D. Roberts and A. G. Williams, "Dyson-Schwinger equations and their application to hadronic physics," Prog. Part. Nucl. Phys. 33, 477 (1994), arXiv:hep-ph/9403224 [hep-ph].

[45] R. Alkofer and L. von Smekal, "The Infrared behavior of QCD Green's functions: Confinement dynamical symmetry breaking, and hadrons as relativistic bound states," Phys. Rept. 353, 281 (2001), arXiv:hep-ph/0007355 [hep-ph].

[46] C. S. Fischer, "Infrared properties of QCD from Dyson-Schwinger equations," J. Phys. G32, R253 (2006), arXiv:hep-ph/0605173 [hep-ph].

[47] D. Binosi and J. Papavassiliou, "Pinch Technique: Theory and Applications," Phys. Rept. 479, 1 (2009), arXiv:0909.2536 [hep-ph].

[48] A. Maas, "Describing gauge bosons at zero and finite temperature," Phys. Rept. 524, 203 (2013), arXiv:1106.3942 [hep-ph].

[49] G. Eichmann, H. Sanchis-Alepuz, R. Williams, R. Alkofer, and C. S. Fischer, "Baryons as relativistic three-quark bound states," Prog. Part. Nucl. Phys. 91, 1 (2016), arXiv:1606.09602 [hep-ph].

[50] A. Wipf, "Statistical approach to quantum field theory," Lect. Notes Phys. 864, pp.1 (2013).

[51] L. P. Kadanoff, "Scaling laws for Ising models near T(c)," Physics Physique Fizika 2, 263 (1966).

[52] K. G. Wilson, "Renormalization group and critical phenomena. 1. Renormalization group and the Kadanoff scaling picture," Phys. Rev. B4, 3174 (1971).

[53] K. G. Wilson, "Renormalization group and critical phenomena. 2. Phase space cell analysis of critical behavior," Phys. Rev. B4, 3184 (1971).

[54] J. Polchinski, "Renormalization and Effective Lagrangians," Nucl. Phys. B231, 269 (1984).

[55] J. Braun, M. Leonhardt, and J. M. Pawlowski, "Renormalization group consistency and low-energy effective theories," SciPost Phys. 6, 056 (2019), arXiv:1806.04432 [hep-ph].

[56] D. F. Litim, J. M. Pawlowski, and L. Vergara, "Convexity of the effective action from functional flows," (2006), arXiv:hep-th/0602140 [hep-th].

[57] N. Christiansen, B. Knorr, J. Meibohm, J. M. Pawlowski, and M. Reichert, "Local Quantum Gravity," Phys. Rev. D92, 121501 (2015), arXiv:1506.07016 [hep-th].

[58] D. F. Litim, "Derivative expansion and renormalization group flows," JHEP 11, 059 (2001), arXiv:hep-th/0111159 [hep-th].

[59] D. F. Litim, "Optimized renormalization group flows," Phys. Rev. D64, 105007 (2001), arXiv:hep-th/0103195 [hep-th].

[60] B.-J. Schaefer and H.-J. Pirner, "Renormalization group flow and equation of state of quarks and mesons," Nucl. Phys. A660, 439 (1999), arXiv:nucl-th/9903003 [nucl-th].

[61] H. Gies, J. Jaeckel, J. M. Pawlowski, and C. Wetterich, "Do instantons like a colorful background?" Eur. Phys. J. C49, 997 (2007), arXiv:hep-ph/0608171 [hep-ph].

[62] T. K. Herbst, M. Mitter, J. M. Pawlowski, B.-J. Schaefer, and R. Stiele, "Thermodynamics of QCD at vanishing density," Phys. Lett. B731, 248 (2014), arXiv:1308.3621 [hep-ph].

[63] M. Mitter, J. M. Pawlowski, and N. Strodthoff, "Chiral symmetry breaking in continuum QCD," Phys. Rev. D91, 054035 (2015), arXiv:1411.7978 [hep-ph].

[64] A. K. Cyrol, M. Mitter, J. M. Pawlowski, and N. Strodthoff, "Nonperturbative quark, gluon, and meson correlators of unquenched QCD," Phys. Rev. D97, 054006 (2018), arXiv:1706.06326 [hep-ph].

[65] J. Braun, L. Fister, J. M. Pawlowski, and F. Rennecke, "From Quarks and Gluons to Hadrons: Chiral Symmetry Breaking in Dynamical QCD," Phys. Rev. D94, 034016 (2016), arXiv:1412.1045 [hep-ph].

[66] A. K. Cyrol, L. Fister, M. Mitter, J. M. Pawlowski, and N. Strodthoff, "Landau gauge Yang-Mills correlation functions," Phys. Rev. D94, 054005 (2016), arXiv:1605.01856 [hep-ph].

[67] L. Corell, A. K. Cyrol, M. Mitter, J. M. Pawlowski, and N. Strodthoff, "Correlation functions of three-dimensional Yang-Mills theory from the FRG," SciPost Phys. 5, 066 (2018), arXiv:1803.10092 [hep-ph].

[68] N. Christiansen, D. F. Litim, J. M. Pawlowski, and A. Rodigast, "Fixed points and infrared completion of quantum gravity," Phys. Lett. B728, 114 (2014), arXiv:1209.4038 [hep-th].

[69] N. Christiansen, B. Knorr, J. M. Pawlowski, and A. Rodigast, "Global Flows in Quantum Gravity," Phys. Rev. D93, 044036 (2016), arXiv:1403.1232 [hep-th].

[70] J. Meibohm, J. M. Pawlowski, and M. Reichert, "Asymptotic safety of gravity-matter systems," Phys. Rev. D93, 084035 (2016), arXiv:1510.07018 [hep-th].

[71] J. Meibohm and J. M. Pawlowski, "Chiral fermions in asymptotically safe quantum gravity," Eur. Phys. J. C76, 285 (2016), arXiv:1601.04597 [hep-th].

[72] T. Denz, J. M. Pawlowski, and M. Reichert, "Towards apparent convergence in asymptotically safe quantum gravity," Eur. Phys. J. C78, 336 (2018), arXiv:1612.07315 [hep-th].

[73] N. Christiansen, K. Falls, J. M. Pawlowski, and M. Reichert, "Curvature dependence of quantum gravity," Phys. Rev. D97, 046007 (2018), arXiv:1711.09259 [hep-th].

[74] A. Eichhorn, P. Labus, J. M. Pawlowski, and M. Reichert, "Effective universality in quantum gravity," SciPost Phys. 5, 031 (2018), arXiv:1804.00012 [hep-th].

[75] A. Eichhorn, S. Lippoldt, J. M. Pawlowski, M. Reichert, and M. Schiffer, "How perturbative is quantum gravity?" Phys. Lett. B792, 310 (2019), arXiv:1810.02828 [hep-th].

[76] P. Strack, R. Gersch, and W. Metzner, "Renormalization group flow for fermionic superfluids at zero temperature," Phys. Rev. B78, 014522 (2008), arXiv:0804.3994 [cond-mat.str-el].

[77] W. Metzner, M. Salmhofer, C. Honerkamp, V. Meden, and K. Schonhammer, "Functional renormalization group approach to correlated fermion systems," Rev. Mod. Phys. 84, 299 (2012), arXiv:1105.5289 [cond-mat.str-el].

[78] D. S. de la Peña, J. Lichtenstein, and C. Honerkamp, "Competing electronic instabilities of extended Hubbard models on the honeycomb lattice: A functional Renormalization Group calculation with high wavevector resolution," Phys. Rev. B95, 085143 (2017), arXiv:1606.01124 [cond-mat.str-el].

[79] T. Denz, M. Mitter, J. M. Pawlowski, C. Wetterich, and M. Yamada, "Partial bosonisation for the two-dimensional Hubbard model: How well does it work?" (2019), arXiv:1910.08300 [cond-mat.str-el].

[80] J. P. Blaizot, R. Mendez Galain, and N. Wschebor, "A New method to solve the non perturbative renormalization group equations," Phys. Lett. B632, 571 (2006), arXiv:hep-th/0503103 [hep-th].

[81] M. E. Carrington, W.-J. Fu, P. Mikula, and D. Pickering, "Four-point vertices from the 2PI and 4PI effective actions," Phys. Rev. D89, 025013 (2014), arXiv:1310.4352 [hep-ph].

[82] A. K. Cyrol, M. Q. Huber, and L. von Smekal, "A Dyson–Schwinger study of the four-gluon vertex," Eur. Phys. J. C75, 102 (2015), arXiv:1408.5409 [hep-ph].

[83] C. Hille, F. B. Kugler, C. J. Eckhardt, Y.-Y. He, A. Kauch, C. Honerkamp, A. Toschi, and S. Andergassen, "Quantitative functional renormalization-group description of the two-dimensional Hubbard model," (2020), arXiv:2002.02733 [cond-mat.str-el].

[84] G. Eichmann, R. Williams, R. Alkofer, and M. Vujinovic, "Three-gluon vertex in Landau gauge," Phys. Rev. D89, 105014 (2014), arXiv:1402.1365 [hep-ph].

[85] G. Eichmann, C. S. Fischer, and W. Heupel, "Four-point functions and the permutation group S4," Phys. Rev. D92, 056006 (2015), arXiv:1505.06336 [hep-ph].

[86] J. Zinn-Justin, *Quantum field theory and critical phenomena* (Clarendon Press, 1996).

[87] M. E. Peskin, *An introduction to quantum field theory* (CRC press, 2018).

[88] J. Zinn-Justin, "Quantum field theory at finite temperature: An Introduction," (2000), arXiv:hep-ph/0005272 [hep-ph].

[89] J. I. Kapusta and C. Gale, *Finite-temperature field theory: Principles and applications*, Cambridge Monographs on Mathematical Physics (Cambridge University Press, 2011).

[90] M. L. Bellac, *Thermal Field Theory*, Cambridge Monographs on Mathematical Physics (Cambridge University Press, 2011).

[91] M. Laine and A. Vuorinen, "Basics of thermal field theory," Lect. Notes Phys 925 (2016).

[92] C. Ford, U. G. Mitreuter, T. Tok, A. Wipf, and J. M. Pawlowski, "Monopoles, Polyakov loops and gauge fixing on the torus," Annals Phys. 269, 26 (1998), arXiv:hep-th/9802191 [hep-th].

[93] J. Braun, H. Gies, and J. M. Pawlowski, "Quark Confinement from Color Confinement," Phys. Lett. B684, 262 (2010), arXiv:0708.2413 [hep-th].

[94] F. Marhauser and J. M. Pawlowski, "Confinement in Polyakov Gauge," (2008), arXiv:0812.1144 [hep-ph].

[95] L. Fister and J. M. Pawlowski, "Confinement from Correlation Functions," Phys. Rev. D88, 045010 (2013), arXiv:1301.4163 [hep-ph].

[96] C. Becchi, A. Rouet, and R. Stora, "Renormalization of Gauge Theories," Annals Phys. 98, 287 (1976).

[97] I. V. Tyutin, "Gauge Invariance in Field Theory and Statistical Physics in Operator Formalism," (1975), arXiv:0812.0580 [hep-th].

[98] M. Henneaux and C. Teitelboim, *Quantization of gauge systems* (1992).

[99] U. Ellwanger, M. Hirsch, and A. Weber, "Flow equations for the relevant part of the pure Yang-Mills action," Z. Phys. C69, 687 (1996), arXiv:hep-th/9506019 [hep-th].

[100] U. Ellwanger, M. Hirsch, and A. Weber, "The Heavy quark potential from Wilson's exact renormalization group," Eur. Phys. J. C1, 563 (1998), arXiv:hep-ph/9606468 [hep-ph].

[101] J. M. Pawlowski, "Wilsonian flows in non-abelian gauge theories," Thphys. Uni-Heidelberg. De .

[102] W. R. Inc., "Mathematica, Version 11.3," Champaign, IL, 2018.

[103] M. Q. Huber and J. Braun, "Algorithmic derivation of functional renormalization group equations and Dyson-Schwinger equations," Comput. Phys. Commun. 183, 1290 (2012), arXiv:1102.5307 [hep-th].

[104] M. Q. Huber, A. K. Cyrol, and J. M. Pawlowski, "DoFun 3.0: Functional equations in Mathematica," Comput. Phys. Commun. 248, 107058 (2020), arXiv:1908.02760 [hep-ph].

[105] C. S. Fischer, A. Maas, and J. M. Pawlowski, "On the infrared behavior of Landau gauge Yang-Mills theory," Annals Phys. 324, 2408 (2009), arXiv:0810.1987 [hep-ph].

[106] A. K. Cyrol, *Non-perturbative QCD correlation functions*, Ph.D. thesis, Heidelberg U. (2017).

[107] A. Sternbeck, E. M. Ilgenfritz, M. Muller-Preussker, A. Schiller, and I. L. Bogolubsky, "Lattice study of the infrared behavior of QCD Green's functions in Landau gauge," *Proceedings, 24th International Symposium on Lattice Field Theory (Lattice 2006): Tucson, USA, July 23-28, 2006*, PoS LAT2006, 076 (2006), arXiv:hep-lat/0610053 [hep-lat].

[108] A. Maas, "Constraining the gauge-fixed Lagrangian in minimal Landau gauge," (2019), arXiv:1907.10435 [hep-lat].

[109] L. von Smekal, R. Alkofer, and A. Hauck, "The Infrared behavior of gluon and ghost propagators in Landau gauge QCD," Phys. Rev. Lett. 79, 3591 (1997), arXiv:hep-ph/9705242 [hep-ph].

[110] J. M. Pawlowski, D. F. Litim, S. Nedelko, and L. von Smekal, "Infrared behavior and fixed points in Landau gauge QCD," Phys. Rev. Lett. 93, 152002 (2004), arXiv:hep-th/0312324 [hep-th].

[111] D. Zwanziger, "Nonperturbative Landau gauge and infrared critical exponents in QCD," Phys. Rev. D65, 094039 (2002), arXiv:hep-th/0109224 [hep-th].

[112] C. Lerche and L. von Smekal, "On the infrared exponent for gluon and ghost propagation in Landau gauge QCD," Phys. Rev. D65, 125006 (2002), arXiv:hep-ph/0202194 [hep-ph].

[113] C. S. Fischer, R. Alkofer, and H. Reinhardt, "The Elusiveness of infrared critical exponents in Landau gauge Yang-Mills theories," Phys. Rev. D65, 094008 (2002), arXiv:hep-ph/0202195 [hep-ph].

[114] R. Alkofer, C. S. Fischer, and F. J. Llanes-Estrada, "Vertex functions and infrared fixed point in Landau gauge SU(N) Yang-Mills theory," Phys. Lett. B611, 279 (2005), [Erratum: Phys. Lett.B670,460(2009)], arXiv:hep-th/0412330 [hep-th].

[115] C. S. Fischer and J. M. Pawlowski, "Uniqueness of infrared asymptotics in Landau gauge Yang-Mills theory," Phys. Rev. D75, 025012 (2007), arXiv:hep-th/0609009 [hep-th].

[116] R. Alkofer, M. Q. Huber, and K. Schwenzer, "Infrared singularities in Landau gauge Yang-Mills theory," Phys. Rev. D81, 105010 (2010), arXiv:0801.2762 [hep-th].

[117] C. S. Fischer and J. M. Pawlowski, "Uniqueness of infrared asymptotics in Landau gauge Yang-Mills theory II," Phys. Rev. D80, 025023 (2009), arXiv:0903.2193 [hep-th].

[118] A. C. Aguilar, D. Binosi, and J. Papavassiliou, "Gluon and ghost propagators in the Landau gauge: Deriving lattice results from Schwinger-Dyson equations," Phys. Rev. D78, 025010 (2008), arXiv:0802.1870 [hep-ph].

[119] P. Boucaud, J. P. Leroy, A. Le Yaouanc, J. Micheli, O. Pene, and J. Rodriguez-Quintero, "On the IR behaviour of the Landau-gauge ghost propagator," JHEP 06, 099 (2008), arXiv:0803.2161 [hep-ph].

[120] J. Braun, M. Leonhardt, and M. Pospiech, "Fierz-complete NJL model study: Fixed points and phase structure at finite temperature and density," Phys. Rev. D96, 076003 (2017), arXiv:1705.00074 [hep-ph].

[121] J. Braun, M. Leonhardt, and M. Pospiech, "Fierz-complete NJL model study. II. Toward the fixed-point and phase structure of hot and dense two-flavor QCD," Phys. Rev. D97, 076010 (2018), arXiv:1801.08338 [hep-ph].

[122] J. Braun, M. Leonhardt, and M. Pospiech, "Fierz-complete NJL model study III: Emergence from quark-gluon dynamics," Phys. Rev. D101, 036004 (2020), arXiv:1909.06298 [hep-ph].

[123] J. Braun and H. Gies, "Chiral phase boundary of QCD at finite temperature," JHEP 06, 024 (2006), arXiv:hep-ph/0602226 [hep-ph].

[124] H. Gies and C. Wetterich, "Renormalization flow of bound states," Phys. Rev. D65, 065001 (2002), arXiv:hep-th/0107221 [hep-th].

[125] R. L. Stratonovich, "A method for the computation of quantum distribution functions," in *Doklady Akademii Nauk*, Vol. 115 (Russian Academy of Sciences, 1957) pp. 1097–1100.

[126] J. Hubbard, "Calculation of partition functions," Physical Review Letters 3, 77 (1959).

[127] H. Gies and C. Wetterich, "Universality of spontaneous chiral symmetry breaking in gauge theories," Phys. Rev. D69, 025001 (2004), arXiv:hep-th/0209183 [hep-th].

[128] J. Braun, "The QCD Phase Boundary from Quark-Gluon Dynamics," Eur. Phys. J. C64, 459 (2009), arXiv:0810.1727 [hep-ph].

[129] S. Floerchinger and C. Wetterich, "Exact flow equation for composite operators," Phys. Lett. B680, 371 (2009), arXiv:0905.0915 [hep-th].

[130] S. Floerchinger, "Exact Flow Equation for Bound States," Eur. Phys. J. C69, 119 (2010), arXiv:1001.4497 [hep-th].

[131] W. H. Reed and T. Hill, *Triangular mesh methods for the neutron transport equation*, Tech. Rep. (Los Alamos Scientific Lab., N. Mex.(USA), 1973).

[132] C. Johnson and J. Pitkäranta, "An analysis of the discontinuous galerkin method for a scalar hyperbolic equation," Mathematics of computation 46, 1 (1986).

[133] T. E. Peterson, "A note on the convergence of the discontinuous galerkin method for a scalar hyperbolic equation," SIAM Journal on Numerical Analysis 28, 133 (1991).

[134] Lin and Zhou, "Convergence of the discontinuous galerkin method for a scalar hyperbolic equation," Acta Mathematica Scientia 13, 207 (1993).

[135] B. Cockburn and J. Guzmán, "Error estimates for the runge–kutta discontinuous galerkin method for the transport equation with discontinuous initial data," SIAM Journal on Numerical Analysis 46, 1364 (2008).

[136] J. S. Hesthaven and T. Warburton, *Nodal discontinuous Galerkin methods: algorithms, analysis, and applications* (Springer Science & Business Media, 2007).

[137] O. C. Zienkiewicz, R. L. Taylor, P. Nithiarasu, and J. Zhu, *The finite element method*, Vol. 3 (McGraw-hill London, 1977).

[138] R. J. LeVeque, *Finite volume methods for hyperbolic problems*, Vol. 31 (Cambridge university press, 2002).

[139] L. Rezzolla and O. Zanotti, *Relativistic hydrodynamics* (Oxford University Press, 2013).

[140] P. D. Lax, "Weak solutions of nonlinear hyperbolic equations and their numerical computation," Communications on pure and applied mathematics 7, 159 (1954).

[141] M. D'Attanasio and T. R. Morris, "Large N and the renormalization group," Phys. Lett. B409, 363 (1997), arXiv:hep-th/9704094 [hep-th].

[142] N. Tetradis and D. F. Litim, "Analytical solutions of exact renormalization group equations," Nucl. Phys. B464, 492 (1996), arXiv:hep-th/9512073 [hep-th].

[143] D. Litim and N. Tetradis, "Approximate solutions of exact renormalization group equations," (1995), arXiv:hep-th/9501042 [hep-th].

[144] D. F. Litim, "Critical exponents from optimized renormalization group flows," Nucl. Phys. B631, 128 (2002), arXiv:hep-th/0203006 [hep-th].

[145] K.-I. Aoki, S.-I. Kumamoto, and M. Yamada, "Phase structure of NJL model with weak renormalization group," Nucl. Phys. B931, 105 (2018), arXiv:1705.03273 [hep-th].

[146] A. C. Hindmarsh, P. N. Brown, K. E. Grant, S. L. Lee, R. Serban, D. E. Shumaker, and C. S. Woodward, "SUNDIALS: Suite of nonlinear and differential/algebraic equation solvers," ACM Transactions on Mathematical Software (TOMS) 31, 363 (2005).

[147] C.-W. Shu and S. Osher, "Efficient implementation of essentially non-oscillatory shock-capturing schemes," Journal of computational physics 77, 439 (1988).

[148] L. Del Zanna, O. Zanotti, N. Bucciantini, and P. Londrillo, "ECHO: an Eulerian Conservative High Order scheme for general relativistic magnetohydrodynamics and magnetodynamics," Astron. Astrophys. 473, 11 (2007), arXiv:0704.3206 [astro-ph].

[149] L. Del Zanna, V. Chandra, G. Inghirami, V. Rolando, A. Beraudo, A. De Pace, G. Pagliara, A. Drago, and F. Becattini, "Relativistic viscous hydrodynamics for heavy-ion collisions with ECHO-QGP," Eur. Phys. J. C73, 2524 (2013), arXiv:1305.7052 [nucl-th].

[150] S. Floerchinger and E. Grossi, "Causality of fluid dynamics for high-energy nuclear collisions," JHEP 08, 186 (2018), arXiv:1711.06687 [nucl-th].

[151] S. Floerchinger, E. Grossi, and J. Lion, "Fluid dynamics of heavy ion collisions with Mode expansion (FluiduM)," (2018), arXiv:1811.01870 [nucl-th].

[152] F. Fambri, M. Dumbser, S. Köppel, L. Rezzolla, and O. Zanotti, "ADER discontinuous Galerkin schemes for general-relativistic ideal magnetohydrodynamics," Mon. Not. Roy. Astron. Soc. 477, 4543 (2018), arXiv:1801.02839 [physics.comp-ph].

[153] W. Bangerth, R. Hartmann, and G. Kanschat, "deal.II – a general purpose object oriented finite element library," ACM Trans. Math. Softw. 33, 24/1 (2007).

[154] M. Blatt, A. Burchardt, A. Dedner, C. Engwer, J. Fahlke, B. Flemisch, C. Gersbacher, C. Gräser, F. Gruber, C. Grüninger, *et al.*, "The distributed and unified numerics environment, version 2.4," Archive of Numerical Software 4, 13 (2016).

[155] S. Müthing, M. Piatkowski, and P. Bastian, "High-performance implementation of matrix-free high-order discontinuous galerkin methods," arXiv preprint arXiv:1711.10885 (2017).

[156] E. Tadmor, "Filters, mollifiers and the computation of the gibbs phenomenon," Acta Numerica 16, 305 (2007).

[157] A. Bonanno and G. Lacagnina, "Spontaneous symmetry breaking and proper time flow equations," Nucl. Phys. B693, 36 (2004), arXiv:hep-th/0403176 [hep-th].

[158] M. Peláez and N. Wschebor, "Ordered phase of the $O(N)$ model within the nonperturbative renormalization group," Phys. Rev. E94, 042136 (2016), arXiv:1510.05709 [cond-mat.stat-mech].

[159] J. Borchardt and B. Knorr, "Global solutions of functional fixed point equations via pseudospectral methods," Phys. Rev. D91, 105011 (2015), [Erratum: Phys. Rev.D93,no.8,089904(2016)], arXiv:1502.07511 [hep-th].

[160] F. Rennecke, "Vacuum structure of vector mesons in QCD," Phys. Rev. D92, 076012 (2015), arXiv:1504.03585 [hep-ph].

[161] J. A. Adams, J. Berges, S. Bornholdt, F. Freire, N. Tetradis, and C. Wetterich, "Solving nonperturbative flow equations," Mod. Phys. Lett. A10, 2367 (1995), arXiv:hep-th/9507093 [hep-th].

[162] G. Papp, B.-J. Schaefer, H. Pirner, and J. Wambach, "On the convergence of the expansion of renormalization group flow equation," Phys.Rev. D61, 096002 (2000), arXiv:hep-ph/9909246 [hep-ph].

[163] O. Bohr, B. J. Schaefer, and J. Wambach, "Renormalization group flow equations and the phase transition in O(N) models," Int. J. Mod. Phys. A16, 3823 (2001), arXiv:hep-ph/0007098 [hep-ph].

[164] B.-J. Schaefer and J. Wambach, "The Phase diagram of the quark meson model," Nucl.Phys. A757, 479 (2005), arXiv:nucl-th/0403039 [nucl-th].

[165] R.-A. Tripolt, N. Strodthoff, L. von Smekal, and J. Wambach, "Spectral Functions for the Quark-Meson Model Phase Diagram from the Functional Renormalization Group," Phys. Rev. D89, 034010 (2014), arXiv:1311.0630 [hep-ph].

[166] T. Yokota, T. Kunihiro, and K. Morita, "Functional renormalization group analysis of the soft mode at the QCD critical point," PTEP 2016, 073D01 (2016), arXiv:1603.02147 [hep-ph].

[167] J. M. Pawlowski, M. Reichert, C. Wetterich, and M. Yamada, "Higgs scalar potential in asymptotically safe quantum gravity," Phys. Rev. D99, 086010 (2019), arXiv:1811.11706 [hep-th].

[168] J. Borchardt and B. Knorr, "Solving functional flow equations with pseudo-spectral methods," Phys. Rev. D94, 025027 (2016), arXiv:1603.06726 [hep-th].

[169] J. Borchardt, H. Gies, and R. Sondenheimer, "Global flow of the Higgs potential in a Yukawa model," Eur. Phys. J. C76, 472 (2016), arXiv:1603.05861 [hep-ph].

[170] C. S. Fischer and H. Gies, "Renormalization flow of Yang-Mills propagators," JHEP 10, 048 (2004), arXiv:hep-ph/0408089 [hep-ph].

[171] L. Fister, *On the Phase Diagram of QCD with Dynamical Quarks*, Ph.D. thesis, Heidelberg U. (2012).

[172] S. Bornholdt, N. Tetradis, and C. Wetterich, "Coleman-Weinberg phase transition in two scalar models," Phys. Lett. B348, 89 (1995), arXiv:hep-th/9408132 [hep-th].

[173] S. Bornholdt, N. Tetradis, and C. Wetterich, "High temperature phase transition in two scalar theories," Phys. Rev. D53, 4552 (1996), arXiv:hep-ph/9503282 [hep-ph].

[174] J. Berges and C. Wetterich, "Equation of state and coarse grained free energy for matrix models," Nucl. Phys. B487, 675 (1997), arXiv:hep-th/9609019 [hep-th].

[175] J. Berges, N. Tetradis, and C. Wetterich, "Coarse graining and first order phase transitions," Phys. Lett. B393, 387 (1997), arXiv:hep-ph/9610354 [hep-ph].

[176] N. Tetradis, "The Exact renormalization group and first order phase transitions," *The exact renormalization group. Proceedings, 2nd Conference, Rome, Italy, September 18-22, 2000*, Int. J. Mod. Phys. A16, 1927 (2001), arXiv:hep-th/0012107 [hep-th].

[177] M. Reichert, A. Eichhorn, H. Gies, J. M. Pawlowski, T. Plehn, and M. M. Scherer, "Probing baryogenesis through the Higgs boson self-coupling," Phys. Rev. D97, 075008 (2018), arXiv:1711.00019 [hep-ph].

[178] X. Zhong and C.-W. Shu, "A simple weighted essentially nonoscillatory limiter for runge–kutta discontinuous galerkin methods," Journal of Computational Physics 232, 397 (2013).

[179] A. Jüttner, D. F. Litim, and E. Marchais, "Global Wilson–Fisher fixed points," Nucl. Phys. B921, 769 (2017), arXiv:1701.05168 [hep-th].

[180] D. F. Litim, E. Marchais, and P. Mati, "Fixed points and the spontaneous breaking of scale invariance," Phys. Rev. D95, 125006 (2017), arXiv:1702.05749 [hep-th].

[181] S. Yabunaka and B. Delamotte, "Why Might the Standard Large N Analysis Fail in the O(N) Model: The Role of Cusps in the Fixed Point Potentials," Phys. Rev. Lett. 121, 231601 (2018), arXiv:1807.04681 [cond-mat.stat-mech].

[182] B. Cockburn and C.-W. Shu, "The local discontinuous galerkin method for time-dependent convection-diffusion systems," SIAM Journal on Numerical Analysis 35, 2440 (1998).

[183] D. N. Arnold, F. Brezzi, B. Cockburn, and L. D. Marini, "Unified analysis of discontinuous galerkin methods for elliptic problems," SIAM journal on numerical analysis 39, 1749 (2002).

[184] S. Brdar, A. Dedner, and R. Klöfkorn, "Compact and stable discontinuous galerkin methods for convection-diffusion problems," SIAM Journal on Scientific Computing 34, A263 (2012).

[185] J. M. Pawlowski and F. Rennecke, "Higher order quark-mesonic scattering processes and the phase structure of QCD," Phys. Rev. D90, 076002 (2014), arXiv:1403.1179 [hep-ph].

[186] G. P. Vacca and L. Zambelli, "Multimeson Yukawa interactions at criticality," Phys. Rev. D91, 125003 (2015), arXiv:1503.09136 [hep-th].

[187] B. Knorr, "Ising and Gross-Neveu model in next-to-leading order," Phys. Rev. B94, 245102 (2016), arXiv:1609.03824 [cond-mat.str-el].

[188] H. Gies, R. Sondenheimer, and M. Warschinke, "Impact of generalized Yukawa interactions on the lower Higgs mass bound," Eur. Phys. J. C77, 743 (2017), arXiv:1707.04394 [hep-ph].

[189] L. Fister and J. M. Pawlowski, "Functional renormalization group in a finite volume," Phys. Rev. D92, 076009 (2015), arXiv:1504.05166 [hep-ph].

[190] D. U. Jungnickel and C. Wetterich, "Effective action for the chiral quark-meson model," Phys. Rev. D53, 5142 (1996), arXiv:hep-ph/9505267 [hep-ph].

[191] D. U. Jungnickel and C. Wetterich, "Flow equations for phase transitions in statistical physics and QCD," in *The exact renormalization group. Proceedings, Workshop, Faro, Portugal, September 10-12, 1998* (1998) pp. 41–113, arXiv:hep-ph/9902316 [hep-ph].

[192] B.-J. Schaefer and J. Wambach, "Renormalization group approach towards the QCD phase diagram," *Helmholtz International Summer School on Dense Matter in Heavy Ion Collisions and Astrophysics Dubna, Russia, August 21-September 1, 2006*, Phys. Part. Nucl. 39, 1025 (2008), arXiv:hep-ph/0611191 [hep-ph].

[193] F. Rennecke and B.-J. Schaefer, "Fluctuation-induced modifications of the phase structure in (2+1)-flavor QCD," Phys. Rev. D96, 016009 (2017), arXiv:1610.08748 [hep-ph].

[194] J. Glimm and A. M. Jaffe, *QUANTUM PHYSICS. A FUNCTIONAL INTEGRAL POINT OF VIEW* (1987).

[195] G. Cuniberti, E. De Micheli, and G. A. Viano, "Reconstructing the thermal Green functions at real times from those at imaginary times," Commun. Math. Phys. 216, 59 (2001), arXiv:cond-mat/0109175 [cond-mat.str-el].

[196] A. J. Helmboldt, J. M. Pawlowski, and N. Strodthoff, "Towards quantitative precision in the chiral crossover: masses and fluctuation scales," Phys. Rev. D91, 054010 (2015), arXiv:1409.8414 [hep-ph].

[197] J. M. Pawlowski and N. Strodthoff, "Real time correlation functions and the functional renormalization group," Phys. Rev. D92, 094009 (2015), arXiv:1508.01160 [hep-ph].

[198] A. Das, *Finite Temperature Field Theory*, World scientific lecture notes in physics (World Scientific, 1997).

[199] E. E. Salpeter, "Wave Functions in Momentum Space," Phys. Rev. 84, 1226 (1951).

[200] E. E. Salpeter and H. A. Bethe, "A Relativistic equation for bound state problems," Phys. Rev. 84, 1232 (1951).

[201] S. Aoki *et al.*, "Review of lattice results concerning low-energy particle physics," Eur. Phys. J. C77, 112 (2017), arXiv:1607.00299 [hep-lat].

[202] A. C. Aguilar, D. Binosi, and J. Papavassiliou, "Schwinger mechanism in linear covariant gauges," Phys. Rev. D95, 034017 (2017), arXiv:1611.02096 [hep-ph].

[203] A. C. Aguilar, D. Binosi, C. T. Figueiredo, and J. Papavassiliou, "Evidence of ghost suppression in gluon mass scale dynamics," Eur. Phys. J. C78, 181 (2018), arXiv:1712.06926 [hep-ph].

[204] N. Alkofer and R. Alkofer, "Features of ghost-gluon and ghost-quark bound states related to BRST quartets," Phys. Lett. B702, 158 (2011), arXiv:1102.2753 [hep-th].

[205] A. Bashir, L. Chang, I. C. Cloet, B. El-Bennich, Y.-X. Liu, C. D. Roberts, and P. C. Tandy, "Collective perspective on advances in Dyson-Schwinger Equation QCD," Commun. Theor. Phys. 58, 79 (2012), arXiv:1201.3366 [nucl-th].

[206] H. Sanchis-Alepuz and R. Williams, "Hadronic Observables from Dyson-Schwinger and Bethe-Salpeter equations," *Proceedings, 4th Symposium on Prospects in the Physics of Discrete Symmetries (DISCRETE 2014): London, UK, December 2-6, 2014*, J. Phys. Conf. Ser. 631, 012064 (2015), arXiv:1503.05896 [hep-ph].

[207] T. Hilger, M. Gómez-Rocha, A. Krassnigg, and W. Lucha, "Aspects of open-flavour mesons in a comprehensive DSBSE study," Eur. Phys. J. A53, 213 (2017), arXiv:1702.06262 [hep-ph].

[208] C. Chen, B. El-Bennich, C. D. Roberts, S. M. Schmidt, J. Segovia, and S. Wan, "Structure of the nucleon's low-lying excitations," Phys. Rev. D97, 034016 (2018), arXiv:1711.03142 [nucl-th].

[209] F. E. Serna, B. El-Bennich, and G. Krein, "Charmed mesons with a symmetry-preserving contact interaction," Phys. Rev. D96, 014013 (2017), arXiv:1703.09181 [hep-ph].

[210] J. Carbonell, T. Frederico, and V. A. Karmanov, "Bound state equation for the Nakanishi weight function," Phys. Lett. B769, 418 (2017), arXiv:1704.04160 [hep-ph].

[211] A. Stadler, S. Leitão, M. T. Peña, and E. P. Biernat, "Heavy and heavy-light mesons in the Covariant Spectator Theory," *Proceedings, Frontiers in Light Front Hadron Physics: Theory and Experiment (Light Cone 2017): Mumbai, Maharashtra, India, September 18-22, 2017*, Few Body Syst. 59, 32 (2018), arXiv:1803.00519 [hep-ph].

[212] A. Castro, E. Ydrefors, W. de Paula, T. Frederico, J. H. De Alvarenga Nogueira, and P. Maris, "The Bethe-Salpeter approach to bound states: from Euclidean to Minkowski space," (2019), arXiv:1901.04266 [hep-ph].

[213] R. Williams, C. S. Fischer, and W. Heupel, "Light mesons in QCD and unquenching effects from the 3PI effective action," Phys. Rev. D93, 034026 (2016), arXiv:1512.00455 [hep-ph].

[214] U. Ellwanger and C. Wetterich, "Evolution equations for the quark - meson transition," Nucl. Phys. B423, 137 (1994), arXiv:hep-ph/9402221 [hep-ph].

[215] A. Jakovác and A. Patkós, "Bound states in Functional Renormalization Group," Int. J. Mod. Phys. A34, 1950154 (2019), arXiv:1811.09418 [hep-th].

[216] A. Jakovác and A. Patkós, "Interacting two-particle states in the symmetric phase of the chiral Nambu-Jona-Lasinio model," (2019), arXiv:1902.06492 [hep-th].

[217] S. Floerchinger, "Analytic Continuation of Functional Renormalization Group Equations," JHEP 05, 021 (2012), arXiv:1112.4374 [hep-th].

[218] N. Strodthoff, "Self-consistent spectral functions in the O(N) model from the functional renormalization group," Phys. Rev. D95, 076002 (2017), arXiv:1611.05036 [hep-th].

[219] K. Kamikado, N. Strodthoff, L. von Smekal, and J. Wambach, "Real-time correlation functions in the $O(N)$ model from the functional renormalization group," Eur. Phys. J. C74, 2806 (2014), arXiv:1302.6199 [hep-ph].

[220] R.-A. Tripolt, L. von Smekal, and J. Wambach, "Flow equations for spectral functions at finite external momenta," Phys. Rev. D90, 074031 (2014), arXiv:1408.3512 [hep-ph].

[221] C. Jung, F. Rennecke, R.-A. Tripolt, L. von Smekal, and J. Wambach, "In-Medium Spectral Functions of Vector- and Axial-Vector Mesons from the Functional Renormalization Group," Phys. Rev. D95, 036020 (2017), arXiv:1610.08754 [hep-ph].

[222] Z. Wang and P. Zhuang, "Meson spectral functions at finite temperature and isospin density with the functional renormalization group," Phys. Rev. D96, 014006 (2017), arXiv:1703.01035 [hep-ph].

[223] T. Yokota, T. Kunihiro, and K. Morita, "Tachyonic instability of the scalar mode prior to the QCD critical point based on the functional renormalization-group method in the two-flavor case," Phys. Rev. D96, 074028 (2017), arXiv:1707.05520 [hep-ph].

[224] M. Haas, L. Fister, and J. M. Pawlowski, "Gluon spectral functions and transport coefficients in Yang–Mills theory," Phys. Rev. D90, 091501 (2014), arXiv:1308.4960 [hep-ph].

[225] F. Rose, F. Léonard, and N. Dupuis, "Higgs amplitude mode in the vicinity of a $(2+1)$-dimensional quantum critical point: a nonperturbative renormalization-group approach," Phys. Rev. B91, 224501 (2015), arXiv:1503.08688 [cond-mat.quant-gas].

[226] R.-A. Tripolt, I. Haritan, J. Wambach, and N. Moiseyev, "Threshold energies and poles for hadron physical problems by a model-independent universal algorithm," Phys. Lett. B774, 411 (2017), arXiv:1610.03252 [hep-ph].

[227] R.-A. Tripolt, P. Gubler, M. Ulybyshev, and L. Von Smekal, "Numerical analytic continuation of Euclidean data," Comput. Phys. Commun. 237, 129 (2019), arXiv:1801.10348 [hep-ph].

[228] P. Springer, J. Braun, S. Rechenberger, and F. Rennecke, "QCD-inspired determination of NJL model parameters," *Proceedings, 12th Conference on Quark Confinement and the Hadron Spectrum (Confinement XII): Thessaloniki, Greece*, EPJ Web Conf. 137, 03022 (2017), arXiv:1611.06020 [hep-ph].

[229] J. Eser, F. Divotgey, M. Mitter, and D. H. Rischke, "Low-energy limit of the $O(4)$ quark-meson model from the functional renormalization group approach," Phys. Rev. D98, 014024 (2018), arXiv:1804.01787 [hep-ph].

[230] J. Eser, F. Divotgey, and M. Mitter, "Low-energy limit of the $O(4)$ quark-meson model," (2019) arXiv:1902.04804 [hep-ph].

[231] R. Alkofer and H. Reinhardt, "Chiral quark dynamics," Lect. Notes Phys. Monogr. 33, 1 (1995).

[232] F. Rennecke, *The Chiral Phase Transition of QCD*, Ph.D. thesis, Heidelberg U. (2015).

[233] G. Markó, U. Reinosa, and Z. Szép, "Loss of solution in the symmetry improved phi-derivable expansion scheme," Nucl. Phys. B913, 405 (2016), arXiv:1604.04193 [hep-ph].

[234] L. Schlessinger, "Use of analyticity in the calculation of nonrelativistic scattering amplitudes," Phys. Rev. 167, 1411 (1968).

[235] Y. Burnier, M. Laine, and L. Mether, "A Test on analytic continuation of thermal imaginary-time data," Eur. Phys. J. C71, 1619 (2011), arXiv:1101.5534 [hep-lat].

[236] A. S. Wightman and L. Garding, "Fields as operator-valued distributions in relativistic quantum theory," Arkiv Fys. 28 (1965).

[237] N. N. Bogolubov, A. Logunov, and I. T. Todorov, *Introduction to axiomatic quantum field theory* (1975).

[238] T. S. Evans, "N point finite temperature expectation values at real times," Nucl. Phys. B374, 340 (1992).

[239] T. S. Evans, "THREE POINT FUNCTIONS AT FINITE TEMPERATURE," Phys. Lett. B249, 286 (1990).

[240] T. S. Evans, "Spectral representation of three point functions at finite temperature," Phys. Lett. B252, 108 (1990).

[241] R. Balian and C. De Dominicis, "Sur la fonction de green à une particule en mécanique statistique quantique," Nuclear Physics 16, 502 (1960).

[242] K.-c. Chou, Z.-b. Su, B.-l. Hao, and L. Yu, "Equilibrium and Nonequilibrium Formalisms Made Unified," Phys. Rept. 118, 1 (1985).

[243] R. L. Kobes and G. W. Semenoff, "Discontinuities of Green Functions in Field Theory at Finite Temperature and Density," Nucl. Phys. B260, 714 (1985).

[244] R. L. Kobes and G. W. Semenoff, "Discontinuities of Green Functions in Field Theory at Finite Temperature and Density. 2," Nucl. Phys. B272, 329 (1986).

[245] P. Aurenche and T. Becherrawy, "A Comparison of the real time and the imaginary time formalisms of finite temperature field theory for 2, 3, and 4 point Green's functions," Nucl. Phys. B379, 259 (1992).

[246] R. Baier and A. Niegawa, "Analytic continuation of thermal N point functions from imaginary to real energies," Phys. Rev. D49, 4107 (1994), arXiv:hep-ph/9307362 [hep-ph].

[247] F. Guerin, "Retarded - advanced N point Green functions in thermal field theories," Nucl. Phys. B432, 281 (1994), arXiv:hep-ph/9306210 [hep-ph].

[248] M. E. Carrington and U. W. Heinz, "Three point functions at finite temperature," Eur. Phys. J. C1, 619 (1998), arXiv:hep-th/9606055 [hep-th].

[249] J. Bros and D. Buchholz, "Axiomatic analyticity properties and representations of particles in thermal quantum field theory," Ann. Inst. H. Poincare Phys. Theor. 64, 495 (1996), arXiv:hep-th/9606046 [hep-th].

[250] D.-f. Hou and U. W. Heinz, "Three point spectral functions in resummed phi**3 in six-dimensions theory at finite temperature," Eur. Phys. J. C4, 129 (1998), arXiv:hep-ph/9704392 [hep-ph].

[251] H. A. Weldon, "Finite temperature retarded and advanced fields," Nucl. Phys. B534, 467 (1998), arXiv:hep-ph/9803478 [hep-ph].

[252] D.-f. Hou, E. Wang, and U. W. Heinz, "n point functions at finite temperature," J. Phys. G24, 1861 (1998), arXiv:hep-th/9807118 [hep-th].

[253] D.-f. Hou, M. E. Carrington, R. Kobes, and U. W. Heinz, "Four point spectral functions and Ward identities in hot QED," Phys. Rev. D61, 085013 (2000), [Erratum: Phys. Rev.D67,049902(2003)], arXiv:hep-ph/9911494 [hep-ph].

[254] H. A. Weldon, "Thermal four-point functions with analytic extensions," Phys. Rev. D72, 096005 (2005).

[255] D. Bodeker and M. Sangel, "Lepton asymmetry rate from quantum field theory: NLO in the hierarchical limit," JCAP 1706, 052 (2017), arXiv:1702.02155 [hep-ph].

[256] G. Kallen, "On the definition of the Renormalization Constants in Quantum Electrodynamics," Helv. Phys. Acta 25, 417 (1952), [,509(1952)].

[257] H. Lehmann, "Über eigenschaften von ausbreitungsfunktionen und renormierungskonstanten quantisierter felder," Il Nuovo Cimento (1943-1954) 11, 342 (1954).

[258] L. Hormander, *An introduction to complex analysis in several variables* (Elsevier, 1973).

[259] T. S. Evans, "What is being calculated with thermal field theory?" in *Proceedings, 9th Lake Louise Winter Institute: Particle Physics and Cosmology (LLWI 1994): Lake Louise, Alberta, Canada, February 20-26, 1994* (1994) pp. 0343–352, arXiv:hep-ph/9404262 [hep-ph].

[260] H. Kamiya, A. Takemura, and H. Terao, "Ranking patterns of unfolding models of codimension one," Advances in Applied Mathematics 47, 379 (2011).

[261] N. Early, "Combinatorics and representation theory for generalized permutohedra i: simplicial plates," arXiv preprint arXiv:1611.06640 (2016).

[262] P. Lowdon, "Nonperturbative structure of the photon and gluon propagators," Phys. Rev. D96, 065013 (2017), arXiv:1702.02954 [hep-th].

[263] P. Lowdon, "Non-perturbative constraints on the quark and ghost propagators," Nucl. Phys. B935, 242 (2018), arXiv:1711.07569 [hep-th].

[264] N. N. Bogolyubov, A. A. Logunov, A. I. Oksak, and I. T. Todorov, *General principles of quantum field theory* (1990).

[265] G. Baym and N. D. Mermin, "Determination of thermodynamic green's functions," Journal of Mathematical Physics 2, 232 (1961).

[266] H. A. Weldon, "Simple Rules for Discontinuities in Finite Temperature Field Theory," Phys. Rev. D28, 2007 (1983).

[267] G. Markó, U. Reinosa, and Z. Szép, "Padé approximants and analytic continuation of Euclidean Φ-derivable approximations," Phys. Rev. D96, 036002 (2017), arXiv:1706.08726 [hep-ph].

[268] S. Jia and M. R. Pennington, "Exact Solutions to the Fermion Propagator Schwinger-Dyson Equation in Minkowski space with on-shell Renormalization for Quenched QED," Phys. Rev. D96, 036021 (2017), arXiv:1705.04523 [nucl-th].

[269] G. Leibbrandt, "Introduction to the Technique of Dimensional Regularization," Rev. Mod. Phys. 47, 849 (1975).

[270] A. K. Rajantie, "Feynman diagrams to three loops in three-dimensional field theory," Nucl. Phys. B480, 729 (1996), [Erratum: Nucl. Phys.B513,761(1998)], arXiv:hep-ph/9606216 [hep-ph].

[271] S.-x. Qin and D. H. Rischke, "Quark Spectral Function and Deconfinement at Nonzero Temperature," Phys. Rev. D88, 056007 (2013), arXiv:1304.6547 [nucl-th].

[272] D. Dudal, O. Oliveira, and P. J. Silva, "Källén-Lehmann spectroscopy for (un)physical degrees of freedom," Phys. Rev. D89, 014010 (2014), arXiv:1310.4069 [hep-lat].

[273] N. Christiansen, M. Haas, J. M. Pawlowski, and N. Strodthoff, "Transport Coefficients in Yang–Mills Theory and QCD," Phys. Rev. Lett. 115, 112002 (2015), arXiv:1411.7986 [hep-ph].

[274] A. Rothkopf, "Bayesian inference of nonpositive spectral functions in quantum field theory," Phys. Rev. D95, 056016 (2017), arXiv:1611.00482 [hep-ph].

[275] E.-M. Ilgenfritz, J. M. Pawlowski, A. Rothkopf, and A. Trunin, "Finite temperature gluon spectral functions from $N_f = 2 + 1 + 1$ lattice QCD," Eur. Phys. J. C78, 127 (2018), arXiv:1701.08610 [hep-lat].

[276] C. S. Fischer, J. M. Pawlowski, A. Rothkopf, and C. A. Welzbacher, "Bayesian analysis of quark spectral properties from the Dyson-Schwinger equation," Phys. Rev. D98, 014009 (2018), arXiv:1705.03207 [hep-ph].

[277] P. J. Silva, O. Oliveira, D. Dudal, and M. Roelfs, "Finite temperature gluon propagator in Landau gauge: non-zero Matsubara frequencies and spectral densities," *Proceedings, 35th International Symposium on Lattice Field Theory (Lattice 2017): Granada, Spain, June 18-24, 2017*, EPJ Web Conf. 175, 07038 (2018), arXiv:1711.02584 [hep-lat].

[278] D. Dudal, O. Oliveira, M. Roelfs, and P. Silva, "Spectral representation of lattice gluon and ghost propagators at zero temperature," Nucl. Phys. B952, 114912 (2020), arXiv:1901.05348 [hep-lat].

[279] N. Astrakhantsev, V. Braguta, and A. Kotov, "Temperature dependence of shear viscosity of $SU(3)$–gluodynamics within lattice simulation," JHEP 04, 101 (2017), arXiv:1701.02266 [hep-lat].

[280] S. Borsányi, Z. Fodor, M. Giordano, S. D. Katz, A. Pasztor, C. Ratti, A. Schäfer, K. K. Szabo, and B. Tóth, "High statistics lattice study of stress tensor correlators in pure $SU(3)$ gauge theory," Phys. Rev. D98, 014512 (2018), arXiv:1802.07718 [hep-lat].

[281] S. W. Mages, S. Borsányi, Z. Fodor, A. Schäfer, and K. Szabó, "Shear Viscosity from Lattice QCD," *Proceedings, 32nd International Symposium on Lattice Field Theory (Lattice 2014): Brookhaven, NY, USA, June 23-28, 2014*, PoS LATTICE2014, 232 (2015).

[282] N. Yu. Astrakhantsev, V. V. Braguta, and A. Yu. Kotov, "Study of shear viscosity of SU(2)-gluodynamics within lattice simulation," JHEP 09, 082 (2015), arXiv:1507.06225 [hep-lat].

[283] H. B. Meyer, "A Calculation of the bulk viscosity in SU(3) gluodynamics," Phys. Rev. Lett. 100, 162001 (2008), arXiv:0710.3717 [hep-lat].

[284] H. B. Meyer, "A Calculation of the shear viscosity in SU(3) gluodynamics," Phys. Rev. D76, 101701 (2007), arXiv:0704.1801 [hep-lat].

[285] M. Hobson and A. Lasenby, "The entropic prior for distributions with positive and negative values," Mon. Not. Roy. Astron. Soc. 298, 905 (1998), arXiv:astro-ph/9810240 [astro-ph].

[286] M. Jarrell and J. E. Gubernatis, "Bayesian inference and the analytic continuation of imaginary-time quantum Monte Carlo data," Phys. Rept. 269, 133 (1996).

[287] M. Asakawa, T. Hatsuda, and Y. Nakahara, "Maximum entropy analysis of the spectral functions in lattice QCD," Prog. Part. Nucl. Phys. 46, 459 (2001), arXiv:hep-lat/0011040 [hep-lat].

[288] A. C. Aguilar and J. Papavassiliou, "Gluon mass generation in the PT-BFM scheme," JHEP 12, 012 (2006), arXiv:hep-ph/0610040 [hep-ph].

[289] S.-x. Qin, L. Chang, Y.-x. Liu, and C. D. Roberts, "Quark spectral density and a strongly-coupled QGP," Phys. Rev. D84, 014017 (2011), arXiv:1010.4231 [nucl-th].

[290] N. Su and K. Tywoniuk, "Massless Mode and Positivity Violation in Hot QCD," Phys. Rev. Lett. 114, 161601 (2015), arXiv:1409.3203 [hep-ph].

[291] R. Oehme and W. Zimmermann, "Gauge field propagator and the number of fermion fields," Physical Review D 21, 1661 (1980).

[292] R. Oehme, "On superconvergence relations in quantum chromodynamics," Phys. Lett. B252, 641 (1990).

[293] R. Oehme and W.-T. Xu, "Asymptotic limits and sum rules for gauge field propagators," Phys. Lett. B333, 172 (1994), arXiv:hep-th/9406081 [hep-th].

[294] J. M. Cornwall, "Positivity violations in QCD," Mod. Phys. Lett. A28, 1330035 (2013), arXiv:1310.7897 [hep-ph].

[295] T. Kugo and I. Ojima, "Local Covariant Operator Formalism of Nonabelian Gauge Theories and Quark Confinement Problem," Prog. Theor. Phys. Suppl. 66, 1 (1979).

[296] R. Alkofer, W. Detmold, C. S. Fischer, and P. Maris, "Analytic properties of the Landau gauge gluon and quark propagators," Phys. Rev. D70, 014014 (2004), arXiv:hep-ph/0309077 [hep-ph].

[297] M. Q. Huber and L. von Smekal, "On the influence of three-point functions on the propagators of Landau gauge Yang-Mills theory," JHEP 04, 149 (2013), arXiv:1211.6092 [hep-th].

[298] A. C. Aguilar, D. Binosi, D. Ibañez, and J. Papavassiliou, "Effects of divergent ghost loops on the Green's functions of QCD," Phys. Rev. D89, 085008 (2014), arXiv:1312.1212 [hep-ph].

[299] M. Pelaez, M. Tissier, and N. Wschebor, "Three-point correlation functions in Yang-Mills theory," Phys. Rev. D88, 125003 (2013), arXiv:1310.2594 [hep-th].

[300] A. Blum, M. Q. Huber, M. Mitter, and L. von Smekal, "Gluonic three-point correlations in pure Landau gauge QCD," Phys. Rev. D89, 061703 (2014), arXiv:1401.0713 [hep-ph].

[301] U. Reinosa, J. Serreau, M. Tissier, and N. Wschebor, "How nonperturbative is the infrared regime of Landau gauge Yang-Mills correlators?" Phys. Rev. D96, 014005 (2017), arXiv:1703.04041 [hep-th].

[302] J. A. Gracey and R. M. Simms, "Renormalization of QCD in the interpolating momentum subtraction scheme at three loops," Phys. Rev. D97, 085016 (2018), arXiv:1801.10415 [hep-th].

[303] J. A. Gracey, "Symmetric point four-point functions at one loop in QCD," Phys. Rev. D95, 065013 (2017), arXiv:1703.01094 [hep-ph].

[304] J. A. Gracey, "Symmetric point quartic gluon vertex and momentum subtraction," Phys. Rev. D90, 025011 (2014), arXiv:1406.1618 [hep-ph].

[305] J. M. Bell and J. A. Gracey, "Maximal abelian and Curci-Ferrari gauges in momentum subtraction at three loops," Phys. Rev. D92, 125001 (2015), arXiv:1511.00854 [hep-th].

[306] J. A. Gracey, "Low momentum propagators at two loops in gluon mass model," J. Phys. A47, 445401 (2014), arXiv:1409.0455 [hep-ph].

[307] A. Cucchieri, A. Maas, and T. Mendes, "Infrared properties of propagators in Landau-gauge pure Yang-Mills theory at finite temperature," Phys. Rev. D75, 076003 (2007), arXiv:hep-lat/0702022 [hep-lat].

[308] A. Cucchieri and T. Mendes, "Constraints on the IR behavior of the gluon propagator in Yang-Mills theories," Phys. Rev. Lett. 100, 241601 (2008), arXiv:0712.3517 [hep-lat].

[309] A. Cucchieri and T. Mendes, "Constraints on the IR behavior of the ghost propagator in Yang-Mills theories," Phys. Rev. D78, 094503 (2008), arXiv:0804.2371 [hep-lat].

[310] A. Maas, J. M. Pawlowski, D. Spielmann, A. Sternbeck, and L. von Smekal, "Strong-coupling study of the Gribov ambiguity in lattice Landau gauge," Eur. Phys. J. C68, 183 (2010), arXiv:0912.4203 [hep-lat].

[311] A. Maas, "Constructing non-perturbative gauges using correlation functions," Phys. Lett. B689, 107 (2010), arXiv:0907.5185 [hep-lat].

[312] R. Aouane, V. G. Bornyakov, E. M. Ilgenfritz, V. K. Mitrjushkin, M. Muller-Preussker, and A. Sternbeck, "Landau gauge gluon and ghost propagators at finite temperature from quenched lattice QCD," Phys. Rev. D85, 034501 (2012), arXiv:1108.1735 [hep-lat].

[313] A. Maas, J. M. Pawlowski, L. von Smekal, and D. Spielmann, "The Gluon propagator close to criticality," Phys. Rev. D85, 034037 (2012), arXiv:1110.6340 [hep-lat].

[314] A. Cucchieri, D. Dudal, T. Mendes, and N. Vandersickel, "Massive gluon propagator at zero and finite temperature," (2012), arXiv:1202.0639 [hep-lat].

[315] A. Sternbeck and M. Müller-Preussker, "Lattice evidence for the family of decoupling solutions of Landau gauge Yang-Mills theory," Phys. Lett. B726, 396 (2013), arXiv:1211.3057 [hep-lat].

[316] P. J. Silva, O. Oliveira, P. Bicudo, and N. Cardoso, "Gluon screening mass at finite temperature from the Landau gauge gluon propagator in lattice QCD," Phys. Rev. D89, 074503 (2014), arXiv:1310.5629 [hep-lat].

[317] A. Maas, "Some more details of minimal-Landau-gauge SU(2) Yang-Mills propagators," Phys. Rev. D91, 034502 (2015), arXiv:1402.5050 [hep-lat].

[318] A. Maas, "More on the properties of the first Gribov region in Landau gauge," Phys. Rev. D93, 054504 (2016), arXiv:1510.08407 [hep-lat].

[319] A. Athenodorou, D. Binosi, P. Boucaud, F. De Soto, J. Papavassiliou, J. Rodriguez-Quintero, and S. Zafeiropoulos, "On the zero crossing of the three-gluon vertex," Phys. Lett. B761, 444 (2016), arXiv:1607.01278 [hep-ph].

[320] A. G. Duarte, O. Oliveira, and P. J. Silva, "Lattice Gluon and Ghost Propagators, and the Strong Coupling in Pure SU(3) Yang-Mills Theory: Finite Lattice Spacing and Volume Effects," Phys. Rev. D94, 014502 (2016), arXiv:1605.00594 [hep-lat].

[321] P. Boucaud, F. De Soto, J. Rodríguez-Quintero, and S. Zafeiropoulos, "Comment on "Lattice gluon and ghost propagators and the strong coupling in pure $SU(3)$ Yang-Mills theory: Finite lattice spacing and volume effects"," Phys. Rev. D96, 098501 (2017), arXiv:1704.02053 [hep-lat].

[322] P. Boucaud, F. De Soto, J. Rodríguez-Quintero, and S. Zafeiropoulos, "Refining the detection of the zero crossing for the three-gluon vertex in symmetric and asymmetric momentum subtraction schemes," Phys. Rev. D95, 114503 (2017), arXiv:1701.07390 [hep-lat].

[323] P. Boucaud, F. De Soto, K. Raya, J. Rodríguez-Quintero, and S. Zafeiropoulos, "Discretization effects on renormalized gauge-field Green's functions, scale setting, and the gluon mass," Phys. Rev. D98, 114515 (2018), arXiv:1809.05776 [hep-ph].

[324] S. Zafeiropoulos, P. Boucaud, F. De Soto, J. Rodríguez-Quintero, and J. Segovia, "Strong Running Coupling from the Gauge Sector of Domain Wall Lattice QCD with Physical Quark Masses," Phys. Rev. Lett. 122, 162002 (2019), arXiv:1902.08148 [hep-ph].

[325] A. C. Aguilar, F. De Soto, M. N. Ferreira, J. Papavassiliou, J. Rodríguez-Quintero, and S. Zafeiropoulos, "Gluon propagator and three-gluon vertex with dynamical quarks," (2019), arXiv:1912.12086 [hep-ph].

[326] F. Gao, S.-X. Qin, C. D. Roberts, and J. Rodriguez-Quintero, "Locating the Gribov horizon," Phys. Rev. D97, 034010 (2018), arXiv:1706.04681 [hep-ph].

[327] D. Dudal, O. Oliveira, and P. J. Silva, "High precision statistical Landau gauge lattice gluon propagator computation vs. the Gribov–Zwanziger approach," Annals Phys. 397, 351 (2018), arXiv:1803.02281 [hep-lat].

[328] S. W. Li, P. Lowdon, O. Oliveira, and P. J. Silva, "The generalised infrared structure of the gluon propagator," Phys. Lett. B803, 135329 (2020), arXiv:1907.10073 [hep-th].

[329] S. Strauss, C. S. Fischer, and C. Kellermann, "Analytic structure of the Landau gauge gluon propagator," Phys. Rev. Lett. 109, 252001 (2012), arXiv:1208.6239 [hep-ph].

[330] L. Baulieu, D. Dudal, M. S. Guimaraes, M. Q. Huber, S. P. Sorella, N. Vandersickel, and D. Zwanziger, "Gribov horizon and i-particles: About a toy model and the construction of physical operators," Phys. Rev. D82, 025021 (2010), arXiv:0912.5153 [hep-th].

[331] G. Curci and R. Ferrari, "The Unitarity Problem and the Zero-Mass Limit for a Model of Massive Yang-Mills Theory," Nuovo Cim. A35, 1 (1976), [Erratum: Nuovo Cim.A47,555(1978)].

[332] M. Tissier and N. Wschebor, "Infrared propagators of Yang-Mills theory from perturbation theory," Phys. Rev. D82, 101701 (2010), arXiv:1004.1607 [hep-ph].

[333] M. Tissier and N. Wschebor, "An Infrared Safe perturbative approach to Yang-Mills correlators," Phys. Rev. D84, 045018 (2011), arXiv:1105.2475 [hep-th].

[334] J. Serreau and M. Tissier, "Lifting the Gribov ambiguity in Yang-Mills theories," Phys. Lett. B712, 97 (2012), arXiv:1202.3432 [hep-th].

[335] F. Siringo, "Perturbative study of Yang-Mills theory in the infrared," (2015), arXiv:1509.05891 [hep-ph].

[336] F. Siringo, "Analytical study of Yang–Mills theory in the infrared from first principles," Nucl. Phys. B907, 572 (2016), arXiv:1511.01015 [hep-ph].

[337] F. Siringo, "Quasigluon lifetime and confinement from first principles," Phys. Rev. D96, 114020 (2017), arXiv:1705.06160 [hep-ph].

[338] B. Carpenter, A. Gelman, M. Hoffman, D. Lee, B. Goodrich, M. Betancourt, M. Brubaker, J. Guo, P. Li, and A. Riddell, "Stan: A probabilistic programming language," Journal of Statistical Software, Articles 76, 1 (2017).

[339] A. K. Cyrol, M. Mitter, J. M. Pawlowski, and N. Strodthoff, "Nonperturbative finite-temperature Yang-Mills theory," Phys. Rev. D97, 054015 (2018), arXiv:1708.03482 [hep-ph].

[340] D. Guest, K. Cranmer, and D. Whiteson, "Deep Learning and its Application to LHC Physics," Ann. Rev. Nucl. Part. Sci. 68, 161 (2018), arXiv:1806.11484 [hep-ex].

[341] A. Radovic, M. Williams, D. Rousseau, M. Kagan, D. Bonacorsi, A. Himmel, A. Aurisano, K. Terao, and T. Wongjirad, "Machine learning at the energy and intensity frontiers of particle physics," Nature 560, 41 (2018).

[342] Y. LeCun, Y. Bengio, and G. Hinton, "Deep learning," Nature 521, 436 (2015).

[343] J. Schmidhuber, "Deep learning in neural networks: An overview," Neural networks 61, 85 (2015).

[344] J. Carrasquilla and R. G. Melko, "Machine learning phases of matter," Nature Physics 13, 431 (2017).

[345] P. E. Shanahan, D. Trewartha, and W. Detmold, "Machine learning action parameters in lattice quantum chromodynamics," Phys. Rev. D 97, 094506 (2018).

[346] G. Carleo and M. Troyer, "Solving the quantum many-body problem with artificial neural networks," Science 355, 602 (2017).

[347] S. J. Wetzel, "Unsupervised learning of phase transitions: From principal component analysis to variational autoencoders," Phys. Rev. E 96, 022140 (2017).

[348] S. J. Wetzel and M. Scherzer, "Machine learning of explicit order parameters: From the ising model to su(2) lattice gauge theory," Phys. Rev. B 96, 184410 (2017).

[349] L. Wang, "Discovering phase transitions with unsupervised learning," Phys. Rev. B 94, 195105 (2016).

[350] W. Hu, R. R. P. Singh, and R. T. Scalettar, "Discovering phases, phase transitions, and crossovers through unsupervised machine learning: A critical examination," Phys. Rev. E 95, 062122 (2017).

[351] L. Huang and L. Wang, "Accelerated monte carlo simulations with restricted boltzmann machines," Phys. Rev. B 95, 035105 (2017).

[352] J. Liu, Y. Qi, Z. Y. Meng, and L. Fu, "Self-learning monte carlo method," Phys. Rev. B 95, 041101 (2017).

[353] J. Karpie, K. Orginos, A. Rothkopf, and S. Zafeiropoulos, "Reconstructing parton distribution functions from Ioffe time data: from Bayesian methods to Neural Networks," JHEP 04, 057 (2019), arXiv:1901.05408 [hep-lat].

[354] J. M. Urban and J. M. Pawlowski, "Reducing Autocorrelation Times in Lattice Simulations with Generative Adversarial Networks," (2018), arXiv:1811.03533 [hep-lat].

[355] Y. Burnier and A. Rothkopf, "Bayesian Approach to Spectral Function Reconstruction for Euclidean Quantum Field Theories," Phys. Rev. Lett. 111, 182003 (2013), arXiv:1307.6106 [hep-lat].

[356] A. Rothkopf, "Bayesian techniques and applications to QCD," *Proceedings, 13th Conference on Quark Confinement and the Hadron Spectrum (Confinement XIII): Maynooth, Ireland, July 31-August 06, 2018*, PoS Confinement2018, 026 (2018), arXiv:1903.02293 [hep-ph].

[357] V. Shah and C. Hegde, "Solving linear inverse problems using gan priors: An algorithm with provable guarantees," in *2018 IEEE International Conference on Acoustics, Speech and Signal Processing (ICASSP)* (IEEE, 2018) pp. 4609–4613.

[358] H. Li, J. Schwab, S. Antholzer, and M. Haltmeier, "Nett: Solving inverse problems with deep neural networks," Inverse Problems (2020).

[359] R. Anirudh, J. J. Thiagarajan, B. Kailkhura, and T. Bremer, "An unsupervised approach to solving inverse problems using generative adversarial networks," arXiv preprint arXiv:1805.07281 (2018).

[360] L. Ardizzone, J. Kruse, S. Wirkert, D. Rahner, E. W. Pellegrini, R. S. Klessen, L. Maier-Hein, C. Rother, and U. Köthe, "Analyzing inverse problems with invertible neural networks," arXiv preprint arXiv:1808.04730 (2018).

[361] R. Fournier, L. Wang, O. V. Yazyev, and Q. Wu, "Artificial neural network approach to the analytic continuation problem," Physical Review Letters 124, 056401 (2020).

[362] H. Yoon, J.-H. Sim, and M. J. Han, "Analytic continuation via domain knowledge free machine learning," Physical Review B 98, 245101 (2018).

[363] R. Oehme and W. Zimmermann, "Gauge Field Propagator and the Number of Fermion Fields," Phys. Rev. D21, 1661 (1980).

[364] C. N. d. Santos, K. Wadhawan, and B. Zhou, "Learning loss functions for semi-supervised learning via discriminative adversarial networks," arXiv preprint arXiv:1707.02198 (2017).

[365] L. Wu, F. Tian, Y. Xia, Y. Fan, T. Qin, L. Jian-Huang, and T.-Y. Liu, "Learning to teach with dynamic loss functions," in *Advances in Neural Information Processing Systems* (2018) pp. 6466–6477.

[366] T. K. Herbst, J. M. Pawlowski, and B.-J. Schaefer, "The phase structure of the Polyakov–quark–meson model beyond mean field," Phys. Lett. B696, 58 (2011), arXiv:1008.0081 [hep-ph].

[367] V. Skokov, B. Stokic, B. Friman, and K. Redlich, "Meson fluctuations and thermodynamics of the Polyakov loop extended quark-meson model," Phys. Rev. C82, 015206 (2010), arXiv:1004.2665 [hep-ph].

[368] V. Skokov, B. Friman, and K. Redlich, "Quark number fluctuations in the Polyakov loop-extended quark-meson model at finite baryon density," Phys. Rev. C83, 054904 (2011), arXiv:1008.4570 [hep-ph].

[369] T. K. Herbst, J. M. Pawlowski, and B.-J. Schaefer, "Phase structure and thermodynamics of QCD," Phys. Rev. D88, 014007 (2013), arXiv:1302.1426 [hep-ph].

[370] M. Drews and W. Weise, "Functional renormalization group approach to neutron matter," Phys. Lett. B738, 187 (2014), arXiv:1404.0882 [nucl-th].

[371] R.-A. Tripolt, B.-J. Schaefer, L. von Smekal, and J. Wambach, "Low-temperature behavior of the quark-meson model," Phys. Rev. D97, 034022 (2018), arXiv:1709.05991 [hep-ph].

[372] M. Laine and A. Vuorinen, "Basics of Thermal Field Theory," Lect. Notes Phys. 925, pp.1 (2016), arXiv:1701.01554 [hep-ph].

[373] M. Luzum and P. Romatschke, "Conformal Relativistic Viscous Hydrodynamics: Applications to RHIC results at s(NN)**(1/2) = 200-GeV," Phys. Rev. C78, 034915 (2008), [Erratum: Phys. Rev.C79,039903(2009)], arXiv:0804.4015 [nucl-th].

[374] D. A. Teaney, "Viscous Hydrodynamics and the Quark Gluon Plasma," in *Quark-gluon plasma 4*, edited by R. C. Hwa and X.-N. Wang (2010) pp. 207–266, arXiv:0905.2433 [nucl-th].

[375] C. Gale, S. Jeon, and B. Schenke, "Hydrodynamic Modeling of Heavy-Ion Collisions," Int. J. Mod. Phys. A28, 1340011 (2013), arXiv:1301.5893 [nucl-th].

[376] R. Derradi de Souza, T. Koide, and T. Kodama, "Hydrodynamic Approaches in Relativistic Heavy Ion Reactions," Prog. Part. Nucl. Phys. 86, 35 (2016), arXiv:1506.03863 [nucl-th].

[377] A. Dubla, S. Masciocchi, J. M. Pawlowski, B. Schenke, C. Shen, and J. Stachel, "Towards QCD-assisted hydrodynamics for heavy-ion collision phenomenology," Nucl. Phys. A979, 251 (2018), arXiv:1805.02985 [nucl-th].

[378] W. Florkowski, "Basic phenomenology for relativistic heavy-ion collisions," *54th Cracow School of Theoretical Physics: QCD meets experiment: Zakopane, Poland, June 12-20, 2014*, Acta Phys. Polon. B45, 2329 (2014), arXiv:1410.7904 [nucl-th].

[379] P. Braun-Munzinger, V. Koch, T. Schäfer, and J. Stachel, "Properties of hot and dense matter from relativistic heavy ion collisions," Phys. Rept. 621, 76 (2016), arXiv:1510.00442 [nucl-th].

[380] R. Kubo, "Statistical-mechanical theory of irreversible processes. i. general theory and simple applications to magnetic and conduction problems," Journal of the Physical Society of Japan 12, 570 (1957).

[381] A. Hosoya, M.-a. Sakagami, and M. Takao, "Nonequilibrium thermodynamics in field theory: Transport coefficients," Annals of Physics 154, 229 (1984).

[382] M. Martinez, T. Schäfer, and V. Skokov, "Critical behavior of the bulk viscosity in QCD," Phys. Rev. D100, 074017 (2019), arXiv:1906.11306 [hep-ph].

[383] M. Haas, *Spectral functions in finite temperature SU(3) gauge theory and applications to transport phenomena*, Ph.D. thesis, U. Heidelberg (main) (2014).

[384] N. Christiansen, *Non-Perturbative Aspects of QuantumField Theory:From the Quark-Gluon Plasma toQuantum Gravity.*, Ph.D. thesis, U. Heidelberg (main) (2015).

[385] A. V. Nesterenko, "Quark - anti-quark potential in the analytic approach to QCD," Phys. Rev. D62, 094028 (2000), arXiv:hep-ph/9912351 [hep-ph].

[386] S. Borsanyi, G. Endrodi, Z. Fodor, S. D. Katz, and K. K. Szabo, "Precision SU(3) lattice thermodynamics for a large temperature range," JHEP 07, 056 (2012), arXiv:1204.6184 [hep-lat].

[387] P. Kovtun, D. T. Son, and A. O. Starinets, "Viscosity in strongly interacting quantum field theories from black hole physics," Phys. Rev. Lett. 94, 111601 (2005), arXiv:hep-th/0405231 [hep-th].

[388] B. Abelev *et al.* (ALICE), "Centrality dependence of π, K, p production in Pb-Pb collisions at $\sqrt{s_{NN}} = 2.76$ TeV," Phys. Rev. C88, 044910 (2013), arXiv:1303.0737 [hep-ex].

[389] J. Adam *et al.* (ALICE), "Centrality dependence of the charged-particle multiplicity density at midrapidity in Pb-Pb collisions at $\sqrt{s_{\rm NN}} = 5.02$ TeV," Phys. Rev. Lett. 116, 222302 (2016), arXiv:1512.06104 [nucl-ex].

[390] A. Aduszkiewicz *et al.* (NA61/SHINE), "Multiplicity and transverse momentum fluctuations in inelastic proton–proton interactions at the CERN Super Proton Synchrotron," Eur. Phys. J. C76, 635 (2016), arXiv:1510.00163 [hep-ex].

[391] M. Gazdzicki and A. Rybicki (NA61/SHINE), "Overview of Results from NA61/SHINE: Uncovering Critical Structures," *Proceedings, 25th Cracow Epiphany Conference on Advances in Heavy Ion Physics (Epiphany 2019): Cracow, Poland, January 8-11, 2019*, Acta Phys. Polon. B50, 1057 (2019).

[392] J. Adam *et al.* (STAR), "Polarization of Λ ($\bar{\Lambda}$) hyperons along the beam direction in Au+Au collisions at $\sqrt{s_{NN}} = 200$ GeV," Phys. Rev. Lett. 123, 132301 (2019), arXiv:1905.11917 [nucl-ex].

[393] J. Adam *et al.* (STAR), "Net-proton number fluctuations and the Quantum Chromodynamics critical point," (2020), arXiv:2001.02852 [nucl-ex].

[394] J. Adam *et al.* (STAR), "Beam energy dependence of net-Λ fluctuations measured by the STAR experiment at RHIC," (2020), arXiv:2001.06419 [nucl-ex].

[395] J. Adamczewski-Musch *et al.* (HADES), "Proton number fluctuations in $\sqrt{s_{NN}} =$ 2.4 GeV Au+Au collisions studied with HADES," (2020), arXiv:2002.08701 [nucl-ex].

[396] W.-j. Fu, J. M. Pawlowski, F. Rennecke, and B.-J. Schaefer, "Baryon number fluctuations at finite temperature and density," Phys. Rev. D94, 116020 (2016), arXiv:1608.04302 [hep-ph].

[397] V. Vovchenko, C. Greiner, V. Koch, and H. Stoecker, "Critical point signatures in the cluster expansion in fugacities," Phys. Rev. D101, 014015 (2020), arXiv:1909.02276 [hep-ph].

[398] D. Devetak, A. Dubla, S. Floerchinger, E. Grossi, S. Masciocchi, A. Mazeliauskas, and I. Selyuzhenkov, "Global fluid fits to identified particle transverse momentum spectra from heavy-ion collisions at the Large Hadron Collider," (2019), arXiv:1909.10485 [hep-ph].

[399] F. Rennecke, "Review of Critical Point Searches and Beam-Energy Studies," *Proceedings, Hot Quarks 2018: Workshop for Young Scientists on the Physics of Ultrarelativistic Nucleus-Nucleus Collisions (HQ2018): De Krim, Texel Island, Netherlands, September 7-14, 2018*, MDPI Proc. 10, 8 (2019).

[400] V. Koch, A. Bzdak, D. Oliinychenko, and J. Steinheimer, "The QCD phase diagram and statistics friendly distributions," in *28th International Conference on Ultrarelativistic Nucleus-Nucleus Collisions (Quark Matter 2019) Wuhan, China, November 4-9, 2019* (2020) arXiv:2001.11079 [nucl-th].

[401] M. A. Stephanov, "Non-Gaussian fluctuations near the QCD critical point," Phys. Rev. Lett. 102, 032301 (2009), arXiv:0809.3450 [hep-ph].

[402] M. Asakawa, S. Ejiri, and M. Kitazawa, "Third moments of conserved charges as probes of QCD phase structure," Phys. Rev. Lett. 103, 262301 (2009), arXiv:0904.2089 [nucl-th].

[403] B.-J. Schaefer and J. Wambach, "Susceptibilities near the QCD (tri)critical point," Phys. Rev. D75, 085015 (2007), arXiv:hep-ph/0603256 [hep-ph].

[404] M. Nahrgang, S. Leupold, C. Herold, and M. Bleicher, "Nonequilibrium chiral fluid dynamics including dissipation and noise," Phys. Rev. C84, 024912 (2011), arXiv:1105.0622 [nucl-th].

[405] M. Nahrgang, S. Leupold, and M. Bleicher, "Equilibration and relaxation times at the chiral phase transition including reheating," Phys. Lett. B711, 109 (2012), arXiv:1105.1396 [nucl-th].

[406] C. Herold, M. Nahrgang, Y. Yan, and C. Kobdaj, "Dynamical net-proton fluctuations near a QCD critical point," Phys. Rev. C93, 021902 (2016), arXiv:1601.04839 [hep-ph].

[407] M. Nahrgang, M. Bluhm, T. Schaefer, and S. A. Bass, "Diffusive dynamics of critical fluctuations near the QCD critical point," Phys. Rev. D99, 116015 (2019), arXiv:1804.05728 [nucl-th].

[408] M. Agah Nouhou, M. Bluhm, A. Borer, M. Nahrgang, T. Sami, and N. Touroux, "Finite size effects on cumulants of the critical mode," *Proceedings, 18th Hellenic School and Workshops on Elementary Particle Physics and Gravity (CORFU2018): Corfu, Corfu, Greece*, PoS CORFU2018, 179 (2019), arXiv:1906.02647 [nucl-th].

[409] M. Bluhm and M. Nahrgang, "Time-evolution of net-baryon density fluctuations across the QCD critical region," in *18th International Conference on Strangeness in Quark Matter (SQM 2019) Bari, Italy, June 10-15, 2019* (2019) arXiv:1911.08911 [nucl-th].

[410] M. Kitazawa, G. Pihan, N. Touroux, M. Bluhm, and M. Nahrgang, "Critical fluctuations in a dynamically expanding heavy-ion collision," in *28th International Conference on Ultrarelativistic Nucleus-Nucleus Collisions (Quark Matter 2019) Wuhan, China, November 4-9, 2019* (2020) arXiv:2002.07322 [nucl-th].

[411] W.-j. Fu, J. M. Pawlowski, and F. Rennecke, "Strangeness Neutrality and QCD Thermodynamics," (2018), arXiv:1808.00410 [hep-ph].

[412] W.-j. Fu, J. M. Pawlowski, and F. Rennecke, "Strangeness neutrality and baryon-strangeness correlations," Phys. Rev. D100, 111501 (2019), arXiv:1809.01594 [hep-ph].

[413] F. Rennecke, W.-j. Fu, and J. M. Pawlowski, "Strangeness neutrality and the QCD phase diagram," *Proceedings, 18th Hellenic School and Workshops on Elementary Particle Physics and Gravity (CORFU2018): Corfu, Greece, August 18-September 28, 2018*, PoS CORFU2018, 182 (2019), arXiv:1907.08179 [hep-ph].

[414] R. Courant and D. Hilbert, *Methods of Mathematical Physics*, Methods of Mathematical Physics No. v. 2 (Interscience Publishers, 1962).

[415] C. Gauss, "Disquisitiones generales circa seriem infinitam 1+ α β/γx+$\cdots$," Gesammelte Werke 3, 1866 (1812).

[416] A. Gelb and E. Tadmor, "Detection of edges in spectral data ii. nonlinear enhancement," SIAM Journal on Numerical Analysis 38, 1389 (2000).

[417] A. Sheshadri and A. Jameson, "Shock detection and capturing methods for high order discontinuous-galerkin finite element methods," in *32nd AIAA Applied Aerodynamics Conference* (2014) p. 2688.

[418] A. K. Cyrol, M. Mitter, and N. Strodthoff, "FormTracer - A Mathematica Tracing Package Using FORM," Comput. Phys. Commun. 219, 346 (2017), arXiv:1610.09331 [hep-ph].

[419] J. Kuipers, T. Ueda, J. A. M. Vermaseren, and J. Vollinga, "FORM version 4.0," Comput. Phys. Commun. 184, 1453 (2013), arXiv:1203.6543 [cs.SC].

[420] Stan Development Team, "Pystan: the python interface to stan, version 2.17.1.0," `http://mc-stan.org` (2018).

[421] P. Lowdon, "Dyson–Schwinger equation constraints on the gluon propagator in BRST quantised QCD," Phys. Lett. B786, 399 (2018), arXiv:1801.09337 [hep-th].

[422] G. Backus and F. Gilbert, "The resolving power of gross earth data," Geophysical Journal International 16, 169 (1968).

[423] G. Backus and F. Gilbert, "Uniqueness in the inversion of inaccurate gross earth data," Philosophical Transactions of the Royal Society of London. Series A, Mathematical and Physical Sciences 266, 123 (1970).

[424] D. Binosi and R.-A. Tripolt, "Spectral functions of confined particles," Phys. Lett. B801, 135171 (2020), arXiv:1904.08172 [hep-ph].

[425] Stan Development Team. 2017, "Rstan: the r interface to stan. r package version 2.16.2." http://mc-stan.org.